Distribution Agreement

Signature:

______________________________________ ____________
Allisandra Kaeleen Rha Date

MUTUALISM IN NUCLEIC ACID/PEPTIDE DOMAIN ARRAYS: IMPLICATIONS FOR ORIGINS OF LIFE, NANOTECHNOLOGY, AND DISEASE

By

Allisandra K. Rha

Doctor of Philosophy

Graduate Division of Biological and Biomedical Science

Biochemistry, Cell, and Developmental Biology

____
David G. Lynn
Advisor

Committee Members:

____
Dr. Roger Deal

____
Dr. Michael Koval

____
Dr. Ichiro Matsumura

____
Dr. Eric Ortlund

Accepted:

____
Lisa A. Tedesco, Ph.D.
Dean of the James T. Laney School of Graduate Studies

____
Date

MUTUALISM IN NUCLEIC ACID/PEPTIDE DOMAIN ARRAYS: IMPLICATIONS FOR ORIGINS OF LIFE, NANOTECHNOLOGY, AND DISEASE

By

Allisandra K. Rha
B.S., Eastern Nazarene College, 2012

Advisor: David G. Lynn, Ph.D.

An abstract of
A dissertation submitted to the Faculty of the James T. Laney School of Graduate
Studies of Emory University in partial fulfillment of the requirements for the degree of
Doctor of Philosophy in Biochemistry, Cell, and Developmental Biology
2017

Abstract

MUTUALISM IN NUCLEIC ACID/PEPTIDE DOMAIN ARRAYS: IMPLICATIONS FOR ORIGINS OF LIFE, NANOTECHNOLOGY, AND DISEASE

By Allisandra K. Rha

The intricate connections between nucleic acids and proteins in the cell produces a network of spatially and temporally regulated mutualisms. These mutualisms likely preceded cellular life, and are essential to the central dogma. The ribosome, a conglomerate of proteins and ribosomal RNAs is conserved and regarded as the Darwinian threshold for cellular life. Less complex mutualisms are expected to have preceded the ribosome and supported the first cellular networks in protocells. The stabilization and propagation of nucleic acids with homogeneous 5'-3' linkages, a necessary prerequisite to the organization of a replicative system, was likely mediated by proteins or small peptides that served to protect nucleic acids from the harsh prebiotic environment. Peptide assemblies, which may have formed prebiotically upon concentration of peptides as short as two amino acids in a discrete area, are being explored as scaffolds for specific nucleic acid elongation. The use of peptide assemblies as scaffolds is also exploited in nanotechnology where the production of peptide hydrogels for tissue engineering continues. The complementarity of nucleic acids is manipulated in the construction of DNA origami, where its digital-like interactions are fine-tuned for the development of responsive systems. The diversity of DNA secondary structures and their context dependence extends these efforts. Guanine quadruplexes, which demonstrate efficient electron transfer are being explored as wires in bionanocircuitry. Combination of the scaffolding properties of peptide assemblies and the diverse complementary folding landscape of DNA, highlights the fabrication of artificial mutualisms. Extant mutualisms between DNA and RNA binding proteins and their targets in the cell, are responsible for the spatiotemporal regulation of cellular information flow. RNA is processed in membraneless organelles known as ribonucleoprotein granules (RNP). The liquid-liquid phase transitions that characterize the assembly and disassembly of RNP granules is mediated by RNA binding proteins with low complexity domains (LCD). Disruption of transient interactions between LCDs, or seeding of infectious domains by reversible LCD amyloids, is considered a contributor to altered ribostasis in protein misfolding diseases where deposition of RNA at disease lesions has not yet been explained. Here we explore these diverse mutualisms through structural characterization of a novel RNA/peptide co-assembly.

MUTUALISM IN NUCLEIC ACID/PEPTIDE DOMAIN ARRAYS: IMPLICATIONS FOR ORIGINS OF LIFE, NANOTECHNOLOGY, AND DISEASE

By

Allisandra K. Rha

B.S., Eastern Nazarene College, 2012

Advisor: David G. Lynn, Ph.D.

A dissertation submitted to the Faculty of the James T. Laney School of Graduate Studies of Emory University in partial fulfillment of the requirements for the degree of Doctor of Philosophy in Biochemistry, Cell, and Developmental Biology

2017

Table of Contents

Figures

Chapter 1

Chapter 2

Chapter 3

Chapter 4

Chapter 5

Chapter 6

Tables

Chapter 1: Looked at life from both sides now

Original publication source: Smith, J. E., Mowles, A. K., Mehta, A. K., Lynn, D. G. Looked at life from both sides now. *Life* **4,** 887-902 (2014).

From Up and Down, and Still Somehow

Life may best be understood as information on a nanoscale [1]. The sequences of DNA and the vast repertoire of catalytic and structural forms of proteins constitute a dynamic evolving network easily seen in the top–down causality of the tree of life. Most remarkable is the information flow achieved with two biopolymers, so universal as to be termed the Central Dogma of biology [2], locked in mutualistic synergy. Hydrogen-bond donor/acceptor pairs bias the folding pathways of nucleic acids to optimally store "digital-like" information in the genome. In contrast, protein folding is context dependent, coupling "analog-like" conformational distributions with inputs from the changing environments that drive evolution. Coordinating these analog and digital forms of information has been heralded as the Darwinian Threshold of cellular life [3].

Early experiments [4] showed that amino acids and peptides are readily accessible from simple gaseous precursors, providing a source for the building blocks of biogenesis. The discovery that nucleic acids can serve as catalysts, ribozymes [5,6] and deoxyribozymes [7], proved that these polymers could carry both analog and digital functions, and gave substance to an RNA World hypothesis for early life [8]. Genome sequencing from across all three domains of life and the resulting top–down understanding of the progressive growth of molecular information over time was traced back to the critical threshold for cellular life as the emergence of the ribosome [3]. This organelle, the digital-to-analog converter of the Central Dogma, is itself a supramolecular RNA/protein co-assembly [9] composed of integrated biopolymers that emerged simultaneously [10,11]. Today messenger RNA, the intermediate carrier of genetic information, serves in mutualistic synergy with proteins at every stage of the process. From mRNA-binding proteins during transcription to nuclear membrane transport, from being spliced, capped and polyadenylated by ribonucleoprotein complexes (RNPs) to the mRNA-protein complexes necessary for translation in the ribosome, this positive reciprocal relationship between nucleic acids and proteins within dynamic networks provides the foundation for genomic biological information flow [12].

The origins of this protein/nucleic acid biopolymer mutualism can now be reconsidered in light of the discovery of protein-only infectious agents known as prions [13]. Prion proteins undergo Darwinian-like selection and propagation from a clonal population of diverse assembled phases existing within a cellular matrix. While the basis for such selection in disease remains unknown, the process achieves gain-of-function phenotypes from folding and assembly of cross-β forms [14–16] (Figure 1). These scaffolds also serve as adhesives in bacterial biofilms [17,18], as heritable elements in fungi [19], and in one, the Het-s amyloid, the assembly mediates self/non-self recognition to control incompatible fusions [20]. Increasingly beneficial functions of amyloids are being found in multicellular organisms, including the protective egg envelope of *Austrofundulus limnaeus* embryos [21], barnacle adhesives [22], weevil cocoons [23], and *Crysopa flava* (lace-wing fly) silks [15]. Orb2 amyloid oligomers contribute to long-term memory of fruit flies [24] and the Pmel17 amyloid fibers appear to play a role in directing the polymerization of the skin pigment polymer melanin [25]. These current functions of amyloid highlight the evolutionary potential of assembled protein phases and underscore the possibility of independently evolving nucleic acid and protein biopolymers, all of which could enrich the obligate mutualisms seen in biological information networks.

As Joni Mitchell sang over 40 years ago, “I have looked at life from both sides now..., and still somehow..., I don't know life at all". Since that time, the structural and functional analysis of both sides of biological information flow have revealed the richly dynamic far-from-equilibrium networks of nucleic acids and peptides that enable biopolymer evolution. Here we review some of this growth in the context of chemical evolution, looking at life from the above and below that is today informing the potential for the sustained emergence of function in a wider array of dynamic chemical networks.

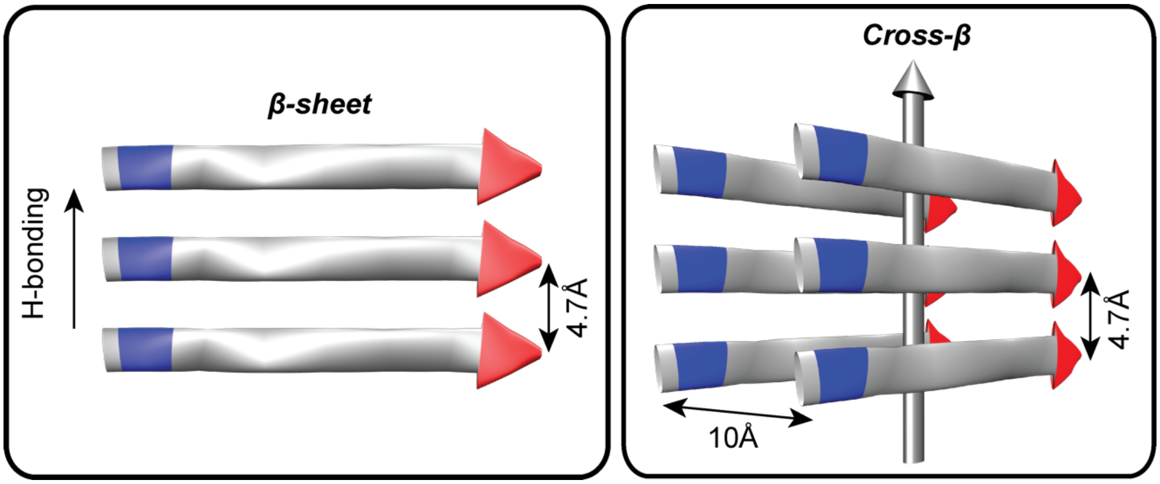

Figure 1-1. The architectural core of prions and amyloids. *Fibers are defined both by the length of the H-bonded β-strands and β-sheet stacking, or lamination. The distance between two H-bonded peptides in a β-sheet is 4.7Å and the approximate distance between laminated β-sheets is 10Å. The amino (N) terminus is colored blue and the carboxy (C) terminus is colored red. The vertical grey arrow indicates the H-bonding direction and the typical direction of the amyloid fiber long axis.*

Biopolymer Diversity

Discrete geometries of hydrogen-bonding donor and acceptor pairs direct genomic information, achieving "digital-like" coding fidelity. In this case, functional diversity is accumulated through mutations within the nucleic acid polymer sequence that is expressed in phenotypic variations mapped to the tree of life. The iconic right-handed B-DNA double helix [26,27] can adopt other antiparallel double helix conformations, including A-DNA, Z-DNA and A-RNA, and their biological roles are still being explored [28–30]. Bulges, hairpins, and cruciform conformations further contribute to the structural diversity and extend the possible functions of this scaffold [31,32]. The ability of nucleic acids to fold into polymorphic non-canonical structures in response to metal coordination (G-quadruplexes) and pH (i-motif) [33–35], and the growing evidence for these structures existing *in vivo* [36,37], have continued to expand the functional possibilities [38,39]. Applications of such structures will be explored in Chapter 3. The extension to new nucleic acid catalysts [5–7] through *in vitro*-directed evolution has been reviewed [40–43]. Clearly the nucleic acid scaffold has remarkable functional potential for both information storage and processing.

Proteins, with an even greater diversity in side chain functionality, are acutely sensitive to amino acid substitutions and are environmentally responsive in their folding dynamics. The polyamide backbone can access α-helices, β-sheets, and turns directed by non-covalent interactions ranging from Van der Waals, hydrophobic effects, aromatic stacking, π-cation interactions, hydrogen-bonding and electrostatic interactions. All these factors influence secondary and tertiary peptide conformations in context-dependent ways [44,45] and provide remarkable diversity that still defies 3°and 4°structural predictions [44,46].

The growing recognition of the prevalence of protein misfolding diseases and prion infections has focused greater attention on defining higher order 4°structures and protein phases [47–49]. A central feature of all known prion and amyloid fibers is the range of accessible paracrystalline cross-β architectures [50,51]. Amyloid fiber cross-section is defined both by the length of the H-bonded β-strand and side-chain interactions that stabilize sheet stacking, or lamination (Figure 1). These fiber ends template the addition of individual peptides, reducing the diverse conformational space any peptide can sample to a single state. Unlike information storage in nucleic acid duplexes, the template cross-β protein strand transmits conformational information to the incoming strand, which then serves as the template for further propagation to the next incoming strand. In prions, specific morphological forms of the peptide cross-β architecture are selected for and propagated from clonal ensembles of diverse amyloid templates [52–55].

The diversity of conformational forms accessible to these peptide templates may be most easily explored in studies with simple peptides. The nucleating core of the Aβ peptide associated with Alzheimer's disease, ^{17}LVFF^{21}A, can access a range of morphological phases, each responsive to pH, media dialectic, surfaces, solvent composition, and various salts [56–59]. Despite this diversity, specific conditions have been found that allow for the growth of phases sufficiently homogeneous for structural characterization. At neutral pH, anti-parallel β-sheet fibrils predominate with Aβ [16–22], Ac-^{16}KLVFFA^{22}E-NH$_2$ (Figure 2). Cross-strand pairing between the positively charged lysine and negatively charged glutamate residues of neighboring H-bonded strands defines an in-register arrangement [59,60]. Protonation of the glutamate at low pH favors a shift of the strands to out-of-register, creating more complementary β-sheet faces that allow the number of sheets to grow (laminate) into ribbons and nanotubes [59,61–63]. The Aβ [16–22] E22L congener, Ac-KLVFFAL-NH$_2$, removes this ionic pairing constraint completely and assembles independent of pH as nanotubes with the same out-of-register β-strands [57,59,63,64]. The context-dependent folding of amyloid assemblies will be a recurring theme in the chapters that follow.

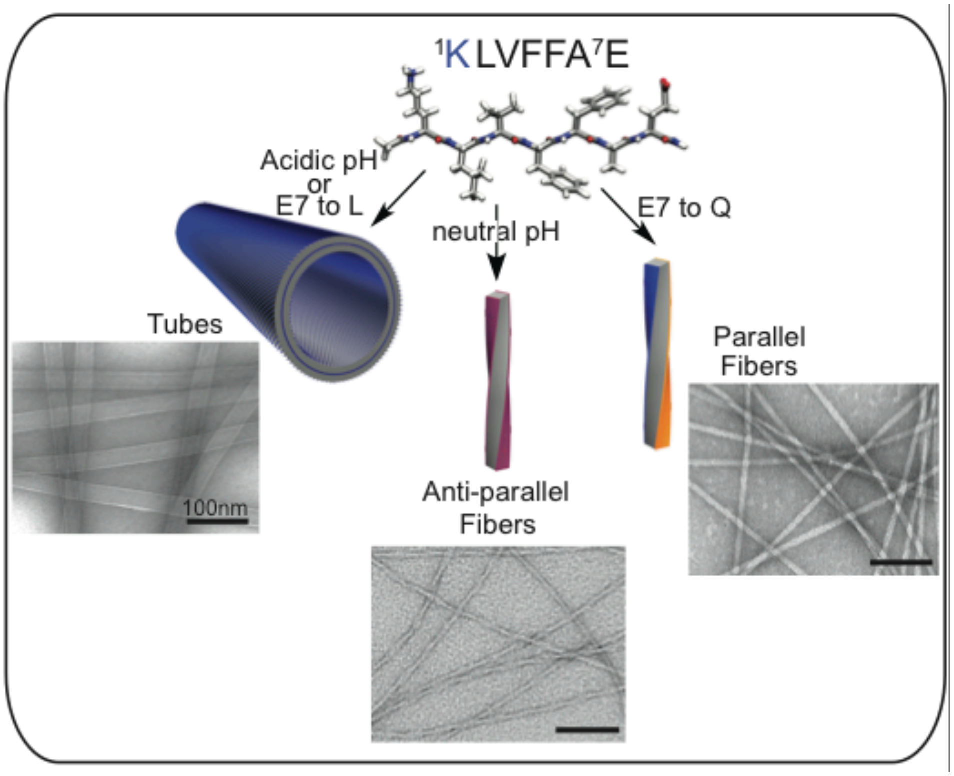

Figure 1-2. Aβ [16–22] peptide assembles into distinct morphologies depending on sequence and conditions. *In the cartoons above, blue represents the positively charged lysine (K), red the negatively charged glutamate (E), and orange the uncharged glutamine (Q). Two of the four faces of the fiber in the anti-parallel β-sheets present lysine and glutamate residues on the surface (purple), whereas the fibers with parallel β-sheets have a lysine surface and a glutamine surface. (Unpublished EM images from members of Lynn Lab.)*

Single molecule experiments have been used to map the phase transitions [65,66] and have begun to reveal intermediate nucleation events during conformational progression [67–69]. The simple change of one ‘O’ for an ‘NH’ in Ac-KLVFFAQ-NH_2 initially assembles as antiparallel β-strands, which arise as a kinetic intermediate controlled by charge repulsion in the initial particle phase. A secondary conformational mutation stabilized by glutamine side chain cross-strand pairing directs the nucleation and propagation of the thermodynamically more stable parallel β-strand registry [68]. This clear demonstration of kinetic intermediates expands the diversity of accessible informational forms that may propagate under different environmental conditions, and highlights the progressive nature of peptide nucleation and propagation as a mechanism for the selection of functional information.

The diversity of these peptide assemblies is derived not only from primary sequence, but also from the varied arrangements accessible to the ordered phases. In the simplest forms, even single aromatic amino acids [70] and dipeptides, containing aromatic [71–74] and aliphatic residues [75,76], can assemble as distinct phases. Aliphatic dipeptides (AI, IA, VV, VI, AV, VA, and IV) assemble into hexagonal prisms to form microporous crystalline materials, zeolites [75,76], and various other complex assemblies [77,78]. Diphenylalanine nanotubes (FF) can react with 2-iminothiolane, in which the subsequent thiolation of the N-terminal primary amine induces a morphological shift from nanotubes to spherical closed cages [74]. The opportunity to exploit even the simplest of peptide-assembly surfaces as templates for further chemistry with subsequent feedback control of the assembly certainly expands the potential functional diversity. As the structural understanding of these assemblies continues to grow and new surfaces are designed as templates for post-assembly modification, the functional diversity of these forms will continue to extend their informational potential.

Functional Assemblies

Genomic information present in the one-dimensional nucleic acid templates, as managed by proteins, produces the functional biopolymers of living dynamic cellular networks. Quite possibly the simplest functional form of this molecular information processing is found in viroids. These single stranded RNAs of only a few hundred nucleotides direct pathogenesis in many plant diseases [79]. Viroids are non-protein coding circular structures that assemble as long rod-like forms with a central conserved region and loops containing complex hydrogen-bonding patterns [80–82]. One class of viroids contains a hammerhead ribozyme for self-cleavage during replication cycles [80,83,84], allowing many of their functions to be self-contained and hailed as vestiges of an RNA World [85]. However, viroids are informational templates and depend on the host's cellular network for functional replication.

The paracrystalline cross-β peptide assemblies of the infectious prions are quite similar [50]. Like viroids, assembly stabilizes the structure against biotic and abiotic destruction and transmissibility is based on their ability to function as templates. These peptide templates also bind generic and functionally diverse small molecules, much like nucleic acids bind histochemical dyes [86–89]. The prototypical dye Congo Red (CR) [88] binds end-to-end along the laminate groove of Ac-KLVFFAE-NH_2 nanotube surfaces [64], and binds in a similar site-specific way to the HET-s prion of the filamentous fungus *Podospora anserine* [90,91]. These amyloid assemblies also bind oligoelectrolytes and poly(thiophene acetic acid) [92,93], much like RNA binding proteins [94], and other biological surfaces [95–101]. Experimental [102,103] and computational [104] evidence indicate that β-sheets can serve as templates for homochiral polymerization of N-carboxyanhydride activated amino acid monomers [103] and in situ activated α-amino acids [102]. Model self-replicating systems of β-sheet [105–107] peptides have been designed and the ability of β-sheets to template the polymerization of homochiral oligopeptides up to 30 residues long has been reviewed [108].

These activities may represent only a small fraction of the functions that provide the basis for the various amyloid diseases, and these capabilities have led to speculation about an amyloid world built on the potential of these surfaces to store and transfer information [109–111]. As impressive as these activities are, neither RNA nor amyloid alone achieve the functional diversity necessary for even the simplest cellular networks. The mutualism so evident in every step of information transmission in a cellular network suggests that life required both sides. In chapter 2, the use of amyloid assemblies as catalysts or scaffolds for prebiotic nucleic acid polymerization will be explored. Through variation to the primary sequence a library of nanostructures is accessible. Four of these nanostructures are evaluated for their potential role in the polymerization of nucleic acids with homogeneous 5’,3’ linkages.

From Both Sides Now

Proteins and nucleic acids both store and process chemical information in cellular networks, but they do so interdependently; proteins are made from nucleic acid templates, and proteins read the templates. To the extent that there is a code or set of rules for such a mutualism may be revealed in the specific recognition of nucleic acids by RNA- and DNA-binding proteins and their elaborate structure–function relationship [112–114]. As mentioned above, the pinnacle may be the nucleic acid/peptide (NA/P) associations in the ribosome [9,115], but small nuclear ribonucleoprotein (snRNP) complexes and nucleases, including Ribonuclease P (RNaseP), provide simpler examples [5]. The woven intricacies of such co-assemblies are increasingly being defined [116,117] and have been reconstituted [9,118]. As rules for co-assembly emerge, co-evolutionary strategies become possible. Figure 3 outlines minimal functional capabilities that might be achieved with the co-assemblies. The nucleation of polymers (red and blue) might propagate as a template (purple) able to catalyze the independent production of more polymers (red and blue) in Figure 3A. Mutations in such a feedback system could allow for a minimal system capable of chemical evolution. This functional capability is of course dependent on the ability of these co-assemblies to transition to some unique functional form (mixture of squares and triangles, purple), as outlined in Figure 3B. While extant biology is a sophisticated network of efficiently functioning molecular partners, the many varied functions necessary for the existence of life, relies on the emergence of such co-assembling information networks capable of sustained growth in molecular order.

Data now exists for prion infectivity being altered by oligonucleotides [119–123], but little structural information is available. Similarly, in vitro guanine $(dG)_{16}$ and cytosine $(dC)_{16}$ hexadecamers, as well as their duplexes, associate with amphiphilic self-assembling peptides. The binding is pH dependent, occurs on a much faster timescale than for assembly of the neat peptide, and indeed gives rise to novel nucleic acid/peptide co-assemblies [124]. In chapters 4 and 5 the global and structural characterization of unique nucleic acid/peptide co-assemblies will be examined. These co-assemblies provide insight to the maturation steps necessary for RNA processing, the origins of disease, and expands on the context-dependent assembly of nanostructures through a reductionist approach. Disease is explored further in chapter 6, where Aβ40 and Aβ42 are assessed for their association with RNA *in vitro*. Results indicate RNA is ordered in the presence of Aβ40/42 and cross-β architecture is maintained in at least Aβ40/RNA co-assemblies.

Hybridization of oligonucleotides containing sticky-ends can also be catalyzed in the presence of self-assembling peptides, mimicking at least one integral step of replication [125]. And a five-nucleotide ribozyme produces multiple translational products, including the dipeptide FF [126]. In principle [127,128], when FF reaches the critical concentration for peptide self-assembly, the resulting peptide nanotube could selectively bind the ribozyme to create a dynamic system under feedback control.

Progress in this growing understanding of peptides and nucleic acids co-assembly may well depend on careful selection of systems, and the rich diversity of functional co-assemblies with existing biopolymers provides an exciting opportunity to define the basic mutualistic codes. In the simple assemblies outlined in Figure 3, the thermodynamic process of assembly would be physically coupled to polymerization of additional polymers from monomer building blocks, with the thermodynamic/kinetic tension manifested as feedback control. Elucidating the mechanisms of association, and the structural and functional diversity of the resulting complexes, will be necessary for a more general understanding of the chemical thresholds for early evolution of molecular mutualism. Simpler synthetic [129,130] and altered biopolymer [11,131,132] networks could then be extended to the dynamic processes of minimal native biopolymer co-assemblies [133–136].

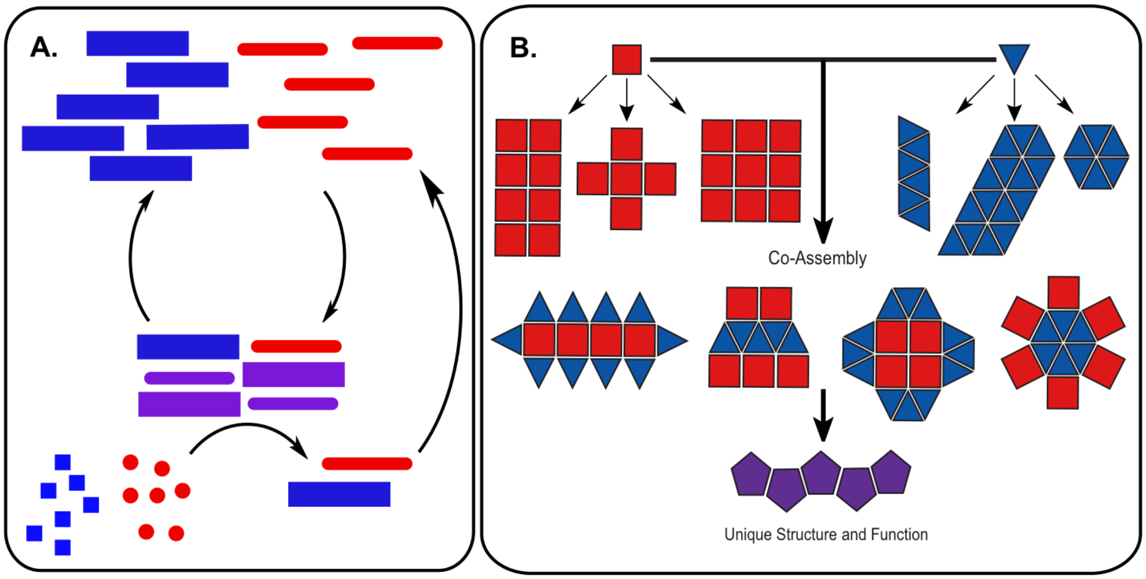

Figure 1-3. Autocatalysis and emergent functions from co-assemblies. *(A) Co-assemblies formed from nucleic acid and peptide polymers catalyze the polymerization of additional polymers from monomer building blocks; (B) Co-assemblies derived from individual nucleic acid or peptide assemblies can significantly increase the structural diversity leading to emergent structures and functions.*

Conclusions: Towards Molecular Mutualisms

The cooperative functioning of nucleic acids and peptides was recognized early with the designation of a central dogma decades ago, and it may well be that our attempts to simplify the system into metabolism-first, RNA-first, or amyloid-first has limited a more extensive exploration of mutualistic networks. Single biopolymer networks have contributed significantly to systems chemistry, but sidestepped the interdependence of metabolism and replication, analog and digital information processing, and the mutualism, so apparent in living systems, that is essential for the emergence of new functions [137]. The recognition of the importance of diverse, structurally complex, non-covalent assemblies in early evolution is certainly highlighted by their prevalence in biology [138–141], and routes to creating an ecology of biomolecules with sufficient functional dynamics to evolve chemically are now emerging. We may have reached the point where the creation of a mutualistic chemical ecology [142,143] can be used to inform the progressive growth of molecular information on Earth and understand the limits on chemical evolution broadly in our Universe [144–146]. As technology and methodologies to analyze complex networks improve, the next scientific discoveries may come from understanding harsh and extreme environments or even new “worlds” with fundamentally different systems of molecular networks [11,147,148]. Certainly we should now be able to define the limits on building to the complex networks we might call living.

In the following chapters we explore several topics including: potential prebiotic interactions between nucleic acids and self-assembling peptides that promote ordering of systems for early cellular networks, the use of DNA secondary structure diversity and the robust context-dependence of peptide self-assembly for bionanotechnology, the maturation of RNA/protein interactions within ribonucleoprotein granules tasked with maintaining RNA homeostasis, and the sequestration of nucleic acids to lesions of protein misfolding diseases. Despite the diversity of these topics, a common theme is prominent. Mutualism between nucleic acids and peptides or proteins likely preceded extant cellular life and underpins every stage of the central dogma. Elucidating the interactions that significantly contribute to these mutualisms will expand our understanding of early cellular networks, the manipulation of complementary peptide and nucleic acid interactions in nanotechnology, RNA processing, and altered ribostasis in protein misfolding diseases. Our findings and their implications are presented here.

References

[1] Mann, S. Life as a nanoscale phenomenon. *Angew. Chem. Int. Ed.* **47,** 5306–5320 (2008).
[2] Crick, F. H. C. The biological replication of macromolecules. *Sym. Soc. Exp. Biol.* **12,** 138–163 (1958).
[3] Woese, C. R. On the evolution of cells. *Proc. Natl. Acad. Sci. USA* **99,** 8742–8747 (2002).
[4] Miller, S. L. A production of amino acids under possible primitive earth conditions. *Science* **117,** 528–529 (1953).
[5] Guerrier-Takada, C., Gardiner, K., Marsh, T., Pace, N., Altman, S. The RNA moiety of Ribonuclease P is the catalytic subunit of the enzyme. *Cell* **35,** 849–857 (1983).
[6] Kruger, K., Grabowski, P. J., Zaug, A. J., Sands, J., Gottschling, D. E., Cech, T. R. Self-splicing RNA: Autoexcision and autocyclization of the ribosomal RNA intervening sequence of Tetrahymena. *Cell* **31,** 147–157 (1982).
[7] Breaker, R. R., Joyce, G. F. A DNA enzyme that cleaves RNA. *Chem. Biol.* **1,** 223–229 (1994).
[8] Gesteland, R. F., Cech, T. R., Atkins, J. F. *The RNA World*, 2nd ed.; Cold Spring Harbor Laboratory Press: New York, NY, USA, 1999.
[9] Fromont-Racine, M., Senger, B., Saveanu, C., Fasiolo, F. Ribosome assembly in eukaryotes. *Gene* **313,** 17–42 (2003).
[10] Harish, A., Caetano-Anolles, G. Ribosomal history reveals origins of modern protein synthesis. *PLoS One* **7,** doi:10.1371/journal.pone.0032776 (2012).
[11] Goodwin, J. T., Mehta, A. K., Lynn, D. G. Digital and analog chemical evolution. *Acc. Chem. Res.* **45,** 2189–2199 (2012).
[12] Moore, M. J. From birth to death: The complex lives of eukaryotic mRNAs. *Science* **309,** 1514–1518 (2005).
[13] Bolton, D. C., McKinley, M. P., Prusiner, S. B. Identification of a protein that purifies with the scrapie prion. *Science* **218,** 1309–1311 (1982).
[14] Astbury, W. T., Dickinson, S., Bailey, K. The X-ray interpretation of denaturation and

the structure of the seed globulins. *Biochem. J.* **29,** 2351–2360 (1935).
[15] Parker, K. D., Rudall, K. M. Structure of the silk of chrysopa egg-stalks. *Nature* **179,** 905–906 (1957).
[16] Geddes, A. J., Parker, K. D., Atkins, E. D. T., Beighton, E. “Cross-β” conformation in proteins. *J. Mol. Biol.* **32,** 343–358 (1968).
[17] Hammer, N. D., Schmidt, J. C., Chapman, M. R. The curli nucleator protein, CsgB, contains an amyloidogenic domain that directs CsgA polymerization. *Proc. Natl. Acad. Sci. USA* **104,** 12494–12499 (2007).
[18] Romero, D., Aguilar, C., Losick, R., Kolter, R. Amyloid fibers provide structural integrity to Bacillus subtilis biofilms. *Proc. Natl. Acad. Sci. USA* **107,** 2230–2234 (2010).
[19] Tessier, P. M., Lindquist, S. Unraveling infectious structures, strain variants and species barriers for the yeast prion [*PSI*+]. *Nat. Struct. Mol. Biol.* **16,** 598–605 (2009).
[20] Inge-Vechtomov, S. G., Zhouravleva, G. A., Chernoff, Y. O. Biological roles of prion domains. *Prion* **1,** 228–235 (2007).
[21] Iconomidou, V. A., Hamodrakas, S. J. Natural protective amyloids. *Curr. Protein Pept. Sci.* **9,** 291–309 (2008).
[22] Barlow, D. E. *et al.* Characterization of the adhesive plaque of the barnacle Balanus amphitrite: Amyloid-like nanofibrils are a major component. *Langmuir* **26,** 6549–6556 (2010).
[23] Kenchington, W. The larval silk of *Hypera* spp. (Coleoptera: Curculionidae). A new example of the cross-β protein conformation in an insect silk. *J. Insect Physiol.* **29,** 355–361 (1983).
[24] Majumdar, A., *et al.* Critical role of amyloid-like oligomers of Drosophila Orb2 in the persistence of memory. *Cell* **148,** 515–529 (2012).
[25] Fowler, D. M. *et al.* Functional amyloid formation within mammalian tissue. *PLoS Biol.* **4,** doi:10.1371/journal.pbio.0040006 (2006).
[26] Kemp, M. The *Mona Lisa* of modern science. *Nature* **421,** 416–420 (2003).
[27] Watson, J. D., Crick, F. H. C. Molecular structures of nucleic acids. *Nature* **171,** 737–738 (1953).
[28] Rich, A.; Zhang, S. Z-DNA: The long road to biological function. *Nat. Rev. Genet.* **4,** 566–572 (2003).
[29] Hermann, T., Westhof, E. Non-Watson-Crick base pairs in RNA-protein recognition. *Chem. Biol.* **6,** R335–R343 (1999).
[30] Zhao, J., Bacolla, A., Wang, G., Vasquez, K. M. Non-B DNA structure-induced genetic instability and evolution. *Cell. Mol. Life Sci.* **67,** 43–62 (2010).
[31] Choi, J., Majima, T. Conformational changes of non-B DNA. *Chem. Soc. Rev.* **40,** 5893–5909 (2011).
[32] Saini, N., Zhang, Y., Usdin, K., Lobachev, K. S. When secondary comes first—The importance of non-canonical DNA structures. *Biochimie* **95,** 117–123 (2013).
[33] Collie, G. W., Parkinson, G. N. The application of DNA and RNA G-quadruplexes to therapeutic medicines. *Chem. Soc. Rev.* **40,** 5867–5892 (2011).
[34] Burge, S., Parkinson, G. N., Hazel, P., Todd, A. K., Neidle, S. Quadruplex DNA: Sequence, topology and structure. *Nucleic Acids Res.* **34,** 5402–5415 (2006).
[35] Miyoshi, D., Matsumura, S., Li, W., Sugimoto, N. Structural polymorphism of telomeric DNA regulated by pH and divalent cation. *Nucleosides Nucleotides Nucl. Acids* **22,** 203–221 (2003).
[36] Biffi, G., Tannahill, D., McCafferty, J., Balasubramanian, S. Quantitative visualization of DNA G-quadruplex structures in human cells. *Nat. Chem.* **5,** 182–186 (2013).
[37] Lipps, H. J., Rhodes, D. G-quadruplex structures: *In vivo* evidence and function. *Trends Cell Biol.* **19,** 414–422 (2009).

[38] Baral, A., Kumar, P., Pathak, R., Chowdhury, S. Emerging trends in G-quadruplex biology—Role in epigenetic and evolutionary events. *Mol. Biosyst.* **9,** 1568–1575 (2013).

[39] Bochman, M. L., Paeschke, K., Zakian, V. A. DNA secondary structures: Stability and function of G-quadruplex structures. *Nat. Rev. Genet.* **13,** 770–780 (2012).

[40] Hiller, D. A., Strobel, S. A. The chemical versatility of RNA. *Phil. Trans. R. Soc. B* **366,** 2929–2935 (2011).

[41] Doudna, J. A., Cech, T. R. The chemical repertoire of natural ribozymes. *Nature* **418,** 222–228 (2002).

[42] Ward, W. L., Plakos, K., DeRose, V. J. Nucleic acid catalysis: Metals, nucleobases, and other cofactors. *Chem. Rev.* **114,** 4318–4342 (2014).

[43] Silverman, S. K. Deoxyribozymes: DNA catalysts for bioorganic chemistry. *Org. Biomol. Chem.* **2,** 2701–2706 (2004).

[44] Dill, K. A., MacCallum, J. L. The protein-folding problem, 50 years on. *Science* **338,** 1042–1046 (2012).

[45] Dill, K. A. Dominant forces in protein folding. *Biochemistry* **29,** 7133–7155 (1990).

[46] Compiani, M., Capriotti, E. Computational and theoretical methods for protein folding. *Biochemistry* **52,** 8601–8624 (2013).

[47] Vabulas, R. M., Raychaudhuri, S., Hayer-Hartl, M., Hartl, F. U. Protein folding in the cytoplasm and the heat shock response. *Cold Spring Harb. Perspect. Biol.* **2,** doi:10.1101/cshperspect.a004390 (2010).

[48] Chien, P., Weissman, J. S., DePace, A. H. Emerging principles of conformation-based prion inheritance. *Annu. Rev. Biochem.* **73,** 617–656 (2004).

[49] Dobson, C. M. Protein folding and misfolding. *Nature* **426,** 884–890 (2003).

[50] Jucker, M., Walker, L. C. Self-propagation of pathogenic protein aggregates in neurodegenerative diseases. *Nature* **501,** 45–51 (2013).

[51] Sawaya, M. R. *et al.* Atomic structures of amyloid cross-β spines reveal varied steric zippers. *Nature* **447,** 453–457 (2007).

[52] Ghaemmaghami, S. *et al.* Conformational transformation and selection of synthetic prion strains. *J. Mol. Biol.* **413,** 527–542 (2011).

[53] Li, J., Browning, S., Mahal, S. P., Oelschlegel, A. M., Weissmann, C. Darwinian evolution of prions in cell culture. *Science* **327,** 869–872 (2010).

[54] Collinge, J., Clarke, A. R. A general model of prion strains and their pathogenicity. *Science* **318,** 930–936 (2007).

[55] Tanaka, M., Chien, P., Naber, N., Cooke, R., Weissman, J. S. Conformational variations in an infectious protein determine prion strain differences. *Nature* **428,** 323–328 (2004).

[56] Childers, W. S., Mehta, A. K., Bui, T. Q., Liang, Y., Lynn, D. G. In *Molecular Self-Assembly—Advances and Applications*, 1st ed.; Li, A., Ed.; Pan Stanford Publishing Pte Ltd.: Singapore, Singapore, pp. 1–36 (2012).

[57] Childers, W. S., Anthony, N. R., Mehta, A. K., Berland, K. M., Lynn, D. G. Phase networks of cross-β peptide assemblies. *Langmuir* **28,** 6386–6395 (2012).

[58] Debeljuh, N., Barrow, C. J., Byrne, N. The impact of ionic liquids on amyloid fibrilization of Aβ16–22: Tuning the rate of fibrilization using a reverse Hofmeister strategy. *Phys. Chem. Chem. Phys.* **13,** 16534–16536 (2011).

[59] Mehta, A. K. *et al.* Facial symmetry in protein self-assembly. *J. Am. Chem. Soc.* **130,** 9829–9835 (2008).

[60] Balbach, J. J. *et al.* Amyloid fibril formation by Aβ16–22, a seven-residue fragment of the Alzheimer's β-amyloid peptide, and structural characterization by solid state NMR. *Biochemistry* **39,** 13748–13759 (2000).

[61] Lu, K., Jacob, J., Thiyagarajan, P., Conticello, V. P., Lynn, D. G. Exploiting amyloid fibril lamination for nanotube self-assembly. *J. Am. Chem. Soc.* **125,** 6391–6393 (2003).

[62] Dong, J., Lu, K., Lakdawala, A., Mehta, A. K., Lynn, D. G. Controlling amyloid growth in multiple dimensions. *Amyloid* **13,** 206–215 (2006).
[63] Liang, Y. *et al.* Cross-strand pairing and amyloid assembly. *Biochemistry* **47,** 10018–10026 (2008).
[64] Childers, W. S., Mehta, A. K., Lu, K., Lynn, D. G. Templating molecular arrays in amyloid's cross-β grooves. *J. Am. Chem. Soc.* **131,** 10165–10172 (2009).
[65] Anthony, N. R., Mehta, A. K., Lynn, D. G., Berland, K. M. Mapping amyloid-β(16–22) nucleation pathways using fluorescence lifetime imaging microscopy. *Soft Matter* **10,** 4162–4172 (2014).
[66] Liang, Y., Lynn, D. G., Berland, K. M. Direct observation of nucleation and growth in amyloid self-assembly. *J. Am. Chem. Soc.* **132,** 6306–6308 (2010).
[67] Buchanan, L. E. *et al.* Mechanism of IAPP amyloid fibril formation involves an intermediate with a transient β-sheet. *Proc. Natl. Acad. Sci. USA* **110,** 19285–19290 (2013).
[68] Liang, C. *et al.* Kinetic intermediates in amyloid assembly. *J. Am. Chem. Soc.* **136,** 15146–15149 (2014).
[69] Lin, D. *et al.* Investigation of the aggregation process of amyloid-β-(16–22) peptides and the dissolution of intermediate aggregates. *Langmuir* **30,** 3170–3175 (2014).
[70] Perween, S., Chandanshive, B., Kotamarthi, H. C., Khushalani, D. Single amino acid based self-assembled structure. *Soft Matter* **9,** 10141–10145 (2013).
[71] Frederix, P. W. J. M., Ulijn, R. V., Hunt, N. T., Tuttle, T. Virtual screening for dipeptide aggregation: Toward predictive tools for peptide self-assembly. *J. Phys. Chem. Lett.* **2,** 2380–2384 (2011).
[72] Reches, M., Gazit, E. Casting metal nanowires within discrete self-assembled peptide nanotubes. *Science* **300,** 625–627 (2003).
[73] De Groot, N. S., Parella, T., Aviles, F. X., Vendrell, J., Ventura, S. Ile-Phe dipeptide self-assembly: Clues to amyloid formation. *Biophys. J.* **92,** 1732–1741 (2007).
[74] Reches, M., Gazit, E. Formation of closed-cage nanostructures by self-assembly of aromatic dipeptides. *Nano Lett.* **4,** 581–585 (2004).
[75] Soldatov, D. V., Moudrakovski, I. L., Ripmeester, J. A. Dipeptides as microporous materials. *Angew. Chem. Int. Ed.* **43,** 6308–6311 (2004).
[76] Gorbitz, C. H. Nanotubes from hydrophobic dipeptides: Pore size regulation through side chain substitution. *New J. Chem.* **27,** 1789–1793 (2003).
[77] Gorbitz, C. H. Structures of dipeptides: The head-to-tail story. *Acta Cryst.* **B66,** 84–93 (2010).
[78] Gorbitz, C. H. Microporous organic materials from hydrophobic dipeptides. *Chem. Eur. J.* **13,** 1022–1031 (2007).
[79] Flores, R., Hernandez, C., Martinez de Alba, A. E., Daros, J. A., di Serio, F. Viroids and viroid-host interactions. *Annu. Rev. Phytopathol.* **43,** 117–139 (2005).
[80] Flores, R., Serra, P., Minoia, S., di Serio, F., Navarro, B. Viroids: From genotype to phenotype just relying on RNA sequence and structural motifs. *Front. Microbiol.* **3,** doi:10.3389/ fmicb.2012.00217 (2012).
[81] Sanger, H. L., Klotz, G., Riesner, D., Gross, H. J., Kleinschmidt, A. K. Viroids are single-stranded covalently closed circular RNA molecules existing as highly base-paired rod-like structures. *Proc. Natl. Acad. Sci. USA* **73,** 3852–3856 (1976).
[82] Sano, T., Candresse, T., Hammond, R. W., Diener, T. O., Owens, R. A. Identification of multiple structural domains regulating viroid pathogenicity. *Proc. Natl. Acad. Sci. USA* **89,** 10104–10108 (1992).
[83] Daros, J. A., Marcos, J. F., Hernandez, C., Flores, R. Replication of avocado sunblotch viroid: Evidence for a symmetric pathway with two rolling circles and hammerhead ribozyme processing. *Proc. Natl. Acad. Sci. USA* **91,** 12813–12817 (1994).

[84] Hutchins, C. J., Rathjen, P. D., Forster, A. C., Symons, R. H. Self-cleavage of plus and minus RNA transcripts of avocado sunblotch viroid. *Nucleic Acids Res.* **14,** 3627–3640 (1986).
[85] Flores, R., Gago-Zachert, S., Serra, P., Sanjuan, R., Elena, S. F. Viroids: Survivors from the RNA world? *Annu. Rev. Microbiol.* **68,** 395–414 (2014).
[86] Buell, A.K. *et al.* Probing small molecule binding to amyloid fibrils. *Phys. Chem. Chem. Phys.* **13,** 20044–20052 (2011).
[87] Levine, H. Thioflavine T interactions with synthetic Alzheimers Disease β-amyloid peptides—detection of amyloid aggregation in solution. *Protein Sci.* **2,** 404–410 (1993).
[88] Divry, P., Florkin, M. The optic properties of amyloid. *Comptes Rendus des Seances de la Societe de Biologie et de ses Filiales* **97,** 1808–1810 (1927). (In French)
[89] Buxbaum, J. N., Linke, R. P. A molecular history of the amyloidoses. *J. Mol. Biol.* **421,** 142–159 (2012).
[90] Schutz, A. K. *et al.* The amyloid-Congo red interface at atomic resolution. *Angew. Chem. Int. Ed.* **50,** 5956–5960 (2011).
[91] Dos Reis, S. *et al.* The HET-s prion protein of the filamentous fungus Podospora anserina aggregates *in vitro* into amyloid-like fibrils. *J. Biol. Chem.* **277,** 5703–5706 (2002).
[92] Bäcklund, F. G., Wigenius, J., Westerlund, F., Inganäs, O., Solin, N. Amyloid fibrils as dispersing agents for oligothiophenes: Control of photophysical properties through nanoscale templating and flow induced fibril alignment. *J. Mater. Chem. C* **2,** 7811–7822 (2014).
[93] Herland, A., Bjork, P., Hania, P. R., Scheblykin, I. G., Inganas, O. Alignment of a conjugated polymer onto amyloid-like protein fibrils. *Small* **3,** 318–325 (2007).
[94] Lunde, B. M., Moore, C., Varani, G. RNA-binding proteins: Modular design for efficient function. *Nat. Rev. Mol. Cell Bio.* **8,** 479–490 (2007).
[95] Saha, S., Deep, S. Switch in the aggregation pathway of bovine serum albumin mediated by electrostatic interactions. *J. Phys. Chem. B* **118,** 9155–9166 (2014).
[96] Gilbert, J., Campanella, O., Jones, O. G. Electrostatic stabilization of β-lactoglobulin fibrils at increased ph with cationic polymers. *Biomacromolecules* **15,** 3119–3127 (2014).
[97] Nielsen, S. B. *et al.* Multiple roles of heparin in the aggregation of p25alpha. *J. Mol. Biol.* **421,** 601–615 (2012).
[98] Matsuzaki, K., Kato, K., Yanagisawa, K. Aβ polymerization through interaction with membrane gangliosides. *Biochim. Biophys. Acta* **1801,** 868–877 (2010).
[99] Li, S. *et al.* Neurofibrillar Tangle Surrogates: Histone H1 Binding to Patterned Phosphotyrosine Peptide Nanotubes. *Biochemistry* **53,** 4225–4227 (2014).
[100] Suk, J. Y., Zhang, F., Balch, W. E., Linhardt, R. J., Kelly, J. W. Heparin accelerates gelsolin amyloidogenesis. *Biochemistry* **45,** 2234–2242 (2006).
[101] Terzi, E., Holzemann, G., Seelig, J. Interaction of Alzheimer β-amyloid peptide (1–40) with lipid membranes. *Biochemistry* **36,** 14845–14852 (1997).
[102] Illos, R. A. *et al.* Oligopeptides and copeptides of homochiral sequence, via β-sheets, from mixtures of racemic alpha-amino acids, in a one-pot reaction in water; relevance to biochirogenesis. *J. Am. Chem. Soc.* **130,** 8651–8659 (2008).
[103] Rubinstein, I., Eliash, R., Bolbach, G., Weissbuch, I., Lahav, M. Racemic beta sheets in biochirogenesis. *Angew. Chem. Int. Ed.* **46,** 3710–3713 (2007).
[104] Wagner, N., Rubinov, B., Ashkenasy, G. β-Sheet-induced chirogenesis in polymerization of oligopeptides. *Chemphyschem* **12,** 2771–2780 (2011).
[105] Rubinov, B., Wagner, N., Rapaport, H., Ashkenasy, G. Self-replicating amphiphilic β-sheet peptides. *Angew. Chem. Int. Ed.* **48,** 6683–6686 (2009).
[106] Takahashi, Y., Mihara, H. Construction of a chemically and conformationally self-replicating system of amyloid-like fibrils. *Bioorgan. Med. Chem.* **12,** 693–699 (2004).

[107] Rubinov, B. *et al.* Transient Fibril Structures Facilitating Nonenzymatic Self-Replication. *ACS Nano* **6,** 7893–7901 (2012).
[108] Weissbuch, I., Illos, R. A., Bolbacj, G., Lahav, M. Racemic β-sheets as templates of relevance to the origin of homochirality of peptides: Lessons from crystal chemistry. *Acc. Chem. Res.* **42,** 1128–1140 (2009).
[109] Maury, C. P. J. Self-propagating β-sheet polypeptide structures as prebiotic informational molecular entities: The amyloid world. *Orig. Life Evol. Biosph.* **39,** 141–150 (2009).
[110] Childers, W. S., Ni, R., Mehta, A. K., Lynn, D. G. Peptide membranes in chemical evolution. *Curr. Opin. Chem Biol.* **13,** 652–659 (2009).
[111] Brack, A., Orgel, L. E. β Structures of alternating polypeptides and their prebiotic significance. *Nature* **256,** 383–387 (1975).
[112] Hoffman, M. M. *et al.* AANT: The amino acid-nucleotide interaction database. *Nucleic Acids Res.* **32,** D174–D181 (2004).
[113] Jones, S., van Heyningens, P., Berman, H. M., Thornton, J. M. Protein-DNA interactions: A structural analysis. *J. Mol. Biol.* **287,** 877–896 (1999).
[114] Nadassy, K., Wodak, S. J., Janin, J. Structural features of protein-nucleic acid recognition sites. *Biochemistry* **38,** 1999–2017 (1999).
[115] Wool, I. G. The structure and function of eukaryotic ribosomes. *Annu. Rev. Biochem.* **48,** 719–754 (1979).
[116] Esakova, O., Krasilnikov, A. S. Of proteins and RNA: The RNase P/MRP family. *RNA* **16,** 1725–1747 (2010).
[117] Frank, D. N., Pace, N. Ribonuclease P: Unity and diversity in a tRNA processing ribozyme. *Annu. Rev. Biochem.* **67,** 153–180 (1998).
[118] Woodson, S.A. RNA folding and ribosome assembly. *Curr. Opin. Chem. Biol.* **12,** 667–673 (2008).
[119] Macedo, B. *et al.* Nonspecific prion protein-nucleic acid interactions lead to different aggregates and cytotoxic species. *Biochemistry* **51,** 5402–5413 (2012).
[120] Supattapone, S. Biochemistry. What makes a prion infectious? *Science* **327,** 1091–1092 (2010).
[121] Geoghegan, J. C. *et al.* Selective incorporation of polyanionic molecules into hamster prions. *J. Biol. Chem.* **282,** 36341–36353 (2007).
[122] Deleault, N. R. *et al.* Protease-resistant prion protein amplification reconstituted with partially purified substrates and synthetic polyanions. *J. Biol. Chem.* **280,** 26873–26879 (2005).
[123] Grossman, A., Zeiler, B., Sapirstein, V. Prion protein interactions with nucleic acid: Possible models for prion disease and prion function. *Neurochem. Res.* **28,** 955–963 (2003).
[124] Wang, M., Law, M., Duhamel, J., Chen, P. Interaction of a self-assembling peptide with oligonucleotides: Complexation and aggregation. *Biophys. J.* **93,** 2477–2490 (2007).
[125] Braun, S.; Humphreys, C.; Fraser, E.; Brancale, A.; Bochtler, M.; Dale, T. Amyloid-associated nucleic acid hybridisation. *PLoS One*, **6,** doi:10.1371/journal.pone.0019125 (2011).
[126] Turk, R. M., Chumachenko, N. V., Yarus, M. Multiple translational products from a five-nucleotide ribozyme. *Proc. Natl. Acad. Sci. USA* **107,** 4585–4589 (2010).
[127] Carny, O., Gazit, E. A model for the role of short self-assembled peptides in the very early stages of the origin of life. *FASEB J.* **19,** 1051–1055 (2005).
[128] Carny, O., Gazit, E. Creating prebiotic sanctuary: Self-assembling supramolecular peptide structures bind and stabilize RNA. *Orig. Life Evol. Biosph.* **41,** 121–132 (2011).
[129] Otto, S., Furlan, R. L., Sanders, J. K. Dynamic combinatorial libraries of macrocyclic disulfides in water. *J. Am. Chem. Soc.* **122,** 12063–12064 (2000).

[130] Carnell, J. *et al.* Mechanosensitive self-replication driven by self-organization. *Science* **327,** 1502–1506 (2010).
[131] Ivnitski, D. Introducing charge transfer functionality into prebiotically relevant β-sheet peptide fibrils. *Chem. Commun.* **50,** 6733–6736 (2014).
[132] Goodwin, J. T., Lynn, D. G. Template-directed synthesis: Use of a reversible reaction. *J. Am. Chem. Soc.* **114,** 9197–9198 (1992).
[133] McCleskey, S. C., Griffin, M. J., Schneider, S. E., McDevitt, J. T., Anslyn, E. V. Differential receptors create patterns diagnostic for ATP and GTP. *J. Am. Chem. Soc.* **125,** 1114–1115 (2003).
[134] Schneider, S. E., O'Neil, S. N., Anslyn, E. V. Coupling rational design with libraries leads to the production of an ATP selective chemosensor. *J. Am. Chem. Soc.* **122,** 542–543 (2000).
[135] Butterfield, S. M. Sweeney, M. M., Waters, M. L. The recognition of nucleotides with model β-hairpin receptors: Investigation of critical contacts and nucleotide selectivity. *J. Org. Chem.* **70,** 1105–1114 (2005).
[136] Butterfield, S. M., Waters, M. L. A designed β-hairpin peptide for molecular recognition of ATP in water. *J. Am. Chem. Soc.* **125,** 9580–9581 (2003).
[137] Norris, V., Loutelier-Bourhis, C., Thierry, A. How did metabolism and genetic replication get married? *Orig. Life Evol. Biosph.* **42,** 487–495 (2012).
[138] Root-Bernstein, R. Simultaneous origin of homochirality, the genetic code and its directionality. *Bioessays* **29,** 689–698 (2007).
[139] Hunding, A. *et al.* Compositional complementarity and prebiotic ecology in the origin of life. *Bioessays* **28,** 399–412 (2006).
[140] Root-Bernstein, R., Dillon, P. F. Molecular Complementarity I: The complementarity theory of the origin and evolution of life. *J. Theor. Biol.* **188,** 447–479 (1997).
[141] Root-Bernstein, R. A modular hierarchy-based theory of the chemical origins of life based on molecular complementarity. *Acc. Chem. Res.* **45,** 2169–2177 (2012).
[142] Dale, T. Protein and nucleic acid together: A mechanism for the emergence of biological selection. *J. Theor. Biol.* **240,** 337–342 (2006).
[143] Segre, D., DBen-Eil, D., Lancet, D. Compositional genomes: Prebiotic information transfer in mutually catalytic noncovalent assemblies. *Proc. Natl. Acad. Sci. USA* **97,** 4112–4117 (2000).
[144] Flores Martinez, C. I. SETI in the light of cosmic convergent evolution. *Acta Astronaut.* **104,** 341–349 (2014).
[145] Chela-Flores, J. From systems chemistry to systems astrobiology: Life in the universe as an emergent phenomenon. *Int. J. Astrobiol.* **12,** 8–16 (2013).
[146] Goodwin, J. T. *et al.* Alternative Chemistries of Life: Empirical Approaches. Available online: http://chemistry.emory.edu/home/ assets/alternativechem.pdf (accessed on 3 December 2014).
[147] Russell, M. J. *et al.* The drive to life on wet and icy worlds. *Astrobiology* **14,** 308–343 (2014).
[148] Ruiz-Mirazo, K., Briones, C., de la Escosura, A. Prebiotic systems chemistry: New perspectives for the origins of life. *Chem. Rev.* **114,** 285–366 (2014).

Chapter 2: Altering peptide nanotube groove morphology to promote nucleic acid elongation

Introduction

Biopolymers are capable of accessing diverse context-dependent morphologies. Nucleic acids, which predominantly fold as anti-parallel B-form or A-form duplexes [1], can also energetically access Z-form duplexes, parallel poly(rA) duplexes, hairpins, pseudoknots, quadruplexes, and other 2°, 3°, and 4° structures [2-6]. This repertoire of accessible nucleic acid morphologies ultimately dictates functional applications. For example, guanine quadruplexes, which play a protective role in telomeres [7,8], are largely nuclease resistant [9]. The catalytic capabilities of RNAs have been explored as a foundation for the "RNA-world" hypothesis of the origins of life [10,11]. Simple ribozymes are capable of catalyzing the synthesis of short polypeptides [12], and the RNA constituent of Ribonuclease P, identified as one of the first ribozymes, is responsible for nuclease activity [13]. The information storage and processing power of RNAs certainly contributes to our understanding of the development of early cellular networks [14].

Proteins are capable of a comparable level of folding diversity and functional applications. Full-length proteins access β-sheets, β-turns, and α-helices, which then form further 3° and 4° contacts [15]. Diversity in folding can most prominently be observed in peptides as short as two amino acids. Aliphatic dipeptides self-assemble as hexagonal prisms [16-19] and diphenylalanine, which assembles as nanotubes [20] can access a diverse set of context-dependent morphologies with ferrocene modification of its terminus [21]. Peptides derived from protein-misfolding diseases provide more insight to the context-dependent nature of supramolecular morphologies [22-26]. Aβ16-22, 'KLVFFAE', self-assembles as nanotubes at acidic pH and fibers at neutral pH [27]. The emergence of environment-specific morphologies contributes to our understanding of amyloid strains in protein-misfolding diseases, most notably prions [28,29].

Despite the clear morphological and functional diversity of proteins and nucleic acids, as was described in chapter 1, neither biopolymer is capable of supporting complex cellular networks on its own. The mutualisms that persist between nucleic acids and proteins at all levels of cellular information processing [30-36] provide strong evidence for a non-exclusive origins of life hypothesis [11]. The mutualistic interactions between nucleic acids and proteins will be a recurring theme in the following chapters as applications to nanotechnology, RNA processing, and disease are explored.

One barrier that many encounter in ascribing RNA as the first information storage and functional entity, is the uncontrolled propagation of heterogeneous linkages under prebiotic conditions. If there truly was a ‘RNA World’, the directed polymerization of specific RNAs would be a prerequisite. Prebiotic condensation of nucleic acids has largely focused on the use of clays including montmorillonite [37-40]. The cationic surface of montmorillonite adsorbs negatively charged nucleotides where proximity-driven condensation occurs [38-40]. This process yields nucleic acids exceeding fifty nucleotides [40] with heterogeneous 3’-5’ 2’-5’ linkages. Cyclic nucleic acids comprise ~1/3 of reaction products [39]. The specificity of this condensation can be improved by fixing the orientation of nucleotides prior to phosphodiester bond formation [39,40]. In this chapter, we describe the use of peptide nanotubes as polymerization scaffolds, fixing nucleotides in a specific orientation to promote homogeneous 5’,3’ or 5’,2’ linkages. Peptide nanotubes, formed from the Aβ16-22 congener KLVFFAL, selectively template aromatic small molecules in the cross-β grooves of its surface [41]. Remarkably, these grooves are also capable of sequestering small molecules for aldol and retro aldol reactions [42]. In this chapter we explore the use of nanotubes as catalysts of selective nucleic acid polymerization.

Results

Nanotube morphology has been characterized extensively for the ‘KLVFFAE’ congener, KLVFFAL [43]. This peptide, which overcomes the bias towards salt-bridge formation at neutral pH, forms robust nanotubes of 54+/-3nm diameter with a characteristic peptide-bilayer wall [44,45]. Nanotube peptide bilayers are characterized by anti-parallel out-of-register peptide orientation and registry, giving rise to a hydrophobic groove on the nanotubes surface primarily made up of leucine residues of the second and C-terminal positions of KLVFFAL (Fig. 2-1) [41-43]. Modification of these grooved surfaces for use in other reactions, including the polymerization of nucleic acids, would support a prebiotic biopolymer collaboration and perhaps, promote linkage specificity.

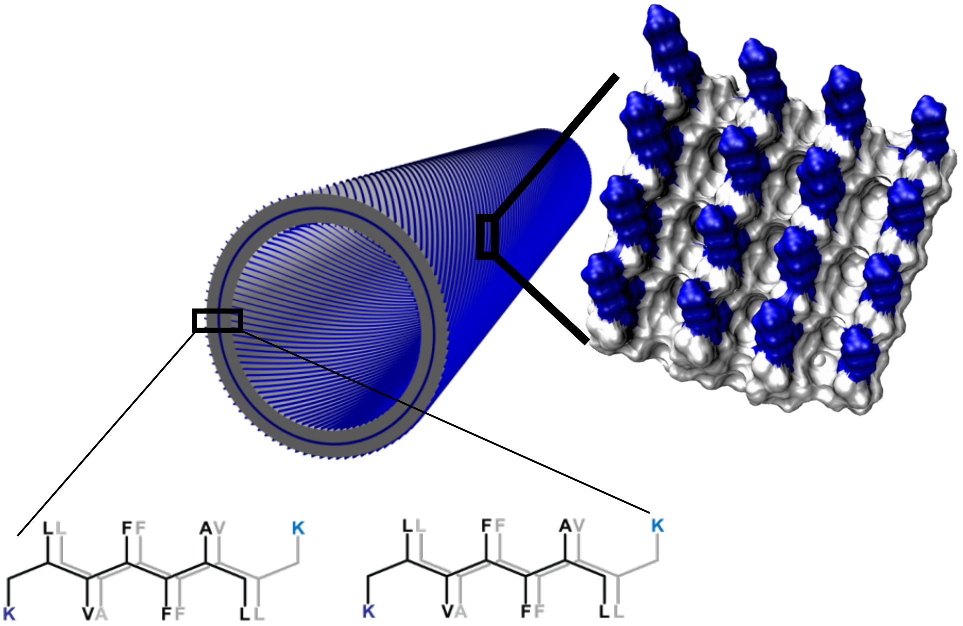

Figure 2-1 Peptide nanotube model highlighting the hydrophobic groove on the surface and the anti-parallel out-of-register peptide bilayer.

Here, we describe the design of self-assembling peptides for the polymerization of linkage-specific nucleic acids. Specifically, we modify key residues that contribute to nanotube surface groove morphology and terminal residues, to produce assemblies that will promote 5’phosphate/3’hydroxyl proximity while eliminating unnecessary side reactions. Microscopic and spectroscopic techniques were used to characterize peptide self-assemblies, and Mass Spectrometry was employed to assess nucleotide polymerization.

Self-assembly of reactive-neutral peptide nanotubes

Peptide Ac-KLVFFAL-NH_2 and Ac-RLVFFAL-NH_2 form homogeneous nanotubes in 40% Acetonitrile and water with trifluoroacetic acid. Ac-KLVFFAL-NH_2 nanotubes catalyze aldol and retro-aldol condensation with the lysine side chain intimately involved in the reaction mechanism [42]. Ferris and others pointed out that the oligomerization of nucleic acids is a proximity driven process [37-39]. As long as the 5’phosphate is within a discernible distance of the 3’hydroxyl, the reaction would likely take place. With lysine’s nucleophilic side chain, side reactions in the oligomerization of nucleic acids are highly probable. To prevent side reactions, including the formation of P-N bonds, we examined the use of arginine (R) as the N-terminal amino acid (Figure 2-2). Arginine has a Guanidinium ion as its side chain, which maintains a positive charge while eliminating nearly all reactivity (Fig. 2-2).

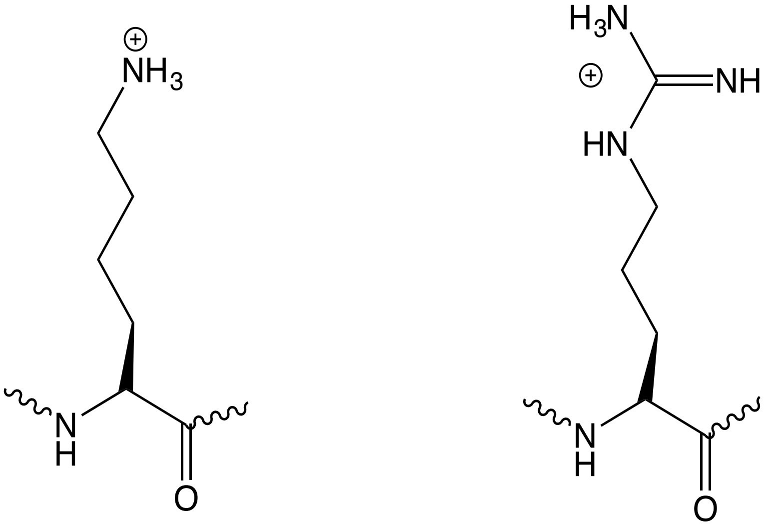

Lysine Arginine

Figure 2-2 Molecular structures of Lysine (left) and arginine (right).

Ac-RLVFFAL-NH$_2$ was synthesized via SPPS and assembled using 40% acetonitrile and water. These assemblies were formed at pH2, which was achieved by adjusting the amount of trifluoroacetic acid (TFA) to approximately 0.1%, and room temperature. TFA acts as a counter ion for the positively charged lysine or arginine residue side chains at both the bilayer leaflet interface and the solvent-exposed nanotube surface (Figure 2-3) [45]. Within the bilayer, in the absence of TFA, electrostatic repulsion would drive peptide leaflets apart. Peptide bilayer formation requires the presence of at least residual TFA from HPLC purification. We examined assemblies at pH2 to ensure a sufficient amount of TFA was present to drive bilayer formation, and to promote homogeneity.

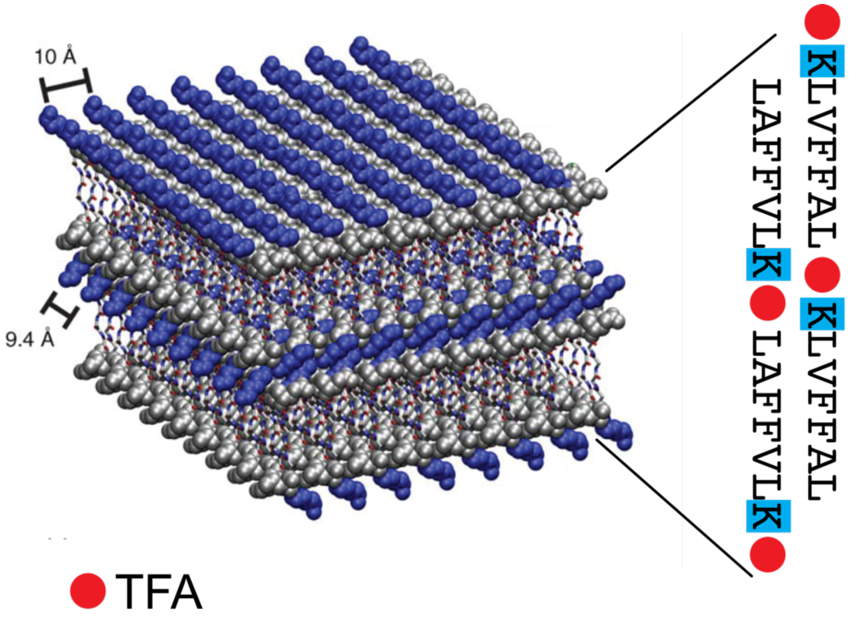

Figure 2-3 Peptide bi-layer model. *Peptides are oriented anti-parallel, out-of-regiter by one amino acid. Distances correspond to intersheet distance (10Å), and distance between solvent exposed lysines (9.4Å).*

Peptides were given 7 days to assemble before examination. Self-assembling peptides undergo phase transitions as they develop into homogeneous structures, and nanotubes often take several weeks before reaching homogeneity [46]. Following initial submersion in the solvent conditions, peptides aggregate to form defined particles. Within the particles, nucleation of cross-beta architecture occurs. Growth of distinct assemblies follow. In the case of nanotubes, sheet formation, flat peptide assemblies with high laminate number, precedes ribbon formation, curvature of the original sheets, which ultimately leads to the formation of nanotubes (Figure 2-4) [46]. This assembly pathway can be monitored by TEM or through fluorescence life-time imaging using rhodamine-LVFFAL-NH_2 mixed with peptide Ac-KLVFFAL-NH_2 [47].

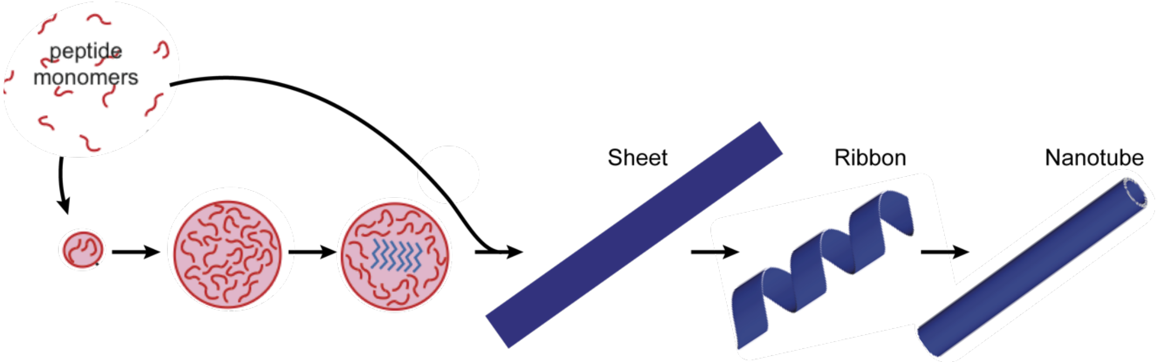

Figure 2-4 Peptide nanotube assembly pathway. *Peptides pass through several phases before reaching terminal assembly.*

Following one week of assembly, nanotube morphology and the formation of beta-sheets was monitored by transmission electron microscopy (TEM) and Circular Dichroism (CD). Prior to examination by TEM and CD, peptides Ac-KLVFFAL-NH_2 and AC-RLVFFAL-NH_2 were spun down and resuspended in water. By resuspending in water, the assembly environment could be easily manipulated for future catalysis. Ac-KLVFFAL-NH_2 and Ac-RLVFFAL-NH_2 assemblies appeared identical and were homogeneously nanotubes by TEM, with widths consistent with the literature [41-43]. By TEM, nanotube morphology can be characterized by the following criteria: 1. Persistent length of assemblies is consistent,

2. Assemblies have distinct white borders, nanotube walls, and 3. Negative stain is able to enter nanotubes, which increases the contrast of white walls [27].

By CD, Ac-KLVFFAL-NH_2 and Ac-RLVFFAL-NH_2 nanotube assemblies, had elliptical minima at 225nm and positive ellipticity at ~200nm, consistent with β-sheets (Figure 2-5). High peptide assembly concentration resulted in saturation of the detector. Therefore, precise determination of the wavelength for the positive ellipticity peak was not possible.

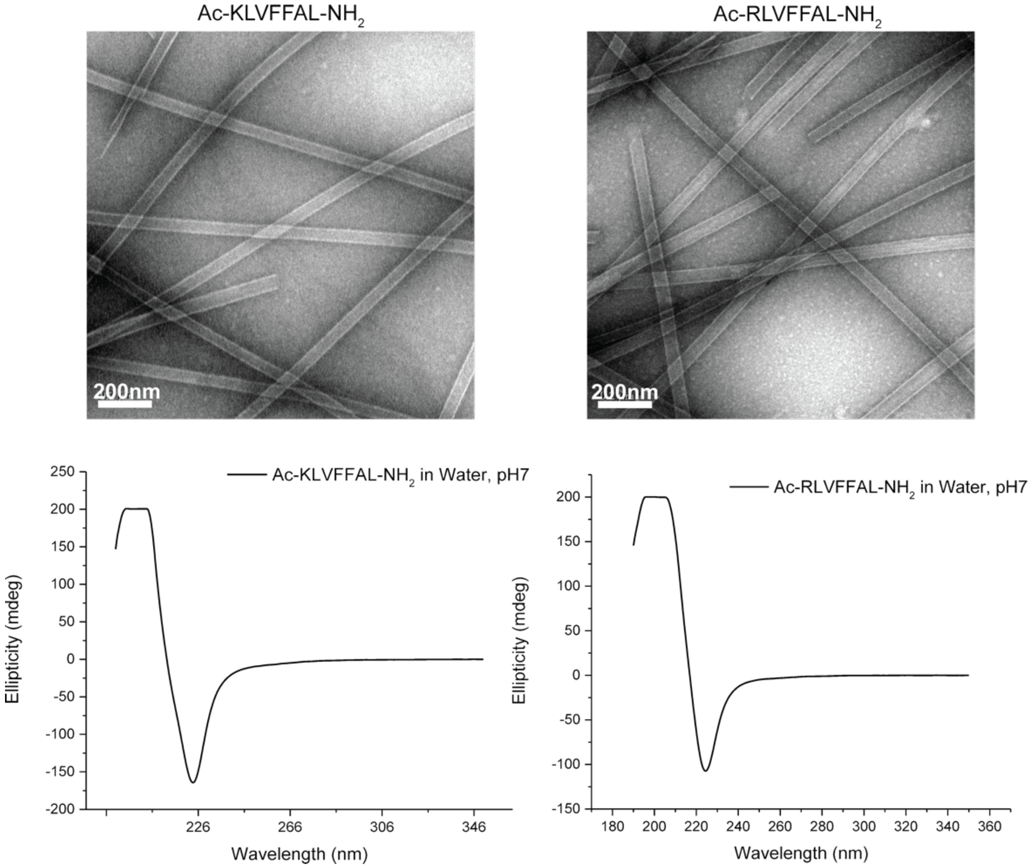

Figure 2-5 Monitoring Ac-KLVFFAL-NH_2 and Ac-RLVFFAL-NH_2 assembly. *Ac-KLVFFAL-NH_2 and Ac-RLVFFAL-NH_2 self-assemble as nanotubes of homogeneous width in 40% acetonitrile, 60% water, 0.1%trifluoroacetic acid at pH2. CD identifies minima at 225nm and a positive elliptical peak at ~200nm. Nanotubes were spun-down and resuspended in water prior to examination by TEM and CD.*

Self-assembly of groove-modified peptide nanostructures

With the successful assembly of reactive-neutral nanotubes by peptide Ac-RLVFFAL-NH_2, increasing our potentially-catalytic assembly repertoire was possible through the design of nanotubes with different surface groove morphologies. Alteration of leucine at position two or seven would theoretically change the groove environment. As an initial candidate, asparagine was examined as a replacement for leucine at position two (Figure 2-6). Maintaining the arginine at the N-terminus, the peptide Ac-RNVFFAL-NH_2 was designed.

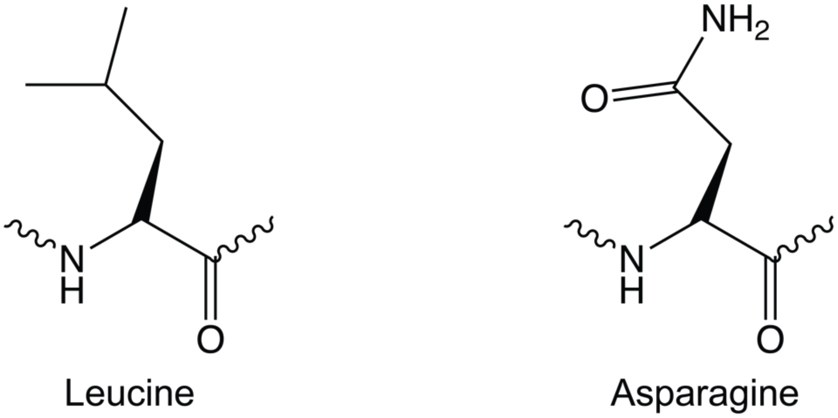

Figure 2-6 ***Molecular structures of Leucine (left) and asparagine (right).***

Asparagine was chosen as an initial candidate to decrease the hydrophobicity of the groove and promote hydrogen-bonding with added nucleotides or other substrates. Peptides containing glutamine have a propensity to form parallel beta-sheets and propagate as fibers. Therefore, glutamine was not explored.

Ac-RNVFFAL-NH_2 was assembled at both 20% and 40% acetonitrile, 0.1%TFA at pH2 to assess optimal assembly conditions. Assembly of Ac-RNVFFAL-NH_2 was monitored by CD over 10 days. At 10 days of assembly, samples were spun down and resuspended in water for analysis by TEM and Fourier Transform-Infrared spectroscopy (FT-IR).

For both Ac-RNVFFAL-NH$_2$ in 20% and 40% acetonitrile, elliptical signatures indicate beta-sheet morphology (Figure 2-7). However, compared with the nanotube ellipticities of Ac-RLVFFAL-NH$_2$, Ac-RNVFFAL-NH$_2$ minima are below 220nm for the majority of time points examined, and have broader peaks. At ten days, both conditions appear to have a spectrum with a single maximum negative ellipticity between 210 and 220nm. This time point was chosen for further analysis of Ac-RNVFFAL-NH$_2$ assemblies.

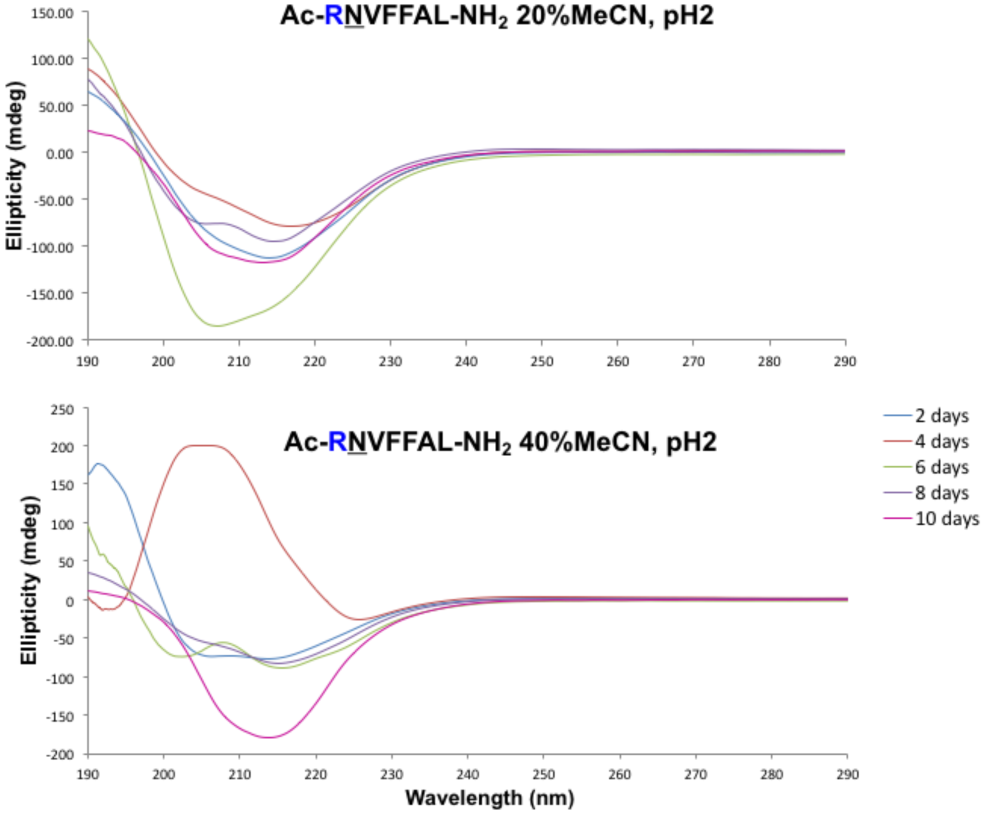

Figure 2-7 Circular Dichroism of Ac-RNVFFAL-NH$_2$ over 10 days of assembly. *Ac-RNVFFAL-NH$_2$ was assembled in 20% acetonitrile and 40% acetonitrile with 0.1%TFA at pH2. Assemblies were monitored over ten days by CD using a 0.1mm quartz cuvette.*

Resuspension of Ac-RNVFFAL-NH$_2$ assemblies in water at ten days revealed fibrous morphology for both assembly conditions. By TEM, fibers appeared straight with no apparent twisting (Figure 2-8). Percentage of acetonitrile does not appear to affect the assembly maturation of Ac-RNVFFAL-NH$_2$. However, the viscosity of Ac-RNVFFAL-NH$_2$ assemblies at 20% acetonitrile appeared higher than that of those assembled at 40% acetonitrile. Decreasing the percentage of acetonitrile in the assembly conditions likely contributed to the kinetics of assembly. Although, not discernible by CD or TEM, a more polar assembly environment often results in a greater degree of heterogeneity and assembly due to hydrophobic collapse and desolvation.

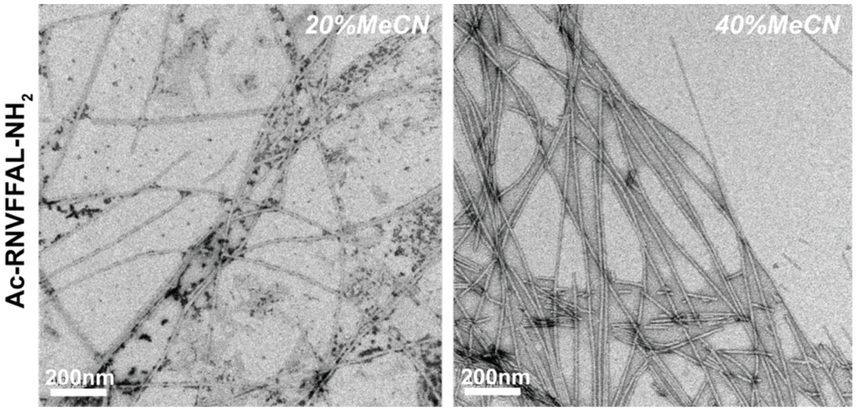

Figure 2-8 Transmission electron micrographs of Ac-RNVFFAL-NH$_2$ assemblies. *Ac-RNVFFAL-NH$_2$, assembled at both 20% and 40% acetonitrile, 0.1% TFA pH2 resuspended in water. For both assembly conditions, fibers are apparent. MeCN = Acetonitrile.*

Ac-RNVFFAL-NH$_2$ fibrous assemblies resuspended in water were examined by FT-IR spectroscopy to confirm secondary structure and begin to examine peptide orientation. As mentioned previously, peptides containing glutamine propagate as parallel beta-sheets and are fibrous in appearance. Asparagine and glutamine differ by a single methylene. Ac-RNVFFAL-NH$_2$ assemblies compared to Ac-KLVFFAE-NH$_2$ fibers at pH7 and nanotubes at pH2, both of which propagate as anti-parallel β-sheets and have two amide I stretches, had one amide I stretch (Figure 2-9). The amide I stretching occurs between 1600cm^{-1} and 1700cm^{-1} for beta sheets and other secondary structures including alpha-helices. Absorbance at ~1625cm^{-1} is consistent with the presence of beta-sheet secondary structure. In an anti-parallel assembly, the amide is placed in two different orientations giving rise to a second amide environment and a second stretching frequency at ~1695cm^{-1}. This small secondary peak can be clearly seen for the fiber and tube controls in Figure 2-9. For Ac-RNVFFAL-NH$_2$ assemblies at both 20% and 40% acetonitrile, the absence of this secondary peak suggests the orientation of peptides in both conditions is parallel.

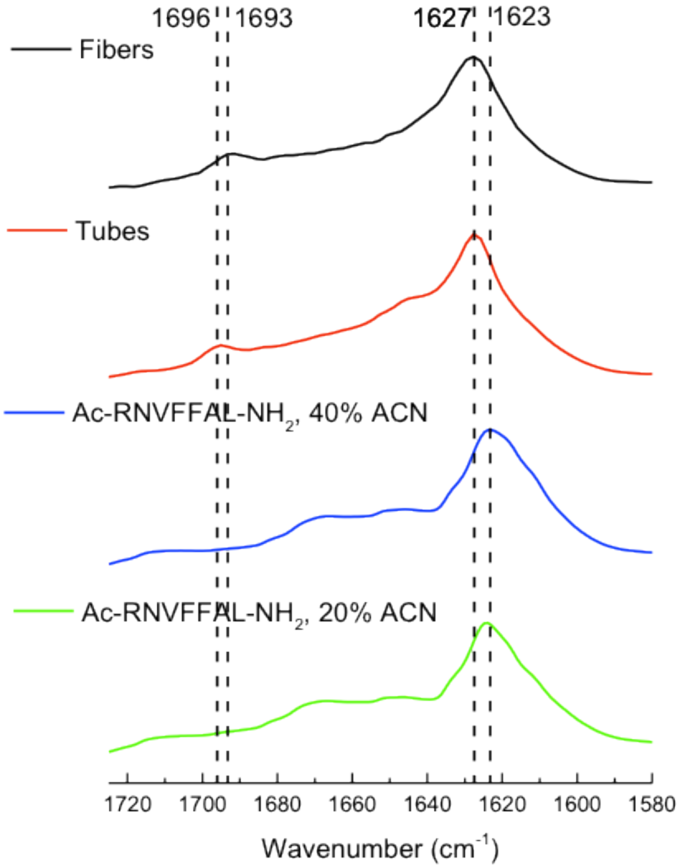

Figure 2-9 FT-IR of Ac-RNVFFAL-NH$_2$ assemblies. *Canonical anti-parallel out-of-register tubes and anti-parallel fibers were used for comparison.*

The appearance of parallel beta-sheets in Ac-RNVFFAL-NH_2 assemblies is supported by published glutamine data [48]. The difference of one methylene does not appear to hinder hydrogen-bonding across the laminate and thus, creates a densely-packed positively charged fiber surface. Instead of altering the groove morphology as had been desired, a cationic surface, much like that of montmorillonite, was created. The adsorption of nucleotides to cationic surfaces is well-documented [38-40], and a flexible cationic amyloid surface may promote nucleotide polymerization. However, the loss of groove structure will likely result in heterogeneous linkages.

As a second candidate for altering groove morphology, tert-leucine was chosen as a replacement for leucine at position two (Figure 2-10). This replacement maintains a hydrophobic environment while bringing the side chain closer to the backbone and potentially altering steric interactions with small-molecules. Arginine was maintained at the N-terminus.

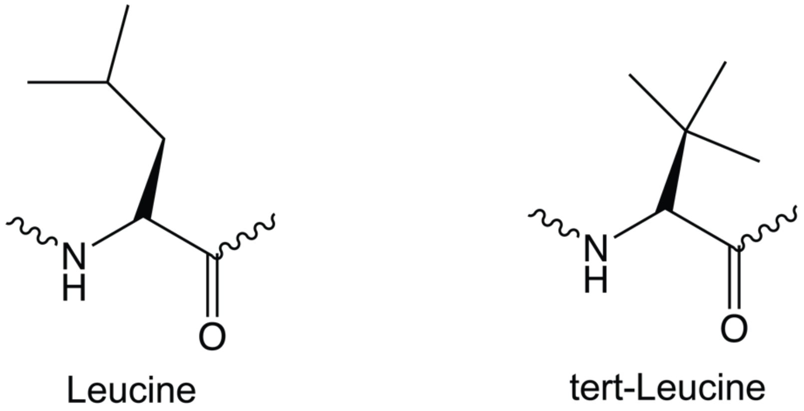

***Figure 2-10* Molecular structures of Leucine (left) and tert-Leucine (right).**

Peptide Ac-RtLVFFAL-NH_2 was synthesized by SPPS and assembled in 40% acetonitrile, 60% water, 0.1% TFA at pH2. Assembly was monitored by TEM and CD, and examined further structurally by FT-IR and powder x-ray diffraction (PXRD).

Ac-RtLVFFAL-NH_2 assembly maturation was monitored by CD and consistent beta-sheet ellipticities were observed with an elliptical minimum at 218nm and a positive ellipticity at 204nm, after two weeks of assembly (Figure 2-11). A shoulder at ~226nm was also noted. Assemblies were spun down and resuspended in water before preparation of TEM grids or analysis by FT-IR and PXRD. Following the resuspension of Ac-RtlVFFAL-NH_2 in water, nanotubes were observed by TEM. The majority of the nanotubes appeared mature. However, several were still ribbonous in morphology, the step preceding nanotube formation in the assembly pathway (Figure 2-4).

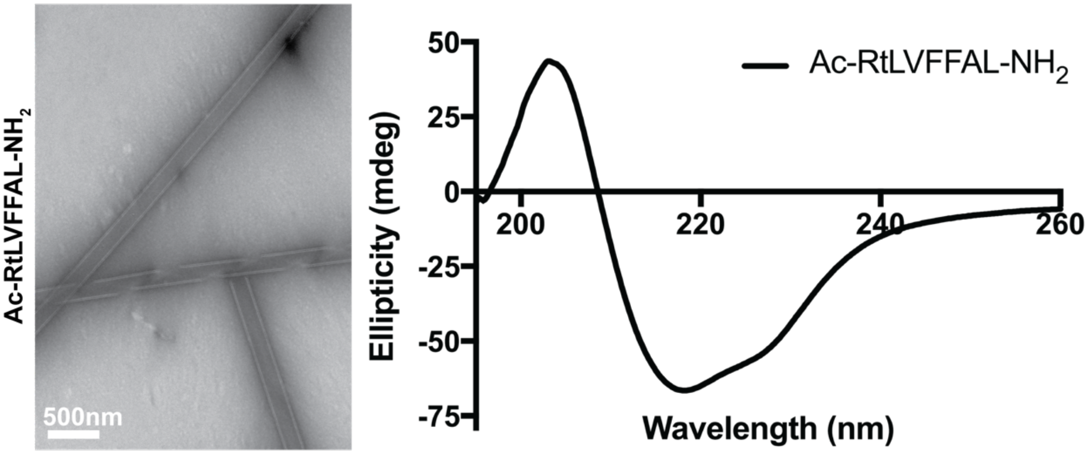

Figure 2-11 Ac-RtLVFFAL-NH2 assembly maturation by CD and TEM. *Ac-RtLVFFAL-NH2 was assembled in 40% acetonitrile, 60% water, and 0.1%TFA at pH2. Ribbons and nanotubes of homogeneous width were present in transmission electron micrographs at two weeks of assembly. Assembly was monitored by CD using a 0.1mm quartz cuvette.*

FT-IR was used to assess orientation of peptides within beta sheets. For all nanotubes examined previously, the orientation and registry of peptides has been anti-parallel out-of-register by one residue as determined by solid state NMR [43]. Because of the similar width and homogeneity of Ac-RtLVFFAL-NH_2 nanotubes as compared to the well-characterized nanotube-forming peptides Ac-KLVFFAL-NH_2, Ac-RLVFFAL-NH_2, and Ac-pYLVFFAL-NH_2 [27,43,44], an anti-parallel orientation as determined by FT-IR was expected. The appearance of a secondary amide I peak at 1696cm^{-1} for mature Ac-RtLVFFAL-NH_2 nanotubes (Figure 2-12) further confirmed expectations of an anti-parallel beta-sheet assembly.

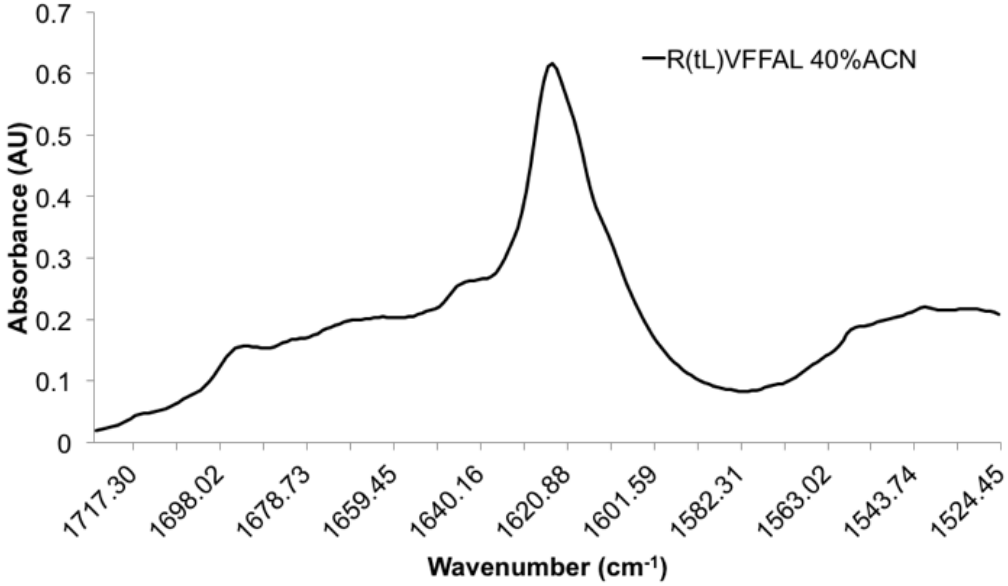

Figure 2-12 Ac-RtLVFFAL-NH_2 assembly orientation is anti-parallel. *Liquid thin-film FT-IR after four weeks of Ac-RtLVFFAL-NH_2 assembly. Maxima at 1627cm^{-1} and 1696cm^{-1}.*

PXRD was used to assess whether Ac-RtLVFFAL-NH_2 nanotubes maintained cross-β architecture. A cross-β assembly is characterized by the positioning of beta-strands orthogonal to the long axis of the nanostructure [27]. Peptides arranged in such a way give rise to a diffraction pattern with two reflections by PXRD. The 4.7Å reflection is consistent with the interstrand distance of hydrogen-bonded beta-strands, while the ~10Å measurement reflects the intersheet or laminate distance. For Ac-RtLVFFAL-NH_2, nanotubes have both a 4.7Å and 10.3Å reflection, consistent with cross-beta criteria. A narrow peak at 10.3Å suggests a highly homogeneous assembly landscape.

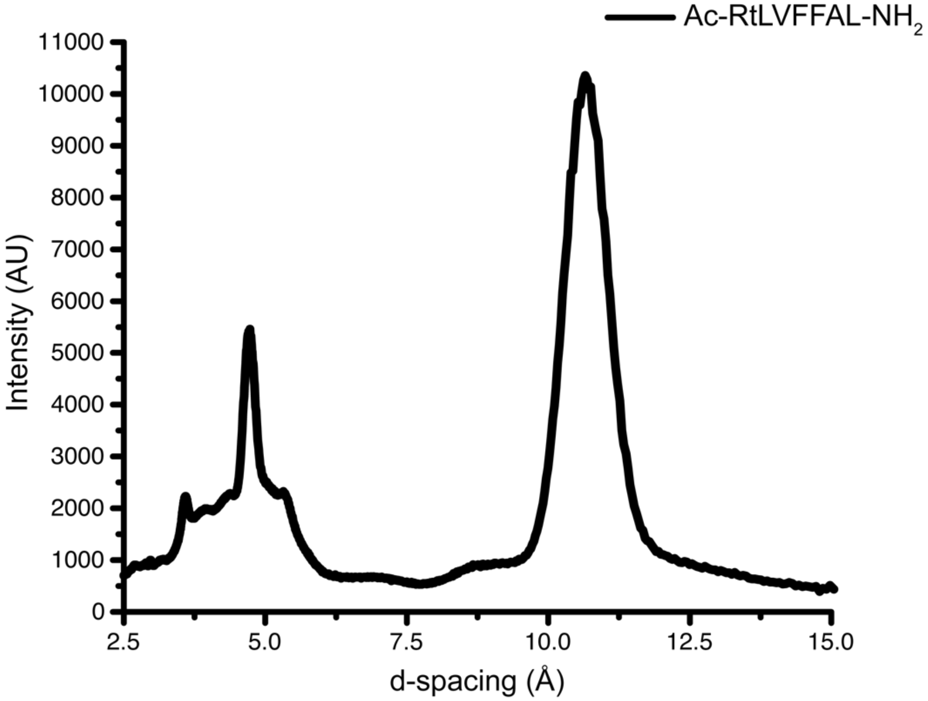

Figure 2-13 PXRD analysis of Ac-RtLVFFAL-NH$_2$ nanotubes. *A 4.7Å and 10.3Å reflection is measured from the resulting diffraction pattern.*

The final candidate for nucleotide polymerization was designed with the intention of maintaining the hydrophobic character of the groove, while also increasing the groove size to accommodate larger molecules, sterically-constrained molecules, and polymers. To address these parameters, alanine was chosen as a replacement for leucine at position two and tert-leucine replaced the C-terminal leucine (Figure 2-14).

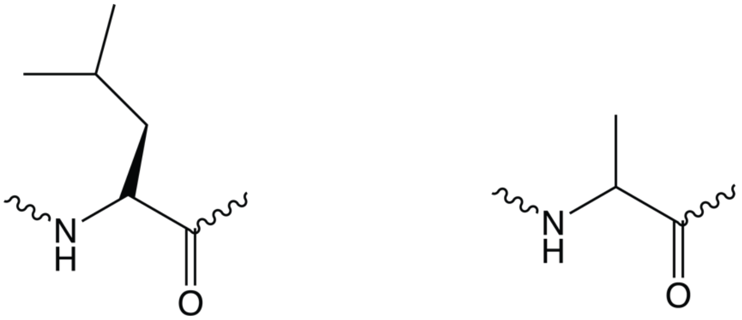

Leucine

Alanine

***Figure 2-14* Molecular structures of Leucine (left) and alanine (right).**

Ac-RAVFFAtL-NH_2 was synthesized by SPPS and assembled in 40% acetonitrile, 60% water, and 0.1% TFA, at pH2. At eight weeks, Ac-RAVFFAtL-NH_2 assembly was still heterogeneous by CD and TEM. Nanotubes were not observed at any time by TEM. Instead, sheets, short fibers, and amorphous aggregates were present in abundance. By replacing the leucine at position two with alanine, the hydrophobic character may have decreased too steeply for nanotube formation, and favorable Van der Waals interactions disrupted. It should also be noted that two amino acids were replaced in this candidate. The replacement of two amino acids that typically maintain intermolecular interactions with smaller hydrophobic amino acids likely resulted in unfavorable solvent accessibility to the groove, preventing nanotube propagation.

By CD, Ac-RAVFFAtL-NH_2 secondary structure was heterogeneous with negative minima at 200nm and 230nm indicating the persistence of random coil/loop and beta-sheet components, respectively (Figure 2-15).

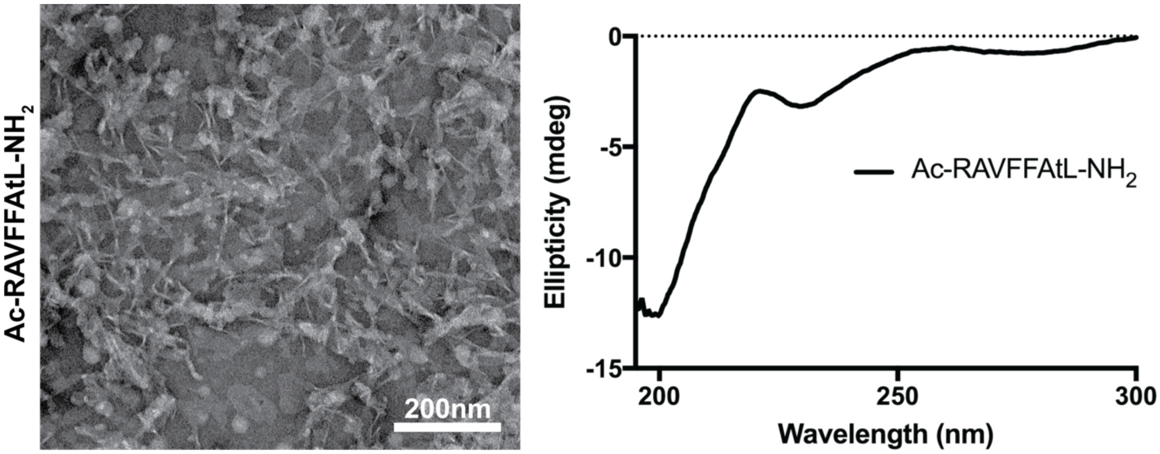

Figure 2-15 Ac-RAVFFAtL-NH$_2$ assembly monitored by TEM and CD. *Transmission electron micrographs and CD spectrum of Ac-RAVFFAtL-NH$_2$ at eight weeks of assembly.*

Ac-RAVFFAtL-NH$_2$ was further examined by FT-IR for a more detailed sampling of amide environments. By FT-IR, the environments of amide I can be assigned confidently. Amide I relies primarily on the stretching frequency of the C=O bond of the peptide backbone. However, side-chain amides also show up in this region. The position of the amide I peak is influenced by its environment, with interstrand hydrogen-bonds contributing significantly to the stretching frequency of the C=O bond. For Ac-RAVFFAtL-NH$_2$, the FT-IR spectrum indicates a beta-sheet component (Figure 2-16), but a peak at ~1695cm^{-1} is not discernible; a broad peak from 1650cm^{-1} to 1700cm^{-1} reduces resolution of the secondary amide I peak. This broad band has been assigned to unassembled peptide monomers. A distinct peak at 1640cm^{-1} may represent the sampling of a distinct C=O bond environment. The 1640cm^{-1} peak is attributed to disordered or amorphous peptide aggregates here.

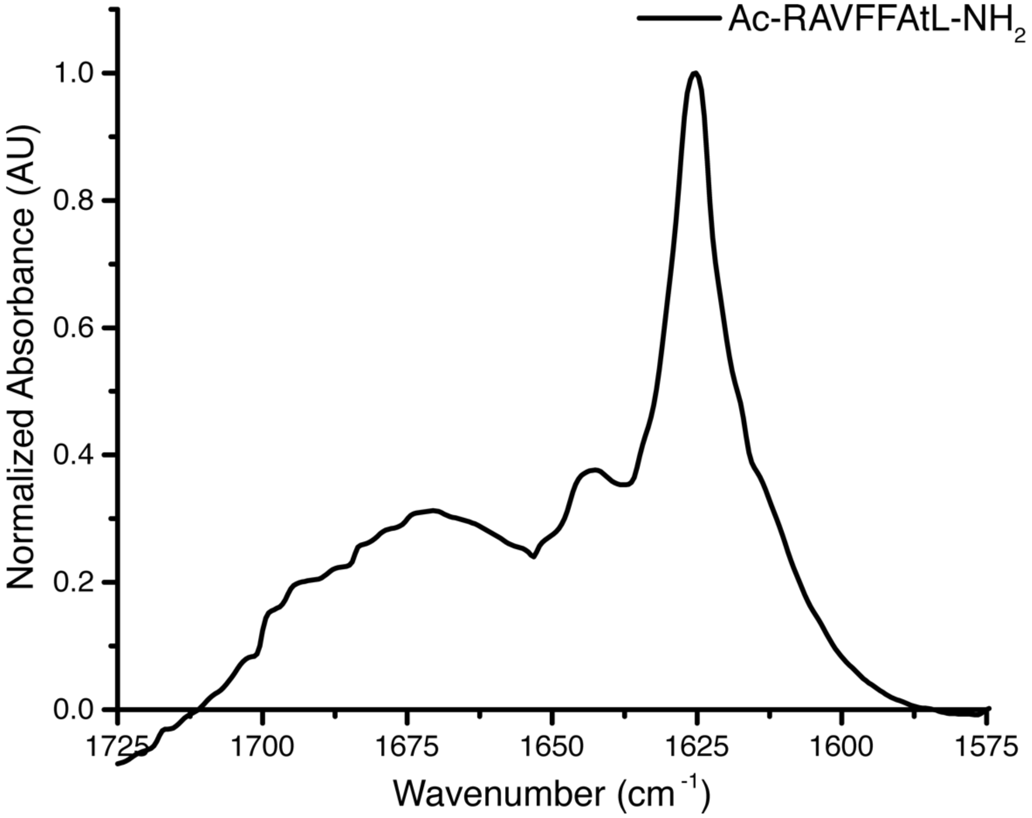

Figure 2-16 FT-IR analysis of Ac-RAVFFAtL-NH$_2$ at eight weeks of assembly. *Liquid thin-film FT-IR spectrum of Ac-RAVFFAtL-NH$_2$. Amide I maxima at 1626cm^{-1}, 1640cm^{-1}, and 1670cm^{-1}.*

Powder x-ray diffraction (PXRD) of Ac-RAVFFAtL-NH$_2$ assemblies reflects other findings. Consistent with what is expected for cross-β assemblies, Ac-RAVFFAtL-NH$_2$ assemblies have two major reflections by PXRD, ~4.6Å and 10.2Å (Figure 2-17). The breadth of the reflection associated with interstrand hydrogen-bonds is consistent with the various C=O environments shown by FT-IR. Laminate/intersheet distance is narrower than expected at 10.2Å, suggesting some level of homogeneity in tertiary assembly.

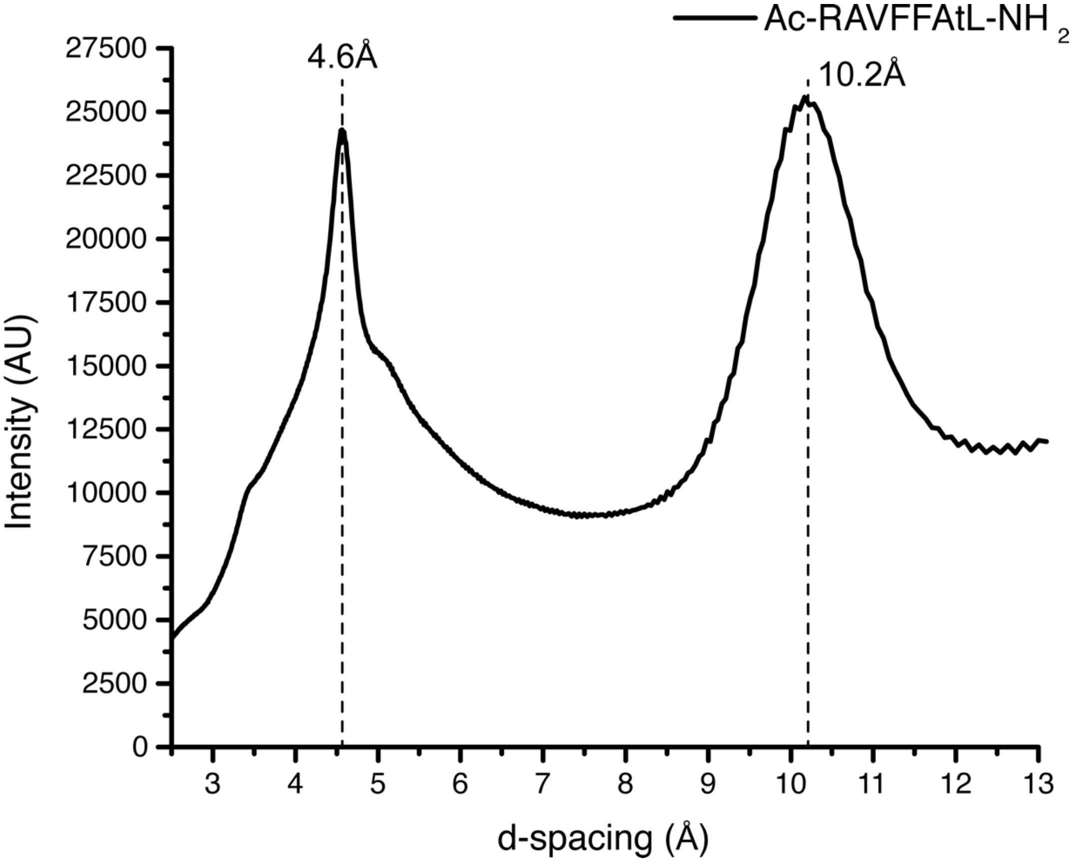

Figure 2-17 PXRD of Ac-RAVFFAtL-NH_2 reveals typical cross-β reflections. *Repeating domains give 4.6Å and 10.2Å reflections, consistent with interstrand and intersheet distance, respectively.*

Synthesis of modified adenine nucleotides

After clearly defining the design of four distinct peptide self-assemblies for nucleotide polymerization, the appropriate choice of nucleotide substrate was essential. Peptide assemblies examined in the following pages are diverse in global morphology, but all maintain a cross-beta or beta-sheet rich component. Peptide self-assemblies include: Ac-RLVFFAL-NH_2 (nanotubes), Ac-RNVFFAL-NH_2 (fibers), Ac-RtLVFFAL-NH_2 (nanotubes), and Ac-RAVFFAtL-NH_2 (fibers and amorphous aggregates).

Adenine was chosen as the initial polymerization candidate nucleotide. Past studies have characterized the binding of aromatic small molecules all containing multiple ring structures [41,42]. Therefore, a purine seemed the appropriate choice for a substrate. Because of guanine's propensity to self-associate through Hoogsteen hydrogen bonds, it was not explored.

To promote phosphodiester bond formation, nucleotides were modified with leaving groups, either imidazole or 2-methylimidazole [49]. Imidazole and methylimidazoles are acceptable activating agents in prebiotic chemistry because their synthesis has been demonstrated in what many agree to be plausibly prebiotic conditions [50]. Addition of imidazole or 2-methylimidazole to the phosphorus of deoxyadenosine monophosphate or adenosine monophosphate promotes phosphodiester bond formation because the release of imidazole changes the nature of the reaction; it is no longer a dehydration synthesis.

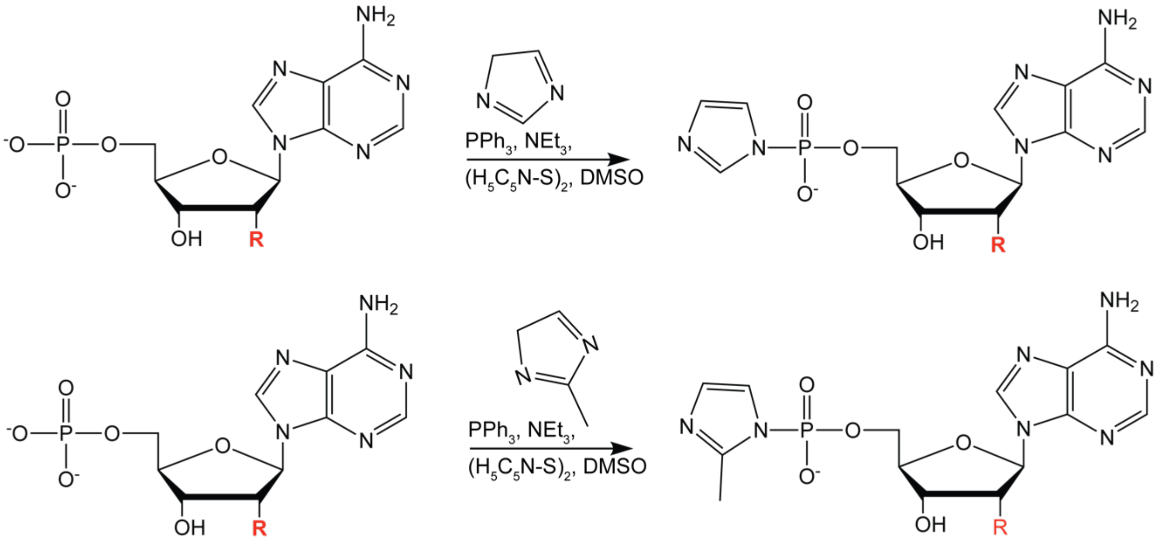

Figure 2-18 Synthetic scheme of phosphorimidazolides for nucleotide polymerization. R=OH or H

Nucleic acid polymerization on nanotubes

Modified nucleotides were combined with each of the designed peptide assemblies with polymerization conditions following closely those of Vogel et al. [37], and including Tris, NaCl, and $MgCl_2$. Peptides were diluted to a concentration of 0.5mM and modified nucleotides were added in 20-fold excess at 10mM. Polymerization was monitored first at 72 hours and later at two months. However, because no change was observed for longer time intervals, only 72-hour time points are included here.

To detect nucleotide and polymer products, liquid chromatography followed by mass spectrometry (LC-MS) was used. Interestingly, modified adenosine monophosphates consistently yielded dimers, while modified deoxyadenosine monophosphates consistently produced trimers (Figure 2-19, 2-20). Relative concentration of each product and remaining starting material was determined based on the starting concentration of the phosphorimidazolide used and the integration of individual peaks.

For Ac-RLVFFAL-NH_2, products and remaining reactant concentrations were compared across samples containing peptide, buffer alone, or a polyuridine or polythymine template for modified adenosine monophosphates and deoxyadenosine monophosphates, respectively (Figure 2-21). Between these samples there was no difference in product formation or monomer loss suggesting Ac-RLVFFAL-NH_2 nanotubes do not catalyze nucleotide polymerization under these conditions.

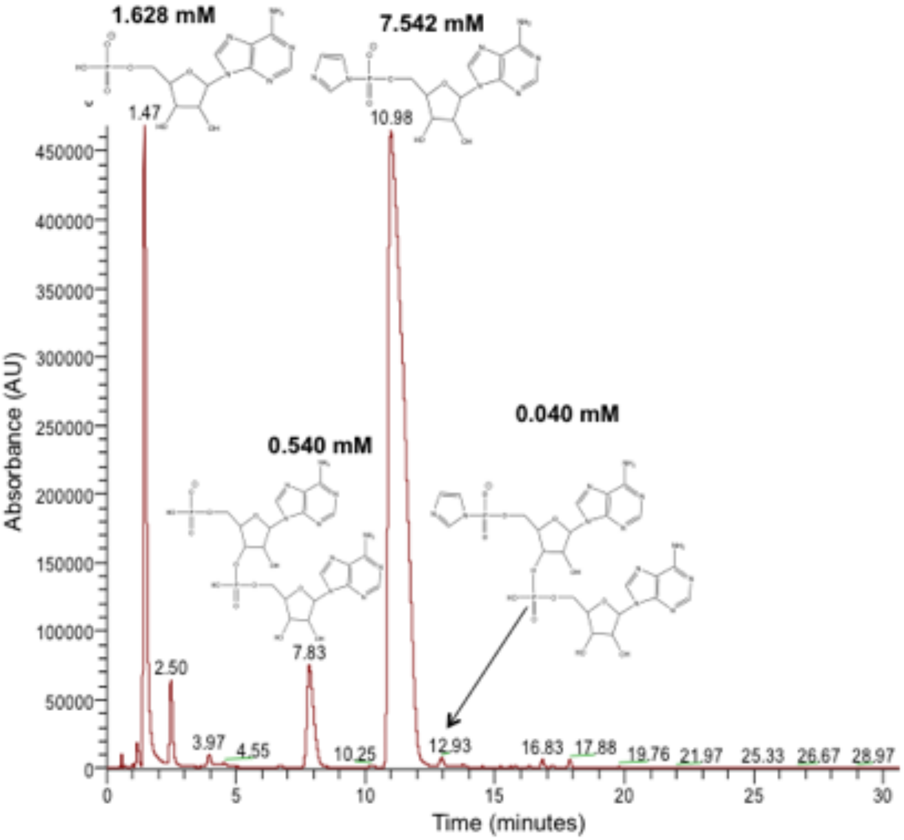

Figure 2-19 Ac-RLVFFAL-NH2 nanotubes combined with imidazole-modified adenosine monophosphates. *Hydrolyzed monomer, dimer, and activated dimer formation are apparent from these LC-MS data. Integration of individual peaks and starting monomer concentration (10mM) was used to calculate the concentrations shown.*

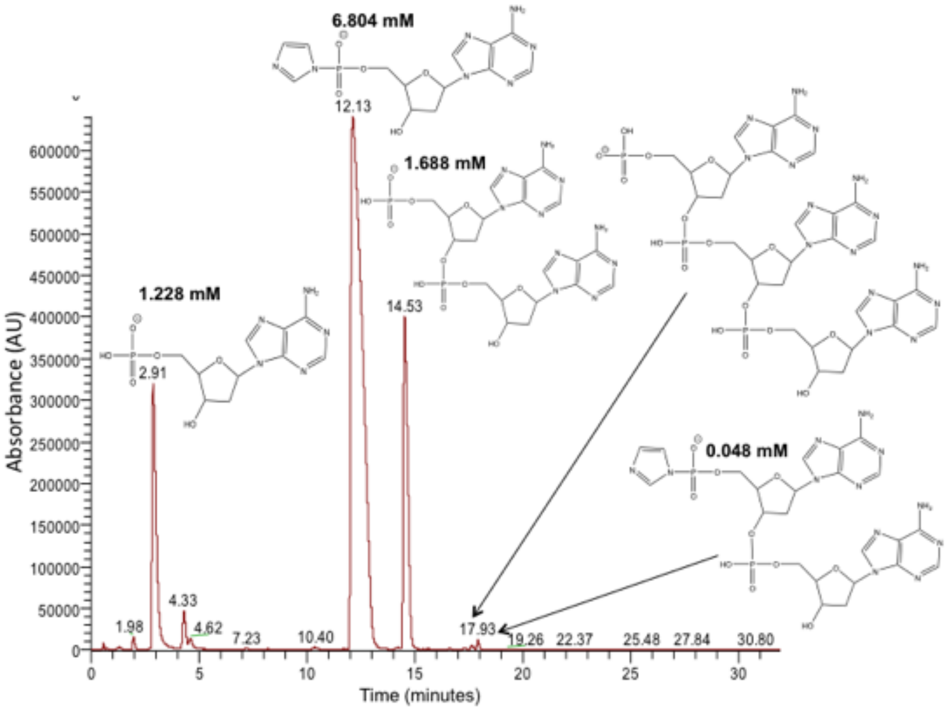

Figure 2-20 Ac-RLVFFAL-NH$_2$ nanotubes combined with imidazole-modified deoxyadenosine monophosphates. *Hydrolyzed monomer, dimer, activated dimer, and hydrolyzed trimer formation are apparent from these LC-MS data. Integration of individual peaks and starting monomer concentration (10mM) was used to calculate the concentrations shown.*

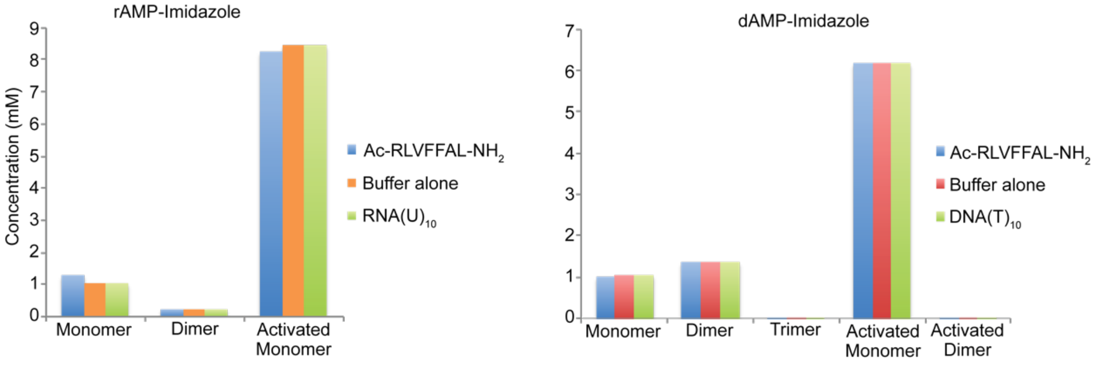

Figure 2-21 Comparison of control polymerization reactions to Ac-RLVFFAL-NH$_2$ driven reactions. *RNA(U)$_{10}$ was used as a template for the polymerization of imidazole-modified adenosine monophosphates. DNA(T)$_{10}$ was used as a template for the*

polymerization of imidazole-modified deoxyadenosine monophosphates. Concentrations were measured from integration of LC-MS data.

Despite the data indicating a lack of catalysis under these conditions, there is a lot we can learn about this system. Upon examination of reaction cocktails containing Ac-RLVFFAL-NH_2 nanotubes by TEM, extensive bundling of tubes was consistently observed. It has been shown that certain divalent salts can induce bundling of nanotubes, and bundling assists in structural characterization. However, the divalent salts that typically cause bundling, $MgSO_4$ and Na_2SO_4, were absent from these reactions. To determine the cause of nanotube bundling, each reaction component was added to the tubes independently (Figure 2-22).

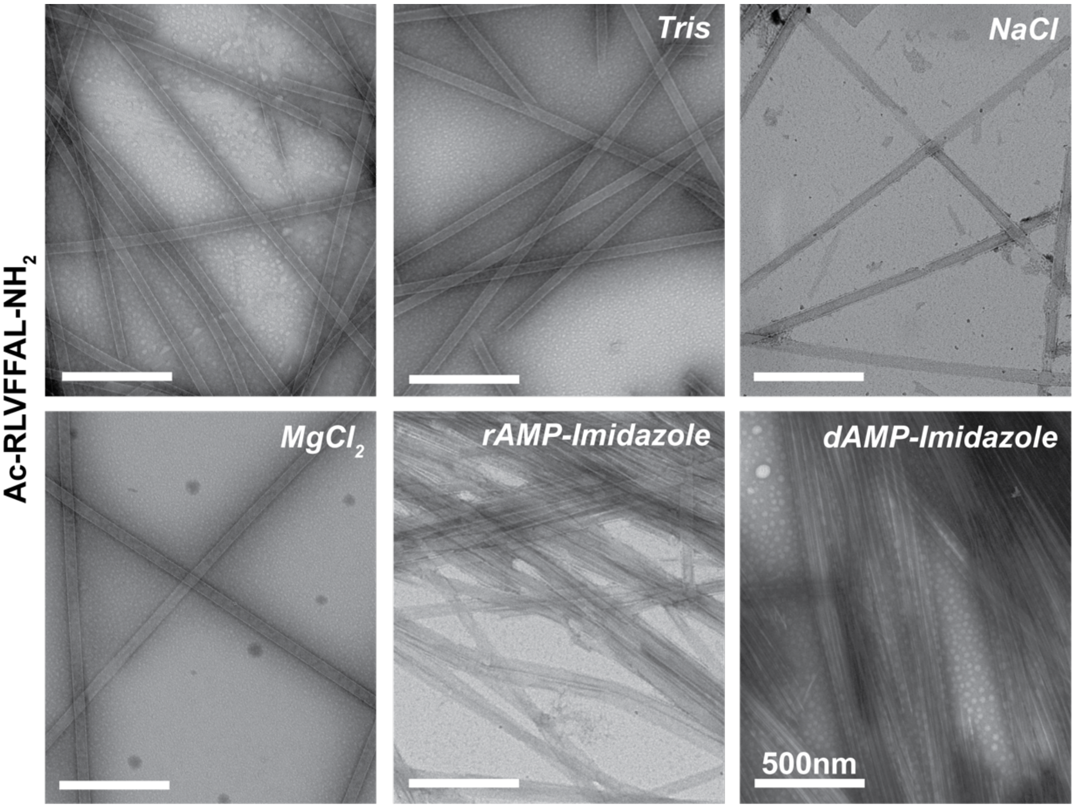

Figure 2-22 Analysis of reaction conditions and the Ac-RLVFFAL-NH_2 nanotube bundling phenotype. *Each reaction component was added to Ac-RLVFFAL-NH2*

nanotubes independently to asses for cause of nanotube bundling observed in reaction conditions. Scale bars are 500nm.

From these analyses, it was apparent that only in the presence of imidazole-modified adenosine monophosphates (rAMP-Imidazole) or imidazole-modified deoxyadenosine monophosphates (dAMP-imidazole) was bundling observed. These data suggest the binding of phosphorimidazolides and/or their reaction products to the tube surface. Binding of these substrates passivated the positively-charged tube surface and caused the extensive bundling of nanotubes. This appearance of bundling may have impeded further polymerization of nucleic acids.

The polymerization of activated nucleotides for the remaining three characterized peptide assemblies yielded similar results to Ac-RLVFFAL-NH_2. Compared to buffer-only controls and template-containing controls, peptide-containing reactions did not significantly catalyze polymer formation.

Modified nucleotides combined with Ac-RNVFFAL-NH_2 fibers revealed the same trend in product formation; imidazole-modified adenosine monophosphates produced dimers at most, while imidazole-modified deoxyadenosine monophosphates produced up to trimers (Figure 2-23, 2-24).

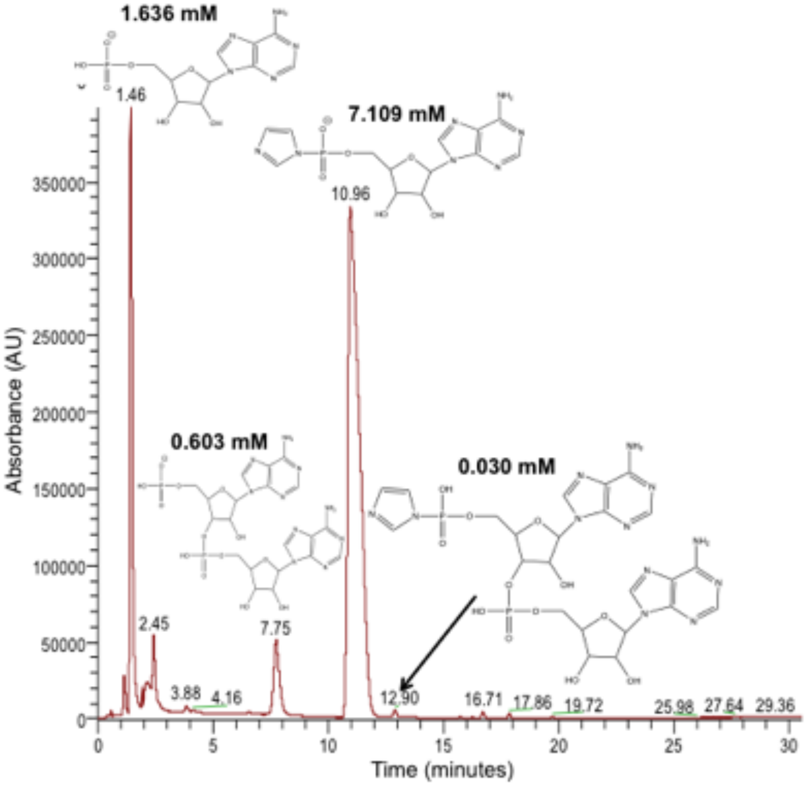

Figure 2-23 Ac-RNVFFAL-NH_2 fibers combined with imidazole-modified adenosine monophosphates. *Hydrolyzed monomer, dimer, and activated dimer formation are apparent from these LC-MS data. Integration of individual peaks and starting monomer concentration (10mM) were used to calculate the concentrations shown.*

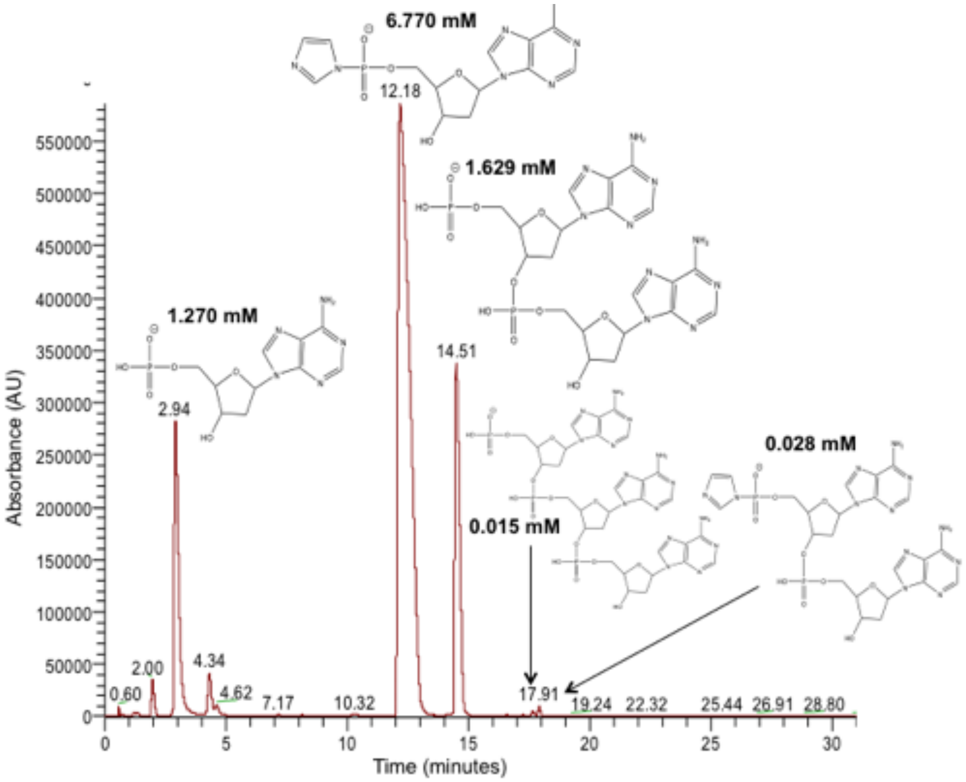

Figure 2-24 Ac-RNVFFAL-NH$_2$ fibers combined with imidazole-modified deoxyadenosine monophosphates. *Hydrolyzed monomer, dimer, activated dimer, and hydrolyzed trimer formation are apparent from these LC-MS data. Integration of individual peaks and starting monomer concentration (10mM) was used to calculate the concentrations shown.*

Visualization of reaction cocktails by TEM revealed particle formation and loss of fibers in both imidazole-modified adenosine monophosphate samples and imidazole-modified deoxyadenosine monophosphate samples (Figure 2-25). Concentration of peptide in the reaction conditions was maintained at 0.5mM, which is above the critical concentration of most ‘Ac-KLVFFAE-NH$_2$’ congeners. However, the critical concentration for Ac-RNVFFAL-NH$_2$ appears to be above 0.5mM from these data. By CD, loss of beta-sheet signal is observed in dilute peptide samples and in samples containing individual reaction components (data not shown).

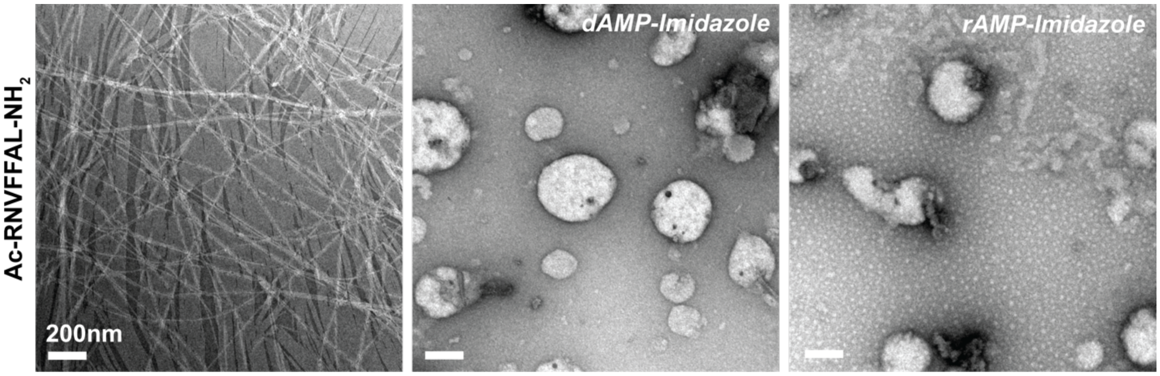

Figure 2-25 Ac-RNVFFAL-NH2 disassembly in the presence of modified nucleotides. *In the transmission electron micrograph on the left, mature Ac-RNVFFAL-NH$_2$ fibers at a concentration of 2.5mM. Peptide is diluted to 0.5mM and reaction components are added: dAMP-Imidazole (middle), and rAMP-imidazole (right). Scale bars are 200nm.*

Examination of Ac-RtLVFFAL-NH$_2$ nanotubes as polymerization catalysts yielded results similar to Ac-RLVFFAL-NH$_2$ nanotubes and Ac-RNVFFAL-NH$_2$ fibers. Formation of hydrolyzed monomer, dimer, and trimer were apparent from LCMS data of deoxyadenosine monophosphate-imidazole polymerization in the presence of Ac-RtLVFFAL-NH$_2$. Retention times differ from previous chromatograms because a different column was used for the liquid chromatography portion of this analysis.

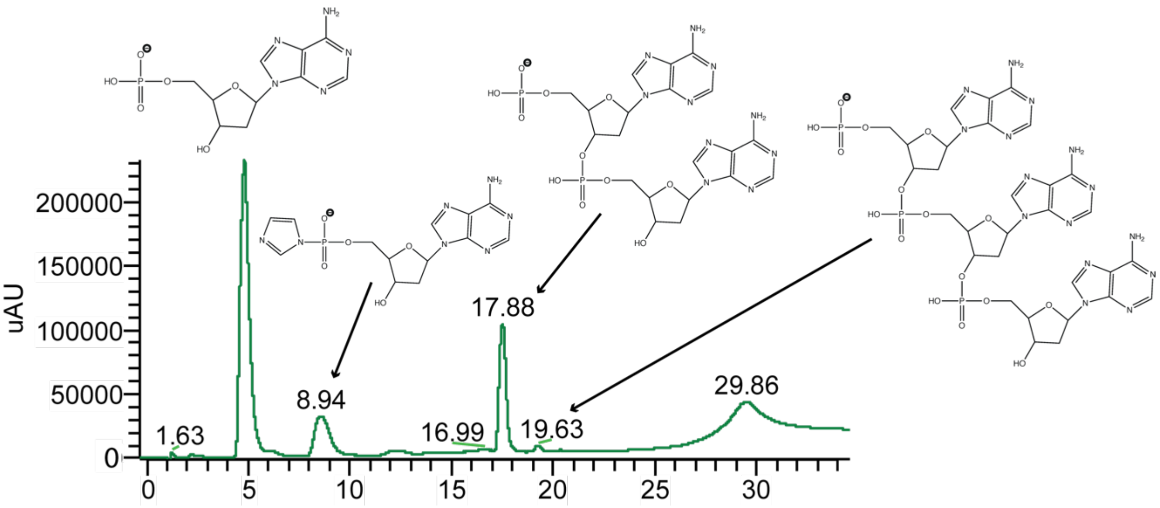

Figure 2-26 LCMS analysis of deoxyadenosine monophosphate -Imidazole polymerization using Ac-RtLVFFAL-NH$_2$. *Hydrolyzed monomer, dimer, and trimer are shown. Values indicate retention time.*

By TEM, Ac-RtLVFFAL-NH$_2$ nanotubes did not produce the same response as Ac-RLVFFAL-NH$_2$ nanotubes in the presence of activated monomer. Instead, positive staining and sheet formation are observed. It appears that nanotubes are now the minor assembly species. Interestingly, the positive staining of assemblies by TEM is usually attributed to the presence of negative charges on the surface. These data suggest a concentration of at least nucleotide monomers on the surface of Ac-RtLVFFAL-NH$_2$ assemblies.

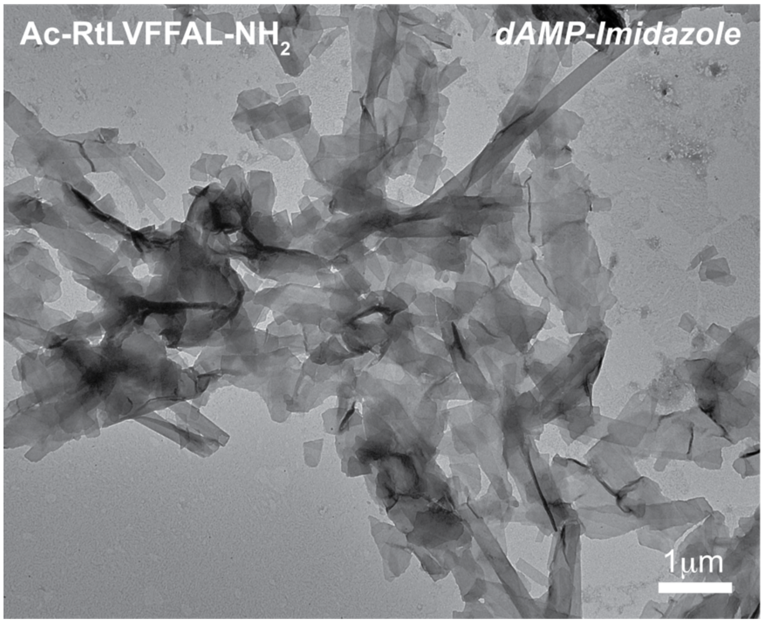

Figure 2-27 Ac-RtLVFFAL-NH$_2$ assemblies following addition of deoxyadenosine monophosphate-imidazole (dAMP-Imidazole).

Examination of Ac-RAVFFAtL-NH_2 assemblies as polymerization catalysts also yielded the formation of hydrolyzed monomers, dimers, and trimers for deoxyadenosine monophosphate-imidazole (Figure 2-28).

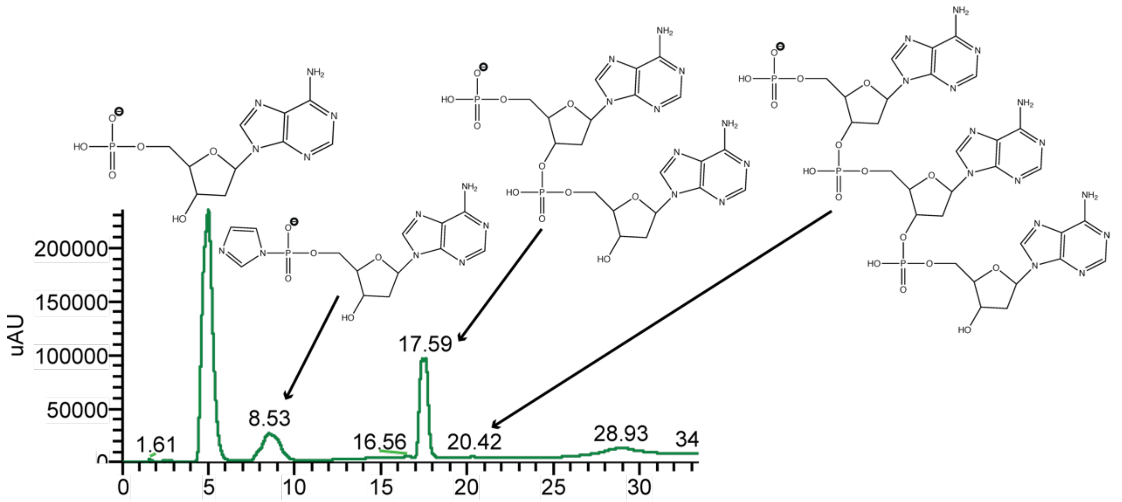

Figure 2-28 LCMS analysis of deoxyadenosine monophosphate-Imidazole polymerization using Ac-RAVFFAtL-NH_2. *Hydrolyzed monomer, dimer, and trimer are shown. Values indicate retention time.*

Conclusions

The condensation of peptides, and the propagation of amyloid fibrils and other peptide assemblies are undoubtedly plausibly prebiotic. However, the surfaces that best promoted the polymerization of nucleic acids with homogeneous 5'-3' linkages necessary for efficient information storage and transfer have not yet been elucidated. From these data we characterize the morphology of four distinct peptide assemblies, all sharing the N-terminal arginine and core 'FF' dyad. The 'FF' dyad alone has been shown to propagate as nanotubes [20], and context variation has defined the specific assembly of several distinct supramolecular architectures [21]. The plasticity of peptide assemblies suggests its persistence in different environments may have contributed to the localized chemistry.

For Ac-RNVFFAL-NH_2 assemblies, parallel fiber formation was observed, resulting in the formation of a dense cationic fiber surface. This surface, like that of montmorillonite should have promoted the adsorption and polymerization of nucleic acids, albeit with heterogeneous linkages in the case of RNA. Despite the absence of polymerization, the specific folding/assembly properties of peptides containing asparagine can be explained further from these data. Asparagine, like glutamine, is capable of interstrand hydrogen-bonding between side chains in the laminate interface. Therefore, asparagine and glutamine should be considered nanotube-breakers and their propensity to form Q- and N-tracts along fibrils, a thermodynamic product of assembly.

For all peptides considered here as polymerization catalysts, the conditions used for polymerization may have limited polymer length. Because the same amount of polymerization/condensation is observed for control samples, I am inclined to believe our method of analysis was not appropriate for this system. LCMS has a low detection threshold and detecting the formation of polyanions by MS is difficult. Therefore, other methods of analysis should be explored. The typical ladder formation by LC was not observed in our chromatograms, so the data is likely accurate in its interpretation of the species existing in solution. Gel electrophoresis of samples from polymerization reactions consistently yielded no bands, suggesting concentrations were too low or no polymers at or above our length threshold of ten nucleotides were present.

The binding of activated monomers to at least Ac-RLVFFAL-NH_2 nanotubes characterized here is a promising start to the polymerization reactions many hope to observe in the future for peptide assemblies, and the electrostatic driving forces of nucleotide binding foreshadow those explored in chapters 4, 5, and 6. The exploration of more desirable conditions for polymerization and more appropriate positive controls will likely improve the potential outcomes of future experiments.

Methods

Peptide Synthesis

Peptides were synthesized using Solid Phase Peptide Synthesis (SPPS) with a Rink-Amide MBHA resin, 0.4mmol/g substitution, and capped at the N-terminus with an acetyl group. Peptides were cleaved and deprotected using a cocktail of 90% TFA, 2% anisole, 3% 1,2-ethanedithiol, and 5% thioanisole. All chemicals were purchased from Sigma-Aldrich. Following cleavage and deprotection, peptides were purified by reverse-phase HPLC using acetonitrile and water with 0.1%TFA and a C18 column to a >98% purity. After purification, acetonitrile was removed by rotavaporation. The remaining aqueous solution was frozen at -80°C or flash frozen using liquid nitrogen and lyophilized to yield a white powder.

Peptide Assembly. Due to the salt sensitivity of peptides used in this study, following purification and lyophilization, peptides were desalted using Sep-Pak® C18 cartridges. Peptides were then placed in 40% Acetonitrile, vortexed briefly and sonicated for 5 minutes to promote solubility. The pH was not adjusted; each sample was examined at pH5. A stock solution of 2mM peptide was used to set up all assemblies. Experimental samples were set up within five minutes of dissolution. All nucleic acid oligomers were purchased from Integrated DNA Technologies. For NA/Peptide co-assemblies, a stock solution of 1mM NA was used. Order of addition was as follows: Peptide, solvent, nucleic acid. Assemblies were kept at 4°C unless otherwise noted. Final peptide concentration in all experimental setups was 1mM. Final nucleic acid concentration was approximately 100μM. All co-assemblies were established with a 1:1 (peptide: nucleic acid) charge ratio.

Transmission electron microscopy

Electron microscopy images were obtained using a Hitachi H-7500 and a Jeoul transmission electron microscope. All samples were placed on 200 mesh copper grids with carbon coating and negatively stained using 2%w/w uranyl acetate (Sigma-Aldrich). The microscope was operated at 75kV. Cross-section images were obtained by embedding pelleted assemblies in resin. Using a microtome, embedded assemblies were sliced 1μm thick and placed on grids for analysis by TEM.

Fourier Transform Infrared (FT-IR) Spectroscopy

FT-IR spectra were acquired using a Jasco FT-IR 4100 (Easton, MD, USA) averaging 750 scans at 2cm^{-1} resolution. For each sample, 8μl of peptide solution was dried as a thin film on a Pike GaldiATR (Madison, WI, USA) ATR diamond surface. The MCT-M detector, having a 5mm aperture and a scanning speed of 4mm/sec was used. Samples were normalized to the amide I stretch at ~1625cm^{-1}.

Circular Dichroism (CD)

A Jasco-810 Spectropolarimeter was used to record CD spectra. Samples were examined at room temperature in a 50μL cell with a 0.1mm path length. The reported spectra were acquired from 260nm to 190nm with a step size of 0.2nm and a speed of 100nm/s, and are the average of three independent scans. Ellipticity, in mdeg, was converted to Molar ellipticity (θ) with $[\theta] = \theta/(10 \times c \times l)$, where ‘c’ is peptide concentration in moles/L and ‘*l*’ is the pathlength in cm. Melting curves of *pep-KG* and NA/*pep-KG* samples were obtained using a gradient of temperature from 4°-60°C and a focal wavelength of 220nm and 260nm, respectively.

Powder X-Ray Diffraction

Experimental samples were flash frozen using liquid nitrogen and lyophilized to yield a white powder. The samples were loaded into mylar capillaries and the diffraction patterns measured using a Bruker APEX-II diffractometer with graphite monochromated Cu radiation, K-alpha radiation, λ=1.54184Å, 40kV and 35mA, with a 0.5 pinhole collimator and with exposure times of 900s per frame. The data integration software XRD2SCAN and the Bruker AXS software were used for analysis of the resulting diffraction patterns. The following equation was used to convert spectra from 2θ to d-spacing(Å):

$$1.54184/(2\times \sin\left(2\theta\times \frac{\frac{\pi}{180}}{2}\right))$$

Synthesis of activated monomers

Synthesis of phosphorimidazolides was carried out according to Vogel et al. Adenosine monophosphate or deoxyadenosine monophosphate (0.44mmol), 2,2'-bipyridine-1,1'-disulfide (1.41mmol), triphenylphosphine (1.41mmol), and imidazole (7.10mmol) were dried at 0.1 Torr for 30 minutes to one hour. Under argon, anhydrous DMSO (3.7mL) was used to dissolve the mixture and gave a clear, colorless solution. Addition of triethylamine (1.01mmol) changed the solution color to yellow. The yellow solution was stirred under argon at room temperature for four hours. After four hours, the solution was added dropwise to a stirred solution of NaClO4 (0.01M) in acetone/diethyl ether (1.4:1, v/v) to give a white/off-white precipitate. The precipitate was isolated by vacuum filtration and washed with acetone/diethyl ether. The precipitate was dried in a vacuum desiccator and placed at -20°C for storage. Product formation was confirmed by ^{31}P NMR and later by mass spectrometry.

Polymerization reactions

Peptide assemblies were combined with Tris, $MgCl_2$, NaCl, and activated monomer to form reaction conditions. Final concentration of reaction components was 0.5mM peptide assembly, 50mM $MgCl_2$, 20mM NaCl, 100mM Tris, and 10mM activated monomer. Reactions were kept at room temperature and analyzed by LCMS after three days.

LTQ-FTMS

For LCMS, a Thermo linear quadrupole ion trap (LTQ) Fourier transform mass spectrometer (FTMS) was used. Samples were first separated by liquid chromatography using acetonitrile and 50mM TEAA. A gradient of 2-14% acetonitrile over 30 minutes was used to separate products. Liquid exiting the column was subject to mass spectrometry analysis. Chromatography peaks correspond with respective mass spectrometry peaks.

References

[1] Kemp, M. The *Mona Lisa* of modern science. *Nature* **421,** 416-420 (2003).

[2] Watson, J. D., Crick, F. H. C. Molecular structures of nucleic acids. *Nature* **171,** 737–738 (1953).

[3] Gleghorn, M. L., Zhao, J., Turner, D. H., Maquat, L. E. Crystal structure of a poly(rA_ staggered zipper at acidic pH: evidence that adenine N1 protonation mediates parallel double helix formation. *Nucleic Acids Res.* **44,** 8417-8424 (2016).

[4] Rich, A., Zhang, S. Z-DNA: The long road to biological function. *Nat. Rev. Genet.* **4,** 566–572 (2003).

[5] Hermann, T., Westhof, E. Non-Watson-Crick base pairs in RNA-protein recognition. *Chem. Biol.* **6,** R335–R343 (1999).

[6] Zhao, J., Bacolla, A., Wang, G., Vasquez, K. M. Non-B DNA structure-induced genetic instability and evolution. *Cell. Mol. Life Sci.* **67,** 43–62 (2010).

[7] Marsh, T. C., Henderson, E. G-wires: self-assembly of a telomeric oligonucleotide, d(GGGGTTGGGG), into large superstructures. *Biochemistry* **33,** 10718-10724 (1994).

[8] Changenet-Barret, P., Hua, Y., Gustavsson, T., Markovitsi, D. Electronic excitations in G-quadruplexes formed by the human telomeric sequence: a time-resolved fluorescence study. *Photochem. Photobiol.* **91,** 759-765 (2015).

[9] Bishop, J. S. *et al.* Intramolecular G-quartet motifs confer nuclease resistance to a potent anti-HIV oligonucleotide. *J. Biol. Chem.* **271,** 5698-5703 (1996).

[10] Gesteland, R. F., Cech, T. R., Atkins, J. F. *The RNA World*, 2nd ed.; Cold Spring Harbor Laboratory Press: New York, NY, USA, (1999).

[11] Hunding, A.; Kepes, F.; Lancet, D.; Minsky, A.; Norris, V.; Raine, D.; Sriram, K.; Root-Bernstein, R. Compositional complementarity and prebiotic ecology in the origin of life. *Bioessays* **28,** 399–412 (2006).

[12] Turk, R.M.; Chumachenko, N.V.; Yarus, M. Multiple translational products from a five-nucleotide ribozyme. *Proc. Natl. Acad. Sci. USA* **107,** 4585–4589 (2010).

[13] Guerrier-Takada, C.; Gardiner, K.; Marsh, T.; Pace, N.; Altman, S. The RNA moiety of Ribonuclease P is the catalytic subunit of the enzyme. *Cell* **35,** 849–857 (1983).

[14] Goodwin, J.T.; Mehta, A.K.; Lynn, D.G. Digital and analog chemical evolution. *Acc. Chem. Res.* **45,** 2189-2199 (2012).

[15] Dobson, C. M. Protein folding and misfolding. *Nature* **426,** 884-890 (2003).

[16] Soldatov, D. V., Moudrakovski, I. L., Ripmeester, J. A. Dipeptides as microporous materials. *Angew. Chem. Int. Ed.* **43,** 6308-6311 (2004).

[17] Gorbitz, C.H. Nanotubes from hydrophobic dipeptides: Pore size regulation through side chain substitution. *New J. Chem.* **27,** 1789-1793 (2003).

[18] Gorbitz, C.H. Structures of dipeptides: The head-to-tail story. *Acta Cryst.* **B66,** 84–93 (2010).

[19] Gorbitz, C.H. Microporous organic materials from hydrophobic dipeptides. *Chem. Eur. J.* **13,** 1022–1031 (2007).

[20] Reches, M., Gazit, E. Formation of closed-cage nanostructures by self-assembly of aromatic dipeptides. *Nano Lett.* **4,** 581-585 (2004).

[21] Wang, Y. *et al.* Rational design of chiral nanostructures from self-assembly of a ferrocene-modified dipeptide. *J. Am. Chem. Soc.* **137,** 7869-7880 (2015).

[22] Mehta, A. K. *et al.* Context dependence of protein misfolding and structural strains in neurodegenerative diseases. *Biopolymers* **100,** 722-730 (2013).

[23] Sunde, M., Blake, C. The structure of amyloid fibrils by electron microscopy and x-ray diffraction. *Adv. Protein Chem.* **50,** 123-159 (1997).

[24] Glenner, G. G. Amyloid deposits and amyloidosis. *N. Engl. J. Med.* **302,** 1283-1292 (1980).

[25] Ow, S., Dunstan, D. E. A brief overview of amyloids and Alzheimer's disease. *Protein Sci.* **23,** 1315-1331 (2014).

[26] Shin, J., Salameh, J. S., Richter, J. D. Impaired neurodevelopment by the low complexity domain of CPEB4 reveals a convergent pathway with neurodegeneration. *Sci. Rep.* **6,** (2016).

[27] Mehta, A. K. *et al.* Facial symmetry in protein self-assembly. *J. Am. Chem. Soc.* **130,** 9829-9835 (2008).

[28] Jones, E. M., Surewicz, W. K. Fibril conformation as the basis of species- and strain-dependent seeding specificity of mammalian prion amyloids. *Cell* **121,** 63-72 (2005).

[29] Guo, J. L. *et al.* Distinct α-Synuclein strains differentially promote tau inclusions in neurons. *Cell* **154,** 103-117 (2013).

[30] Erickson, S. L., Lykke-Andersen, J. Cytoplasmic mRNP granules at a glance. *J. Cell Sci.* **124,** 293-297 (2011).

[31] Moore, M. J. From birth to death: the complex lives of eukaryotic mRNAs. *Science* **309,** 1514–1518 (2005).

[32] Parker, R., Sheth, U. P bodies and the control of mRNA translation and degradation. Mol. *Cell* **25,** 635–646 (2007).

[33] Anderson, P., Kedersha, N. Stress granules. *Curr. Biol.* **19,** R397–R398 (2009).

[34] Buchan, J. R., Parker, R. Eukaryotic stress granules: the ins and outs of translation. *Mol. Cell* **36,** 932–941 (2009).

[35] Fromont-Racine, M., Senger, B., Saveanu, C., Fasiolo, F. Ribosome assembly in eukaryotes. *Gene* **313,** 17–42 (2003).

[36] Harish, A., Caetano-Anolles, G. Ribosomal history reveals origins of modern protein synthesis. *PLoS One* **7,** doi:10.1371/journal.pone.0032776 (2012).

[37] Vogel, S. R., Richert, C. Adenosine residues in the template do not block spontaneous replication steps of RNA. *Chem. Comm.* 1896-1898 (2007).

[38] Ferris, J. P., Hill, Jr., A. R., Liu, R., Orgel, L. E. *Nature* **381,** 59–61 (1996).

[39] Ertem, G., Ferris, J. P. Synthesis of RNA oligomers on heterogeneous templates. *Nature* **379,** 238-240 (1996).

[40] Huang, W., Ferris, J. P. One-step, regioselective synthesis of up to 50-mers of RNA oligomers by montmorillonite catalysis. *J. Am. Chem. Soc.* **128,** 8914-8919 (2006).

[41] Childers, W. S., Mehta, A. K., Lu, K., Lynn, D. G. Templating molecular arrays in amyloid's cross-β grooves. *J. Am. Chem. Soc.* **131,** 10165-10172 (2009).

[42] Omosun, T. O. *et al.* Catalytic Diversity in Self-propagating Peptide Assemblies, *Nat Chem*. In press. (2017).

[43] Childers, W. S., Mehta, A. K., Bui, T. Q., Liang, Y., Lynn, D. G. Toward Intelligent Material. *Molecular Self-Assembly: Advances and Applications*. **1st ed.,** 1-36 (2012).

[44] Li, S. *et al.* Design of asymmetric peptide bilayer membranes. *J. Am. Chem. Soc*. **138,** 3579–3586 (2016).

[45] Childers, W. S., Mehta, A. K., Ni, R., Taylor, J. V., Lynn, D. G. Peptides organized as bilayer membranes. *Angewandte Chemie International Edition* **49,** 4104-4107 (2010).

[46] Childers, W. S., Anthony, N. R., Mehta, A. K., Berland, K. M, Lynn, D. G. Phase networks of cross-b peptide assemblies. *Langmuir* **28,** 6386-6395 (2012).

[47] Anthony, N. R., Berland, K. M., Mehta, A. K., Childers, W. S., Lynn, D. G. Imaging nucleation, growth and heterogeneity in self-assembled amyloid phases. *Bio-nanoimaging,* Boston: Academic Press 27-36 (2014).

[48] Liang, C. *et al.* Kinetic intermediates in amyloid assembly. *J. Am. Chem. Soc.* **136,** 15146-15149 (2014).

[49] Vogel, S. R., Deck, C., Richert, C. Accelerating chemical replication steps of RNA involving activated ribonucleotides and downstream-binding elements. *Chem. Comm.* 4922-4924 (2005).

[50] Yamrom, T., Cortes, S. The prebiotic synthesis of imidazoles and their catalytic role in the synthesis of oligonucleotides. *Fed. Proc.* **42,** 1926 (1983).

Chapter 3: DNA/Peptide chimeras: manipulation of mutualisms for functional applications

Introduction

Complementarity of nucleic acids and the diversity of peptide assembly is exploited in the pursuit of programmable systems for biomolecular nanotechnology [1-3]. The mutualism that exists between nucleic acids and proteins/peptides is continuously challenged in the development of nanostructures and scaffolds [4-7]. The specific Watson-Crick base-pairing of DNA has been examined extensively in the development of two- and three-dimensional origami for a multitude of applications including biosensors, drug delivery, and nanocircuitry [3,8-10]. For example, the construction of nanoactuators [11], tunable DNA-controlled switches, allows for further optimization of devices for sensitive detection of single molecules. Peptide assemblies remain robust, largely non-conductive [12], and capable of accessing a repertoire of context-dependent morphologies [13,14]. These assemblies, which have been largely explored as scaffolds, are also capable of catalyzing chemical reactions. Retroaldol condensation within the grooved surfaces of peptide nanotubes, rely on essential solvent-exposed lysine residues. Modification of peptide assemblies through the tethering of enzymes has also been explored [16].

The coalescence of nucleic acids and peptides, capable of self-assembly, is not novel. Nucleic acids and proteins are continuously in contact in the cell [17,18], and exploitation of these interactions has led to the production of aptamer-based detection methods for disease diagnoses [19]. *In vitro*, studies examining the assembly of DNA/peptide conjugates reveal highly-ordered amyloid-like nanostructures [20,21]. Similarly, peptides modified with two N-terminal cytosines form nucleobase-directed nanotubes that maintain interstrand hydrogen-bonding [5]. These chimeric assemblies highlight the robust properties of peptide assembly, while accommodating nucleobase and nucleic acid specificity.

DNA has become of increasing interest in bionanocircuitry because of its guanine-dependent electron transport [9,22,23]. Guanine, which is highly susceptible to oxidative damage in the cell [24,25], is responsible for the conductivity of double-stranded DNA and other secondary structures [26-30]. Guanine quadruplexes, which are found naturally in telomeric regions, at centromeres, and within certain promoters [31,32], form via Hoogsteen hydrogen bonding in guanine-rich regions of DNA [29,33-35]. Four guanines hydrogen bond to form a single quartet (Figure 3-1a) [29], which then undergoes monovalent cation-dependent stacking with other quartets to form the quadruplex (Figure 3-1b) [36,37]. Although naturally occurring guanine quadruplexes form through the folding of a single strand, synthetic quadruplexes can be formed from one, two, or four strands [35,37-39]. Remarkably, G-quadruplexes are capable of stacking [35,37], producing nanowires micrometers in length [31] that can be used in biomolecular nanotechnology and have been explored as components of biosensors [40].

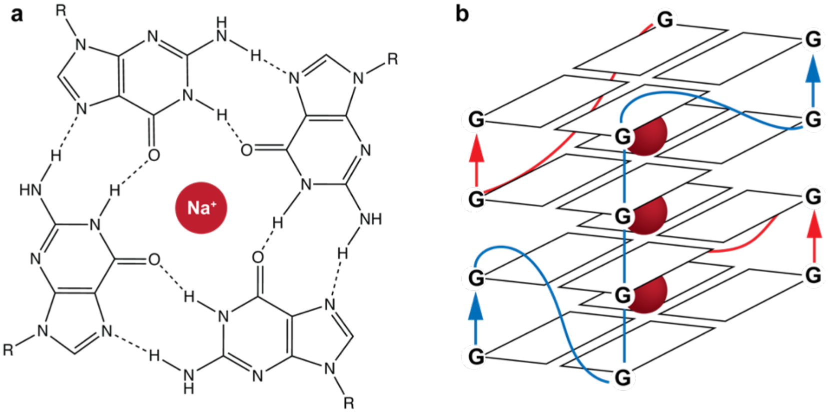

Figure 3-1 Guanine Quadruplex structure. *(a) Guanine quartet forms via Hoogsteen hydrogen bonds. (b) Monovalent cations stabilize quadruplex formation through the stacking of guanine quartets.*

The specific folding of guanine-rich sequences as guanine quadruplexes will be exploited in this chapter. Through conjugation of a guanine-quadruplex-forming sequence to a peptide, the formation of insulated guanine wires is possible. Diluting these DNA/Peptide conjugates with free peptide will promote the formation of peptide self-assemblies while incorporating guanine quadruplexes. Here, we describe the formation of conical nanotube peptide self-assemblies, whose formation is dependent on the proper folding of incorporated guanine quadruplexes. The characterization of these assemblies is an important first step in defining insulated guanine wires for bionanocircuitry, and extending the biomolecular morphological repertoire of DNA/peptide chimeras.

Other DNA secondary structures have also been exploited for nanotechnology. Beyond the specificity of Watson-Crick base-pairs, DNA secondary structures that are responsive to pH or light permit temporal and spatial control of integral elements [41,42]. I-motifs, which rely on the formation of hemiprotonated C-C+ base-pairs (Figure 3-2a) also fold as quadruplexes, but with intercalated bases (Figure 3-2b) [41]. These DNA structures often accompany guanine quadruplexes on complementary strands rich in cytosine [43]. An increase in pH deprotonates cytosines causing loss of structural stability and unfolding [41,42]. The responsiveness of this system has led to its application in a multitude of DNA-controlled devices [44,45].

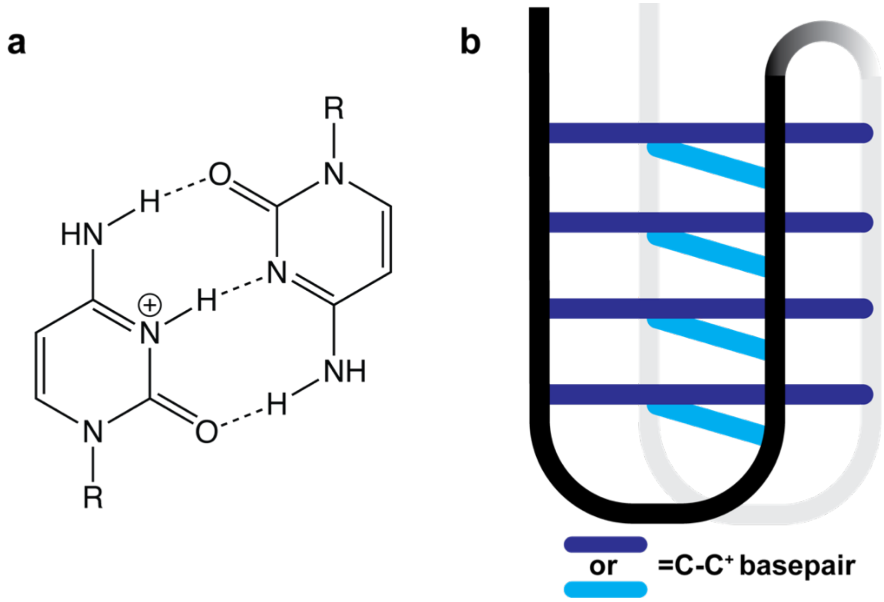

Figure 3-2 I-motif structure. *(a) C-C+ base pairs depend on hemiprotonated state of cytosine. (b) single strand cytosine quadruplex forms through intercalation of C-C+ base pairs.*

In this chapter, we end by describing the formation of DNA/peptide conjugates and their application in responsive hydrogel systems. A proof-of-concept approach is used to define the co-assembly of free peptides and DNA/peptide conjugates capable of forming hydrogels through the introduction of a linker DNA that bridges the gap between nanostructures. The use of i-motifs and other responsive DNA elements within the linker or the DNA conjugated to the peptide would expand our use of hydrogels in drug delivery, tissue engineering, and much more. Chapters 1 and 2 highlighted some of the supramolecular architectures peptide assemblies access, and the context-dependent nature of morphology appearance will be explored further in this chapter and those that follow.

Results

The assembly of peptide nanotubes is resistant to several alterations to the primary amino acid sequence, addition of two cytosine bases to the N-terminus, and the covalent attachment of fatty acid side chains to the N-terminus of incorporated peptides [5,13,46]. The robust assembly of nanotubes is explored further here through the formation of nucleic acid/peptide chimeric assemblies. Peptide Ac-KLVIIAG-NH_2 demonstrates context-dependent nanotube assembly. In high salt, nanotubes appear as the dominant supramolecular architecture. Here, we exploit this context-dependent peptide assembly for the formation of guanine nanowires within peptide nanotubes. Peptide assemblies, which have little conductivity, serve as insulators and prevent potential lateral electron transport with other nanowires [12].

Synthesis of DNA/Peptide conjugates

DNA/peptide conjugates were formed through the copper catalyzed click chemistry of alkyne-modified peptides and azide-modified DNA. Peptide Ac-ELVIIAG-NH_2 was synthesis by solid phase peptide synthesis (SPPS) and purified by reverse phase HPLC using a C18 column. Purified Ac-ELVIIAG-NH_2 was subject to a two-step reaction resulting in the alkynylation of the terminal glutamic acid side chain shown in Figure 3-3 [47]. In the first step, N-hydroxysuccinimide is added to the carboxylic acid of glutamic acid as a leaving group to improve yield of the second step. Propargylamine replaces N-hydroxysuccinimide through it’s reaction with the carbonyl of the glutamic acid side chain.

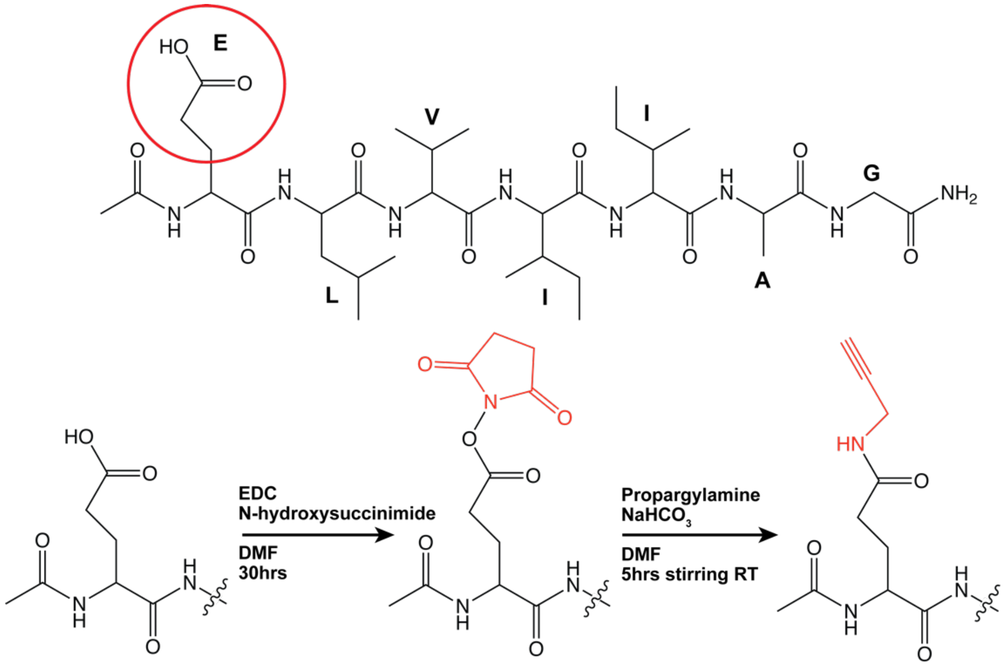

Figure 3-3 Synthesis of alkyne-modified peptides for use in click reactions.

Intermediate and final product synthesis of alkyne-modified peptides was confirmed by MALDI-TOF mass spectrometry. The mass spectrometry results of the final synthetic product are shown in Figure 3-4. The m/z of 814.54 corresponds to alkyne-modified Ac-aELVIIAG-NH_2 (‘a’ denotes alkyne) in association with one sodium ion. Purification of Alkyne-modified peptides proved difficult. Therefore, click reactions were carried out with crude synthetic products.

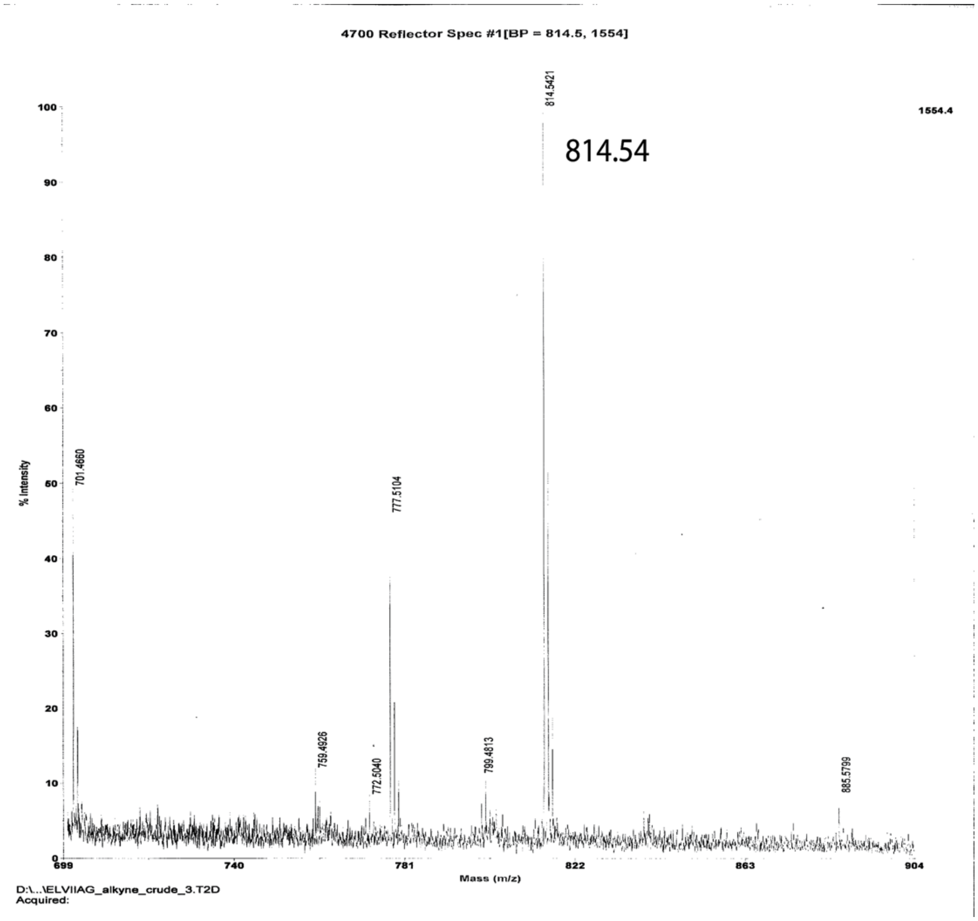

Figure 3-4 MALDI-TOF MS analysis of alkyne-modified Ac-ELVIIAG-NH$_2$.

Azide-modified DNA was purchased from integrated DNA technologies for the purposes of this study. To form the DNA/peptide conjugate, alkyne-modified Ac-aELVIIAG-NH$_2$ was combined with azide-modified DNA in a 4-6nmol click reaction catalyzed by Cu(I) (Figure 3-5). The product of the click reaction and unreacted DNA was ethanol precipitated. Further characterization of DNA/peptide conjugates by mass spectrometry was unsuccessful. The use of mass spectrometry to identify polyanionic macromolecules is challenging, as was eluded to in Chapter 2.

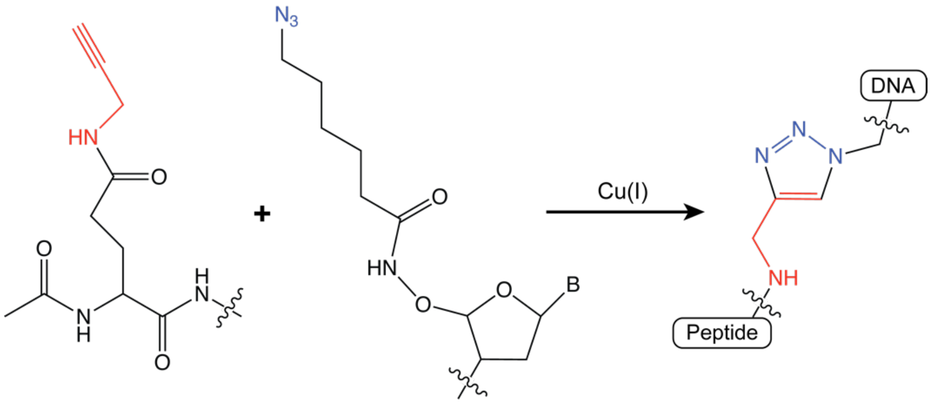

Figure 3-5 Copper catalyzed click chemistry of alkyne-modified peptides and azide-modified nucleic acids.

DNA/peptide conjugation was confirmed by urea-PAGE (Figure 3-6). The DNA ‘N_3-TTTTGGTG4TGG’ was conjugated to Ac-aELVIIAG-NH_2 as a candidate for guanine-wire formation within nanotubes. The retardation of guanine quadruplex-peptide (GQ-peptide) conjugates relative to unreacted ‘N_3-TTTTGGTG4TGG’ (GQ-azide) was consistent with a successful conjugation.

The design of GQ/peptide conjugates (GQPC), was based on the successful formation of guanine-quadruplexes using a two-strand model of sequences originally derived from *Tetrahymena* telomeres [37]. Two strands of the sequence 5’-GGTG4TGG-3’ come together to form parallel guanine-quadruplexes capable of long-range order through stacking of terminal quartet faces [35]. This parallel quadruplex is showcased in Figure 3-1b, where the connecting loops are composed of single thymine nucleosides. A T4-linker was added to the 5’-end of the guanine-quadruplex sequence to permit a greater degree of motion in quadruplex formation.

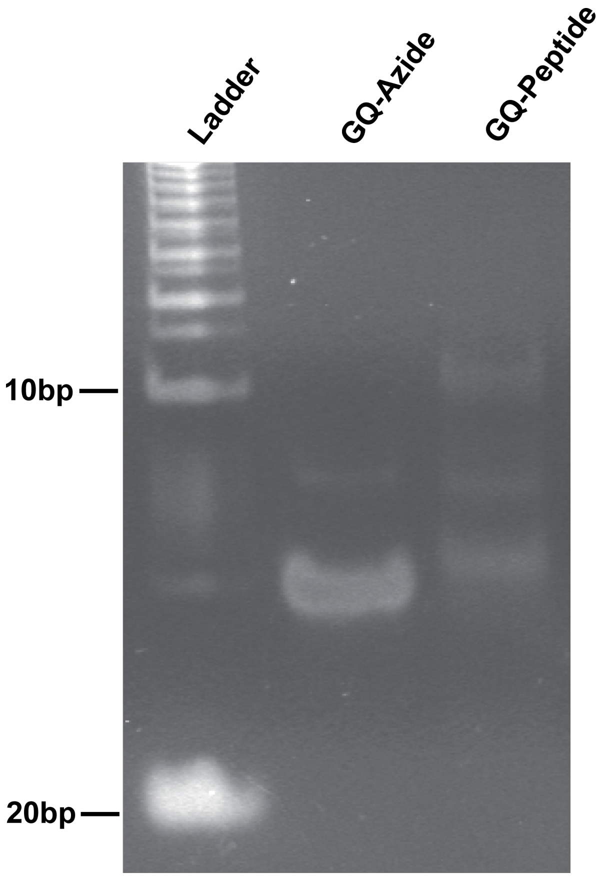

Figure 3-6 Urea-PAGE of guanine quadruplex/peptide conjugate formation. *Lane 1: 10bp ladder. Lane 2:* N_3*-TTTTGGTG4TGG. Lane 3: GQ-Peptide conjugate.*

Spectroscopic identification of guanine quadruplexes

Guanine quadruplex formation of 'GGTG4TGG' DNA was assessed independent of its conjugation to Ac-aELVIIAG-NH_2. Because of the distinct electron transition dipole moments between double-stranded DNA, parallel guanine-quadruplexes, and anti-parallel quadruplexes, circular dichroism (CD) was an effective spectroscopic approach to distinguish between accessible secondary structures [48-51]. Parallel guanine quadruplexes have a characteristic CD signature arising from the stacking of bases and the orientation about the glycosidic bond [48,49,51]. The guanine quadruplex of

'GGTG4TGG' as depicted in Figure 3-1b, has a positive ellipticity at 260nm and a negative ellipticity at 240nm in sodium phosphate buffer (Figure 3-7), consistent with the unique electron transitions of parallel quadruplexes [51]. The sodium in the buffer permits quadruplex assembly, which requires the presence of a monovalent cation for stable stacking of guanine quartets [36,37].

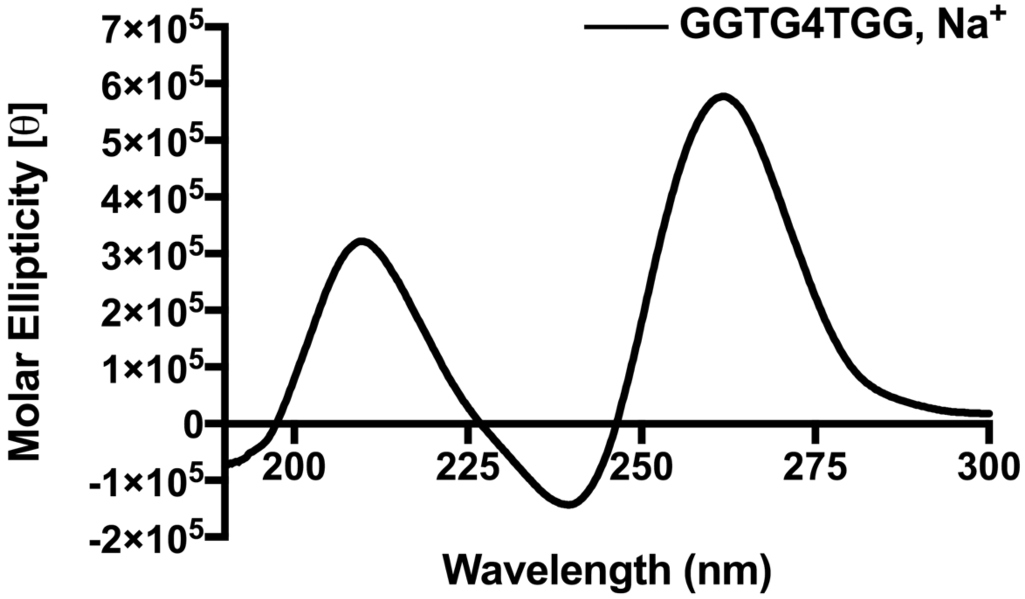

Figure 3-7 Circular Dichroism of parallel quadruplex assembly for the sequence 'GGTG4TGG'. *Maximum ellipticities at 210nm, 240nm, and 260nm.*

Guanine quadruplex formation was further confirmed by use of FT-IR. The C=O stretching frequency of the C6=O6 carbonyl of the guanine base has a maximal absorbance at 1690cm^{-1} in guanine quadruplexes. The presence of the 1690cm^{-1} peak, along with the peak at ~1540cm^{-1}, which is attributed to the N2 N7-H hydrogen bond of Hoogsteen interactions, is consistent with guanine quadruplex assembly (Figure 3-8) [39]. The C6=O6 stretching frequency of guanine bases is observed at ~1666cm^{-1} when it is not involved in hydrogen bonding, and is absent in the spectrum below. The spectrum acquired here is consistent with the published parallel quadruplex spectrum of ‘GGGGTGGGG’ [39].

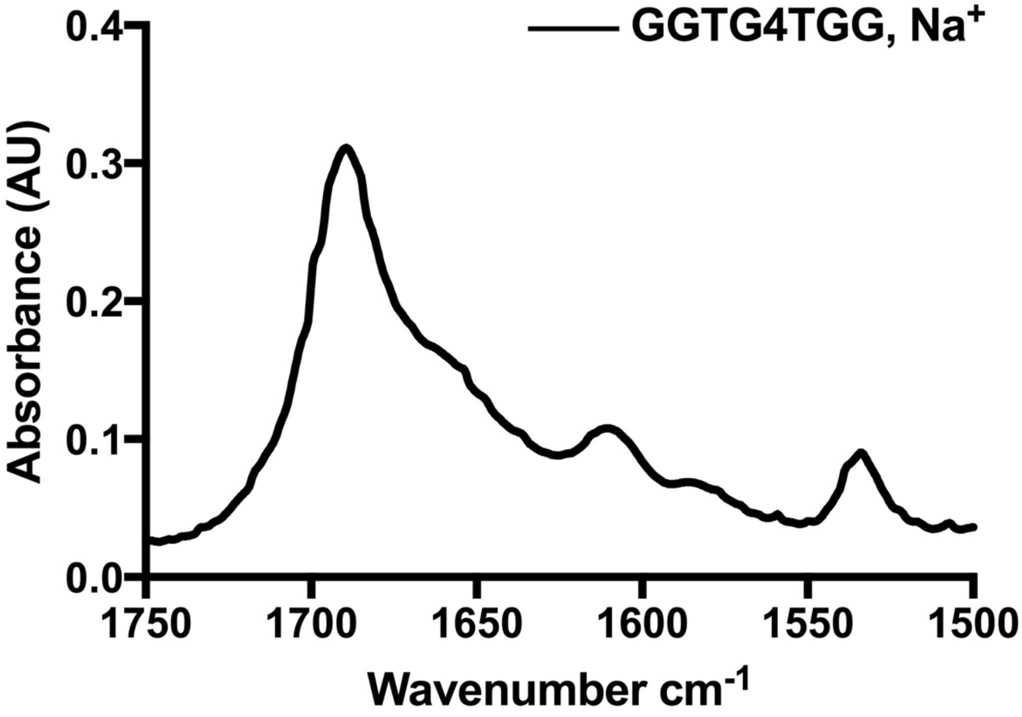

Figure 3-8 FT-IR analysis of ‘GGTG4TGG’ guanine quadruplex assembly.

With the confirmation of guanine quadruplex formation in the buffer conditions, the assembly of peptides, independent of quadruplex presence was essential. Ac-KLVIIAG-NH_2, which selectively forms nanotubes in high-salt conditions, assembles primarily as twisted fibers at a concentration of 0.4mM in sodium phosphate buffer as scored by transmission electron microscopy (TEM) (Figure 3-9). Despite the presence of NaCl, fibers are the major supramolecular species. These observations may be peptide-concentration dependent. By circular dichroism, a weak β-sheet signature is observed with a maximum negative ellipticity at 218nm.

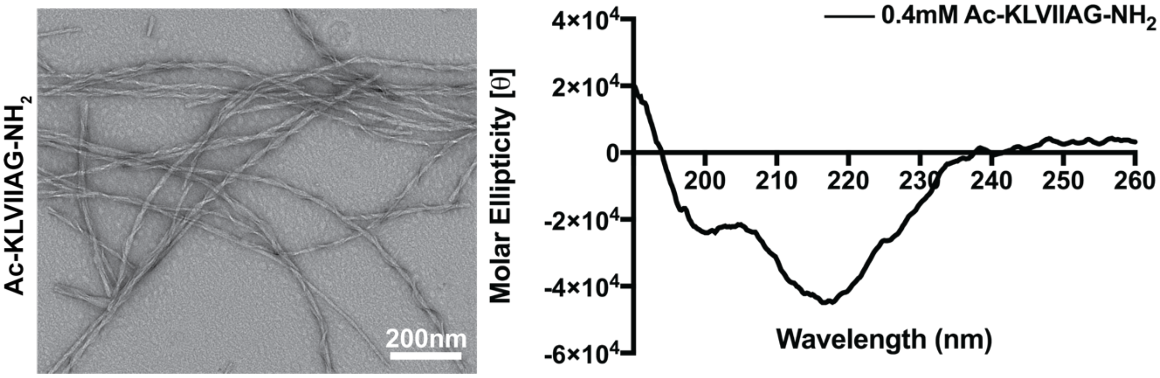

Figure 3-9 TEM and CD analysis of Ac-KLVIIAG-NH$_2$ assembly in NaH$_2$PO$_4$ buffer. *Maximum negative ellipticity observed at 218nm.*

GQPC/Ac-KLVIIAG-NH$_2$ co-assembly characterization

To promote successful assembly, GQPC were co-assembled with free Ac-KLVIIAG-NH$_2$ peptides at a molar ratio of 1:40. The concentration of Ac-KLVIIAG-NH$_2$ was maintained at 0.4mM to maximize the concentration of GQPC added and remain above the critical peptide assembly concentration of ~0.3mM; due to the reaction scale, a minute amount of GQPC was produced. The assembly was biased towards guanine quadruplex formation by heating the mixture to 95°C for five minutes and allowing the components to slowly cool to room temperature [35].

GQPC/Ac-KLVIIAG-NH$_2$ co-assembly resulted in the formation of homogeneous nanostructures resembling nanotubes (Figure 3-10). Unlike other nanotubes examined, GQPC/peptide nanotubes are conical in appearance with a wide end that tapers to a narrow point. Assembly of GQPC/peptide nanostructures follows closely with other peptide nanotubes, where mature assemblies are preceded by ribbon formation [52]. This phenomenon is observed in the bottom right micrograph of Figure 3-10. As discussed in Chapter 2, nanotube morphology is characterized by white walls and a dark interior by TEM. The hollow character of the nanotube allows stain to enter prior to dehydration on grids for analysis [52].

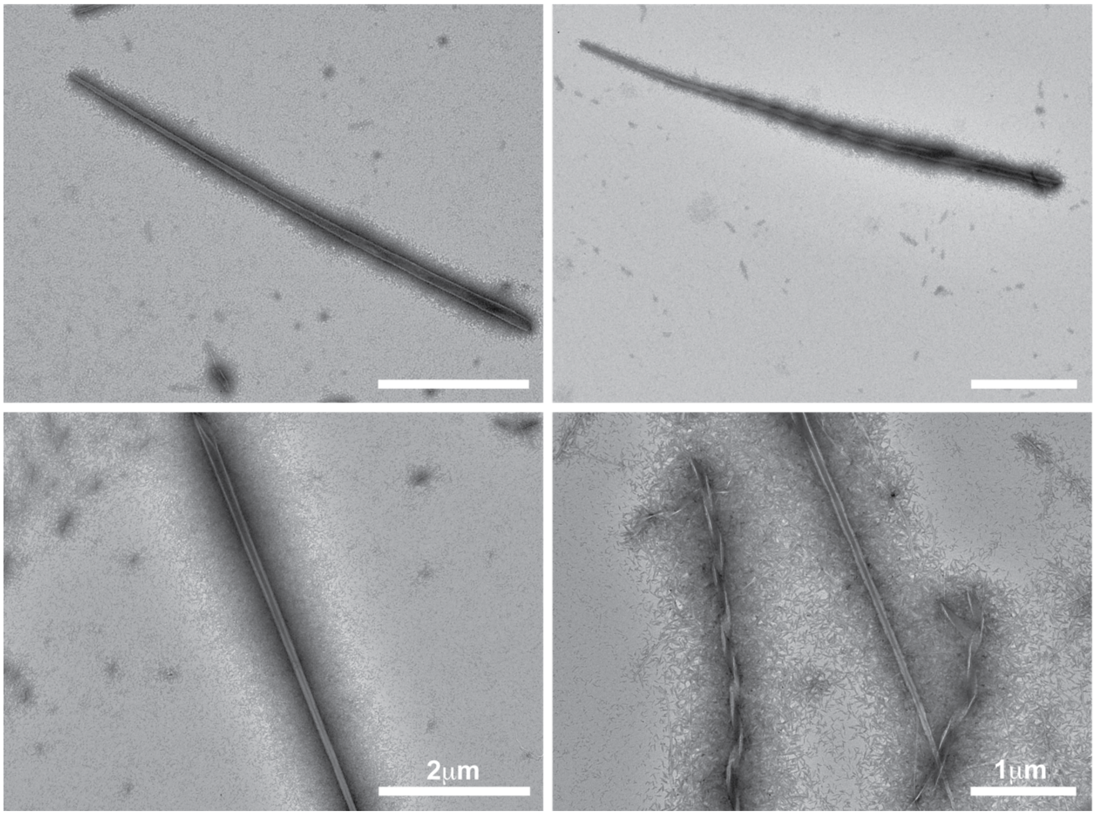

Figure 3-10 TEM analysis of GQPC/Ac-KLVIIAG-NH$_2$ co-assembly. *Examples of conical nanotubes observed by TEM for GQPC/peptide co-assemblies. Scale bars are 2μm, unless otherwise noted.*

The conical property of the nanotubes was examined further through measurement of the distinct ends. For each nanotube, ends were designated as being narrow or wide. Visually, the examination of individual nanotubes and assignment of ends does not appear to be subjective. Measurements made of narrow and wide openings were recorded and compared. As expected, the nanotube openings have significantly different sizes. The narrow openings have a mean width of 58.7nm and a standard deviation of

3.5nm, while wide ends have a mean width of 160.4nm and a standard deviation of 2.1nm.

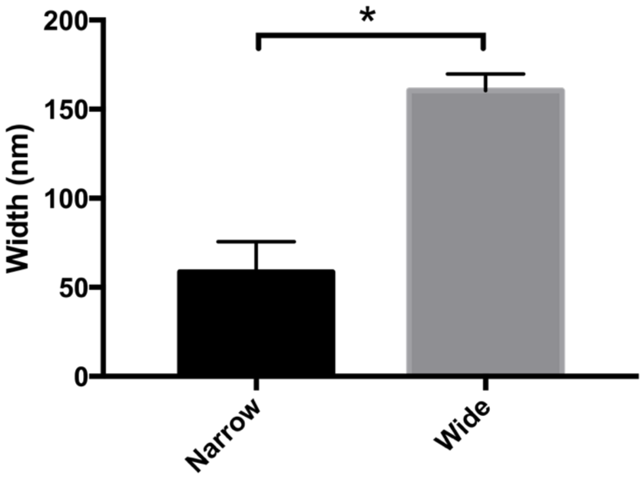

Figure 3-11 GQPC/Ac-KLVIIAG-NH_2 nanotubes are conical. *Width measurements taken at predefined ends of conical nanotubes. Narrow, n=24. Wide, n=20. P<0.0001 Error bars represent standard deviation.*

The formation of conical nanotubes from ribbons was characterized at five days of assembly to assess whether wide or narrow ends form first. According to transmission electron micrographs, the formation of the narrow end precedes the wide end of conical GQPC/peptide nanotubes.

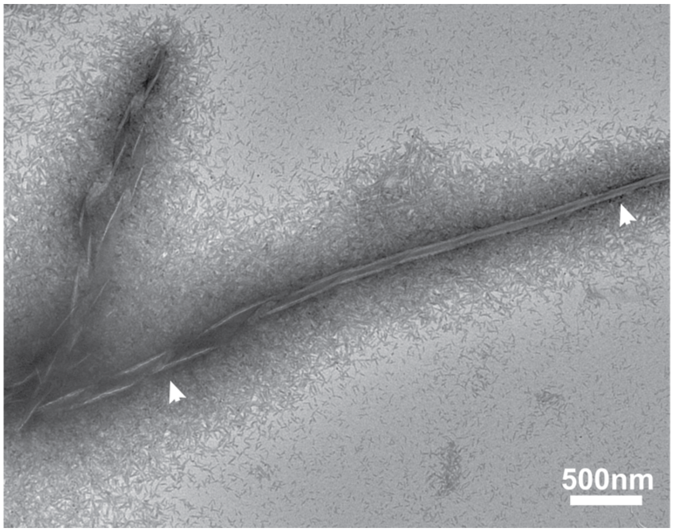

Figure 3-12 Narrow end formation precedes wide end formation in conical GQPC/Ac-KLVIIAG-NH$_2$ nanotube assembly. *Arrowheads point to narrow (right) and wide (left) nanotube openings.*

Spectroscopically, GQPC/peptide conical nanotubes exhibited characteristic β-sheet ellipticities by CD with a maximum negative ellipticity at 222nm and a positive ellipticity at 203nm (Figure 3-13). The observance of guanine quadruplex formation was not possible because the concentration was below the detection threshold of the 0.1mm cuvette used. Increasing the pathlength would permit quadruplex observation by CD within GQPC/peptide co-assemblies in future studies.

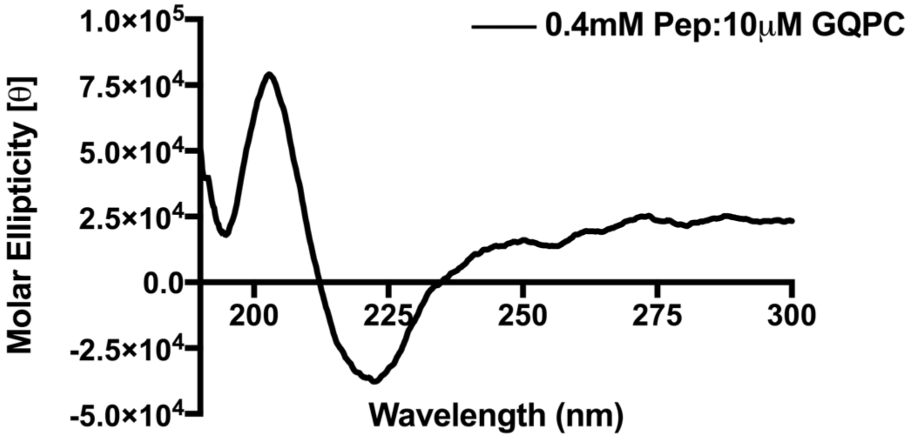

Figure 3-13 CD analysis of GQPC/Ac-KLVIIAG-NH$_2$ nanotubes. *Maximum negative ellipticity is at 222nm.*

To assess whether conical nanotube assembly was dependent on guanine quadruplex formation, lithium phosphate buffer was used. Although lithium is a monovalent cation, its atomic radius is considerably smaller than sodium and potassium, the monovalent cations that contribute most often to quadruplex assembly. Monovalent cations stabilize the stacking of quartets through cation-dipole interactions with up to eight oxygen atoms on neighboring quartets [37]. Lithium is incapable of supporting these electrostatic interactions, and is therefore considered neutral in guanine quadruplex assembly.

The supramolecular morphology of 0.4mM Ac-KLVIIAG-NH$_2$ in lithium phosphate buffer is unchanged; twisted fibers are the predominant nanostructures observed. Co-assembly of GQPC with Ac-KLVIIAG-NH$_2$ in lithium phosphate buffer yields the same fiber morphology as peptide-alone assembly (Figure 3-14). Although some nanotubes are observed, they lack the conical features of GQPC/Ac-KLVIIAG-NH$_2$ nanostructures in sodium phosphate buffer. These data suggest guanine quadruplex formation is essential to the assembly of conical nanotubes.

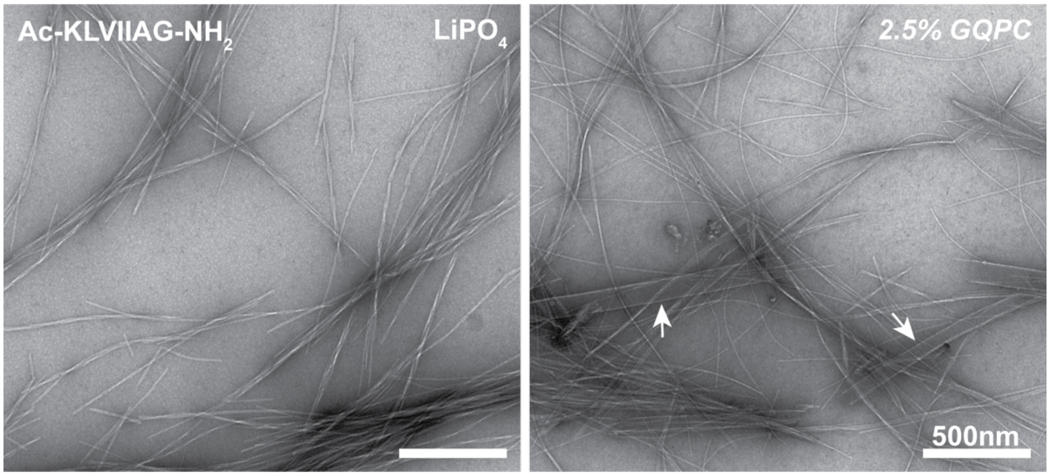

Figure 3-14 Lithium phosphate buffer disrupts conical nanotube assembly. *Ac-KLVIIAG-NH2 assemblies (left). GQPC/Ac-KLVIIAG-NH2 co-assemblies (right). White arrows point to nanotubes. Scale bars are 500nm.*

Guanine Quadruplexes form during conical GQPC/peptide co-assembly

To visualize the formation of guanine quadruplex assembly within GQPC/peptide co-assemblies spectroscopically, the use of intercalating agents was explored. Protoporphyrin IX (PPIX) was selected as an initial candidate of guanine quadruplex detection. Its structure and metal binding pocket (Figure 3-15) suggest it would be an ideal candidate for intercalation between guanine quartets [53].

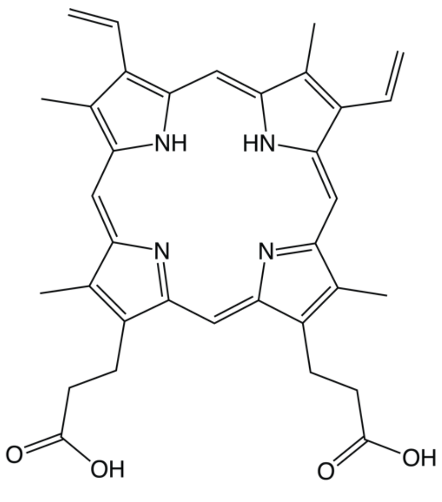

Protoporphyrin IX

Figure 3-15 Protoporphyrin IX (PPIX) structure. *PPIX is a tetrapyrrole with a metal binding pocket at its center.*

PPIX is a tetrapyrrole with extensive conjugation allowing for its action as an efficient chromophore. Its maximum absorbance by UV spectroscopy is at 400nm. Binding of PPIX to GQPC/peptide co-assemblies was observed through an increase in absorbance at 400nm. Compared to PPIX-alone and PPIX bound to 0.4mM peptide assemblies, the UV absorption increased ~3.5-fold. Although PPIX intercalates well with guanine quadruplexes, its specificity is not clear. Binding of PPIX to a double stranded DNA control revealed nonselective binding of PPIX to DNA secondary structures.

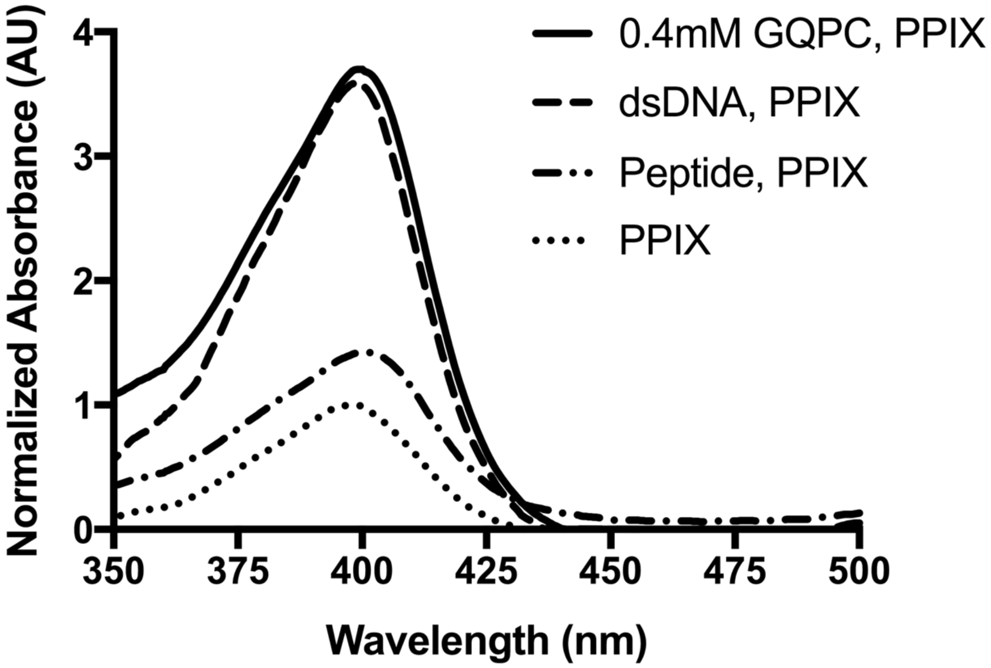

Figure 3-16 PPIX binding by UV-Vis spectroscopy. *GQPC is the GQPC/Ac-KLVIIAG-NH_2 co-assemblies. Peptide refers to Ac-KLVIIAG-NH_2-only assemblies.*

Specific guanine quadruplex recognition

The development of a guanine-quadruplex specific fluorescent dye was undertaken recently by Chen et al. [54]. Although the method of its guanine quadruplex detection has not yet been fully explored, it has profound specificity as a detector of guanine quadruplex formation *in vitro*. The structure of this fluorescent dye, ISCH-oa1, can be seen in Figure 3-17.

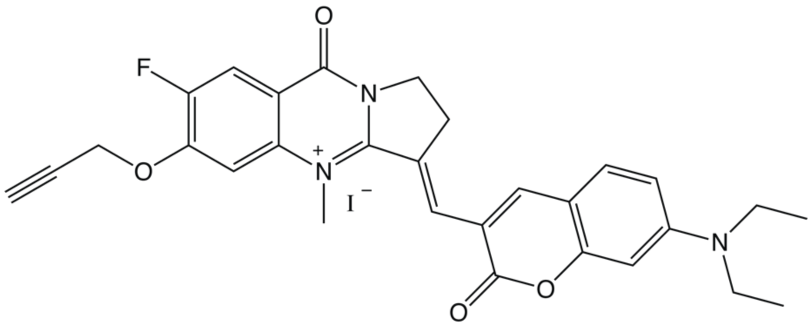

ISCH-oa1

Figure 3-17 Structure of ISCH-oa1, a GQ specific fluorescent dye.

Binding of ISCH-oa1 to GQPC/peptide co-assemblies was examined by fluorescence spectroscopy. ISCH-oa1, when bound to GQPC/peptide co-assemblies had a greater than 16-fold increase in fluorescence intensity. Compared with peptide-alone and double stranded DNA controls, ISCH-oa1 appears to be a specific indicator of guanine quadruplex formation.

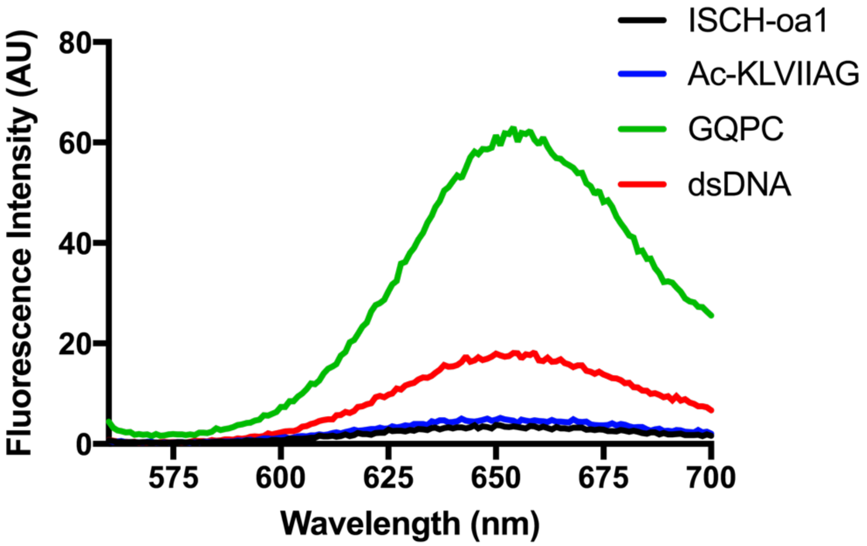

Figure 3-18 ISCH-oa1 binding by fluorescence spectroscopy. *ISCH-oa1 was used at 1μM for all samples. 0.4mM Ac-KLVIIAG-NH2 assemblies were used as a peptide-only control. GQPC corresponds to GQPC/Ac-KLVIIAG-*NH_2 *co-*

assemblies. Double stranded DNA used as a control for the specificity of DNA secondary structure recognition.

The data from Figure 3-18 is quantified in Figure 3-19.

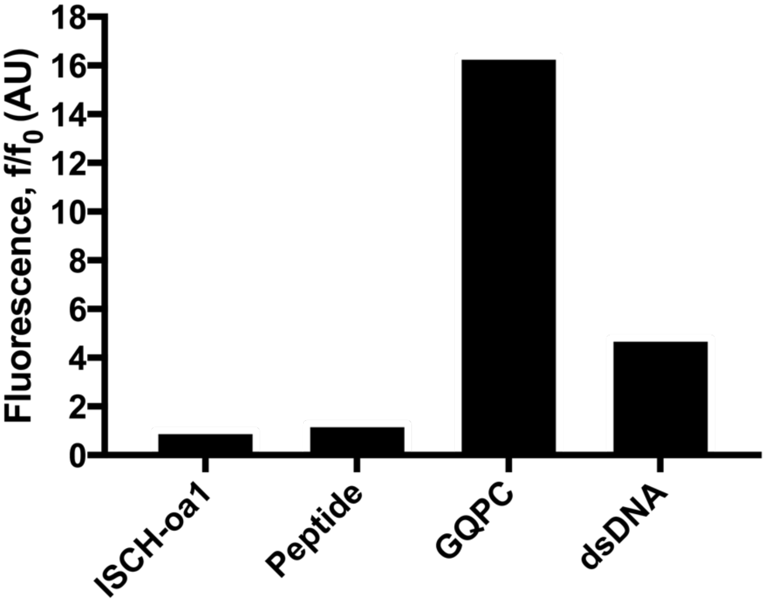

Figure 3-19 Fold fluorescence intensity change for ISCH-oa1 binding from Figure 3-18. *Peptide refers to Ac-KLVIIAG-NH_2. GQPC refers to GQPC/Ac-KLVIIAG-NH_2 co-assemblies.*

Alteration of GQPC/peptide co-assembly concentration in the presence of 1μM ISCH-oa1 was examined as a means to identify the number of guanine quadruplexes within co-assemblies and define the binding properties of ISCH-oa1 (Figure 3-20). Unfortunately, we ran out of GQPC/peptide co-assembly before the experiment could be completed, so this remains an area of active investigation.

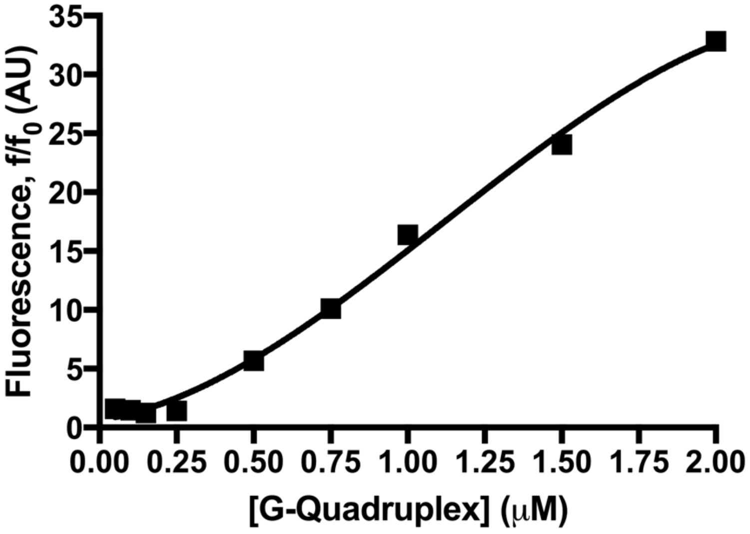

Figure 3-20 ISCH-oa1 titration with GQPC/Ac-KLVIIAG-NH$_2$ by fluorescence spectroscopy. *G-quadruplex concentration determined from initial concentration of 'GGTG4TGG' conjugated to peptides for assembly.*

From these data, the successful formation of GQPC/peptide nanotubes was defined. The formation of insulated guanine wires has applications in many areas of bioelectronics and represents a robust first-look at how guanine quadruplexes and peptides behave when co-assembled.

Creating responsive hydrogels

The remarkable complexity and programmability of DNA substructures has expanded our ability to develop DNA-controlled devices [1-3,8,11]. One such substructure, the i-motif, forms at acidic pH through the hemiprotonation of cytosine base pairs [41]. Increase of the pH to near neutral or alkaline levels disrupts i-motif structural stability through the deprotonation of cytosines. The assembly and disassembly of i-motifs can be used to create systems capable of expansion and contraction [11,45]. The characterization of such DNA-only systems continues to be explored. However, the incorporation of peptide assemblies as flexible or rigid scaffolds has not yet been described.

The development of hydrogels for applications in tissue engineering and drug delivery is underway {55-59]. Many peptide hydrogels are being exploited for their tunable viscoelasticity, structural resemblance to the extracellular matrix, and porous character capable of sufficient oxygen transport [60]. Here, we begin to describe the development of a DNA/peptide hydrogel with the potential for further tuning through variation of pH.

As with the GQPC/peptide co-assemblies described earlier in this chapter, the robust assembly of nanotubes will be exploited as a scaffold for hydrogel formation. The predicted model of hydrogel assembly is shown in Figure 3-21.

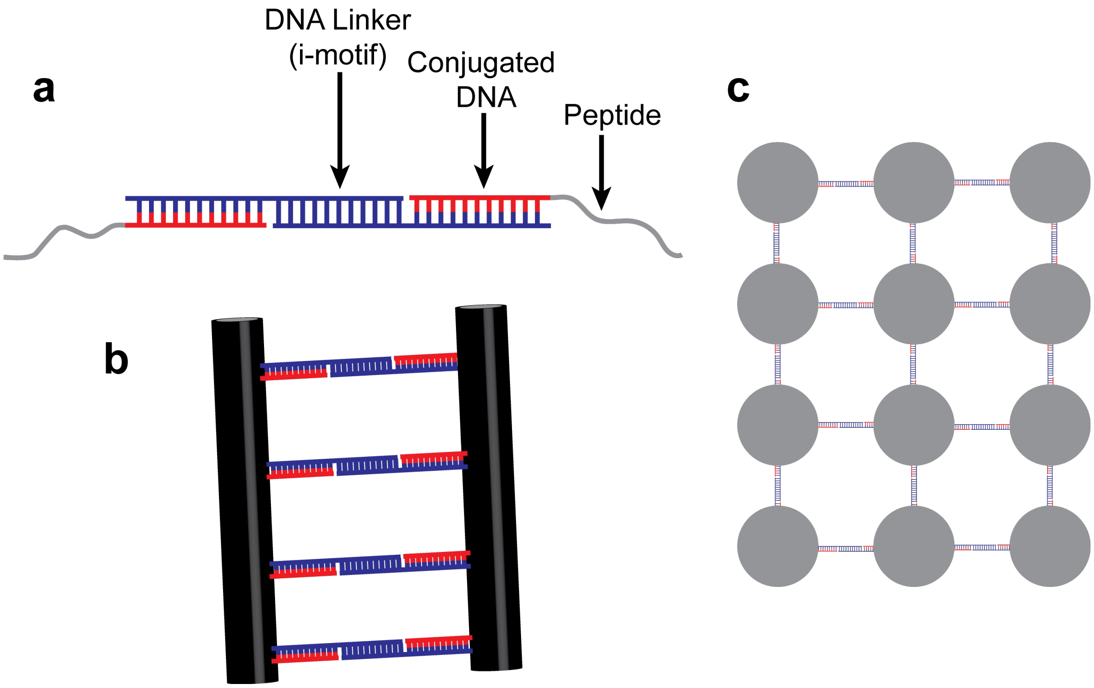

Figure 3-21 Nanotube-based hydrogel assembly. *(a) Structure of DNA/peptide conjugate with DNA linker. (b) Connections between nanotubes mediated by*

linker through Watson-Crick base pairing. (c) Example of possible network formation.

Assembly of Nucleic Acid Peptide Conjugates (NAPC)

Conjugation of DNA to peptides was carried out as described in Figures 3-3 and 3-5. Ac-KLVIIAG-NH2 was used as an initial candidate for Nucleic acid peptide conjugate (NAPC)/peptide co-assembly. Urea-PAGE was used to confirm the successful conjugation of DNA ‘GACACTCGTATGCAT’ to peptide Ac-aELVIIAG-NH_2 (Figure 3-22). The retardation of the DNA-Peptide band compared to the DNA-Azide band, supported successful conjugation. The DNA chosen for conjugation was arbitrary and met the two necessary criteria: thermal stability at room temperature and no self interaction.

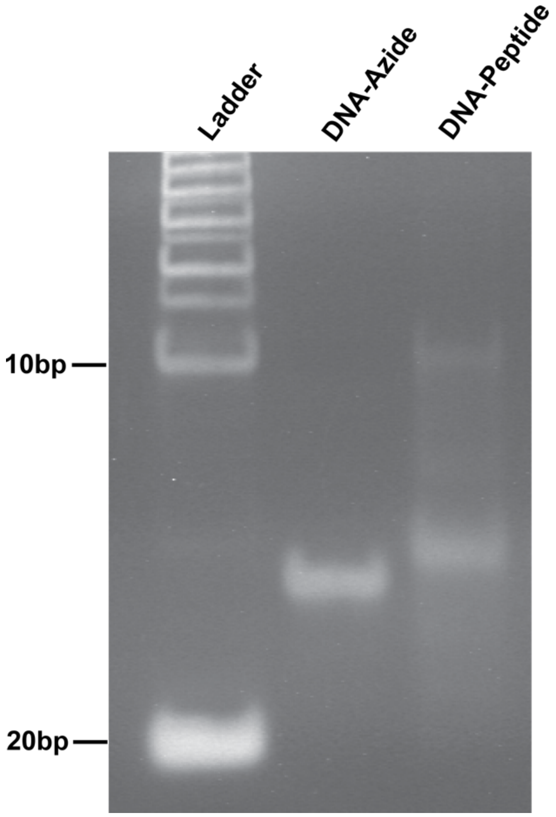

Figure 3-22 Urea-PAGE confirmation of NAPC. *First lane: 10bp ladder. Second lane: unreacted DNA-Azide control. Third lane: NAPC.*

Initial examination of hydrogel formation was performed in Tris-HCl. Because specific assembly conditions are not required for the assembly of double stranded DNA, conditions that favored nanotube assembly were chosen. In Tris-HCl, Ac-KLVIIAG-NH_2 forms β-sheet-rich assemblies by CD. The characteristic β-sheet signature with a maximum ellipticity at 218nm was observed (Figure 3-23).

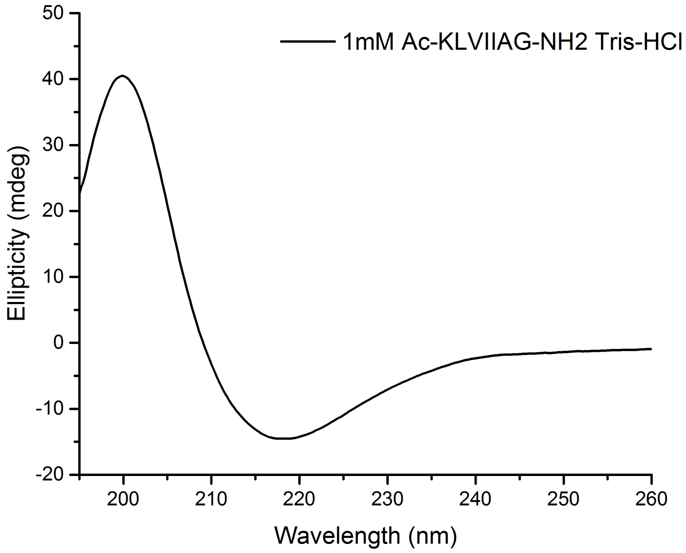

Figure 3-23 CD analysis of Ac-KLVIIAG-NH_2 in Tris-HCl. *Maximum negative ellipticity is at 218nm.*

Analysis of Ac-KLVIIAG-NH_2 assemblies by TEM reveal the formation of nanotubes with heterogeneous widths. Co-assembly of Ac-KLVIIAG-NH2 with variable amounts of NAPC generates heterogeneous assemblies. At a peptide to NAPC ratio of 100:1, nanotubes remain the predominant supramolecular architecture. However, fibers were visible by TEM (Figure 3-24b). With increasing amounts of NAPC, the predominant supramolecular nanostructure is no longer nanotubes; fibers appear to dominate the assembly landscape.

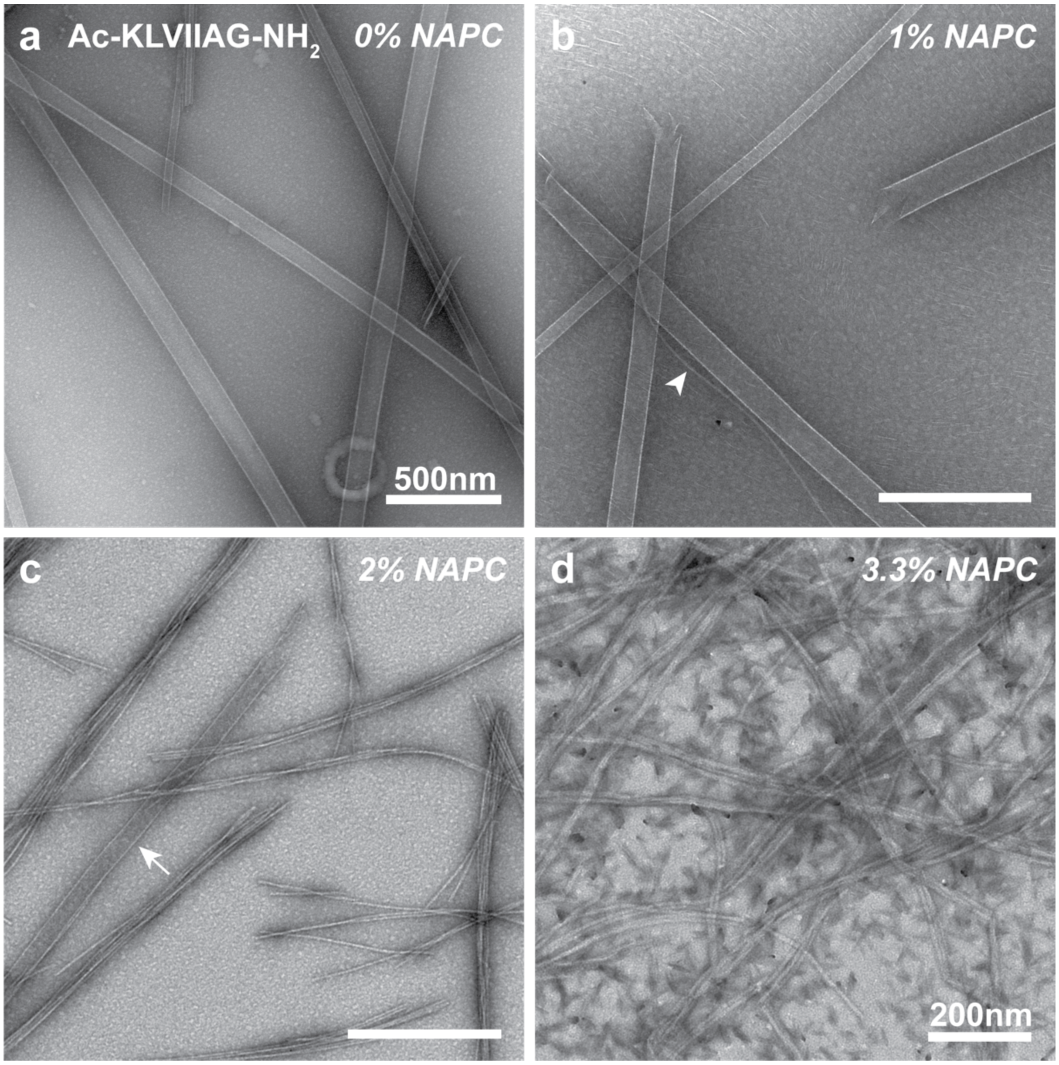

Figure 3-24 Selective co-assembly of NAPC and Ac-KLVIIAG-NH$_2$ assessed by TEM. *(a) Ac-KLVIIAG-NH2 assemblies. (b) 100:1 Ac-KLVIIAG-NH2 to NAPC. White arrowhead points to a fiber. (c) 50:1 Ac-KLVIIAG-NH2 to NAPC. White arrow points to a nanotube. (d) 30:1 Ac-KLVIIAG-NH2 to NAPC. Scale bars are 500nm unless otherwise noted.*

Subsequent examination of Ac-aELVIIAG-NH2 assemblies by TEM revealed the formation of homogeneous fibers suggesting the NAPC biases assembly towards fiber formation.

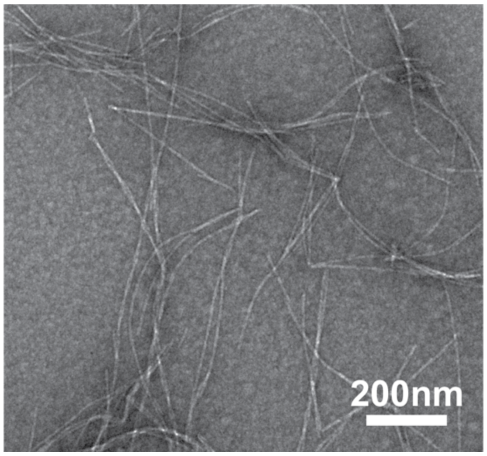

Figure 3-25 Ac-aELVIIAG-NH_2 assembly by TEM.

Addition of a DNA linker to the above assemblies with varied amounts of NAPC (Figure 3-24), was not successful in forming a hydrogel. Several factors likely contribute to the unsuccessful outcomes of this attempt: assembly concentration may not be high enough, nucleic acids are sticking to the positively charged nanotube surfaces, or NAPC are not incorporated into the observed nanostructures.

Phosphorylated tyrosine nanotubes were explored as a second candidate for hydrogel assembly. Ac-pYLVFFAL-NH_2 ('p' indicates phosphorylation), assembles as nanotubes in TEAA and 40% acetonitrile [61]. These nanotubes maintain a negatively charged surface and should prevent any potential electrostatic interactions between the backbone of DNA and positively charged peptides. To co-assemble the NAPC and Ac-pYLVFFAL-NH_2, peptide Ac-aELVFFAL-NH_2 was synthesized (Figure 3-26). Subsequent conjugation to DNA was carried out as described in Figure 3-5. Consistency in the hydrophobic peptide tail is necessary for co-assembly. Due to issues with solubility, acetonitrile was used instead of DMF during synthesis.

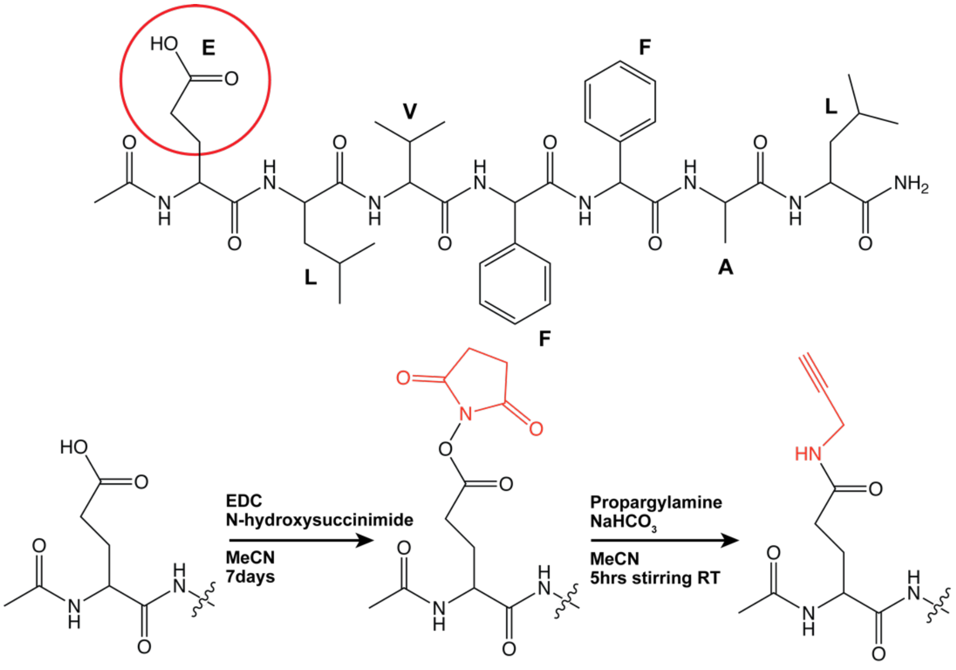

Figure 3-26 Synthesis of alkyne-modified Ac-ELVFFAL-NH$_2$.

Homogeneous Ac-pYLVFFAL-NH$_2$ nanotube assembly was confirmed by TEM in TEAA and 40% MeCN. Co-assembly of NAPC with Ac-pYLVFFAL-NH$_2$ at a ratio of 1:20 resulted in the formation of sheets as the predominant supramolecular architecture. NAPC concentration was increased to 5% to account for sufficient DNA density on assembly surfaces. Nanotubes observed in NAPC/peptide co-assembly samples were larger than those observed for Ac-pYLVFFAL-NH$_2$-alone assemblies as shown in Figure 3-27. Addition of the DNA linker to these co-assemblies was unsuccessful in inducing hydrogel formation. For these co-assembled samples, the primary barrier appears to be homogeneity in nanostructure morphology.

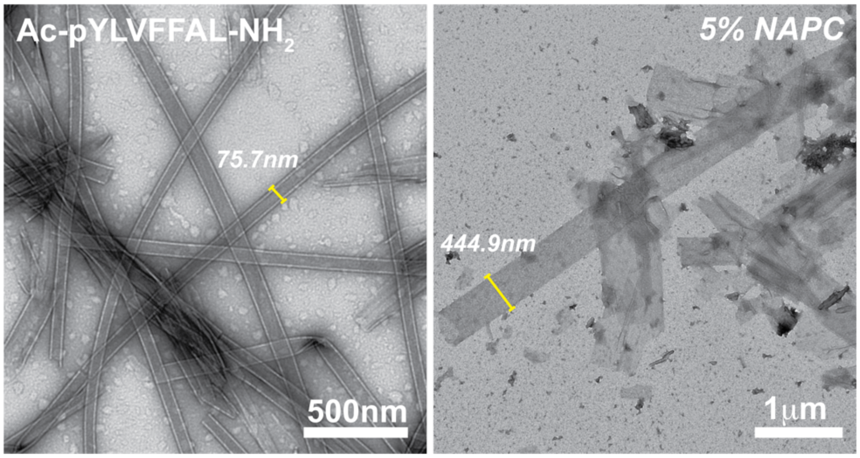

***Figure 3-27 TEM analysis of Ac-pYLVFFAL-NH$_2$ nanotubes and NAPC/Ac-pYLVFFAL-NH$_2$ co-assemblies in TEAA and 40% MeCN.** Measurements indicate nanotube width.*

Conclusions

In this chapter, I described the formation of three DNA/peptide conjugates for application in biomolecular nanotechnology. Through simple modification of the glutamic acid side chain with an alkyne, the successful conjugation to azide-modified DNA was possible. Conjugation of guanine quadruplex-forming DNA to Ac-aELVIIAG-NH$_2$ was confirmed by urea-PAGE, and co-assembly with Ac-KLVIIAG-NH$_2$ revealed formation of homogeneous conical nanotubes. Through buffer variation and subsequent removal of integral monovalent cations, it was determined that conical nanotube assembly was dependent on guanine quadruplex formation. The recent development of a guanine-quadruplex-specific dye, ISCH-oa1, was monumental to our conclusion that guanine quadruplexes form within GQPC/peptide co-assemblies. We have yet to determine the precise location of guanine quadruplexes within the co-assemblies or their degree of stacking, but it is clear the results of these experiments provide a foundation for the development of highly mutualistic functional assemblies, which include peptide insulated guanine nanowires. We have not yet done the experiments to assess conductivity of co-assemblies. However, quadruplex assembly clearly infuences nanostructure gross morphology.

The development of DNA/Peptide conjugates for use in responsive hydrogel formation is still being investigated. Challenges including assembly concentration, electrostatic interactions, homogeneity of co-assemblies, and density of DNA/peptide conjugates must be addressed and conditions optimized for successful hydrogel formation. With a repertoire of peptides and accessible morphologies to sample, there is no doubt the challenges discussed here will be overcome.

These data begin to describe the diverse, mutualistic interactions that can be exploited for application in nanotechnology and beyond. The guanine quadruplex-dependent conical nanotube formation described here foreshadows the following chapters where the presence of nucleic acid influences the gross morphology of peptide assemblies.

Methods

Peptide Synthesis. Peptides were synthesized using Solid Phase Peptide Synthesis (SPPS) with a Rink-Amide MBHA resin, 0.4mmol/g substitution, and capped at the N-terminus with an acetyl group. Peptides were cleaved and deprotected using a cocktail of 90% TFA, 2% anisole, 3% 1,2-ethanedithiol, and 5% thioanisole. All chemicals were purchased from Sigma-Aldrich. Following cleavage and deprotection, peptides were purified by reverse-phase HPLC using acetonitrile and water with 0.1%TFA and a C18 column to a >98% purity. After purification, acetonitrile was removed by rotavaporation. The remaining aqueous solution was frozen at -80°C or flash frozen using liquid nitrogen and lyophilized to yield a white powder.

Peptide Assembly. Due to the salt sensitivity of peptides used in this study, following purification and lyophilization, peptides were desalted using Sep-Pak® C18 cartridges. Ac-KLVIIAG-NH_2 was placed in 10mM $NaPO_4$ buffer with 100mM NaCl at pH6.8, vortexed briefly and sonicated for 5 minutes to promote solubility. A stock solution of 2mM peptide was used to set up all assemblies. Experimental samples were set up within five minutes of dissolution. Nucleic acid peptide conjugate concentration was determined by UV-Vis spectroscopy assuming no peptide influence at 260nm. GQPC/Ac-KLVIIAG-NH_2 samples were set up with a peptide concentration of 0.4mM and a GQPC concentration of 10μM. For NAPC/Ac-KLVIIAG-NH_2 samples, peptide concentration was 1mM and NAPC concentration varied from 10μM to 33μM. For NAPC/Ac-KLVIIAG-NH_2 co-assembly, peptides were dissolved in 50mM Tris-HCl, pH 7.3. NAPC/Ac-pYLVFFAL-NH_2 samples were set up with a peptide concentration of 1mM and a NAPC concentration of 50μM. Ac-pYLVFFAL-NH_2 peptides were dissolved in 40% Acetonitrile and TEAA (final concentration 60mM). For all co-assemblies, order of addition was: peptide, conjugate, buffer. Samples were stored at room temperature.

Alkyne Modified Peptide Synthesis. Peptide (~20mg) and N-hydroxysuccinimide (33.5mg) were dissolved in DMF (2mL). Once dissolved, EDC (55.8mg) was added. Solution was stirred at room temperature for 30 hours. Attachment of N-hydroxysuccinimide to the carboxylic acid was confirmed by MALDI. More N-hydroxysuccinimide can be added to increase yield. A solution of 0.2M $NaHCO_3$ (100uL) was added to the Imide-Peptide/DMF mixture from the previous reaction. Propargylamine (0.15mmol) was added immediately after $NaHCO_3$ to the reaction cocktail. Alkyne-modified peptide was visible by MALDI after 5 hours stirring at room temperature. Addition of more propargylamine may increase yield.

For Ac-ELVFFAL-NH_2, acetonitrile was substituted for DMF in all cases. Instead of stirring for 30hours, solution was stirred for seven days. All other steps remain the same. Product formation was confirmed by MALDI-TOF MS.

Nucleic Acid Peptide Conjugate Synthesis. Nucleic acid/Peptide conjugates were formed via a copper-catalyzed click reaction. All reactions were performed at 4nmol to 6nmol azide-modified nucleic acid and excess alkyne-modified peptide. In one tube combine azide-DNA (~4nmol), alkyne-peptide (in excess, 4μL), 2M TEAA pH7 (4μL), saturated ascorbic acid in H2O (4μL), DMSO to 50% the volume (20μL), and 10mM Cu-TBTA (added last, 4μL). Leave reaction at room temperature for 48 hours. The DNA-Peptide conjugate and any unreacted DNA was ethanol precipitated on ice using 2mL $MgCl_2$ and four times the volumes of 200 proof ethanol for 20 minutes. Precipitate was pelleted and washed with 70% ethanol. The pellet was dried in a vacuum desiccator and analyzed by urea-PAGE.

Urea-PAGE. A 20% 7M urea polyacrylamide gel was used for confirmation of nucleic acid/peptide conjugation. 20% PAGE gels were 1mm thick and run at 100V for 90 minutes. A 10bp ladder was used as a reference for DNA and conjugate migration. Samples were prepared in TBE-urea sample buffer, heated to 95°C for five minutes to prevent secondary structure formation and run on the gel. Gels were incubated in 1X SYBR-Gold in TBE for 20-40 minutes following electrophoresis and visualized using a Bio-rad gel imager.

Transmission Electron Microscopy. Electron microscopy images were obtained using a Hitachi H-7500 and a Jeoul transmission electron microscope. All samples were placed on 200 mesh copper grids with carbon coating and negatively stained using 2%w/w uranyl acetate (Sigma-Aldrich). The microscope was operated at 75kV. Cross-section images were obtained by embedding pelleted assemblies in resin. Using a microtome, embedded assemblies were sliced 1μm thick and placed on grids for analysis by TEM.

Circular Dichroism. A Jasco-810 Spectropolarimeter was used to record CD spectra. Samples were examined at room temperature in a 50μL cell with a 0.1mm path length. The reported spectra were acquired from 260nm to 190nm with a step size of 0.2nm and a speed of 100nm/s, and are the average of three independent scans. Ellipticity, in mdeg, was converted to Molar ellipticity (θ) with $[\theta] = \theta/(10 \times c \times l)$, where 'c' is peptide concentration in moles/L and '*l*' is the pathlength in cm.

Fourier-Transform Infrared Spectroscopy. FT-IR spectra were acquired using a Jasco FT-IR 4100 (Easton, MD, USA) averaging 750 scans at $2cm^{-1}$ resolution. For each sample, 8μl of peptide solution was dried as a thin film on a Pike GaldiATR (Madison, WI, USA) ATR diamond surface. The MCT-M detector, having a 5mm aperture and a scanning speed of 4mm/sec was used.

Fluorescence Spectroscopy. Fluorescence spectroscopy was performed on a Cary Eclipse Fluorescence Spectrophotometer. The emission was fixed at 650nm for identification of the maximum excitation of 550nm. The excitation was then fixed at 550nm and emission spectra were accumulated from 560nm to 700nm. ISCH-oa1 was used at 1μM in all cases. The titration was performed through variation of GQPC/peptide co-assembly concentration. A quartz cuvette with a 3mm pathlength was used for all fluorescence analysis. Fluorescence intensity was normalized to f/f_0, where f is the fluorescence of the sample and f0 is the fluorescence of 1μM ISCH-oa1.

References

[1] Mirkin, C. A., Letsinger, R. L., Mucic, R. C., Storhoff, J. J. A Dna-based method for rationally assembling nanoparticles into macroscopic materials. *Nature* **382,** 607-609 (1996).

[2] Winfree, E., Liu, F., Wenzler, L. A., Seeman, N. C. Design and self-assembly of two-dimensional DNA crystals. *Nature* **394,** 539-544 (1998).

[3] Ke, Y., Ong, L. L., Shih, W. M., Yin, P. Three-Dimensional Structures Self-Assembled from DNA Bricks. *Science* **338,** 1177-1183 (2012).

[4] Lakshmanan, A., Zhang, S. G., Hauser, C. A. E. Short self-assembling peptides as building blocks for modern nanodevices. *Trends Biotechnol.* **30,** 155–165 (2012).

[5] Liu, P. *et al.* Nucleobase-directed amyloid nanotube assembly. *J. Am. Chem. Soc.* **130,** 16867-16869 (2008).

[6] Yuan, D. *et al.* Mixing biomimetic heterodimers of nucleopeptides to generate biocompatible and biostable supramolecular hydrogels. *Angew. Chem. Int. Ed.* **54,** 5705-5708 (2015).

[7] Li, C. *et al.* Rapid formation of a supramolecular polypeptide-DNA hydrogel for in situ three-dimensional multilayer bioprinting. *Angew. Chem. Int. Ed.* **54,** 3957-3961 (2015).

[8] Huang, Y. C., Sen, D. A contractile electronic switch made of DNA. *J. Am. Chem. Soc.* **132,** 2663-2671 (2010).

[9] Bixon, M. *et al.* Long-range charge hopping in DNA. *Proc. Natl. Acad. Sci. USA* **96,** 11713-11716 (1999).

[10] Tian, Y. *et al.* Prescribed nanoparticle cluster architectures and low-dimensional arrays built using octahedral DNA origami frames. *Nat. Nanotechnol.* **10,** 637-645 (2015).

[11] Ke, Y., Meyer, T., Shih, W. M., Bellot, G. Regulation at a distance of biomolecular interactions using a DNA origami nanoactuator. *Nat. Comm.* **7,** 10935 (2016).

[12] Domigan, L. *et al.* Dielectrophoretic manipulation and solubility of protein nanofibrils formed from crude crystallins. *Electrophoresis* **34,** 1105-1112 (2013).

[13] Mehta, A. K. *et al.* Context dependence of protein misfolding and structural strains in neurodegenerative diseases. *Biopolymers* **100,** 722-730 (2013).

[14] Wang, Y. *et al.* Rational design of chiral nanostructures from self-assembly of a ferrocene-modified dipeptide. *J. Am. Chem. Soc.* **137,** 7869-7880 (2015).

[15] Omosun, T. O. *et al.* Catalytic Diversity in Self-propagating Peptide Assemblies, *Nat Chem*. In press. (2017).

[16] Kapil, N., Singh, A., Das, D. Cross-b amyloid nanohybrids loaded with cytochrome C exhibit superactivity in organic solvents. *Angew. Chem. Int. Ed.* **54,** 6492-6495 (2015).

[17] Erickson, S. L., Lykke-Andersen, J. Cytoplasmic mRNP granules at a glance. *J. Cell Sci.* **124,** 293-297 (2011).

[18] Moore, M. J. From birth to death: the complex lives of eukaryotic mRNAs. *Science* **309,** 1514–1518 (2005).

[19] Zhang, L., Lei, J., Liu, L., Li, C., Ju, H. Self-assembled DNA hydrogel as switchable material for aptamer-based fluorescent detection of protein. *Anal. Chem.* **85,** 11077-11082 (2013).

[20] Abraham JN, Gour N, Bolisetty S, Mezzenga R, Nardin C, 2015. Controlled Aggregation of Peptide-DNA Hybrids into Amyloid-Like Fibrils, *European Polymer Journal*, **65**:268-275

[21] Humenik M, Drechsler M, Scheibel T, 2014. Controlled Hierarchical Assembly of Spider Silk-DNA Chimeras into Ribbons and Raft-Like Morphologies, *Nano Letters*, **14**:3999-4004

[22] Tavernier, H. L., Fayer, M. D. Distance dependence of electron transfer in DNA: the role of the reorganization energy and free energy. *J. Phys. Chem.* **104,** 11541-11550 (2000).

[23] Woiczikowski, P. B., Kubar, T., Gutiérrez, R., Cuniberti, G., Elstner, M. Structural stability versus conformational sampling in biomolecular systems: why is the charge transfer efficiency in G4-DNA better than in double-stranded DNA? *J. Chem. Phys.* **133,** 035103 (2010).

[24] Huang, Y. C., Chenge, A. K. H., Yu, H-Z., Sen, D. Charge conduction properties of a parallel-stranded DNA G-quadruplex: Implications for chromosomal oxidative damage. *Biochemistry* **48,** 6794-6804 (2009).

[25] Yang, X., Wang, X-B., Vorpagel, E. R., Wang, L-S. Direct experimental observation of the low ionization potentials of guanine in free oligonucleotides by using photoelectron spectroscopy. *Proc. Natl. Acad. Sci. USA* **101,** 17588-17592 (2004).

[26] Livshits, G. I. Long-range charge transport in single G-quadruplex DNA molecules. *Nat. Nanotechnol.* **9,** 1040-1046 (2014).

[27] Liu, S-P. Direct measurement of electrical transport through G-quadruplex DNA with mechanically controllable break junction electrodes. *Angew. Chem. Int. Ed.* **49,** 3313-3316 (2010).

[28] Calzolari, A., Di Felice, R., Molinari, E., Garbesi, A. Electron channels in biomolecular nanowires. *J. Phys. Chem. B* **108,** 2509-2515 (2004).

[29] Calzolari, A., Di Felice, R., Molinari, E. G-quartet biomolecular nanowires. *Appl. Phys. Lett.* **80,** 3331-3333 (2002).

[30] Shukla, L. I. *et al.* The formation of DNA sugar radicals from photoexcitation of guanine cation radicals. *Radiat. Res.* **161,** 582-590 (2004).

[31] Marsh, T. C., Henderson, E. G-wires: self-assembly of a telomeric oligonucleotide, d(GGGGTTGGGG), into large superstructures. *Biochemistry* **33,** 10718-10724 (1994).

[32] Changenet-Barret, P., Hua, Y., Gustavsson, T., Markovitsi, D. Electronic excitations in G-quadruplexes formed by the human telomeric sequence: a time-resolved fluorescence study. *Photochem. Photobiol.* **91,** 759-765 (2015).

[33] Marsh, T. C., Vesenka, J., Henderson, E. A new DNA nanostructure, the G-wire, imaged by scanning probe microscopy. *Bucleic Acids Res.* **23,** 696-700 (1995).

[34] Lech. C. J., Phan, A. T., Michel-Beyerle, M-E. Electron-hole transfer in G-quadruplexes with different tetrad stacking geometries: a combined QM and MD study. *J. Phys. Chem.* **117,** 9851-9856 (2013).

[35] Ilc, T. *et al.* Formation of G-wires: the role of G:C-base pairing and G-quartet stacking. *J. Phys. Chem.* **117,** 23208-23215 (2013).

[36] Hud, N. V., Smith, F. W., Anet, F. A. L., Feigon, J. The selectivity for K+ versus Na+ in DNA quadruplexes is dominated by relative free energies of hydration: a thermodynamic analysis by ^{1}H NMR. *Biochemistry* **35,** 15383-15390 (1996).

[37] Pontinha, A. D. R., Chiorcea-Paquim, A-M, Eritja, R., Oliveira-Brett, A. M. Quadruplex nanostructures of d(TGGGGT): influence of sodium and potassium ions. *Anal. Chem.* **86,** 5851-5857 (2014).

[38] Chiorcea-Paquim, A-M, Santos, P. V., Eritja, R., Oliveira-Brett, A. M. Self-assembled G-quadruplex nanostructures: AFM and voltammetric characterization. *Phys. Chem. Chem. Phys.* **15,** 9117-9124 (2013).

[39] Guzmán, M. R., Liquier, J., Brahmachari, S. K., Taillandier, E. Characterization of parallel and antiparallel G-tetraplex structures by vibrational spectroscopy. *Spectrochimica Acta Part A* **64,** 495-503 (2006).

[40] Gao, Z. F., Huang, Y. L., Ren, W., Luo H. Q., Li, N. B. Guanine nanowire based amplification strategy: enzyme-free biosensing of nucleic acids and proteins. *Biosens. Bioelectron.* **78,** 351-357 (2016).

[41] Bielecka, P., Juskowiak, B. Fluorescent sensor for pH monitoring based on an i-motif—switching aptamer containing a tricyclic cytosine analogue (tC). *Molecules* **20,** 18511-18525 (2015).

[42] Zhou, J. *et al.* Formation of i-motif structure at neutral and slightly alkaline pH. *Mol. BioSyst.* **6,** 580-586 (2010).

[43] Miyoshi, D., Matsumura, S., Li, W., Sugimoto, N. Structural polymorphism of telomeric DNA regulated by pH and divalent cation. *Nucleosides, Nucleotides, and Nucleic Acids* **22,** 203-221 (2003).

[44] Xiong, X. *et al.* Responsive DNA-based hydrogels and their applications. *Macromol. Rapid Commun.* **34,** 1271-1283 (2013).

[45] Jiang, H., Pan, V., Vivek, S., Weeks, E. R., Ke, Y. Programmable DNA hydrogels assembled from multidomain DNA strands. *ChemBioChem* **17,** 1156-1162 (2016).

[46] Ni, R., Childers, W. S., Hardcastle, K. I., Mehta, A. K., Lynn, D. G. Remodeling cross-β nanotube surfaces with peptide/lipid chimeras. *Angew. Chem. Int. Ed.* **51,** 6635-6638 (2012).

[47] Seo, T. S., Li, Z., Ruparel, H., Ju, J. Click chemistry to construct fluorescent oligonucleotides for DNA sequencing. *J. Org. Chem.* **68,** 609-612 (2003).

[48] Paramasivan, S., Rujan, I., Bolton, P. H. Circular dichroism of quadruplex DNAs: Applications to structure, cation effects and ligand binding. *Methods* **43,** 324-331 (2007).

[49] Vorlíčková, M., Kejnovská, I., Bednárová, K., Renčiuk, D., Kypr, J. Circular dichroism spectroscopy of DNA: from duplexes to quadruplexes. *Chirality* **24,** 691-698 (2012).

[50] Kypr, J., Kejnovská, I., Renčiuk, D., Vorlíčková, M. Circular dichroism and conformational polymorphism of DNA. *Nucleic Acids Res.* 1-13 (2009).

[51] Randazzo, A., Spada, G. P., Webba da Silva, M. Circular dichroism of quadruplex structures. *Top. Curr. Chem.* **330,** 67-86 (2013).

[52] Childers, W. S., Anthony, N. R., Mehta, A. K., Berland, K. M., Lynn, D. G. Phase networks of cross-β peptide assemblies. *Langmuir* **28,** 6386–6395 (2012).

[53] Arthanari, H., Basu, S., Kawano, T. L., Bolton, P. H. Fluorescent dyes specific for quadruplex DNA. *Nucleic Acids Res.* **26,** 3724-3728 (1998).

[54] Chen, S-B. *et al.* Visualization of *NRAS* RNA G-quadruplex structures in cells with an engineered fluorogenic hybridization probe. *J. Am. Chem. Soc.* **138,** 10382-10385 (2016).

[55] Wickremasinghe, N. C., Kumar, V. A., Hartgerink, J. D. Two-step self-assembly of liposome-multidomain peptide nanofiber hydrogel for time-controlled release. *Biomacromolecules* **15,** 3587-3595 (2014).

[56] Wei, G-J. *et al.* Promotion of peripheral nerve regeneration of a peptide compound hydrogel scaffold. *Int. J. Nanomed.* **8,** 3217-3225 (2013).

[57] Liu, J., Zhang, L., Yang, Z., Zhao, X. Controlled release of paclitaxel from a self-assembling peptide hydrogel formed in situ and antitumor study in vitro. *Int. J. Nanomed.* **6,** 2143-2153 (2011).

[58] Liao, S. W. *et al.* Maintaining functional islets through encapsulation in an injectable saccharide-peptide hydrogel. *Biometerials* **34,** 3984-3991 (2014).

[59] Ischakov, R., Adler-Abramovich, L., Buzhansky, L., Shekhter, T., Gazit, E. Peptide-based hydrogel nanoparticles as effective drug delivery agents. *Bioorg. Med. Chem.* **21,** 3517-3522 (2013).

[60] Dasgupta, A., Mondal, J. H., Das, D. Peptide Hydrogels. *RSC Adv.* **3,** 9117-9149 (2013).

[61] Li, S. *et al.* Design of asymmetric peptide bilayer membranes. *J. Am. Chem. Soc.* **138,** 3579–3586 (2016).

Chapter 4: Design and Global Architecture Characterization of Nucleic Acid/Peptide Co-assemblies

Introduction

The intricate macromolecular network connecting RNA, DNA and their nucleic acid binding proteins underpins the spatiotemporal regulation of cellular information flow [1]. Many of the proteins and peptides involved in interactions with nucleic acids have a propensity for self-aggregation, adding further dimensions to this supramolecular network [1-3]. Notably, intrinsically-disordered, low complexity domains (LCDs) of RNA-binding proteins containing repeating dyad arrays of FG, QN, YG, and RG are critical for the sophisticated phase behavior of micron-sized nucleic acid/protein coacervates [3-8], and necessary and sufficient for the spatiotemporal regulation of mRNAs through the assembly of messenger ribonucleoprotein (mRNP) granules [1-6]. These granules are often referred to as membraneless organelles and include the nucleolus where RNA and proteins are assembled into the ribosomal subunits [7-12]. The transient and fluxional behavior of mRNP granules is necessary to guide RNA through the many stages of information processing [1], and the maturation of these granules may be increasingly relevant to a multitude of disease states [13-21]. This will be explored further in Chapter 6.

In an Amyotrophic Lateral Sclerosis model, RNA binding was integral to the nucleation of the LCD-dependent assembly of higher-order FUS RNP fibrils and mediated interactions with the C-terminal domain of RNA Pol II [22]. This and other examples of mRNP granule maturation, including that of Cajal Body self-organization [23], reveal an essential role for nucleic acids in the assembly pathway [24]. Non-canonical RNA sequences have been shown to impact mRNP granule development [25-31], and other evidence suggests transient amyloid assembly mediates mRNP granule maturation as seen in Figure 4-1 [3,7,32-36].

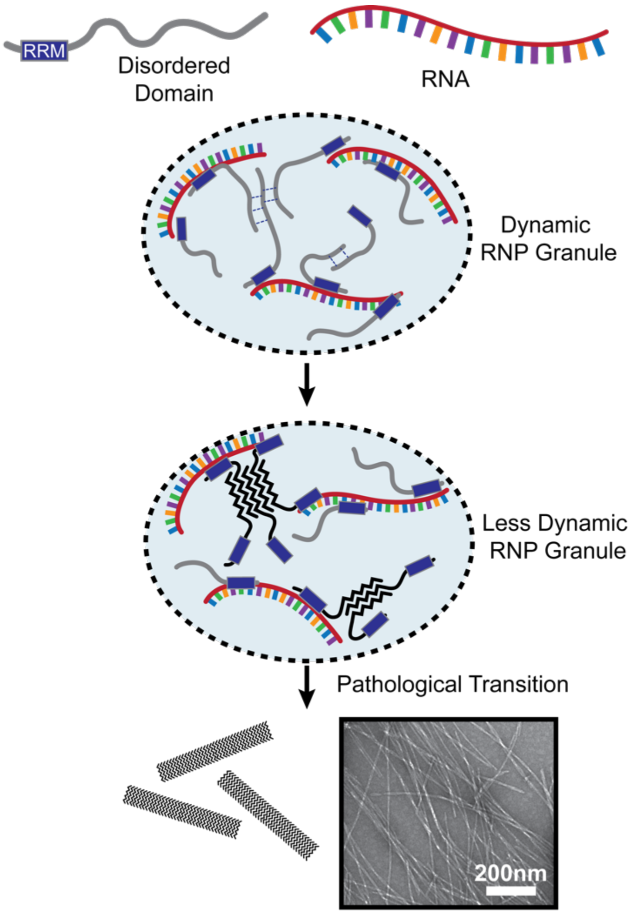

Figure 4-1 Ribonucleoprotein (RNP) granule maturation and the pathological transition. *RNP granules are composed of RNA binding proteins with RNA recognition motifs (RRM) and often disordered domains, and RNA. Maturation of RNP granules to to excessive exposure to stress can lead to the formation of less-dynamic granules. Presence of pathogenic mutations, often found in disordered domains, may lead to a pathological transition to amyloid fibril assembly. TEM shows Ac-KLVIIAG-NH_2 peptide fibers as an example of amyloid assembly.*

Amyloids are characterized by cross-β diffraction patterns arising from the stacking of β-sheets orthogonal to the assembly's long-axis [37,38]. The amyloid-β (Aβ) peptide of Alzheimer's disease, which aggregates as amyloid extracellularly in senile plaques, is perhaps the simplest, and most well-characterized, intrinsically-disordered peptide [37-40]. The canonical Aβ core, amino acids 'KLVFFAE', or Aβ(16-22), has been examined extensively [38,41,42], and shown to be essential for initial nucleation and propagation of fibrillar Aβ assemblies [37-39]. Aβ16-22 and its congeners assemble through a two-stage nucleation process, much like ribonucleoprotein granule assembly with oligonucleotides, but with a higher propensity for assembly [38]. Here, we use this peptide to explore co-assembly with RNA and define through a reductionist approach well-ordered supramolecular assemblies that result from highly specific and mutualistic cross-templating of nucleic acid and amyloid domains. Specific contacts between the surface of the peptide and nucleic acid backbone dominate the assemblies, providing insight to the ubiquitous, and often sequence-independent, association of cellular mRNAs with proteins and their pathogenic impact on mRNP granules [1,43,44]. These co-assemblies are remarkably dynamic, a critical feature of mRNP granules [1,2], and reveal how LCDs and other more aggressive β-sheet-prone infectious domains could structurally intercept cellular stress, development, or other mRNP granules through irreversible nucleic acid/peptide co-assembly.

Results

Sampling of peptide congeners for nucleic acid co-assembly

The liquid-liquid phase separations that give rise to the mRNP granules are entropy-driven desolvation events [1-8,10,31], and the self-solvation energetics in the granules are expected to be dominated by electrostatic forces [26,43-46]. Because of this, we focused our initial examination on nucleic acid chain length and a stoichiometry that achieves overall charge neutrality. G/C-rich nucleic acids are excluded to avoid competing secondary structures including guanine quadruplexes and cytosine i-motifs discussed in detail in Chapter 3. The peptides explored are shown in Figures 4-2 and 4-6. As scored by transmission electron microscopy (TEM), assembly proved to be sensitive to both the terminal and internal amino acids of Aβ(16-22) when in association with A/U RNA oligomers.

Peptides Ac-KLVFFAG-NH_2 and Ac-RLVFFAG-NH_2 maintain the canonical 'LVFFA' hydrophobic core of Aβ(16-22), and form well-defined cross-β structures, but display significant morphological heterogeneity when co-assembled with RNA by TEM (Figure 4-2). Despite its propensity to form a RNA duplex, RNA $(AU)_5$ was used at temperatures at or above its T_m and did not appear to cause significant aberrations in co-assembly structure when compared with single stranded RNAs.

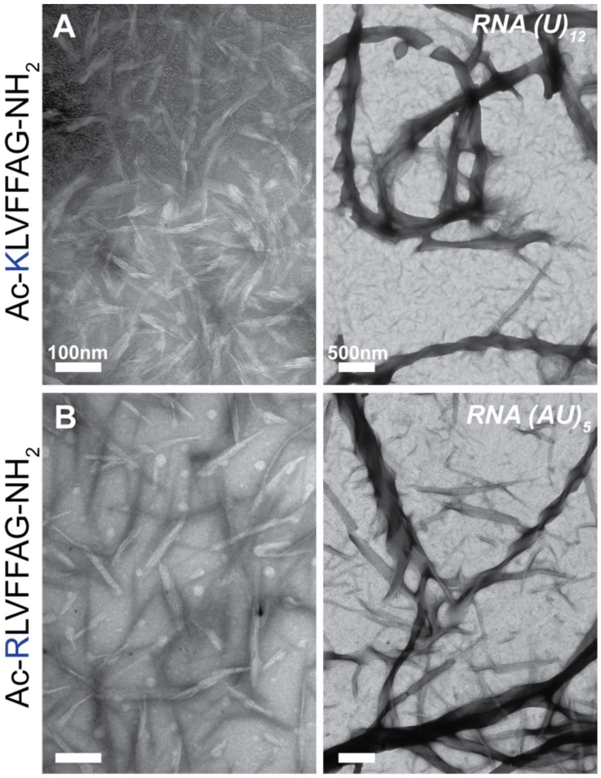

Figure 4-2 Ac-KLVFFAG-NH_2 and Ac-RLVFFAG-NH_2 assembly and co-assembly with RNA. *TEM analysis of Ac-KLVFFAG-NH_2 (A) and Ac-RLVFFAG-NH_2 (B) assembly*

with and without RNA. Scale bars are 100nm in the first column and 500nm in the second column.

Co-assembly of peptide Ac-KLVFFAG-NH_2 with RNA was examined by laser-scanning confocal microscopy to begin to examine RNA localization. The amyloid-specific dye Thioflavin T was used as an indicator of peptide assembly, while RNA was observed via Cy3 fluorescence, which was covalently attached at the 3’-end of $RNA(U)_{10}$. The merge of amyloid and RNA fields confirmed co-localization of the fluorophores and suggested co-assembly of RNA and peptide.

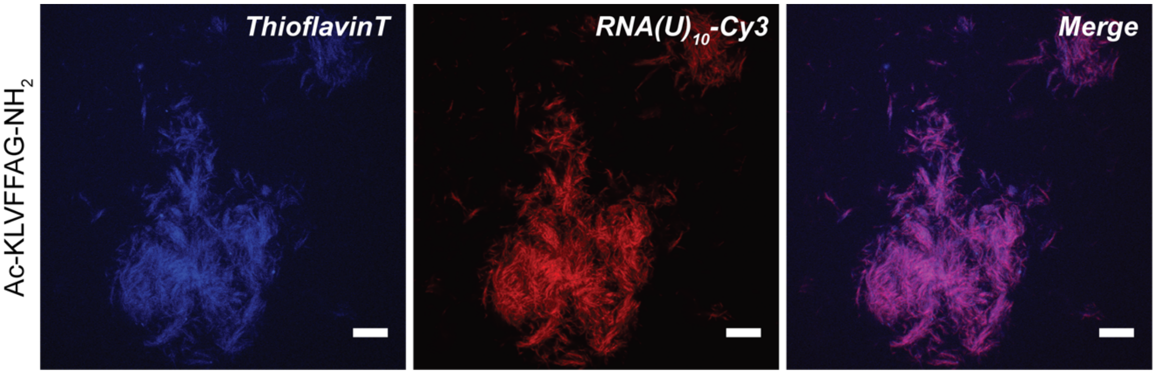

Figure 4-3 Laser scanning confocal microscopy of RNA/Ac-KLVFFAG-NH_2 co-assemblies. *Thioflavin T, amyloid indicator. Cy3 covalently bound to the 3’-end of $RNA(U)_{10}$. Scale bars are 10μm.*

Co-assembly of Ac-KLVFFAG-NH_2 and RNA was examined further using electrostatic force microscopy (EFM). EFM is identical to atomic force microscopy (AFM), except that electrostatic surface forces are probed instead of Van der Waals. By applying a +1V charge bias to the cantilever tip and placing it in non-contact mode, a micrograph revealing charge distribution is produced. Examination of Ac-KLVFFAG-NH_2/RNA co-assemblies by EFM yielded micrographs where co-assembly surfaces were primarily negatively-charged (Figure 4-4). Topography, taken in normal AFM mode, provided a complete depiction of the Ac-KLVFFAG-NH_2/RNA co-assembly.

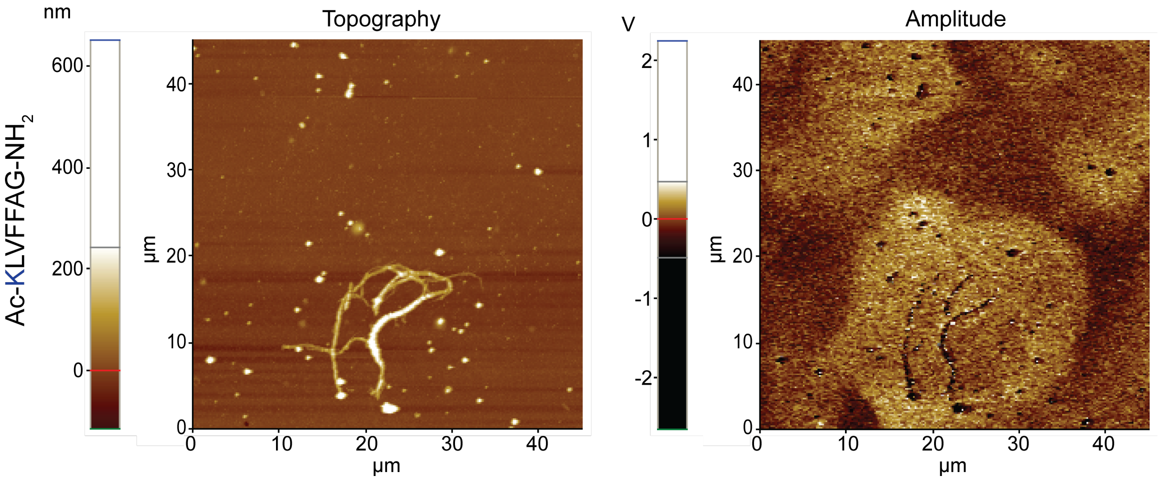

Figure 4-4 Ac-KLVFFAG-NH_2/RNA co-assemblies have negatively-charged surfaces. *Topography, AFM, depicts total co-assembly present. Amplitude, EFM, depicts surface charge distribution for the co-assembly.*

Structurally, Ac-KLVFFAG-NH_2 and Ac-RLVFFAG-NH_2, with and without RNA, maintained cross-beta diffraction patterns consistent with amyloid nanostructures by powder x-ray diffraction. Co-assemblies show persistence of the interstrand distance of 4.7Å and intersheet distance of ~10Å is consistent with maintenance of the amyloid core architecture. These data taken with the micrograph from EFM suggest these amyloid nanostructures are coated with RNA.

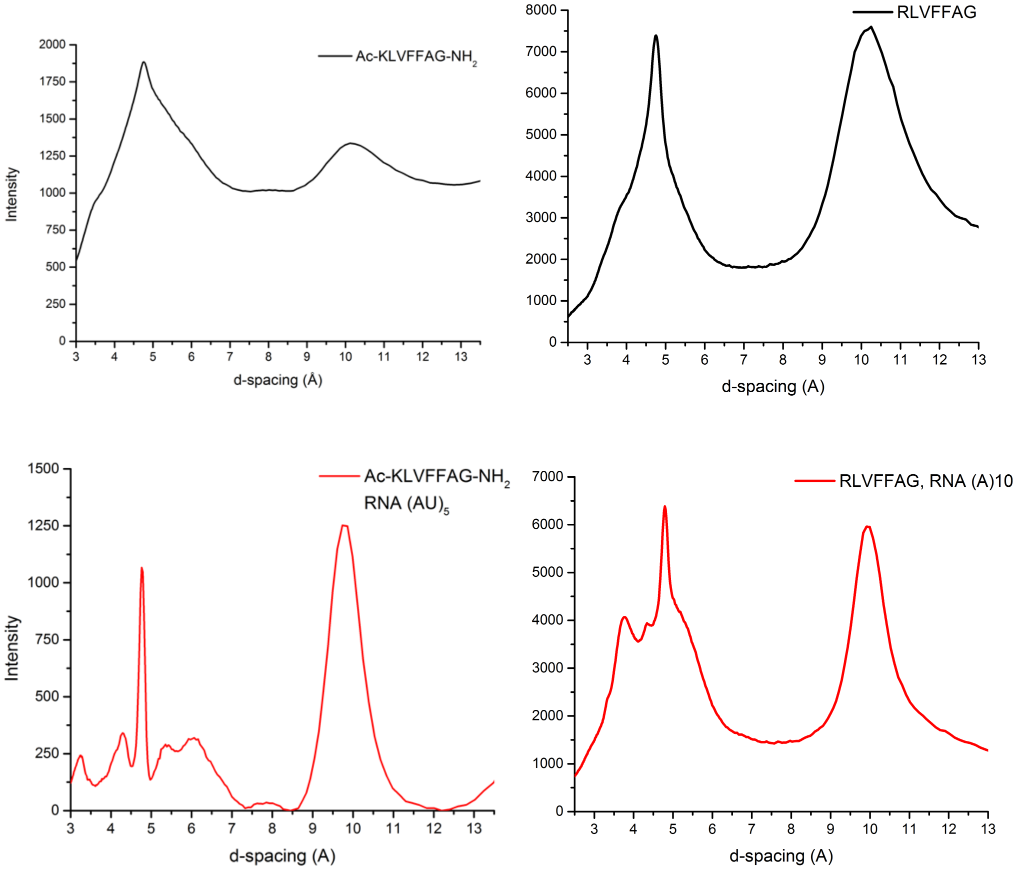

Figure 4-5 Diffraction patterns consistent with amyloid are maintained in Ac-KLVFFAG-NH$_2$ and Ac-RLVFFAG-NH$_2$ co-assemblies. *All assemblies depict reflections at 4.7Å and ~10Å.*

Despite clear co-assembly of Ac-KLVFFAG-NH2 and Ac-RLVFFAG-NH$_2$ with RNA, the heterogeneity of nanostructures makes further structural characterization difficult. To address heterogeneity, we surveyed several peptides that differed in sequence at the 'FF' dyad or C-terminal residue. These positions were chosen based on their contribution to assembly kinetics [47,48] and their influence on nanostructure surface dynamics. The 'FF' dyad, which is oft-touted as being essential for fibril formation was replaced with other hydrophobic residues. The C-terminal glycine was replaced with bulkier hydrophobic amino acids that restrict rotation about the peptide bond. Some of these peptides are shown in Figure 4-6. In all cases, fibers were observed in peptide-alone assembly and bundled fibers or amorphous aggregates emerged in the presence of RNA. Heterogeneity was observed for all peptide co-assemblies in Figure 4-6, and RNA's contribution remained unclear.

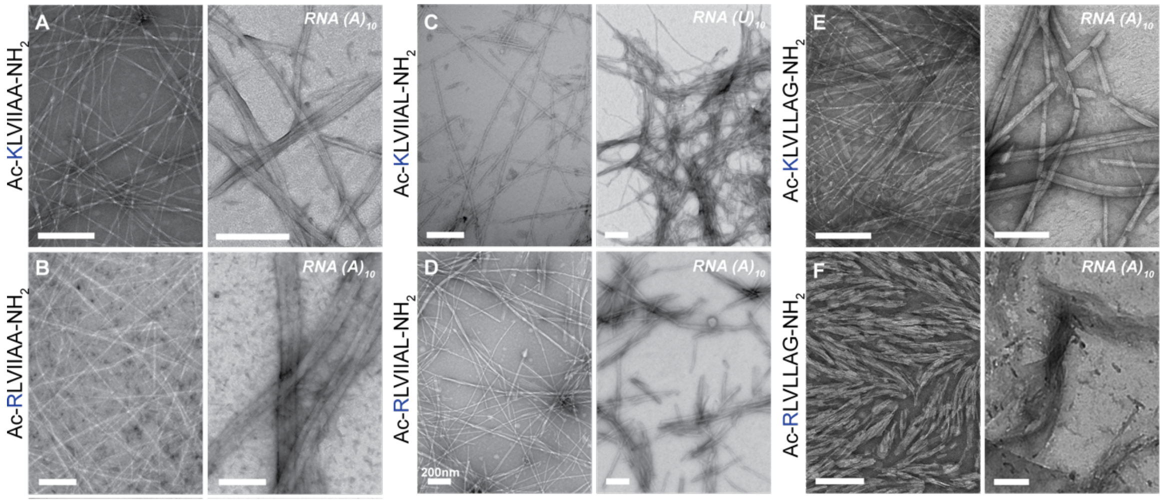

Figure 4-6 Sampling of peptide congeners and their co-assembly with RNA reveals heterogeneity. *Ac-KLVIIAA-NH$_2$ and Ac-RLVIIAA-NH$_2$ with and without RNA(A)$_{10}$ (A,B). Ac-KLVIIAL-NH$_2$ and Ac-RLVIIAL-NH$_2$ with and without RNA (C,D). Ac-KLVLLAG-NH$_2$ and Ac-RLVFFAG-NH$_2$ (E,F).*

Assembly of homogeneous nucleic acid/peptide nanostructures

The isoleucine dyad is closest in hydrophobicity to the FF dyad, according to the Fauchere-Pliska index (Table 4-1), and was selected to reduce the possibility of π-π stacking between peptides and incorporated nucleobases [47,48]. Other hydrophobic dyads also reduce heterogeneity. However, with the internal di-isoleucine and glycine at the C-terminus, homogeneous structures are observed in the nucleic acid/peptide co-assembly. Peptides Ac-KLVIIAG-NH$_2$ and Ac-RLVIIAG-NH$_2$ are explored for the remainder of this Chapter.

Amino Acid	Hydrophobicity	Amino Acid	Hydrophobicity
Alanine	0.310	Leucine	1.700
Arginine	-1.010	Lysine	-0.990
Asparagine	-0.600	Methionine	1.230
Aspartic acid	-0.770	Phenylalanine	1.790
Cysteine	1.540	Proline	0.720
Glutamine	-0.220	Serine	-0.040
Glutamic acid	-0.640	Threonine	0.260
Glycine	0.000	Tryptophan	2.250
Histidine	0.130	Tyrosine	0.960
Isoleucine	1.800	Valine	1.220

Table 4-1 Fauchere-Pliska index – Hydrophobicity was determined from TLC retention time of amino acids.

As shown in Figure 4-7, congeners ‘Ac-KLVIIAG-NH_2’ (*pep-KG*) and ‘Ac-RLVIIAG-NH_2’ (*pep-RG*), maintaining both the cationic N-termini for solubility and a small C-terminal residue to create space in the laminate groove [41], were selected for further analyses. The laminate groove is explained in greater detail in Chapter 2.

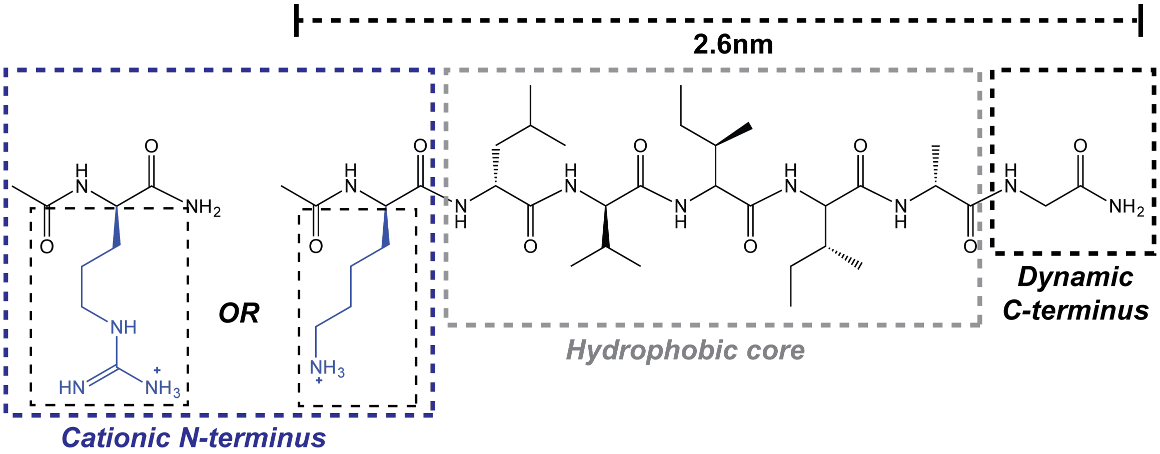

Figure 4-7 Primary sequence of Ac-KLVIIAG-NH_2 (pep-KG) and Ac-RLVIIAG-NH_2 (pep-RG). *Length of extended peptide shown as 2.6nm.*

Initial examination of *pep-KG and pep-RG* showed that both peptides form assemblies with characteristic β-sheet molar ellipticities and infrared transitions (Figure 4-8). A more negative molar ellipticity for *pep-KG* than *pep-RG*, suggests the presence of more beta-sheet-rich assemblies. Fourier Transform Infrared (FT-IR) spectroscopy supports this supposition. Absorbance of *pep-RG* at 1670cm^{-1} is indicative of disordered peptide aggregates and free peptide monomers. It is unclear from the FT-IR spectra whether peptide assemblies are anti-parallel or parallel because the remaining monomer pool has reduced the resolution of peaks at ~1695cm-1. The Amide I stretch is the strongest peptide signal by FT-IR and corresponds to the C=O stretching frequency of the backbone carbonyl. Several peaks can be observed between 1600 and 1700cm-1 for full-length proteins with multiple secondary structures. For amyloid assemblies, β-sheet amide I stretching is observed at ~1625cm-1. When an amyloid assembly contains anti-parallel beta-strands, a second peak may be present at ~1695cm-1. In anti-parallel beta-sheets, the C=O of the peptide backbone experiences two distinct environments. These environments affect its stretching frequency leading to the appearance of a small secondary peak.

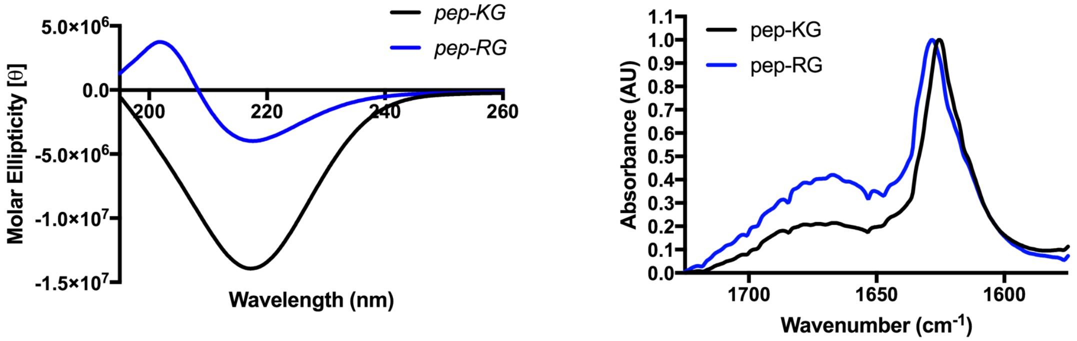

Figure 4-8 Pep-KG and pep-RG form assemblies with characteristic beta-sheet signatures. *CD reveals minima at 218nm. By FT-IR, the amide I stretch is ~1625*cm^{-1}*.*

Both *pep-KG* and *pep-RG* form fibers (Figure 4-9) with mean widths of ~4nm. These results are most consistent with peptide bilayers [49,50]. However, bundling of *pep-KG* fibers as twisted dimers and trimers shifts the mean fiber width to ~8.7nm (Figure 4-10). *Pep-RG* assemblies bundle more extensively making large scale measurements difficult. Co-assembly of *pep-KG* or *pep-RG* with RNA yields homogeneous ribbons at 4°C (Figure 4-9c/d). The inset in Figure 4-9c highlights the finer multi-lamellar architecture of the ribbon wall. This remarkable morphological change is highly reproducible and robust with maintenance of the assembly observed following several freeze-thaw cycles.

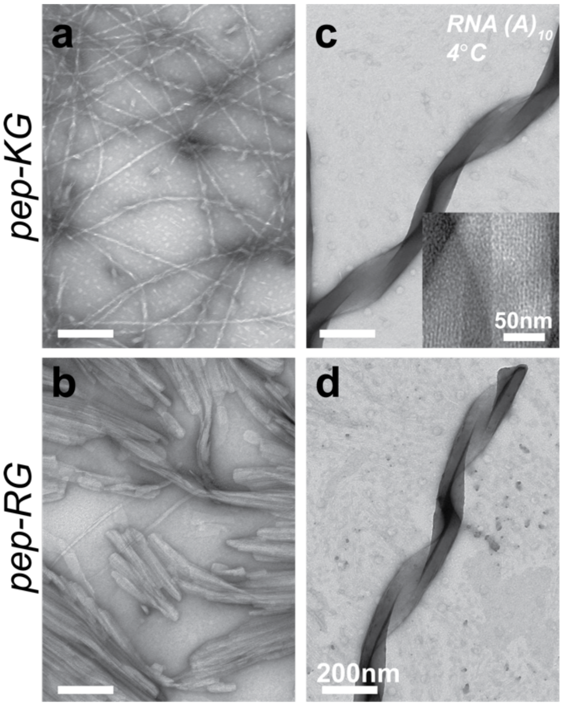

Figure 4-9 Assembly of pep-KG and pep-RG with and without RNA. *(a/b) Pep-Kg and pep-RG self-assemblies in 40% acetonitrile, 60% water. (c/d) Co-assembly of pep-KG or pep-RG with RNA in 40% acetonitrile and 60% water. Inset highlights multi-lamellar wall architecture. Scale bars are 200nm, unless otherwise noted.*

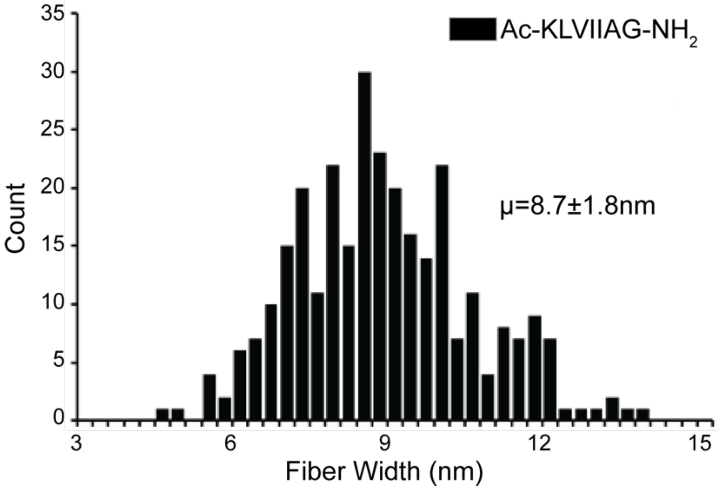

Figure 4-10 Pep-KG fiber width measurements. *Measurements taken perpendicular to the long-axis of the fiber using ImageJ. μ=mean+/-standard deviation.*

Particle formation in RNA/peptide nanostructure assembly

When co-assembled with RNA at 4°C, the assembly proceeds through an initial particle phase, much like mRNP granules (Figure 4-11). Particles in peptide assemblies are essential. Much like protein folding landscapes, amyloid-forming peptides undergo hydrophobic collapse before organized assembly propagates and the lowest energy well is accessed. Hydrophobic collapse results in the concentration of peptides in mostly-spherical particles where energetics produce nucleation events that drive peptide propagation as amyloid nanostructures.

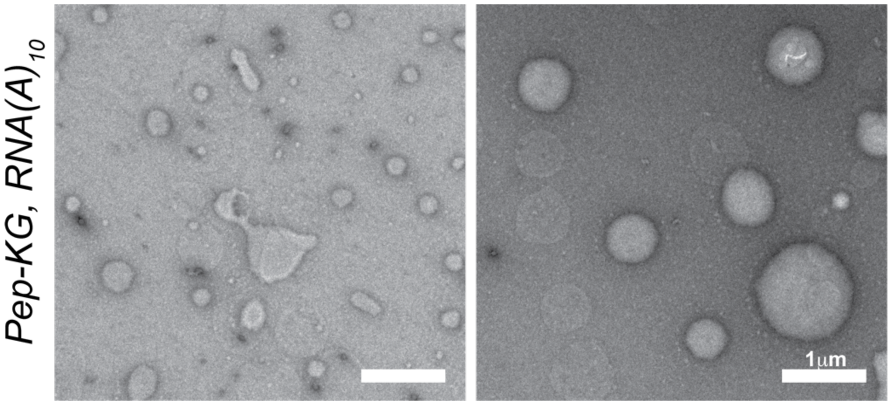

Figure 4-11 Particle phase of **RNA/*pep-KG co-assemblies.*** *TEM analysis of the particle phase at 5 minutes of co-assembly. Both scale bars are 1μm.*

RNA/*Pep-KG* particles mature as ThioflavinT-positive amyloid particles grow and fuse with RNA particles (Figure 4-12). Thioflavin T bound by amyloid has maximum emission at 488nm. The emission of Thioflavin T in particles suggests amyloid formation begins early and independent of RNA. Fusion with RNA-only particles results in the co-localization of fluorophores and, presumably, the co-assembly of the two biopolymers.

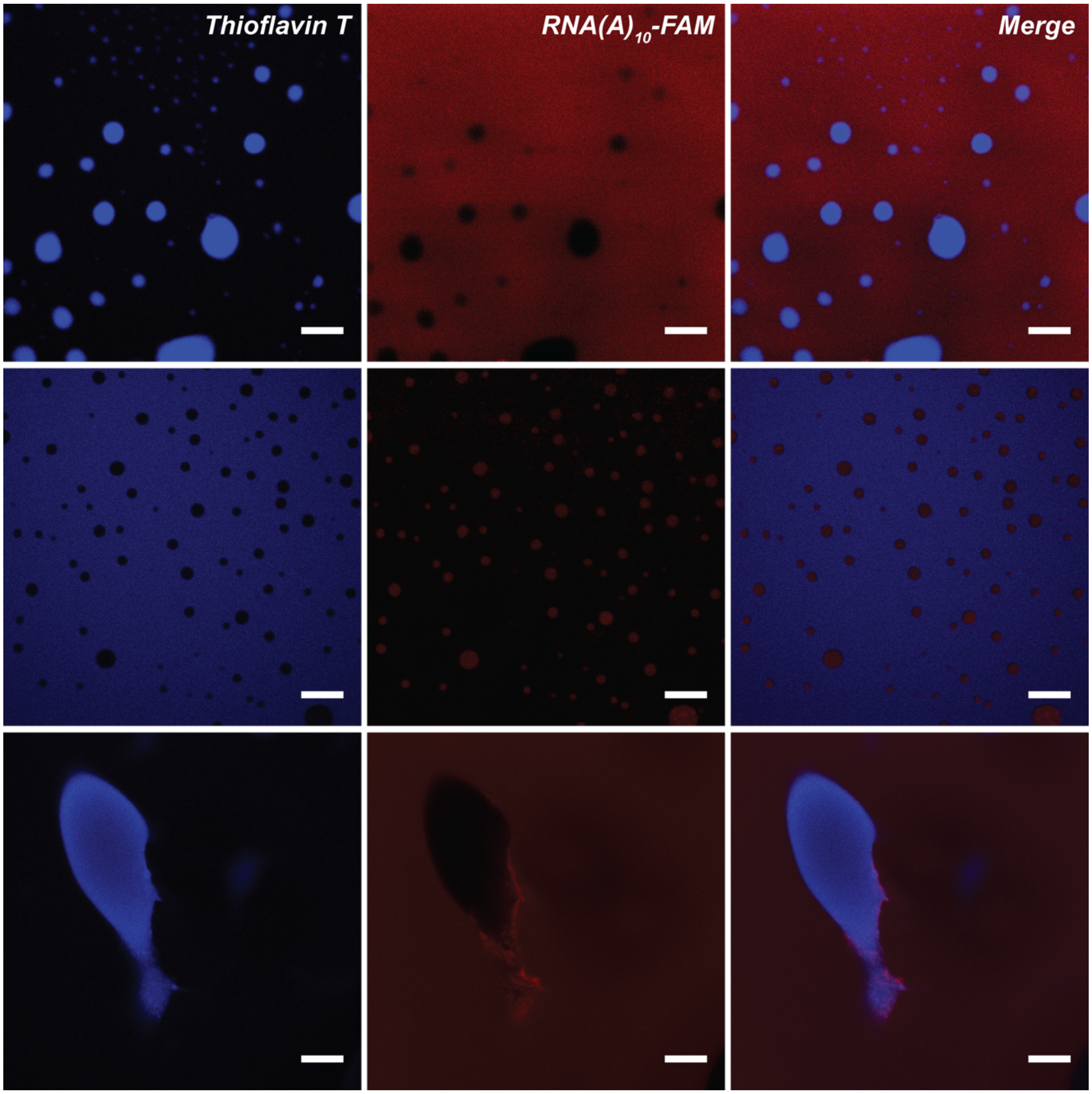

Figure 4-12 RNA/pep-KG particle phase monitored by laser scanning confocal microscopy at 30 minutes post-co-assembly. *First row: Thioflavin T-positive particles. Second row: FAM-positive particles. Third row: Fusion of Thioflavin T- and FAM-positive particles. Scale bars are 10μm.*

Cooperative binding of nucleic acids to peptide assemblies

Nucleic acids are necessary for the nucleation and propagation of ribbonous co-assemblies, with each occurring independent of polynucleotide length. While at least 6 nucleotides are required (Figure 4-13), either DNA or RNA are sufficient to produce ribbons and DNA strands up to 7,560 nucleotides maintain a ribbonous co-assembly (Figure 4-14). This independence of chain length suggests that diverse nucleic acid packing arrangements are accommodated within these homogeneous co-assemblies. DNA below six nucleotides is not sufficient to produce multi-lamellar ribbons. Instead, thin-walled nanotubes are observed, similar to those observed for *pep-KG* and *pep-RG* in the presence of salt alone (Figure 4-15). This length-dependence suggests a cooperative component to nucleic acid binding that nucleic acids less than six nucleotides cannot fulfill.

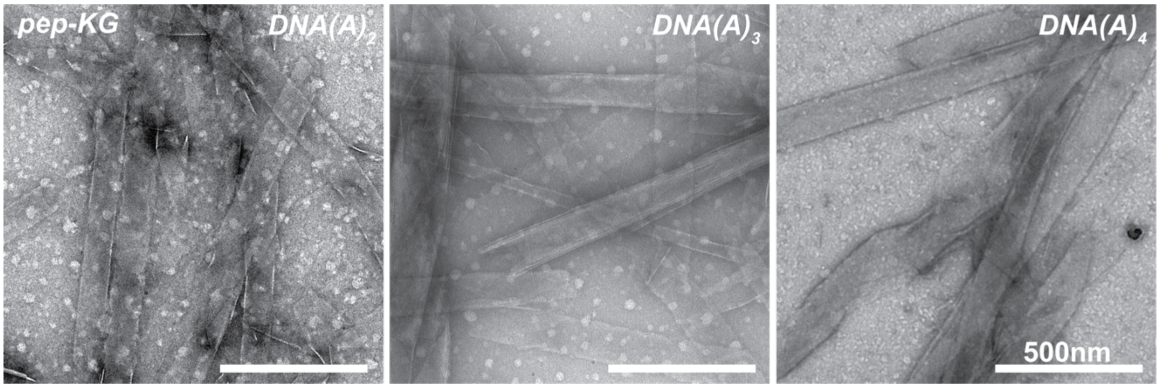

Figure 4-13 Co-assembly of pep-KG with DNA(A)$_2$, DNA(A)$_3$, or DNA(A)$_4$ by TEM.

Scale bars are all 500nm.

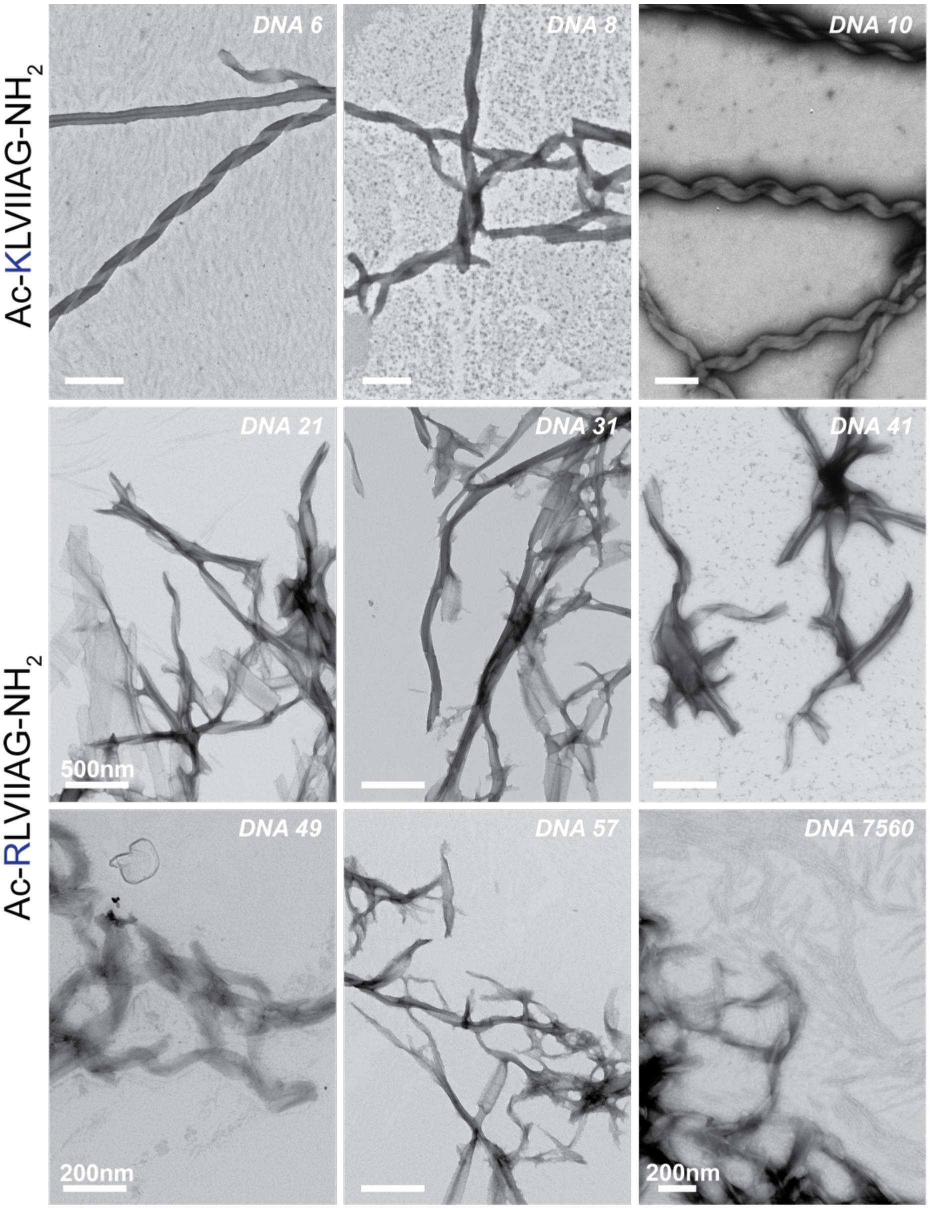

Figure 4-14 Co-assembly of pep-KG or pep-RG with varying lengths of single stranded DNA. *Length of incorporated DNA is in the top right corner of each micrograph. Scale bars are 500nm unless otherwise noted.*

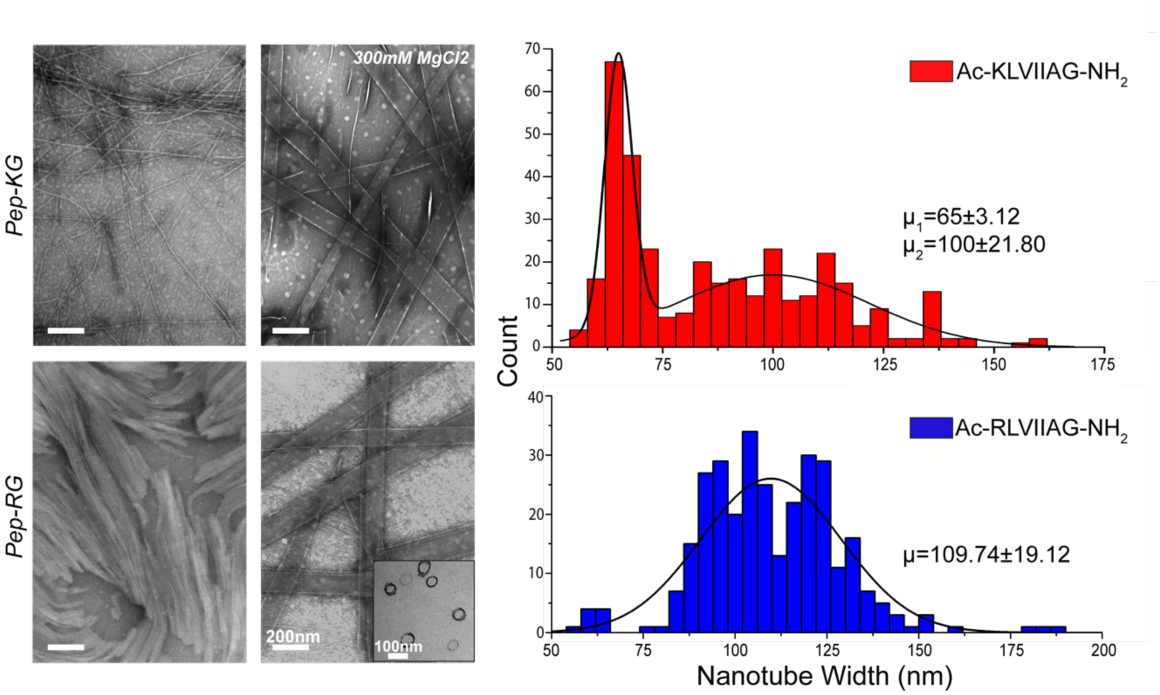

Figure 4-15 Assembly of pep-KG and pep-RG with and without MgCl2. *First column of transmission electron micrographs depicts peptide-alone assembly. Second column depicts assembly of pep-KG and pep-RG in the presence of 300mM MgCl2. Inset features cross-sections of nanotubes. Nanotube width values are taken from TEM and measured using ImageJ. μ=mean +/- standard deviation.*

Temperature affects global co-assembly architecture

Remarkably, both *pep-KG* and *pep-RG* co-assemblies transition into well-defined multi-lamellar nanotubes with mean diameters of ~205 nm at 37°C (Figure 4-16 and 4-17). The insets in Figure 4-16a/b feature cross-sections of the nanotubes taken perpendicular to the tube long-axis. It is from these cross-sections that diameter measurements were carefully made. From the cross-sections of these co-assemblies at 37°C, maintenance of the multi-lamellar wall phenotype is also observed. Longitudinal cross-sections shown in Figure 4-16c/d reveal a narrow interior and thick, layered tube walls. The temperature dependence to RNA/Peptide co-assembly maturation suggests the ribbons arrested at

4°C are intermediates in the assembly pathway. An increase in temperature to 37°C is necessary for the transition to symmetrical nanotubes.

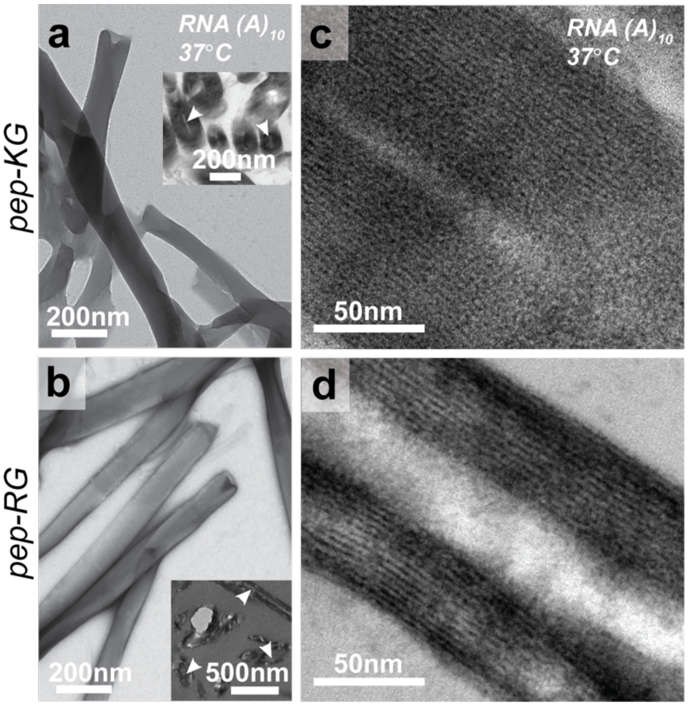

Figure 4-16 Pep-KG and pep-RG co-assembly with RNA(A)$_{10}$ at 37℃ yields symmetrical nanotubes. *(a/b) Co-assembly of pep-KG and pep-RG with RNA(A)$_{10}$ at 37℃. Insets feature cross-sections of nanotubes. White arrowheads point to hollow nanotube interior. (c/d) Longitudinal cross-sections of nanotubes; white interior and dark multi-lamellar walls are apparent. Scale bars are as noted.*

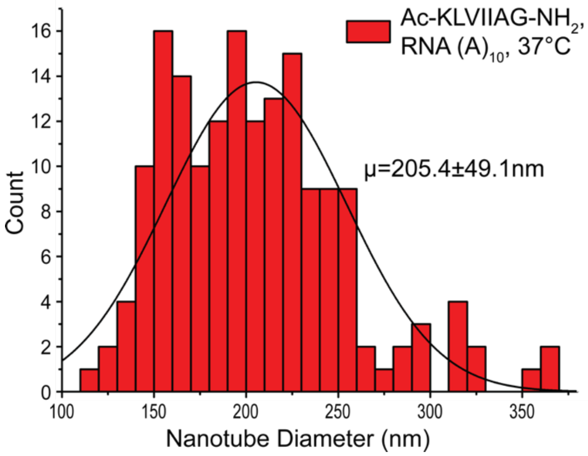

Figure 4-17 Nanotube diameter measurements taken from pep-KG/RNA nanotube cross-sections at 37°C. *Measurements made in ImageJ. μ=mean+/-standard deviation.*

In Figure 4-18, measurements taken from individual lamella of the multi-lamellar walls of these nanotubes reveal repeating widths of 2.4±0.3nm and 2.5±0.3nm for *pep-KG* and *pep-RG*, respectively. This spacing distance is the same as the extended peptide length of 2.6 nm (Figure 4-7), and consistent with a single β-sheet peptide monolayer defining each lamella.

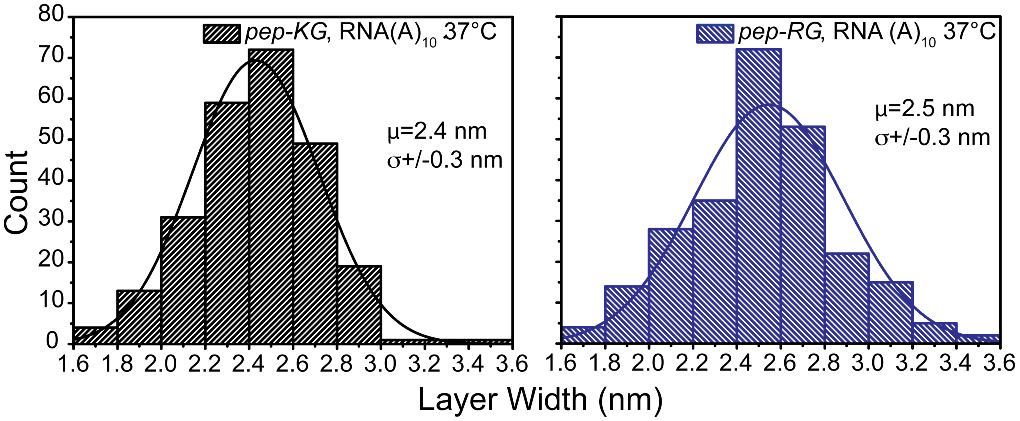

Figure 4-18 Individual lamella width taken from longitudinal cross-sections of pep-KG/RNA and pep-RG/RNA co-assemblies at 37°C. *Measurements made using ImageJ. μ= mean σ =standard deviation.*

A cartoon depiction summarizing the conditions sampled for *pep*-KG and *pep-RG* with and without RNA is shown in Figure 4-19.

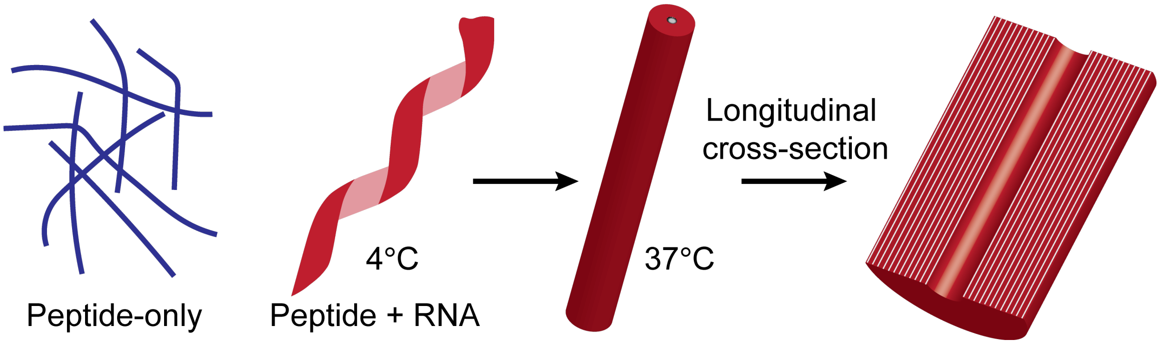

Figure 4-19 Summary of the morphological transitions and depictions of pep-KG and pep-RG assemblies with and without RNA.

Microscopy confirms co-assembly

To confirm co-assembly and begin to examine the position of the RNA, constructs prepared with Cy3 bound to the 3'-end of RNA$(A)_{10}$ were co-assembled with *pep-KG* or *pep-RG* and co-stained with the amyloid-specific dye ThioflavinT (ThT). Both RNA/*pep-KG* and RNA/*pep-RG* co-assemblies show co-localization of ThT and Cy3 signals (Figure 4-20). Aggregation of ribbons at 4°C is common. Therefore, clustering of ThT and Cy3 fluorophores is expected. The co-localization of ThT and Cy3 supports the co-assembly of RNA and peptide in the observed nanostructures.

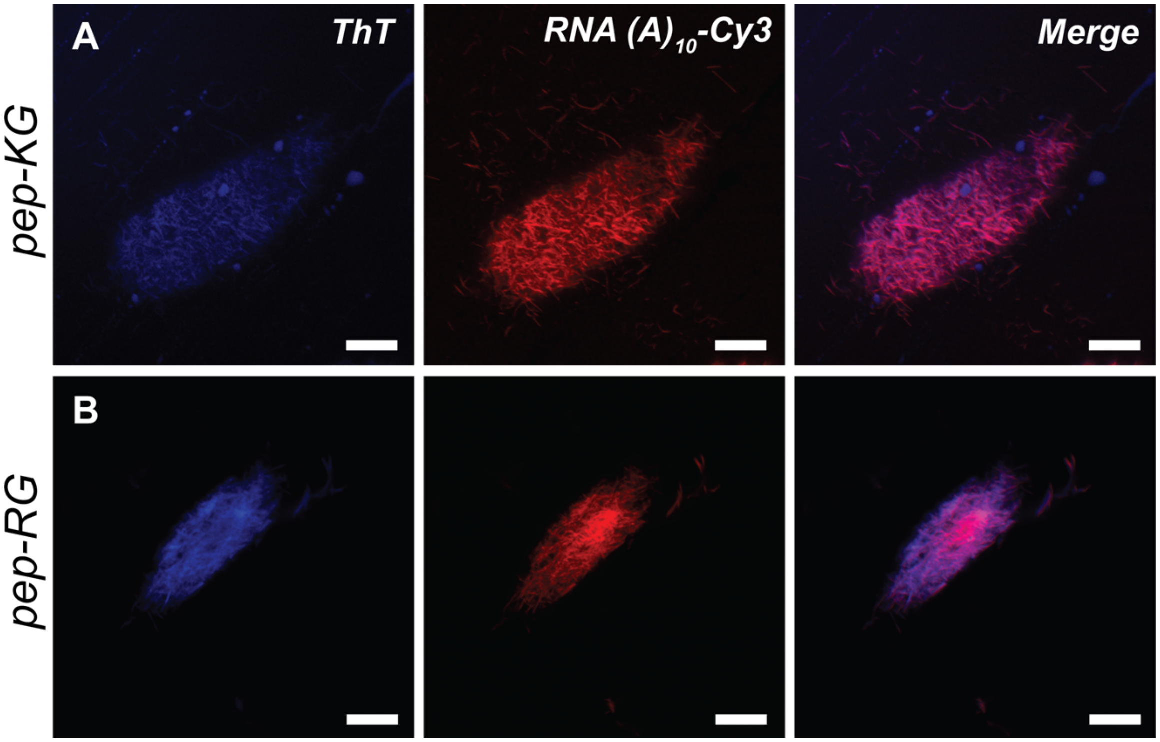

Figure 4-20 RNA/Pep-KG and RNA/pep-RG co-assemblies examined by laser scanning confocal microscopy. *Pep-KG and pep-RG co-assembled with RNA(A)$_{10}$-Cy3 were co-stained with Thioflavin T (ThT). Merge indicates combination of ThT and Cy3 fields. Cy3 covalently attached to the 3'-end of RNA(A)$_{10}$.*

Surface mapping of the ribbons with electrostatic force microscopy (EFM) further confirms the presence of RNA on the external surfaces of the assemblies (Figure 4-21). For EFM amplitude, negatively-charged regions are dark. The low resolution of images makes resolving ribbon internal surfaces difficult. However, a predominantly negative external surface is apparent. Since the peptides themselves are positively charged, a negative surface charge is only possible if RNA is coating the peptide assembly.

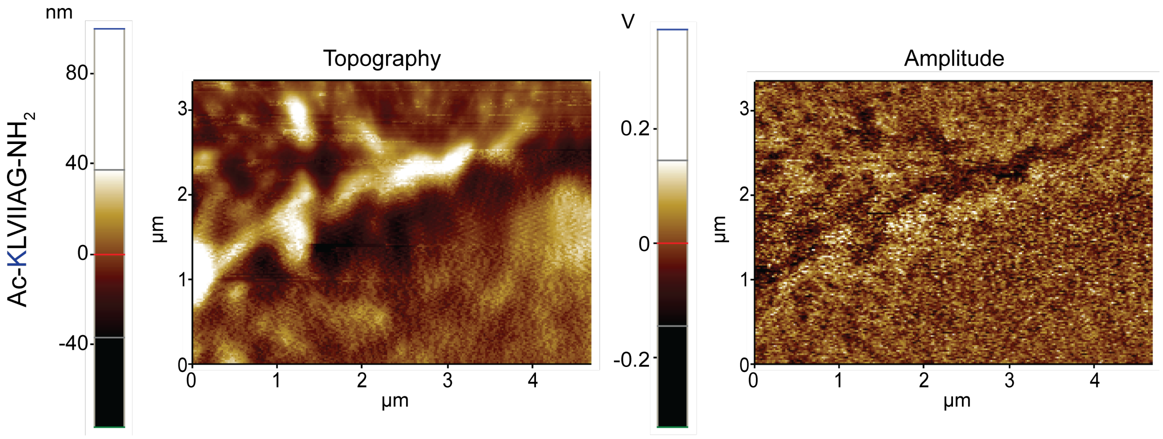

Figure 4-21 Single RNA/pep-KG ribbon examined by AFM and EFM. *Topography indicates normal AFM mode; Van der Waals interactions. Amplitude indicates EFM mode; electrostatic interactions.*

Evaluating the electrostatic contribution to RNA/peptide co-assembly

Since it has now been established that RNA and *pep-KG* or *pep-RG* co-assemble, understanding the forces that dictate co-assembly will provide insight to the assembly landscape and information for the development of more comprehensive models depicting amyloid/RNA dynamics in protein-misfolding diseases.

When assembled with excess $MgCl_2$, RNA/peptide co-assembly nanotube widths are reduced to ~100nm, and contain fewer lamellae (Figure 4-22). The decrease in lamellae is highlighted in the insets of Figure 4-22. From TEM, it would appear the salt out-competes the RNA during assembly. Transmission electron micrographs appear similar to those of *pep-KG* or *pep-RG* with $MgCl_2$ alone (Figure 4-15).

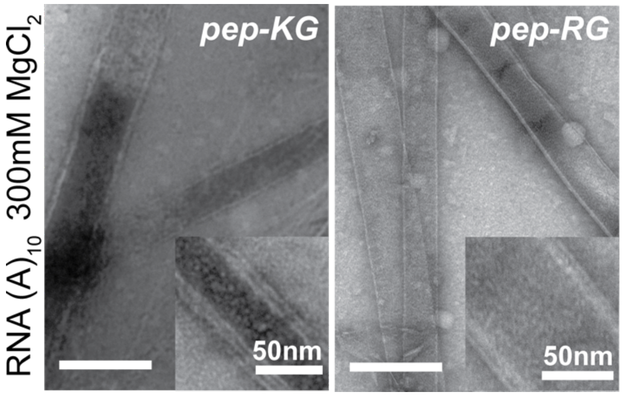

Figure 4-22 Pep-KG and Pep-RG assembled with RNA(A)$_{10}$ and MgCl$_2$ to modulate electrostatics. *Excess MgCl$_2$ (300mM) is added to RNA and peptide at the time of assembly. Insets feature nanotubes with fewer lamellae. Scale bars are 200nm unless otherwise noted.*

Despite appearance of loss of co-assembly by TEM, some lamellae remain and laser scanning confocal fluorescence microscopy provides a clearer look at the localization of the biopolymers. While the electrostatics appear to be modulated by the Mg^{+2}, the overall assembly is retained and the RNA remains co-localized with the peptide assembly (Figure 4-23); Thioflavin T and Cy3 co-localization indicate the maintenance of RNA/peptide co-assembly even in the presence of excess MgCl$_2$. With high MgCl$_2$ concentration, the nucleic acid and peptides co-assemble as thinner-walled nanotubes of heterogeneous widths containing fewer lamellae. A similar result is obtained with nucleic acid oligomers containing fewer than six nucleotides, supporting a strand length threshold for cooperative assembly (Figure 4-13).

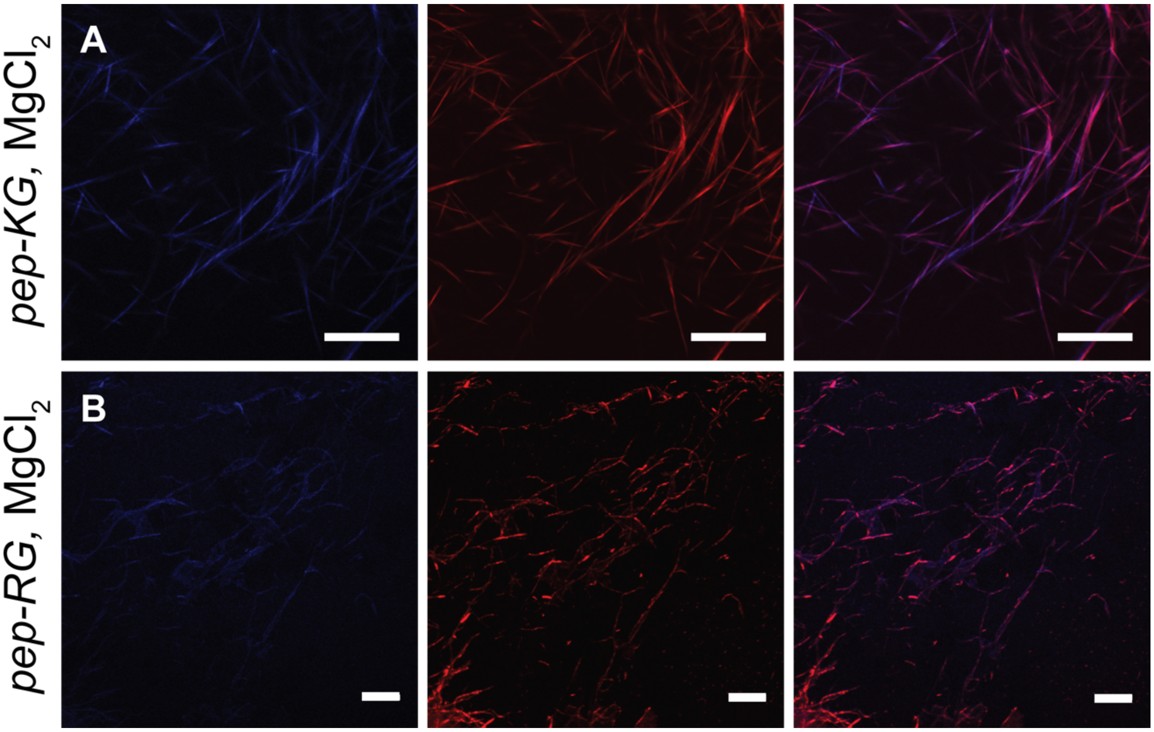

Figure 4-23 Examination of pep-KG and pep-RG assemblies in the presence of $MgCl_2$ and RNA. *Co-localization of Thioflavin T (first column) and Cy3 (second column) is shown in the third column.*

Electrostatics were examined further through the complete removal of the positive charge from the peptide. Removal of the positive charge was achieved with Ac-ELVIIAG-NH_2 (*pep-EG*), which assembles under these conditions as bundled fibers (Figure 4-24). The presence of DNA at 4°C has little influence on the assembled morphology, and there is no evidence for co-localization of peptide and nucleic acid fields by laser scanning confocal microscopy (Figure 4-25). Despite eliminating electrostatic interactions between N-terminal peptide residues and the phosphate backbone of RNA/DNA, if other interactions existed within co-assemblies they would be maintained in DNA/*pep-EG* or RNA/*pep-EG* co-assemblies. Because of the complete loss of fluorophore co-localization observed, electrostatic interactions likely contribute the most to the nucleation and propagation of RNA/peptide co-assemblies.

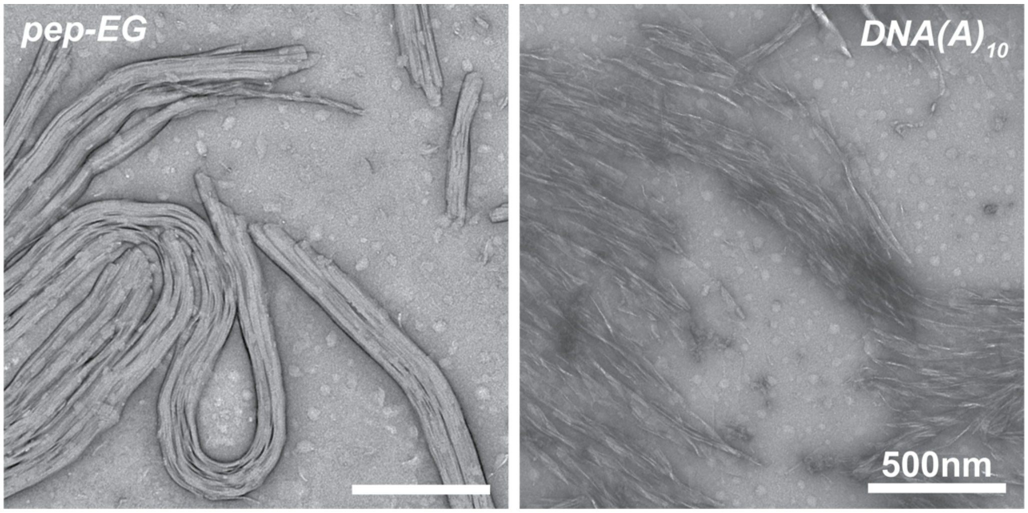

Figure 4-24 Assembly of pep-EG with and without DNA(A)$_{10}$. *Transmission electron micrographs of pep-EG assembly with (right) and without (left) DNA(A)$_{10}$. Scale bars are 500nm.*

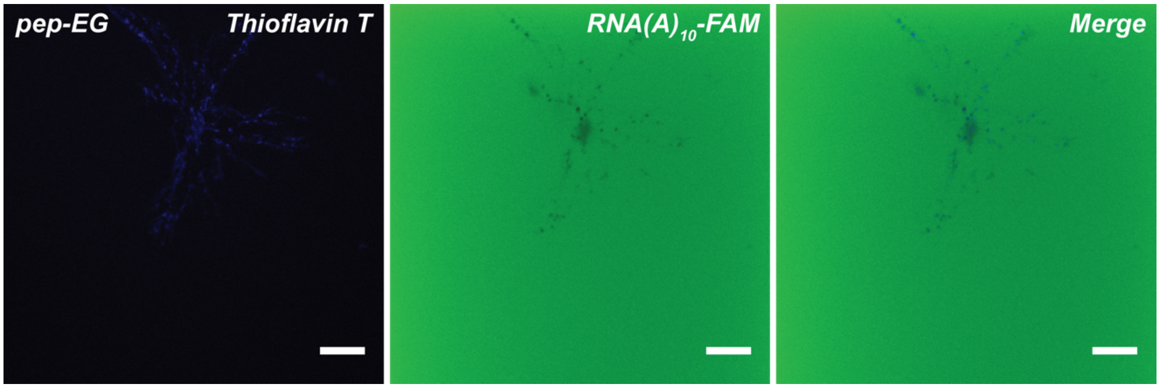

Figure 4-25 Laser-scanning confocal microscopy of RNA/pep-EG co-assemblies. *FAM is covalently attached at the 3'-end of RNA(A)$_{10}$. The merge of Thioflavin T and FAM is shown in the third panel (right). Scale bars are 10μm.*

To determine the importance of phosphate periodicity on co-assembly, a linear polyphosphate with approximately 50 phosphates was prepared and shown to reconstitute the multi-lamellar co-assembly morphologies achieved with RNA (Figure 4-26). These results further highlight the positional plasticity of the RNA/peptide interface. Not only can nucleic acid oligomers from six to 7,560 nucleotides be accommodated, but polyphosphates, which are the same only in anion can also recapitulate co-assembly morphology.

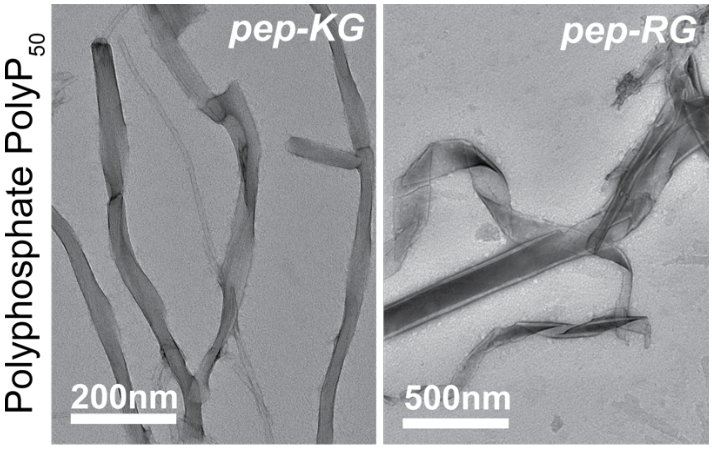

Figure 4-26 Co-assembly of pep-KG and pep-RG with PolyP$_{50}$ recapitulates multi-lamellar morphology. *TEM examination of pep-KG and pep-RG co-assembled with polyphosphate PolyP$_{50}$. Scale bars are as shown.*

RNA/peptide co-assemblies remain dynamic

As with the mRNP granules, these paracrystalline assemblies remain dynamic. Melting of the *pep-KG* fibers, determined by loss of peptide negative ellipticity at 220nm, gives a T_m of 38°C, while the T_m of the DNA co-assemblies, determined by the hyperchromic shift of the positive ellipticity of the nucleic acid bases at 260nm, is 42°C (Figure 4-27). Although this crystalline phase likely contributes to the pathology of many, if not all, protein-misfolding diseases, the co-assemblies remain dynamic. This makes possible the development of therapeutics and other interventions for amyloid dispersal.

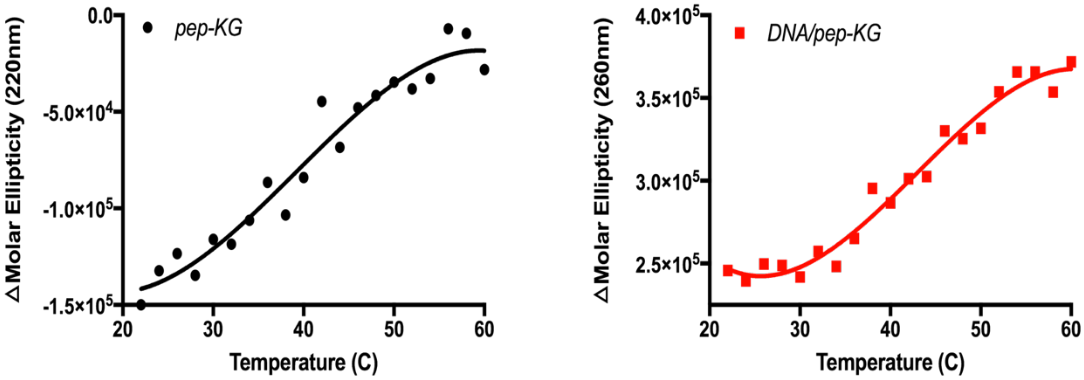

Figure 4-27 Melting temperature of pep-KG and DNA/pep-KG assemblies. *Circular Dichroism used to assess* T_m *of pep-KG and DNA/pep-KG assemblies. For pep-KG assemblies, loss of ellipticity at 220nm was monitored from 20°C to 60°C. For DNA/pep-KG co-assemblies, the hyperchromic shift at 260nm was monitored from 20°C to 60°C.*

Sensitivity to nucleases represents another mechanism of dynamic control in nucleic acid processing. A 30-minute exposure to RNase_{If} at room temperature resulted in disassembly of the RNA/*pep-KG* nanostructures by TEM, and urea-PAGE confirmed the hydrolysis of the incorporated RNA (Figure 4-28). Loss of co-assembly in the presence of nucleases confirms the essential role of nucleic acid in co-assembly maintenance, and highlights the accessibility of the incorporated nucleic acid to the external environment. The co-assembly's sensitivity to nucleases provides context for a feedback mechanism describing assembly and disassembly, and how the two processes can be intimately regulated in the cell.

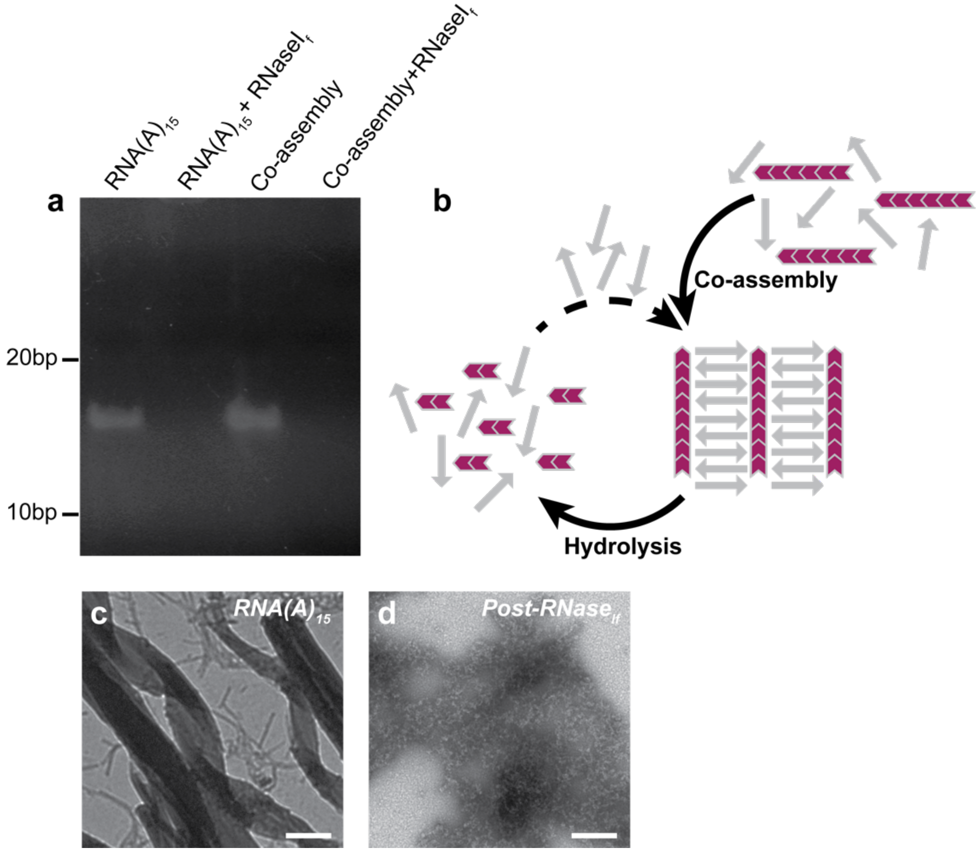

Figure 4-28 RNA/Pep-KG co-assemblies are sensitive to nuclease digestion. *(a) Urea-PAGE analysis of RNaseI$_f$ digest. Lane 1, RNA(A)$_{15}$ control; Lane 2, RNA(A)$_{15}$ after 30 minute RNaseI$_f$ digestion; Lane 3, Co-assembly before digestion; Lane 4, Co-assembly RNA(A)$_{15}$ after 30 minute RNaseI$_f$ digestion. (b) Feedback mechanism describing pathways for co-assembly and disassembly. (c,d) RNA/Pep-KG co-assembly before and after RNaseI$_f$ digestion. Scale bars are 200nm.*

Co-assembly of dsDNA and *pepKG/RG*

Not only are co-assemblies capable of accommodating short and long strands of primarily single stranded nucleic acids and responsiveness to their environment, incorporation of double-stranded DNA (dsDNA) also recapitulates co-assembly architecture. Unlike single-stranded DNA and RNA at 4°C, co-assembly of *pep-KG* or *pep-RG* with dsDNA at 4°C leads to the prevalence of thick-walled nanotubes. By TEM, thick-walled nanotubes are abundant. The rigidity and periodicity of organized dsDNA may influence assembly energetics and bias the system towards nanotube formation.

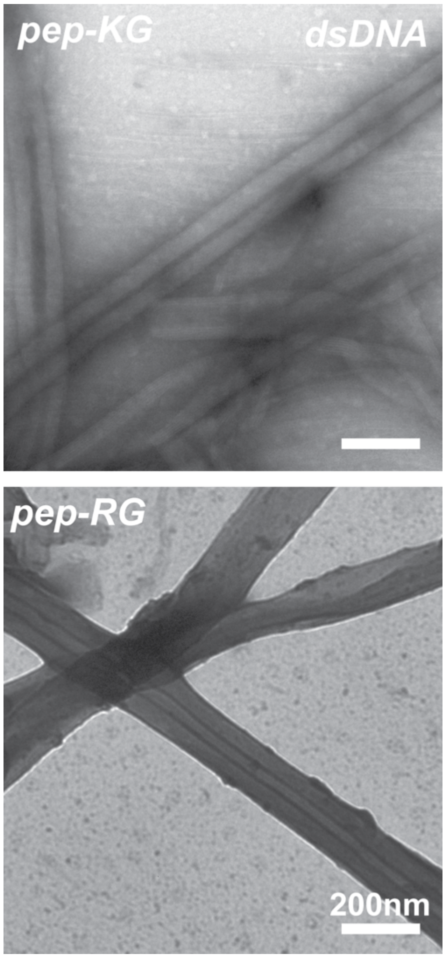

Figure 4-29 Pep-KG and pep-RG co-assembly with dsDNA(AT)$_{10}$. *TEM analysis of dsDNA/Peptide co-assemblies. Scale bars are 200nm.*

Co-assembly of dsDNA and *pep-KG* or *pep-RG* was characterized as before. Amyloid-specific, Thioflavin T was used as a marker of peptide assembly, while Cy3 covalently attached to the 3’-end of one strand of dsDNA was used to monitor dsDNA localization. Co-localization of the two signals provided support for the co-assembly of dsDNA and peptides.

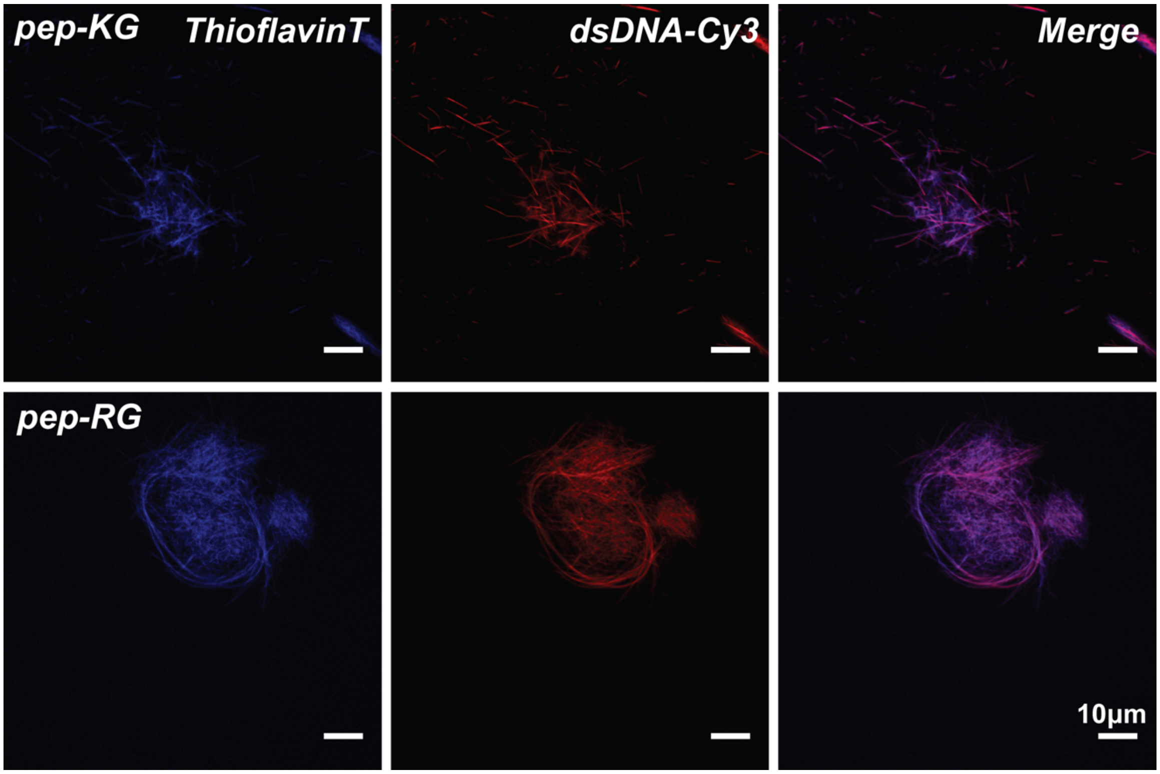

Figure 4-30 Laser-scanning confocal fluorescence microscopy of dsDNA/peptide co-assemblies. *Thioflavin T, first column. Cy3, second column. Merge of the two fluorophores, third column. All scale bars are 10μm.*

Conclusions

Our models for the transient and dynamic interception of mRNP granules, by high-propensity amyloid-forming domains, expands our understanding of protein-misfolding disease etiology. Within this chapter we designed and globally characterized the co-assembly architecture of RNA/peptide nanostructures. At 4°C, the co-assembly of RNA and peptide was arrested at homogeneous ribbons. By increasing the temperature to 37°C further assembly is permitted and the transition to symmetrical nanotubes observed. In these systems, ribbons appear to represent an intermediate along the assembly pathway. Through perturbation of intermolecular interactions, electrostatics were shown to be the primary contributor of RNA/peptide co-assembly maintenance. With high $MgCl_2$ concentration, the nucleic acid and peptides co-assemble as thinner-walled nanotubes of heterogeneous widths containing fewer lamellae. With a similar morphology observed for peptides co-assembled with nucleic acids less than six nucleotides in length, a strand threshold for cooperative assembly was established.

Even these highly ordered paracrystalline co-assemblies remain remarkably responsive to enzymatic digestion and environmental perturbations, consistent with the reversible associations necessary for RNA processing [1,2,6,7,31]. Through further exploration of the co-assemblies characterized here, elucidation of the exact mechanism that drives crystalline phase transitions in mRNP granules and their impact on RNA processing may be possible [51-54]. For example, altered ribostasis [18] has been offered as a mechanism for degenerative disease etiology. Particularly in neurons, where long-range RNA transfers are critical, cellular dysfunction and autophagy may be particularly sensitive to changes in information management [21,55].

Methods

Peptide Synthesis. Peptides were synthesized using Solid Phase Peptide Synthesis (SPPS) with a Rink-Amide MBHA resin, 0.4mmol/g substitution, and capped at the N-terminus with an acetyl group. Peptides were cleaved and deprotected using a cocktail of 90% TFA, 2% anisole, 3% 1,2-ethanedithiol, and 5% thioanisole. All chemicals were purchased from Sigma-Aldrich. Following cleavage and deprotection, peptides were purified by reverse-phase HPLC using acetonitrile and water with 0.1%TFA and a C18 column to a >98% purity. After purification, acetonitrile was removed by rotavaporation. The remaining aqueous solution was frozen at -80°C or flash frozen using liquid nitrogen and lyophilized to yield a white powder.

Peptide Assembly. Due to the salt sensitivity of peptides used in this study, following purification and lyophilization, peptides were desalted using Sep-Pak® C18 cartridges. Peptides were then placed in 40% Acetonitrile, vortexed briefly and sonicated for 5 minutes to promote solubility. The pH was not adjusted; each sample was examined at pH5. A stock solution of 2mM peptide was used to set up all assemblies. Experimental samples were set up within five minutes of dissolution. All nucleic acid oligomers were purchased from Integrated DNA Technologies. For NA/Peptide co-assemblies, a stock solution of 1mM NA was used. Order of addition was as follows: Peptide, solvent, nucleic acid. Assemblies were kept at 4°C unless otherwise noted. For the NA/Peptide samples at 37°C, the order of addition was identical. Final peptide concentration in all experimental setups was 1mM. Final nucleic acid concentration depended on length. All co-assemblies were established with a 1:1 (peptide: nucleic acid) charge ratio.

Electron Microscopy. Electron microscopy images were obtained using a Hitachi H-7500 and a Jeoul transmission electron microscope. All samples were placed on 200 mesh copper grids with carbon coating and negatively stained using 2%w/w uranyl acetate (Sigma-Aldrich). The microscope was operated at 75kV. Cross-section images were obtained by embedding pelleted assemblies in resin. Using a microtome, embedded assemblies were sliced 1μm thick and placed on grids for analysis by TEM.

Laser Scanning Confocal Microscopy. Fluorescence micrographs were obtained using an Olympus FluoView 1000 (FV1000) laser-scanning confocal microscope. Samples were prepared on microscope slides, with coverslips sealed using clear nail polish. Samples were examined using the 60X 1.42NA oil immersion objective. Thioflavin T was added to samples at a final concentration of 2mM prior to sample prep and the 405nm laser line was used to visualize its staining. The RNA$(A)_{10}$ with Cy3 or

FAM covalently attached at the 3'-end was purchased from Integrated DNA Technologies. The 488nm or 559nm laser line was used to visualize FAM and Cy3 signals, repsectively. Images for Thioflavin T and FAM or Cy3 fields were obtained concurrently and processed using Fiji [56].

Circular Dichroism (CD). A Jasco-810 Spectropolarimeter was used to record CD spectra. Samples were examined at room temperature in a 50µL cell with a 0.1mm path length. The reported spectra were acquired from 260nm to 190nm with a step size of 0.2nm and a speed of 100nm/s, and are the average of three independent scans. Ellipticity, in mdeg, was converted to Molar ellipticity (θ) with $[\theta] = \theta/(10 \times c \times l)$, where 'c' is peptide concentration in moles/L and '*l*' is the pathlength in cm. Melting curves of *pep-KG* and NA/*pep-KG* samples were obtained using a gradient of temperature from 4°-60°C and a focal wavelength of 220nm and 260nm, respectively.

Fourier Transform Infrared (FT-IR) Spectroscopy. FT-IR spectra were acquired using a Jasco FT-IR 4100 (Easton, MD, USA) averaging 750 scans at 2cm^{-1} resolution. For each sample, 8µl of peptide solution was dried as a thin film on a Pike GaldiATR (Madison, WI, USA) ATR diamond surface. The MCT-M detector, having a 5mm aperture and a scanning speed of 4mm/sec was used. Samples were normalized to the amide I stretch at ~1625cm^{-1}.

Electrostatic Force Microscopy. A Park System XE-100 AFM was used to carry out EFM measurements. With a charge bias of +1V applied between the cantilever and the sample, an electrostatic field was created allowing for the surveying of charge upon the assembly surface. Pt-Ir coated cantilevers that are electrically conductive were used in non-contact mode to map electrical properties on the sample surface. The cantilever tip radius was <20nm and had a force constant of 2.8 N/m. Prior to EFM imaging, the NA/Peptide samples were deposited on gold film, Si/SiO_2 substrates. The thickness of the oxide layer was 300nm. The co-assemblies were deposited as 10 µL droplets suspended in acetonitrile and water. Samples were dried over 12 hours before examination. The topography (AFM) and amplitude (EFM) were obtained.

Polyphosphate Synthesis. Polyphosphate ($PolyP_{50}$) was synthesized according to the literature. KH_2PO_4 was melted 450^o for 4 hours and the resulting glass purified by stepwise precipitations in Acetone-Water mixtures [57]. The length was determined from ^{31}P NMR peak integration [58].

$RNAse_{If}$ Assay. NA/*pep-KG* co-assemblies with RNA(A)15 incorporated were exposed to $RNAse_{If}$, a non-specific ssRNA nuclease. 500 units RNAseIf was combined with NA/*pep-KG* co-assembly containing 1nmol $RNA(A)_{15}$ and a $RNA(A)_{15}$ control for 30minutes with 1XNEB Buffer. NA/*pep-KG* without $RNAse_{If}$ and $RNA(A)_{15}$ without $RNAse_{If}$ were also included as controls. After 30 minutes, all four samples were loaded onto a 1mm UREA-PAGE gel and run for 90 minutes at constant 100V. A 10bp ladder was used. The gel was removed from the gel box after 90 minutes and stained for 20 minutes using a 1X solution of SYBR Gold in TBE. A BIO-RAD gel imager was used and Quantity One was used to visualize the gel.

References

[1] Erickson, S. L., Lykke-Andersen, J. Cytoplasmic mRNP granules at a glance. *J. Cell Sci.* **124,** 293-297 (2011).

[2] Castilla-Llorente, V., Ramos, A. PolyQ-mediated regulation of mRNA granules assembly, *Biochem. Soc. Trans.* **42,** 1246-1250 (2014).

[3] Kato, M. *et al*. Cell-free formation of RNA granules: low complexity sequence domains form dynamic fibers within hydrogels. *Cell* **149,** 753–767 (2012).

[4] Han, T. W. *et al.* Cell-free formation of RNA granules: bound RNAs identify features and components of cellular assemblies. *Cell* **149,** 768–779 (2012).

[5] Calabretta, S., Richard, S. Emerging roles of disordered sequences in RNA-binding proteins. *Trends Biochem. Sci.* **40,** 662-672 (2015).

[6] Aumiller Jr, W. M., Keating, C. D. Phosphorylation-mediated RNA/Peptide complex coacervation as a model for intracellular liquid organelles. *Nat. Chem.* **8,** 129-137 (2016).

[7] Hyman, A. A., Brangwynne, C. P. Beyond stereospecificity: liquids and mesoscale organization of cytoplasm. *Dev. Cell.* **21,** 14-16 (2011).

[8] Wilson, E. B. The structure of protoplasm. *Science* **10,** 33-45 (1899).

[9] Warner, J. R. The assembly of ribosomes in HeLa cells. *J. Mol. Biol.* **19,** 383-398 (1966).

[10] Feric, M. *et al.* Coexisting liquid phases underlie nucleolar subcompartments. *Cell* **165,** 1686-1697 (2016).

[11] Pederson, T. The plurifunctional nucleolus. *Nucleic Acids Res.* **26,** 3871-3876 (1998).

[12] Montgomery, T. S. Comparative cytological studies, with especial regard to the morphology of the nucleolus. *J. Morphol.* **15,** 265-582 (1898).

[13] Lim, L., Wei, Y., Lu, Y., Song, J. ALS-causing mutations significantly perturb the self-assembly and interaction with nucleic acid of the intrinsically disordered prion-Like domain of TDP-43. *PLOS Biology* **14,** (2016).

[14] Marcinkiewics, M. βAPP and Furin mRNA concentrates in immature senile plaques in the brain of Alzheimer patients. *J. Neuropathol. Exp. Neurol.* **61,** 815-829 (2002).

[15] Macedo, B. *et al.* Nonspecific prion protein-nucleic acid interactions lead to different aggregates and cytotoxic species. *Biochemistry* **51,** 5402-5413 (2012).

[16] Supattapone, S. What makes a prion infectious? *Science* **327,** 1091-1092 (2010).

[17] Geoghegan, J. C. *et al.* Selective incorporation of polyanionic molecules into hamster prions. *J. Biol. Chem.* **282,** 36341-36353 (2007).

[18] Ramaswami, M., Taylor, J. P., Parker, R. Altered ribostasis: RNA-protein granules in degenerative disorders. *Cell* **154,** 727-736 (2013).

[19] Ginsberg, S. D. *et al.* Predominance of neural mRNAs in individual Alzheimer's Disease senile plaques. *Ann. Neurol.* **45,** 174-181 (1999).

[20] Cherny, D., Hoyer, W., Subramaniam, V., Jovin, T. M. Double-stranded DNA

stimulates the fibrillation of α-Synuclein *in vitro* and is associated with the mature fibrils: an electron microscopy study, *J. Mol. Biol.* **344,** 929-938 (2004).

[21] Aguzzi, A., Altmeyer, M. Phase separation: linking cellular compartmentalization to disease. *Trends in Cell Biol.* **26,** 547-558 (2016).

[22] Schwartz, J. C., Wang, X., Podell, E. R., Cech, T. R. RNA seeds higher-order assembly of FUS protein. *Cell Rep.* **5,** 918-925 (2013).

[23] Cajal, S. R. Un sencillo metodo de coloracion seletiva del reticulo pro-toplasmatico y sus efectos en los diversos organos nerviosos de vertebrados e invertebrados. *Trab. Lab. Invest. Biol. Univ. Madrid* **2,**129-221 (1903).

[24] Kaiser, T. E., Intine, R. V., Dundr, M. De novo formation of a subnuclear body. *Science* **322,** 1713-1717 (2013).

[25] Giraldo, R. Defined DNA sequences promote the assembly of a bacterial protein into distinct amyloid nanostructures. *Proc. Natl. Acad. Sci. USA* **104,** 17388-17393 (2007).

[26] Wang, M., Law, M., Duhamel, J., Chen, P. Interaction of a self-assembling peptide with oligonucleotides: complexation and aggregation. *Biophys. J.* **93,** 2477-2490 (2007).

[27] Braun, S. *et al.* Amyloid-Associated Nucleic Acid Hybridisation, *PLoS one* **6,** e19125 (2011).

[28] Baltzinger, M., Sharma, K. K., Mély, Y., Altschuh, D. Dissecting the oligonucleotide binding properties of a disordered chaperone protein using surface plasmon resonance. *Nucleic Acids Res.* **41,** 10414-10425 (2013).

[29] Zaman, M. DNA induced aggregation of stem bromelain; a mechanistic insight. *Royal Soc. Chem. Adv.* **6,** 37591-37599 (2016).

[30] Shoeman, R. L., Hartig, R., Traub, P. Characterization of the nucleic acid binding region of the intermediate filament protein vimentin by fluorescence polarization. *Biochemistry* **38,** 16802-16809 (1999).

[31] Guo, L., Shorter, J. It's raining liquids: RNA tunes viscoelasticity and dynamics of membraneless organelles. *Mol. Cell* **60,** 189-192 (2015).

[32] Banani, S. F. *et al.* Compositional control of phase-separated cellular bodies. *Cell* **166,** 651-663 (2016).

[33] Hayes, M. H., Weeks, D. L. Amyloids assemble as part of recognizable structures during oogenesis in *Xenopus*. *Biol. Open* **5,** 801-806 (2016).

[34] Patel, A. *et al.* A liquid-to-solid phase transition of the ALS Protein FUS accelerated by disease mutation. *Cell* **162,** 1066-1077 (2015).

[35] Jones, E. M., Surewicz, W. K. Fibril conformation as the basis of species- and strain-dependent seeding specificity of mammalian prion amyloids. *Cell* **121,** 63-72 (2005).

[36] Guo, J. L. *et al.* Distinct α-Synuclein strains differentially promote tau inclusions in neurons. *Cell* **154,** 103-117 (2013).

[37] Sunde, M., Blake, C. The structure of amyloid fibrils by electron microscopy and x-ray diffraction. *Adv. Protein Chem.* **50,** 123-159 (1997).

[38] Childers, W. S., Anthony, N. R., Mehta, A. K., Berland, K. M., Lynn, D. G. Phase networks of cross-β peptide assemblies. *Langmuir* **28,** 6386–6395 (2012).

[39] Ow, S., Dunstan, D. E. A brief overview of amyloids and Alzheimer's disease. *Protein Sci.* **23,** 1315-1331 (2014).

[40] Childers, W. S., Mehta, A. K., Bui, T. Q., Liang, Y., Lynn, D. G. Toward Intelligent Material. *Molecular Self-Assembly: Advances and Applications*. **1st ed.,** 1-36 (2012).

[41] Jucker, M., Walker, L. C. Self-propagation of pathogenic protein aggregates in neurodegenerative diseases. *Nature* **501,** 45–51 (2013).

[42] Childers, W. S., Mehta, A. K., Lu, K., Lynn, D. G. Templating molecular arrays in amyloid's cross-β grooves. *J. Am. Chem. Soc.* **131,** 10165-10172 (2009).

[43] Balbach, J. J. *et al.* Amyloid Fibril Formation by $A\beta_{16\text{-}22}$, a Seven-Residue Fragment of the Alzheimer's β-Amyloid Peptide, and Structural Characterization by Solid State NMR. *Biochemistry* **39,** 13748-13759 (2000).

[44] Holbrook, J. A., Tsodikov, O. V., Saecker, R. M., Record Jr, M. T. Specific and non-specific interactions of integration host factor with DNA: thermodynamic evidence for disruption of multiple IHF surface salt-bridges coupled to DNA binding. *J. Mol. Biol.* **310,** 379-401 (2001).

[45] Tsodikov, O. V., Holbrook, J. A., Shkel, I. A., Record Jr., M. T. Analytic binding isotherms describing competitive interactions of a protein Ligand with specific and nonspecific sites on the same DNA oligomer. *Biophys. J.* **81,** 1960-1969 (2001).

[46] Nadassy, K., Wodak, S. J., Janin, J. Structural features of protein-nucleic acid recognition sites. *Biochemistry* **38,** 1999-2017 (1999).

[47] Armstrong, A. H., Chen, J., McKoy, A. F., Hecht, M. H. Mutations that replace aromatic side chains promote aggregation of the Alzheimer's Aβ peptide. *Biochemistry* **50,** 4058-4067 (2011).

[48] Senguen, F. T., Doran, T. M., Anderson, E. A., Nilsson, B. L. Clarifying the influence of core amino acid hydrophobicity, secondary structure propensity, and molecular volume on amyloid-β 16-22 self-assembly. *Molecular BioSystems* **7,** 497-510 (2011).

[49] Li, S. *et al.* Design of asymmetric peptide bilayer membranes. *J. Am. Chem. Soc*. **138,** 3579–3586 (2016).

[50] Childers, W. S., Mehta, A. K., Ni, R., Taylor, J. V., Lynn, D. G. Peptides organized as bilayer membranes. *Angewandte Chemie International Edition* **49,** 4104-4107 (2010).

[51] Schmidt, H. B., Görlich, D. Transport selectivity of nuclear pores, phase separation, and membraneless organelles. *Trends Biochem. Sci.* **41,** 46-61 (2016).

[52] Bellini, T. *et al.* Liquid crystal self-assembly of random-sequence DNA oligomers. *Proc. Natl. Acad. Sci. USA* **109,** 1110-1115 (2012).

[53] Nielsen, F. C., Hansen, H. T., Christiansen, J. RNA assemblages orchestrate complex cellular processes. *Bioessays* **38,** 674-681 (2016)

[54] Courchaine, E. M., Lu, A., Neugebauer, K. M. Droplet organelles. *EMBO J.* **35,** 1603-1612 (2016).

[55] Shin, J., Salameh, J. S., Richter, J. D. Impaired neurodevelopment by the low complexity domain of CPEB4 reveals a convergent pathway with neurodegeneration. *Sci. Rep.* **6,** (2016).

[56] Schindelin, J. *et al.* Fiji: an open-source platform for biological-image analysis. *Nature Methods* **9,** 676-682 (2012).

[57] Van Wazer, J. Structure and Properties of the Condensed Phosphates .3. Solubility Fractionation of Other Solubility Studies. *J. Am. Chem. Soc.* **72,** 647–655 (1950).

[58] Smith, S. A. *et al.* Polyphosphate exerts differential effects on blood clotting, depending on polymer size. *Blood* **116,** 4353–4359 (2010).

Chapter 5: Passivation of the Cross-β interface by Nucleic Acids

Introduction

Dysregulation of post-transcriptional RNA has been implicated in the accumulation of mRNA at the site of protein/peptide aggregation in multiple neurodegenerative diseases [1-8], and the seeding by strongly amyloidogenic peptides in mRNP granules could induce a transition to paracrystalline structures similar to those described here [9-16]. Evidence supports the reconstitution of disease-relevant forms of these assemblies *in vitro*. For example, in prion diseases, the isolation of nucleic acid and lipids in association with prions led to the examination of their affect on prion toxicity. Nucleic acid introduced *in vitro* to prions and injected into the brains of mice accelerated the infectious prion state [3], and enhanced cytoxicity was observed in cells exposed to prion/nucleic acid aggregates in culture [2]. The methods outlined here and in the previous chapter, can now be used to correlate structure with disease relevant strains.

In Chapter 4, the design and global morphological characterization of two nucleic acid/peptide co-assemblies was described. Here, we examine these RNA/peptide co-assemblies in greater detail with an emphasis on structure. These data expound upon the arrangement of nucleic acids when in complex with amyloid nanostructures, and pave the way for the development of comprehensive models for the interception of RNA processing in protein-misfolding diseases and others [17].

Results

Disease associated and synthetic amyloids are identified based on their cross-β diffraction pattern [18]. Over 20 diseases have now been characterized as amyloidosis [19,20], and many amyloid deposits have been implicated in the pathogenesis of neurodegeneration [21]. In Alzheimer's disease, the context-dependent folding of β-amyloid peptides [22] has been attributed to the degree of disease pathogenesis and its structural differences offered as an explanation for the presence of senile plaques in non-diseased brains; the presence of neurotoxic or nontoxic amyloid strains [23,24]. Because of the environment-specific morphology of amyloid fibrils, identification of substances that impact amyloid fibril gross morphology is necessary. Nucleic acids sequestered in amyloidosis likely affect the nucleation and propagation of amyloid nanostructures and contribute to disease progression. Thus, we have chosen to focus our investigation on the structural characterization of a β-sheet-rich RNA/peptide co-assembly.

Peptide and RNA/peptide assemblies maintain cross-β architecture

As an initial approach to characterizing RNA/peptide co-assembly structure, powder x-ray diffraction (PXRD) was used. PXRD analyses of the peptide and RNA co-assemblies identified d-spacings of 4.7Å and 11Å shown in Figure 5-1, consistent with those of cross-β nanostructures (Figure 5-2) [25]. Therefore, these distances were assigned to the interstrand H-bonding and β-sheet laminate distances of cross-β nanostructures, respectively (Figure 5-2) [18]. The width of diffraction peaks is attributed to the heterogeneity of assembled populations with that specific repeating distance. When compared to each other, the width of the 11Å peak of *pep-RG* assemblies is greater than that of *pep-KG* assemblies supporting the CD and FT-IR data of Chapter 4 (Figure 4-8). The PXRD profiles of peptide-alone assemblies also reveal wider peaks than either RNA/peptide co-assembly, suggesting a greater degree of homogeneity in samples assembled with RNA.

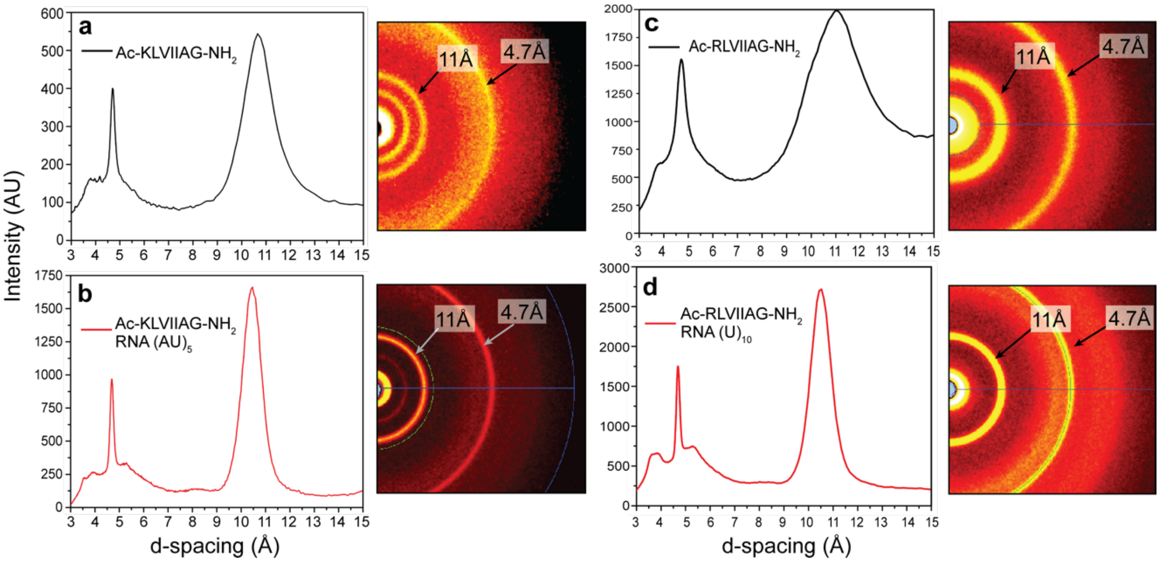

Figure 5-1 Powder x-ray diffraction identifies cross-b as the central architecture in peptide-alone and RNA/peptide co-assemblies. *Diffraction patterns identify two distances, 4.7Å and 11Å for all assemblies examined.*

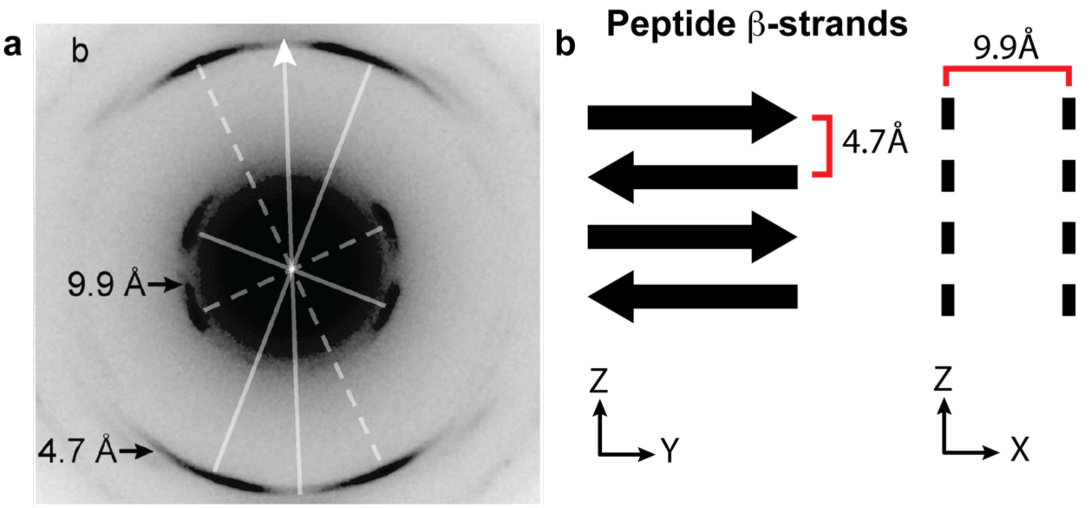

Figure 5-2 Cross-beta diffraction pattern adapted with permission from Mehta, A. K. et al. J. Am. Chem. Soc. 2008, 130, 9829-9835. Copyright 2008 American Chemical Society [25]. *(a) Electron diffraction of Ac-KLVFFAE-NH$_2$ nanotubes. (b) Diagram highlighting the interstrand distance and intersheet distance calculated from (a).*

Co-assemblies form homogeneous anti-parallel in-register β-sheet monolayers

From the PXRD data constraints, the design of peptides for solid-state nuclear magnetic resonance analyses was possible. With solid state NMR, the determination of strand orientation and registry within the β-sheets is possible [26,27]. Figure 5-3 highlights the possible orientations peptides within cross-β assemblies will likely populate. Orientation in this case refers to parallel or anti-parallel β-strands, while registry refers to the interstrand alignment of residues. An in-register assembly is one in which all residues are aligned and H-bonding occurs between every backbone amide. An out-of-register assembly is often characterized by the overhang of one amino acid. In this scenario, solvent exposure of a cationic residue is most common.

To examine peptide orientation and registry by solid state NMR, Rotational-Echo Double-Resonance (REDOR) was used [27]. With this approach, the elucidation of the precise distances between heteronuclei is possible. *Pep-KG* (Ac-K[1-^{13}C]LVII[^{15}N]AG-NH$_2$), enriched with [1-^{13}C]-Leucine and ^{15}N-Alanine, was synthesized for use in ^{13}C{^{15}N}REDOR experiments. For ^{13}C{^{15}N}REDOR, the relaxation rate of ^{13}C nuclei in the assembly is first recorded (S$_0$). Once the relaxation rate of ^{13}C nuclei-alone has been established, ^{15}N π-pulses are introduced to the system. The impact of the presence of ^{15}N nuclei on the relaxation rate of ^{13}C nuclei (S) is directly related to the distance between the two nuclei. The design of peptides for REDOR experiments, must place ^{13}C and ^{15}N nuclei far enough apart that solid state NMR measurements only correspond with interstrand distances and are not influenced by intrastrand dipolar recoupling.

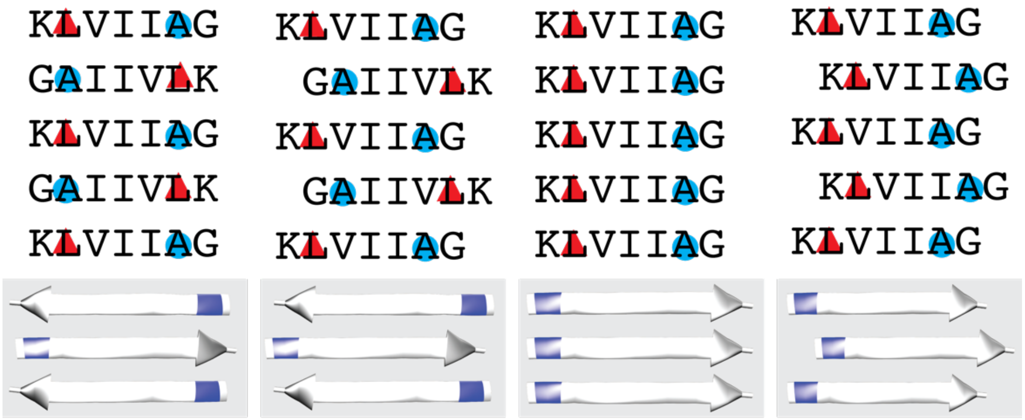

▲ [1-13C]Leu ● [15N]Ala

Figure 5-3 Design of isotope-enriched pep-KG for ^{13}C{^{15}N}REDOR. *Four possible organization modes are displayed. Peptide orientation and registry is precisely determined by ^{13}C{^{15}N}REDOR. Pep-KG (Ac-K[1-^{13}C]LVII[^{15}N]AG-NH$_2$) was synthesized for ^{13}C{^{15}N}REDOR.*

To interpret data accurately, molecular modeling was used to simulate potential REDOR curves. Because REDOR is used to measure the distance between heteronuclei, the measurement of parallel beta-sheet assemblies is not possible with the current isotope-enrichment positions. To identify parallel assemblies another solid state NMR technique is used, and will be discussed in great detail later on in this chapter. Constraints provided by PXRD data allow for the precise positioning of peptides in a molecular model. Distances between ^{13}C and ^{15}N nuclei can be estimated, and their dipolar recoupling used to generate the curves shown in Figure 5-4. The slope of the generated curve is directly related to the strength of the dipolar recoupling and the distance between isotope-enriched nuclei in the peptide assembly. As noted previously, parallel assemblies place the isotope-enriched nuclei too far apart for interpretation of data by REDOR.

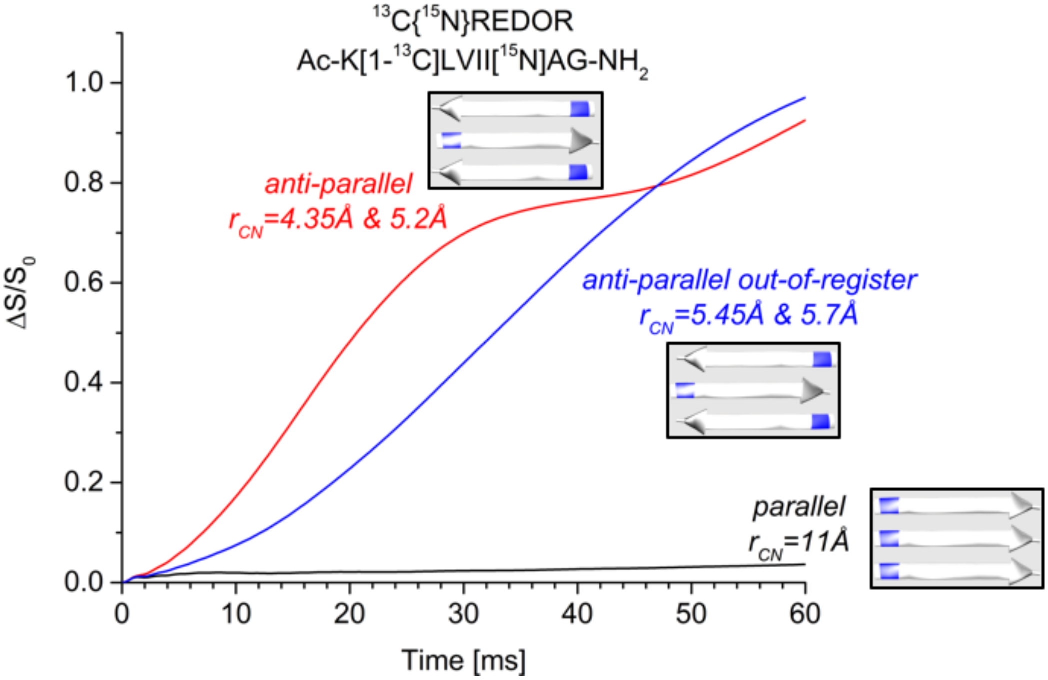

Figure 5-4 Simulated curves of $^{13}C\{^{15}N\}$REDOR data for pep-KG assemblies.

Curves are generated from molecular models. r_{CN} corresponds to the distances between ^{15}N and ^{13}C nuclei. ^{13}C nuclei are dephased by two ^{15}N nuclei on neighboring beta-strands in anti-parallel peptide assemblies.

For solid state NMR, approximately 40mg of isotopically-enriched peptides were assembled in 40% acetonitrile and 60% water, at pH5. Two samples were generated: *pep-KG* assemblies alone and DNA$(A)_{10}$/*pep-KG co-assemblies.* DNA was used for solid state NMR analysis because of the quantity necessary for an assembly of this scale. Assembly of *pep-KG* fibers and DNA/*pep-KG* ribbons was scored by TEM. To prepare samples for solid state NMR, assemblies were centrifuged at 4,000rpm for 30 minutes until pellet formation was apparent. Because *pep-KG* fibers were more dispersed and smaller in width, $MgSO_4$ was used to bundle fibers prior to centrifugation. After pelleting of assemblies, the supernatant was removed and the pellet was flash frozen for lyophilization. TEM was used to examine assemblies before and after lyophilization and confirmed maintenance of gross morphology (Figure 5-5).

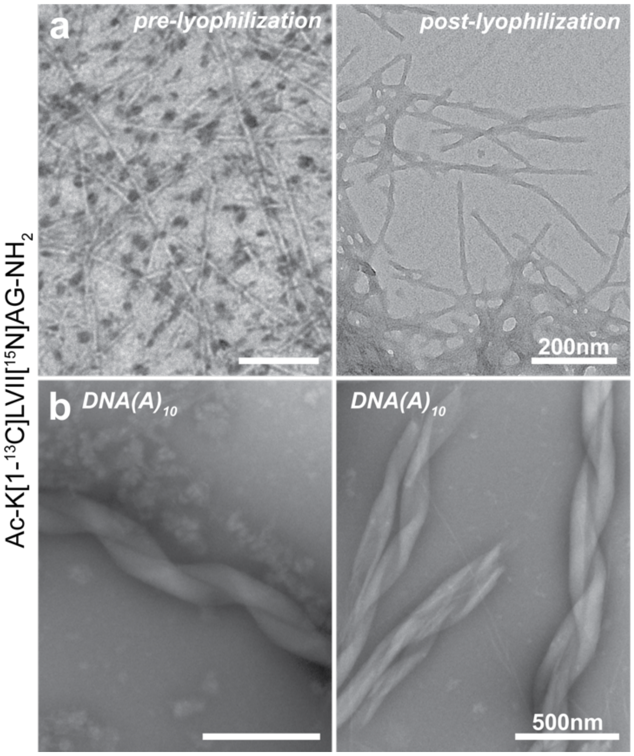

Figure 5-5 Pep-KG and DNA/pep-KG before and after lyophilization prior to examination by ^{13}C{^{15}N}REDOR. *(a) Pep-KG fibers before and after bundling with $MgSO_4$ and lyophilization. (b) DNA/Pep-KG ribbons before and after lyophilization.*

To measure ^{13}C{^{15}N}REDOR, two pulse sequences are used. The first, S_0, establishes the relaxation rate of ^{13}C nuclei by recording the integrated sum of center and sideband peaks over time following cross-polarization and π pulses. This measure represents the relaxation rate of ^{13}C nuclei in an isolated system.

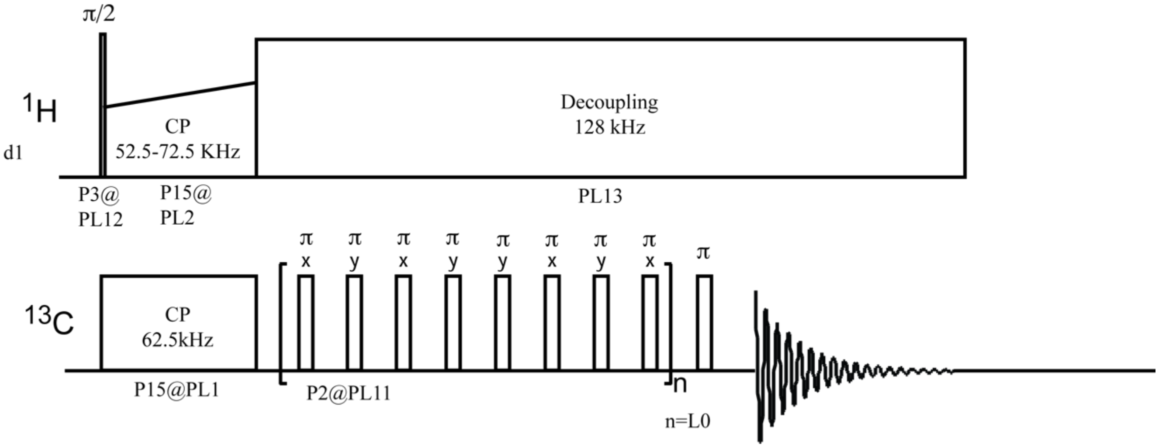

Figure 5-6 ^{13}C S0 pulse sequence for ^{13}C{X}REDOR, where X represents nucleus dephasing ^{13}C. *Cross-polarization of ^{1}H prior to ^{13}C π pulses enhances signal. Following pulse sequences of variable time, the integrated sum of ^{13}C spectrum center and sideband peaks generated is graphed.*

Following S_0 measurements, the introduction of ^{15}N nuclei to the system via the pulse sequence shown in Figure 5-8 results in an observable change in the ^{13}C relaxation rate. This measurement is given the designation ‘S’. Depending on the distance between ^{15}N and ^{13}C nuclei, and the number of ^{15}N nuclei dephasing ^{13}C, the ^{13}C relaxation rate will appear different. By measuring the difference between the ^{13}C relaxation rate in the presence and absence of ^{15}N nuclei, the distance and number of ^{15}N nuclei dephasing each ^{13}C nucleus, and the percentage of ^{13}C nuclei dephased can be extrapolated.

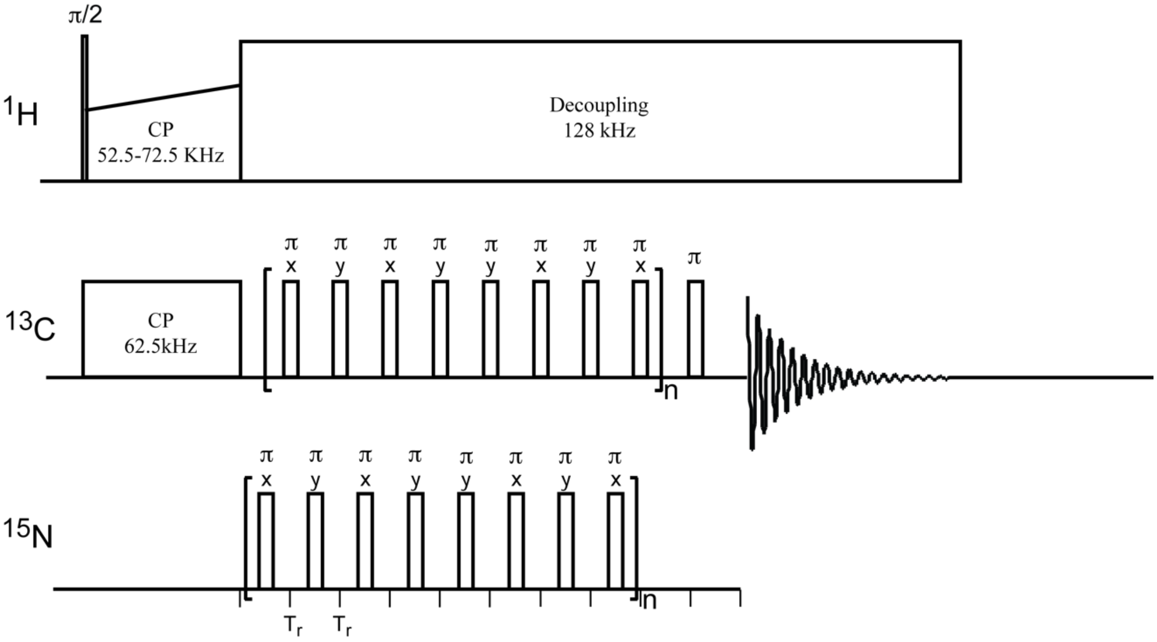

Figure 5-7 $^{13}C\{^{15}N\}$REDOR 'S' pulse sequence. *Introduction of ^{15}N nuclei by π pulses of variable time allows for the measurement of ^{13}C relaxation over time in the presence of ^{15}N nuclei, and the elucidation of internuclear distances.*

For *pep-KG* (Ac-K[1-^{13}C]LVII[^{15}N]AG-NH$_2$) fibrillar assemblies, enriched with [1-^{13}C]-Leucine and ^{15}N-Alanine, $^{13}C\{^{15}N\}$REDOR gave dephasing rates for 37±1.5% of the total ^{13}C population where ^{13}C nuclei were dephased by two ^{15}N nuclei at distances of 4.35Å and 5.2Å. This population was uniquely defined as anti-parallel in-register β-strands and matched with the simulated REDOR curve from molecular modeling. In contrast, $^{13}C\{^{15}N\}$REDOR analyses of DNA(A)$_{10}$/*pep-KG* co-assemblies assigned 92±1.5% of the peptide β-strand population as anti-parallel and in-register (Figure 5-9). Although at the level of transmission electron microscopy, heterogeneity is not apparent for *pep-KG* fibrillar assemblies, by solid state NMR there are clearly at least two populations of assembled ^{13}C nuclei. Dephasing of nearly 100% of the ^{13}C population as anti-parallel in-register β-strands for DNA/*pep-KG* ribbonous assemblies suggests a greater degree of homogeneity in the presence of nucleic acid, and the selection of this peptide orientation and registry during nucleation by selective, cooperative binding of nucleic acid. The REDOR curves are plotted as ΔS/S0, which allows for the direct measurement of the percentage of observed ^{13}C spins dephased by ^{15}N.

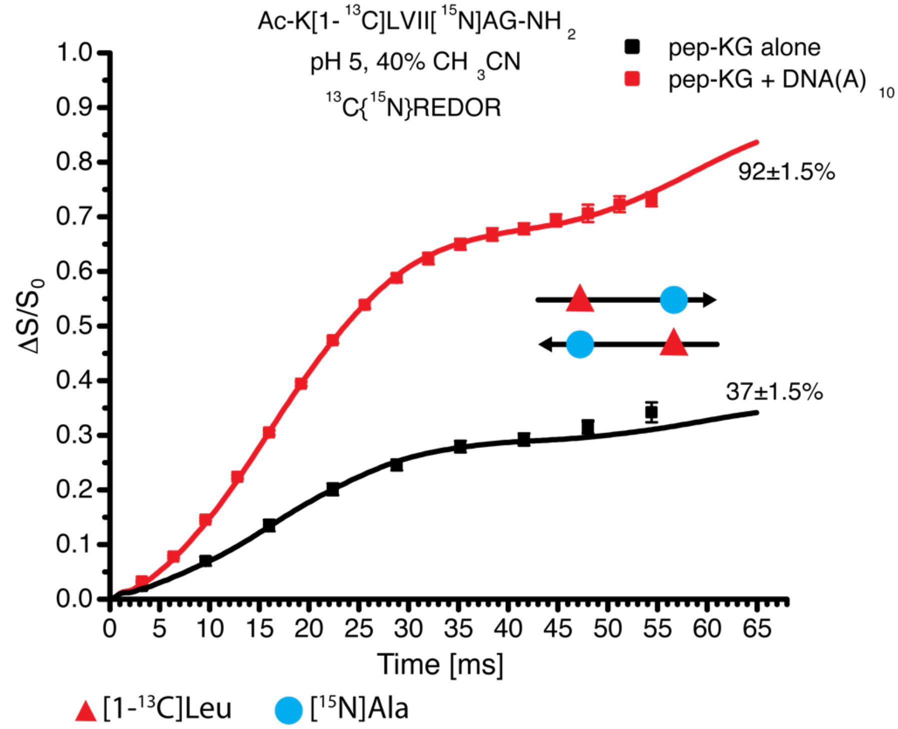

Figure 5-8 ^{13}C{^{15}N}REDOR identifies anti-parallel in-register beta-strand populations of pep-KG and DNA/pep-KG assemblies. *$\Delta S/S_0$ refers to the difference in the relaxation rate of ^{13}C nuclei in the presence and absence of ^{15}N nuclei divided by the relaxation rate of ^{13}C nuclei alone. $\Delta S/S_0$ is directly proportional to the percentage of ^{13}C nuclei in a given environment.*

Examination of lyophilized solid state NMR samples by FT-IR (Figure 5-10) using a pressure tip, confirms the differences between samples obtained by ^{13}C{^{15}N}REDOR. For FT-IR of isotope-enriched samples, two main amide I peaks are taken into consideration. The C=O bond of the peptide backbones, which previously was populated by 98.9% ^{12}C nuclei, now has one position 100% occupied by ^{13}C. This change results in the emergence of a new amide I peak corresponding to ^{13}C=O stretching. Because of the isotope mass, ^{13}C=O stretching occurs at higher wavenumbers than ^{12}C=O stretching. Examination of isotope-enriched peptides by FT-IR is referred to as Isotope-Edited IR. The positions of amide I peaks between samples is nearly identical; DNA/pep-KG ^{12}C and ^{13}C peaks are shifted to slightly higher wavenumbers compared with their pep-KG counterparts. This, taken along with the enormity of the ^{13}C peak of *pep-KG* assemblies, likely accounts for the differences REDOR has begun to unveil. The low resolution of the area beneath the ^{13}C peak of *pep-KG* assemblies suggests heterogeneity.

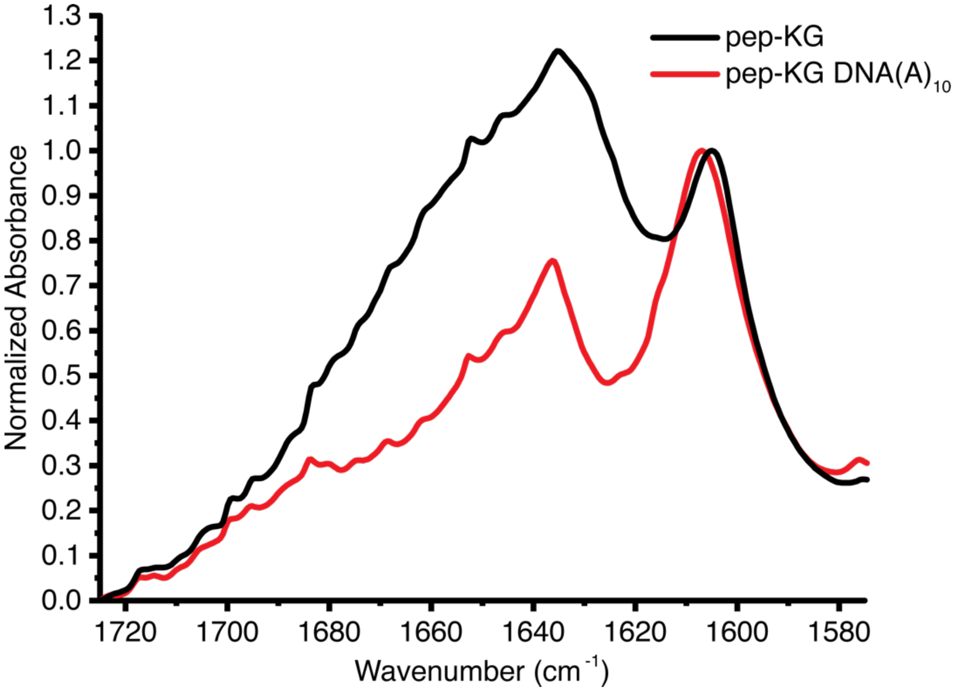

Figure 5-9 Isotope-edited Infrared spectroscopy examination of lyophilized solid state NMR samples for pep-KG and DNA/pep-KG assemblies. *Peaks at ~1606cm^{-1}*

represent ^{12}C=O stretching frequencies of amide I. Peaks at ~1637cm^{-1} represent ^{13}C=O stretching frequencies of amide I. Absorbance is normalized to ^{12}C=O peaks.

To identify the peptide orientation and registry of the remaining population of ^{13}C nuclei not dephased by ^{15}N nuclei, Double-quantum filtered dipolar recoupling with a windowless sequence (DQF-DRAWS) was employed (Figure 5-11) [26]. With DQF-DRAWS, homonuclear recoupling of ^{13}C nuclei defines interstrand distances, which can then be equated to peptide registry in parallel models. Unfortunately, unlike ^{13}C{^{15}N}REDOR, which relies on the loss of the transverse magnetization, DQF-DRAWS is unable to assign a precise percentage of the ^{13}C population to a specific peptide registry. Instead, DQF-DRAWS simply identifies the existence of a peptide registry, and the precise interstrand distance of that registry within a population.

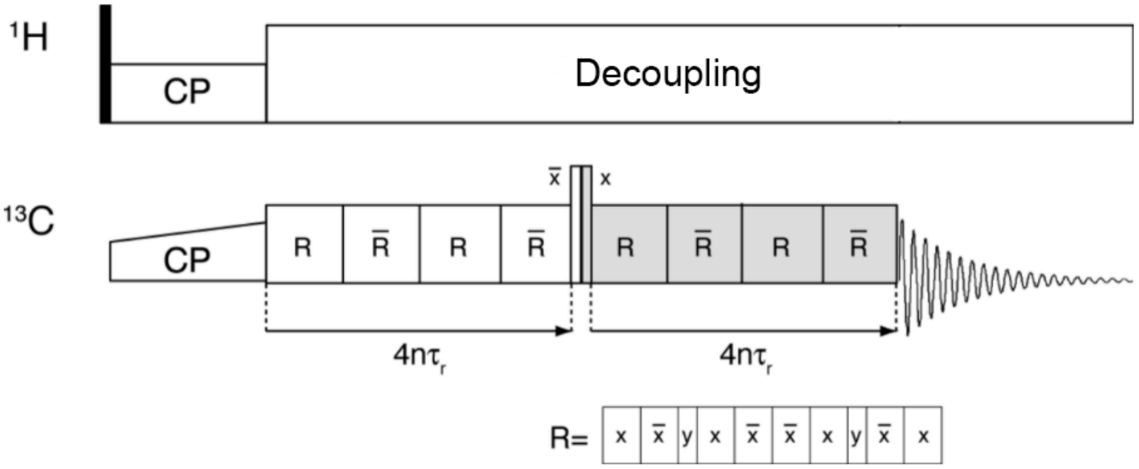

Figure 5-10 DQF-DRAWS pulse sequence. *Following cross-polarization, The DQF-DRAWS sequence was applied. Variable times of dipolar buildup allowed for the precise determination of ^{13}C homonuclear distances.*

From DQF-DRAWS, the existence of a parallel out-of-register by one amino acid peptide arrangement was identified for *pep-KG* assemblies. This population of ^{13}C spins had a homonuclear distance of 7.5Å (Figure 5-12). Although DQF-DRAWS can not assign a specific percentage of the remaining ^{13}C population to these measurements, the clarity of these data suggest this, and the anti-parallel in-register peptide strand orientation discussed earlier, are the only populations in *pep-KG* fibrillar assemblies.

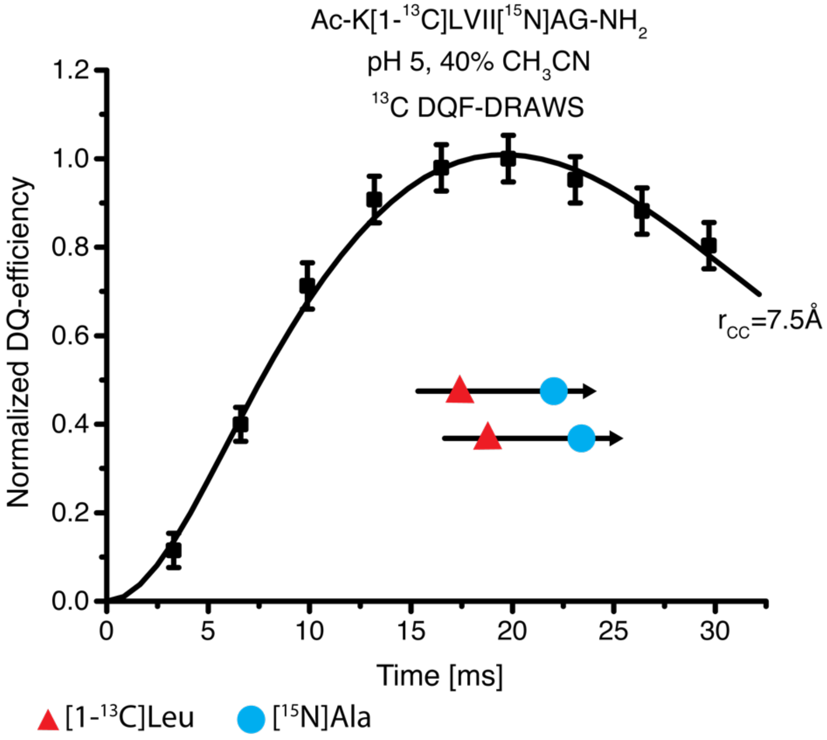

Figure 5-11 DQF-DRAWS analysis of pep-KG fibrillar assemblies identifies a ^{13}C homonuclear distance of 7.5Å. *Peptide orientation is parallel and out-of-register by one residue.*

Nucleic acids passivate the cross-β monolayer interfaces

The precise positioning of DNA within the DNA/*pep-KG* co-assemblies was made possible through use of ^{13}C{^{31}P}REDOR. For examination of nuclei by NMR, the nuclear spin must not be equal to zero [28]. The most abundant phosphorus isotope, ^{31}P, with a nuclear spin of ½, is NMR active, allowing for ease of observation without isotope-enrichment. Based on the peptide orientation and registry identified by $^{13}C\{^{15}N\}$REDOR and the lamellae width measurements described in Chapter 4, a model for the positioning of DNA within the DNA/*pep-KG* co-assemblies was developed. DNA was placed at monolayer interfaces to passivate positively-charged terminal residues and account for the distinct lamella boundaries observed by TEM.

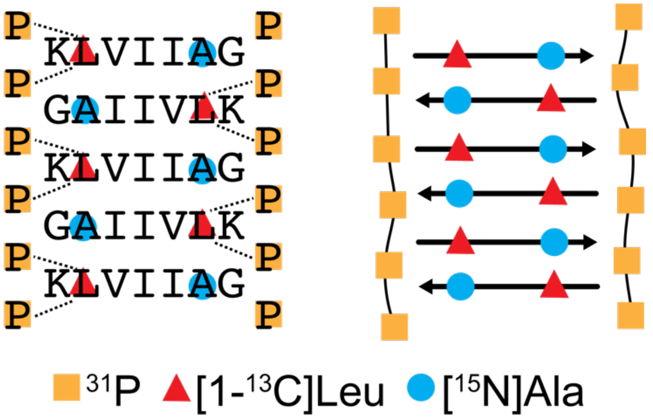

Figure 5-12 Model depicting position of DNA (^{31}P) in DNA/pep-KG co-assemblies. *Left model highlights likely $^{13}C\{^{31}P\}$ measured distances. Right model simplifies DNA/peptide representations.*

For $^{13}C\{^{31}P\}$REDOR experiments, the ^{13}C S_0 pulse sequence is identical to that of $^{13}C\{^{15}N\}$REDOR (Figure 5-7). The S pulse sequence introduces the ^{31}P nuclei to the system via a series of π pulses (Figure 5-14). The integrated sum of center and sideband peaks for the ^{13}C spectra generated following ^{31}P π pulses, is used in the generation of the $^{13}C\{^{31}P\}$REDOR curve.

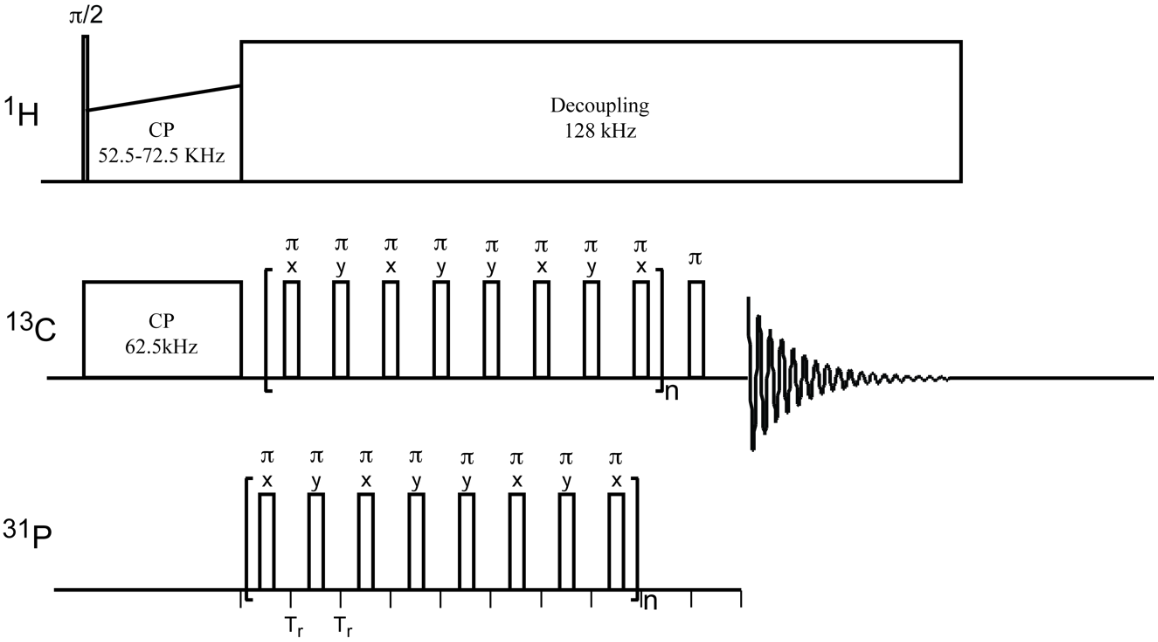

Figure 5-13 ^{13}C{^{31}P}REDOR 'S' pulse sequence. *Introduction of ^{31}P nuclei by π pulses of variable time allows for the measurement of ^{13}C relaxation over time in the presence of ^{31}P nuclei, and the elucidation of internuclear distances.*

Peptide Ac-K[1-^{13}C]LVII[^{15}N]AG-NH$_2$ co-assembly sample from ^{13}C{^{15}N}REDOR was repurposed for ^{13}C{^{31}P}REDOR. For ^{13}C{^{31}P}REDOR, ^{15}N nuclei were not considered. Dephasing of ^{13}C nuclei by ^{31}P provided a single distance for an isolated system assuming one phosphorus dephased each ^{13}C nucleus. Distances acquired from ^{13}C{^{31}P}REDOR place backbone ^{31}P nuclei of the DNA(A)$_{10}$ 8.9Å from all [1-^{13}C]-Leucine carbon nuclei (Figure 5-15). Despite the absence of detectable diffraction assignments for the nucleic acid in the RNA/*pep-KG* co-assemblies, the relative arrangement of the peptide and nucleic acid backbones are highly ordered. Based on these data, nucleic acids passivate the cross-β interface of monolayers, consistent with the model proposed in Figure 5-13.

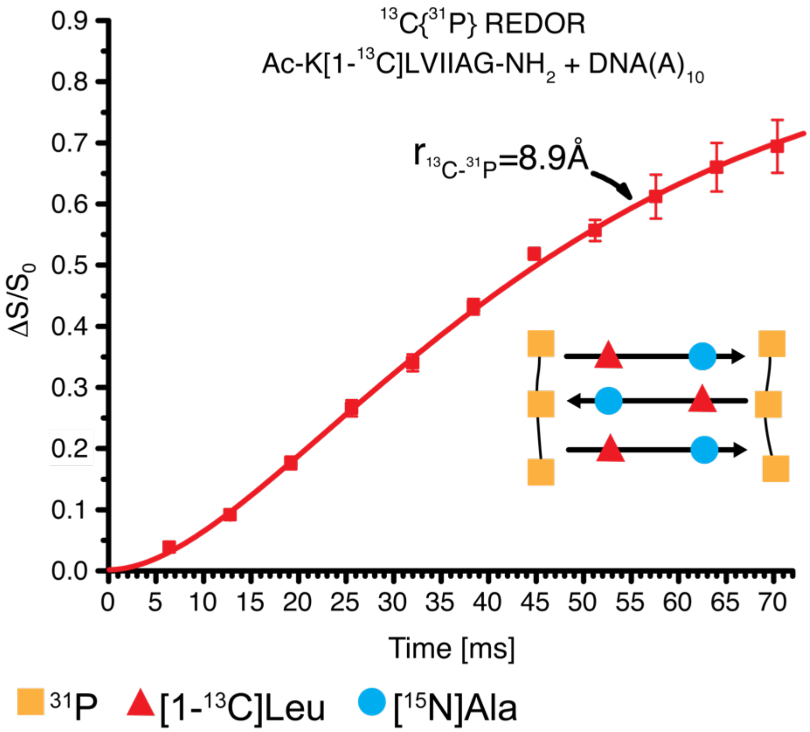

Figure 5-14 ^{13}C{^{31}P}REDOR identifies a distance of 8.9Å for 100% of ^{13}C nuclei dephased by a single phosphorus. *ΔS/S0 is a measure of the difference between ^{13}C relaxation rates in the presence and absence of ^{31}P nuclei divided by the relaxation rate of ^{13}C nuclei in the absence of ^{31}P nuclei.*

Synthesis and characterization of a ^{13}C/^{31}P calibration standard

Since this was the first examination of ^{13}C{^{31}P}REDOR by our spectrometers, and molecular models did not exist prior to our calculations to describe the positioning of DNA, and prepare a simulated curve explaining the data, a crystalline internal control was necessary for accuracy of distance measurements between ^{13}C and ^{31}P nuclei. For consideration as a control for the ^{13}C{^{31}P}REDOR experiments described here, and future experiments, required the satisfaction of the following criteria. First, the control must have a published crystal structure that defines at least one intramolecular ^{13}C/^{31}P distance and second, it must be readily available in isotopically-enriched (^{13}C) form. Several candidates were examined for their use as ^{13}C{^{31}P}REDOR standards. α-D-galactose 1-phosphate and phosphoenolpyruvate, which are soluble in water and easily crystallize following evaporation were explored as initial candidates [29,30]. For solid state NMR calibration standards, it is desired that the T_1 be less than 1s. With a fast T_1, standards can be run quickly and used to confirm accuracy and precision of results. The T_1 is a measure of relaxation that quantifies the rate of energy transfer from the spin system to the surrounding lattice in the z direction. A longer T_1 indicates less motion in the lattice, since motion allows for minor fluctuations in the magnetic field. Therefore, the ideal standard would be a soft crystal. Unfortunately, ease of crystal formation for α-D-galactose 1-phosphate and phosphoenolpyruvate meant the production of crystals with little lattice motion; hard crystals. Their respective T_1 measurements were 23s and 13.5s on the Bruker 600mHz solid state NMR spectrometer used. Our third candidate as a ^{13}C{^{31}P}REDOR standard had a more complicated crystallization and involved some inorganic chemistry. A reaction between zirconyl chloride and glyphosine led to the synthesis of $Zr[(O_3PCH_2)(HO_3PCH_2)NHCH_2COOH]_2{\cdot}2H_2O$ (Figure 5-15) [30]. The precise control of reaction conditions was required because reaction between glyphosine and zirconyl chloride can yield two different crystals with a minor difference in reaction pH. After two weeks of reaction at 80°C in the presence of hydrofluoric acid, a white crystal was produced. X-ray diffraction of the crystal confirmed the homogeneous formation of $Zr[(O_3PCH_2)(HO_3PCH_2)NHCH_2COOH]_2{\cdot}2H_2O$. The product was confirmed to be the correct structure by PXRD with unit cell dimensions as follows: a = 5.44 angstroms, b = 14.95 angstroms, c = 13.31 angstroms, alpha = 90 degrees, beta = 95.26 degrees, gamma = 90 degrees. Testing of the glyphosine candidate through measurement of the T_1 gave a relaxation rate of 1.6s. Although not below 1s as desired, the T_1 was close enough that isotopically-enriched crystal was prepared in large enough quantity for calibration of $^{13}C\{^{31}P\}$REDOR experiments. To reduce the ^{13}C homonuclear recoupling in the crystal, $Zr[(O_3PCH_2)(HO_3PCH_2)NHCH_2COOH]_2{\cdot}2H_2O$ crystals were prepared with isotope-enriched glyphosine diluted with unenriched glyphosine 20:1. This dilution decreased the signal to noise, but allowed for precise measurement of $^{13}C/^{31}P$ internuclear distances within the crystal without ^{13}C homonuclear complications.

$Zr[(O_3PCH_2)(HO_3PCH_2)NHCH_2COOH]_2{\bullet}2H_2O$

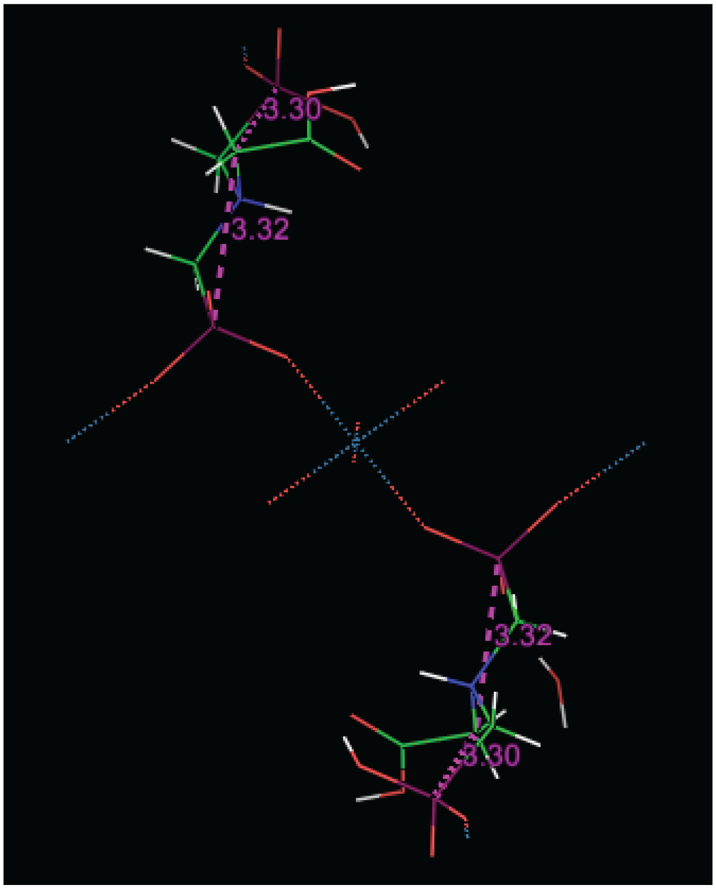

Figure 5-15 $Zr[(O_3PCH_2)(HO_3PCH_2)NHCH_2COOH]_2{\cdot}2H_2O$ crystal structure. *Coordination to Zirconium shown at center. Measurements are distances between ^{13}C and ^{31}P nuclei within 5Å.*

The gyromagnetic ratio of a nucleus is the ratio of its magnetic moment to its angular momentum. Every nucleus has a distinct gyromagnetic ratio. The effect of one gyromagnetic ratio on another is a direct measure of distance between nuclei, which we measure as the relaxation rate. The larger the gyromagnetic ratio, the greater the sphere of influence of that particular nucleus. ^{31}P has a gyromagnetic ratio of 17.235. Compared with ^{13}C at 10.705 and ^{15}N at -4.316, the influence ^{31}P has on the system will be much larger. Because of its large gyromagnetic ratio, long distances between ^{13}C and ^{31}P nuclei can be easily measured; ^{31}P nuclei located farther away will influence the relaxation rate of ^{13}C nuclei. Because of this phenomenon, characterization of the crystal and ^{13}C{^{31}P}REDOR data required inclusion of all ^{31}P nuclei within 10Å of ^{13}C nuclei.

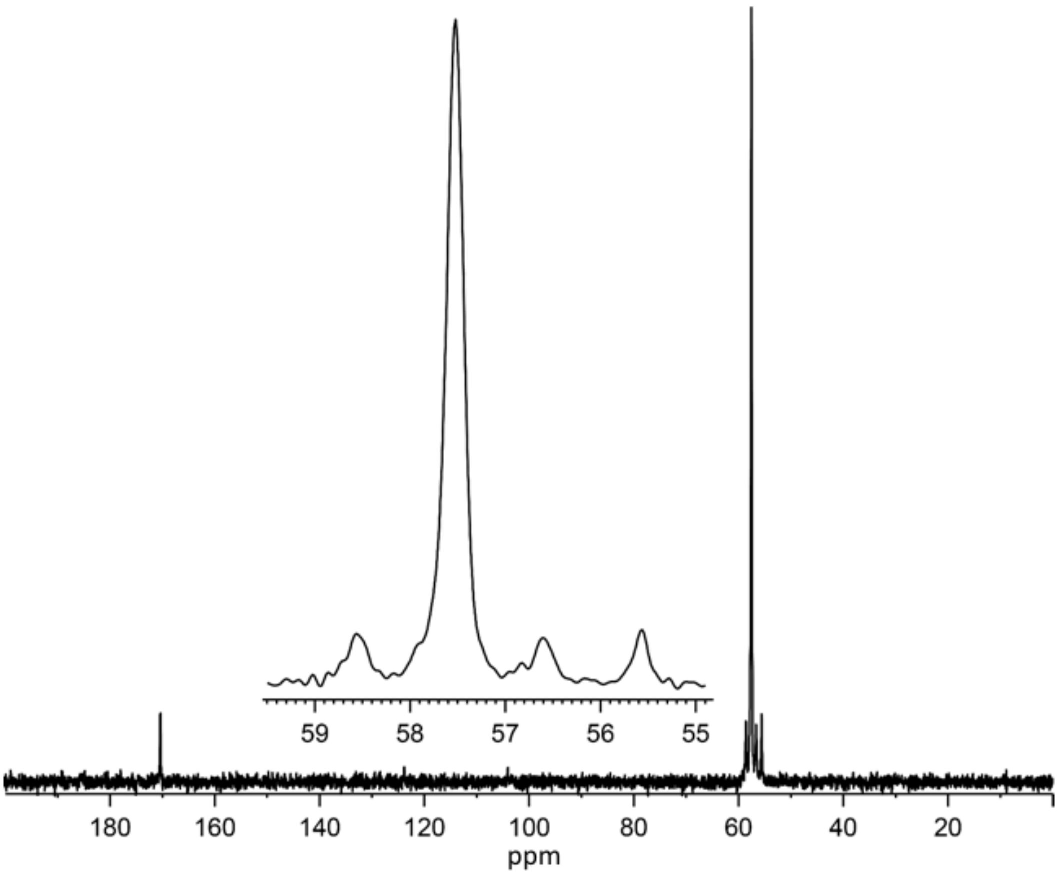

Figure 5-16 ^{13}C spectrum of Zr[(O_3PCH_2)(HO_3PCH_2)$NHCH_2COOH$]$_2$·$2H_2O$ by solid state NMR. *Four CH_2 carbons and one CO carbon is identified. The largest peak corresponds to the site of isotope-enrichment.*

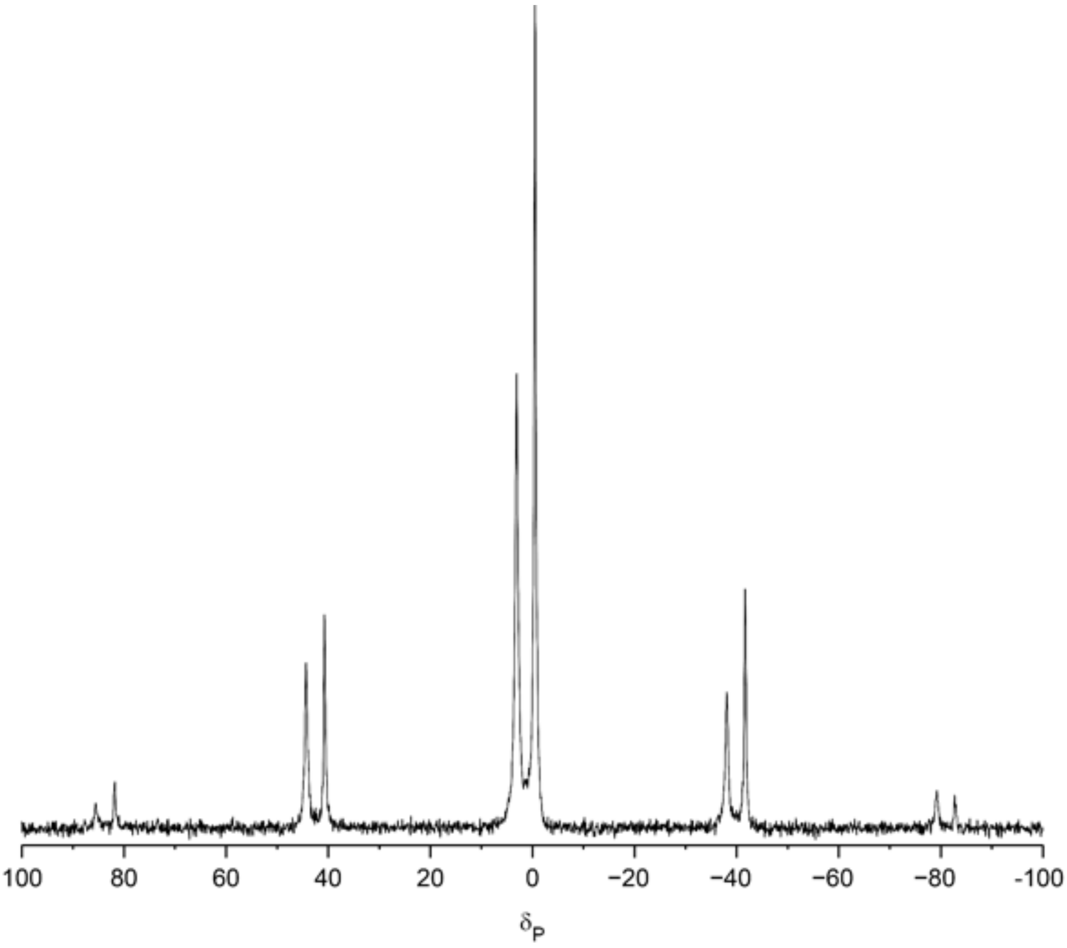

Figure 5-17 ^{13}P spectrum of Zr[(O_3PCH_2)(HO_3PCH_2)$NHCH_2COOH$]$_2$·$2H_2O$ from solid state NMR. *Two phosphates populate the Zr[(O_3PCH_2)(HO_3PCH_2)$NHCH_2COOH$]$_2$·$2H_2O$ crystal. One phosphate coordinates twice to zirconium, while one only coordinates once. This difference in coordination accounts for two populations of ^{31}P nuclei. Center and side bands are shown.*

^{13}C{^{31}P} REDOR calculated from Zr[(O_3PCH_2)(HO_3PCH_2)$NHCH_2COOH$]$_2$·$2H_2O$ crystals allows for the reexamination of ^{13}C{^{31}P}REDOR of DNA/*pep-KG* co-assembly samples.

These data confirm that the 8.9Å measurement between an isolated phosphorus and the [1-^{13}C] of Leucine is accurate and that the number of ^{13}C nuclei dephased by ^{31}P nuclei is close to 100%.

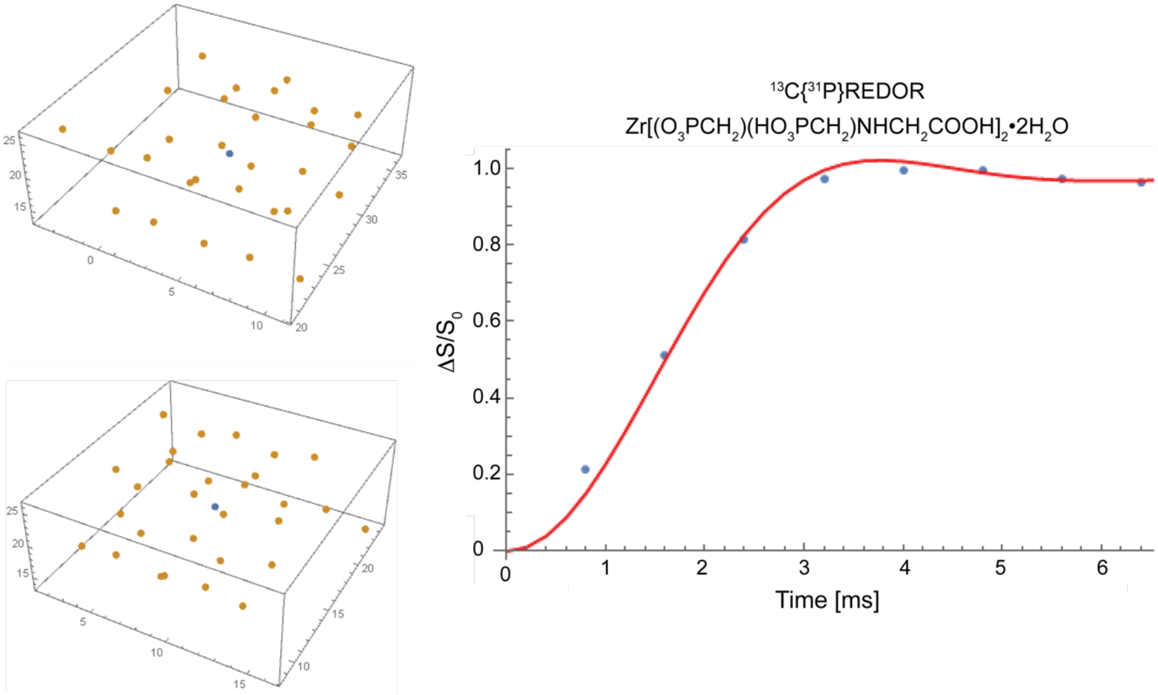

Figure 5-18 ***^{13}C{^{31}P}REDOR of Zr[(O$_3$PCH$_2$)(HO$_3$PCH$_2$)NHCH$_2$COOH]$_2$·2H$_2$O.*** *Blue dots to the left indicate isolated [^{13}C] CH2 nuclei. Yellow dots represent ^{31}P nuclei within 10Å. In total, 29-^{31}P nuclei contributed to the calculation of the REDOR curve to the right. REDOR data suggests 100% of ^{13}C nuclei are dephased by ^{31}P nuclei in the Zr[(O$_3$PCH$_2$)(HO$_3$PCH$_2$)NHCH$_2$COOH]$_2$·2H$_2$O crystal.*

Molecular dynamic simulations of DNA/*pep-KG co-assemblies*

The curve fit to ^{13}C{^{31}P}REDOR data in Figure 5-15 was calculated based on the molecular dynamics simulation of DNA/*pep-KG* co-assemblies and carefully constrained values. The confirmation of calculated measurements from ^{13}C{^{31}P}REDOR of Zr[(O$_3$PCH$_2$)(HO$_3$PCH$_2$)NHCH$_2$COOH]$_2$·2H$_2$O further supports the outcome of molecular dynamics simulations. The assumption of an isolated system where one phosphorus dephased one ^{13}C nucleus at 8.9Å eliminates the contribution of ^{31}P nuclei at distances greater than 8.9Å. Because the ^{31}P nuclei have a greater gyromagnetic ratio, it is important that we consider the influence of all ^{31}P nuclei within at least 10Å of each ^{13}C nucleus. Through the use of molecular dynamics, the space that each nucleus occupies can be more easily estimated and an accurate REDOR curve produced.

For the initial examination of the DNA/*Pep-KG* co-assembly by molecular dynamics, *pep-KG* peptides oriented anti-parallel and in-register in a cross-β monolayer was constructed. Enough $DNA(A)_{10}$ strands to passivate the positively-charged terminal Lysine residues were added to each cross-β interface. $DNA(A)_{10}$ strands were extended and aligned along the H-bonding direction (Figure 5-20). Two molecular dynamic simulations were started, one with phosphates positioned away from lysines and one with phosphates positioned toward lysines. The final frame of both simulations positioned phosphates toward lysines in a nearly identical pattern and bases away from lysines, exposed to water.

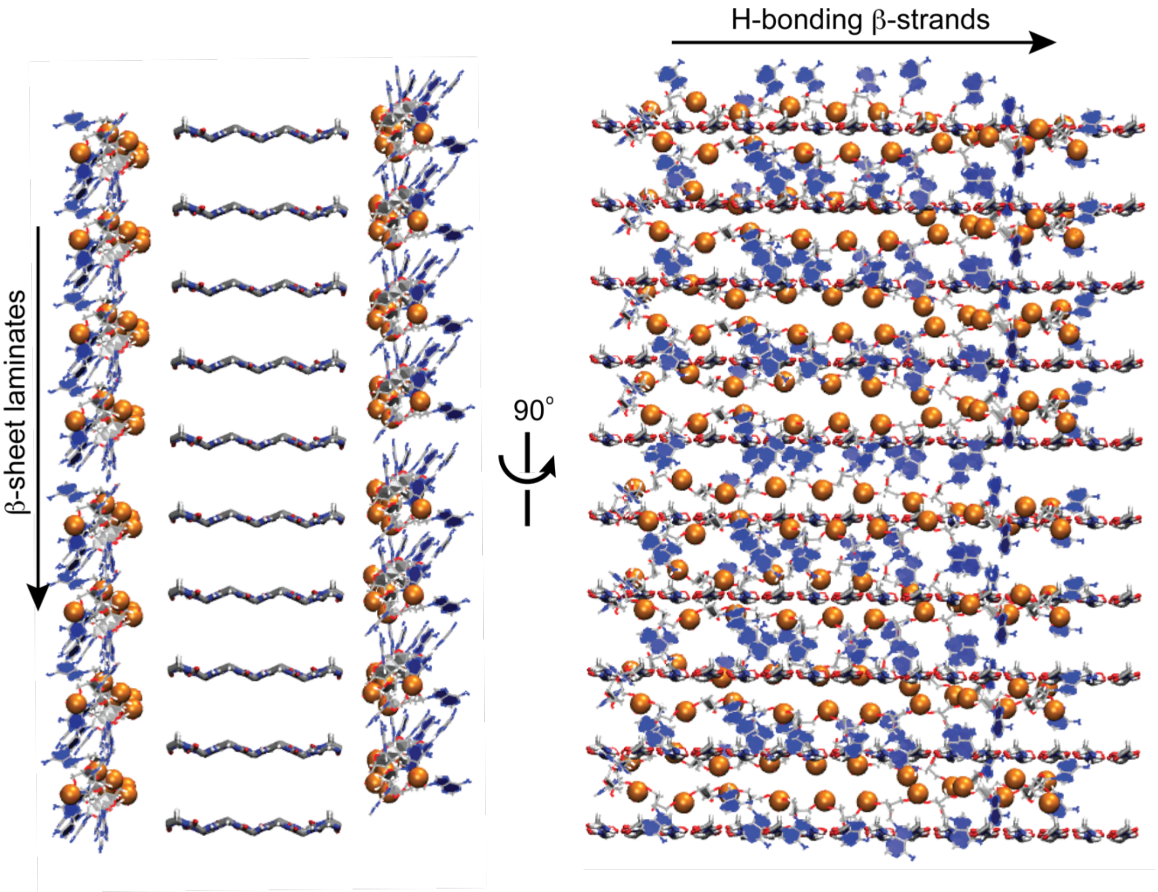

Figure 5-20 DNA/pep-KG co-assembly constructed for molecular dynamics with phosphates positioned toward lysines. *Model simplified for visualization by the removal of amino acid side chains. Charge neutrality is obtained through the passivation of cross-β interfaces with DNA and* Na^+ *ions (not shown). Orange spheres are phosphorus atoms.*

Molecular dynamics simulations were carried out for 1.2ns. At 1.2ns, the positions of DNA$(A)_{10}$ strands changed dramatically from time 0ns with phosphates clustered around lysine residue side chains, positioning most within 10Å of a [1-^{13}C]Leu nucleus (Figure 5-21). DNA$(A)_{10}$ strands condensed by up to ~20Å in most cases, suggesting the density of nucleic acid at the cross-β interface may be higher than previous estimates. In both models, phosphorus is represented by orange spheres.

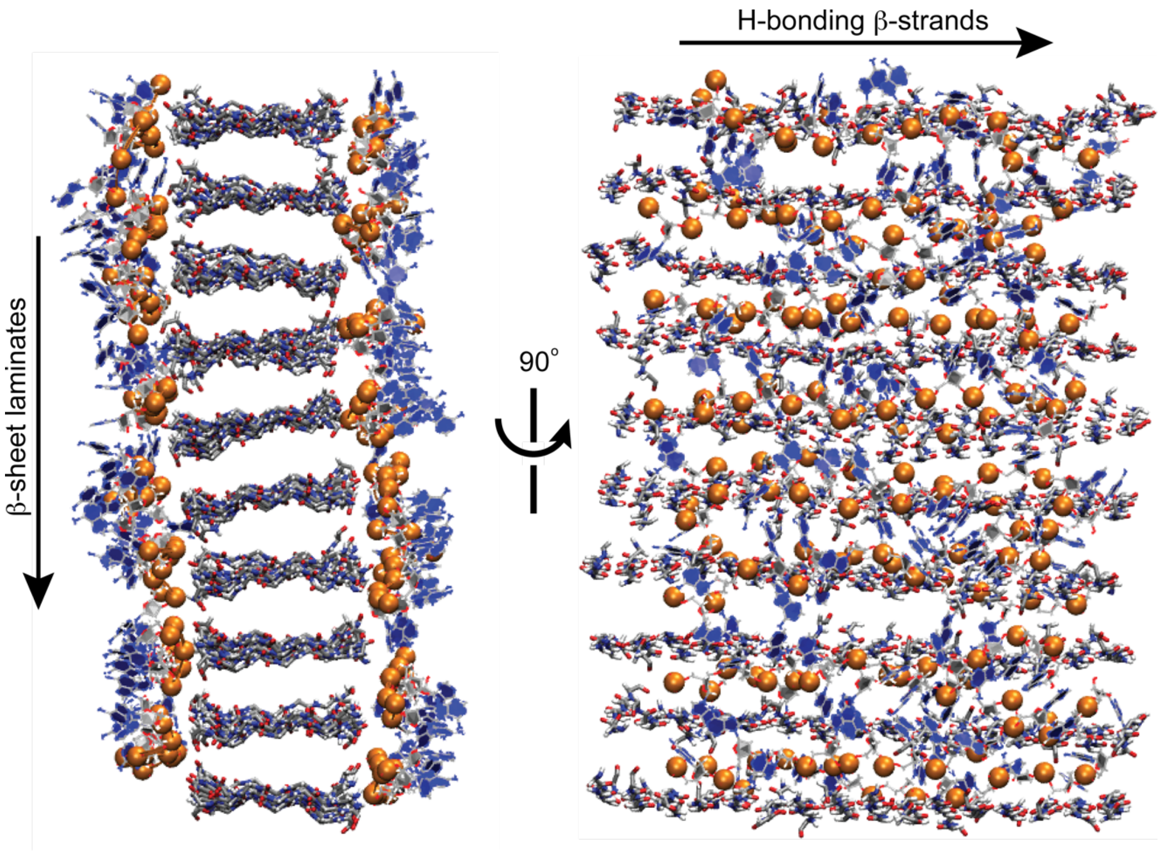

Figure 5-21 Final frame of DNA/pep-KG co-assembly molecular dynamics with phosphates clustered around lysine side chains. *DNA(A)$_{10}$ strands aligned along H-bonding axis. Peptides maintain H-bonding contacts and laminate hydrophobic interactions. Orange spheres are phosphorus atoms.*

The root-mean-square deviation (RMSD) of atomic positions can be used to monitor the movement of different constituents over the course of the simulation. These measurements allow us to approximate whether equilibrium has been achieved in the system. In Figure 5-22, the movement of peptide backbones, DNA, and phosphorus atoms was tracked over the course of the simulation. The initial spike in RMSD is attributed to the warming of the system from 0K. According to the RMSD, it appears the system is at or close to equilibrium by the end of the simulation.

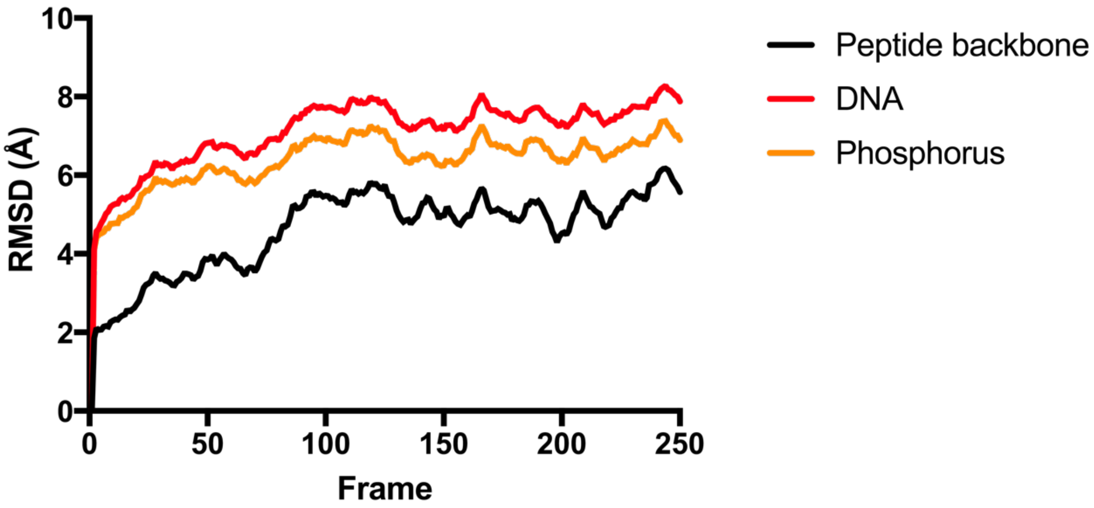

Figure 5-22 Root-mean-square deviation of atomic positions during molecular dynamic simulations. *Peptide backbone, DNA, and phosphorus movement monitored over the course of 1.2ns.*

From these simulations the precise area of phosphorus occupation in DNA/*pep-KG* co-assemblies was determined. The curve fit to the data in Figure 5-15 defines the DNA/*pep-KG* co-assemblies with a ^{13}C-^{31}P distance centered at 8.9Å and a Gaussian distribution of distances with a width of 2.4Å accounting for the distribution of phosphorus nuclei. From these data, all ^{13}C are dephased by ^{31}P illustrating the the highly ordered assembly architecture of DNA/*pep-KG* co-assemblies.

Co-assembly structural model

Data taken from these structural analyses and the global characterization described in Chapter 4 allowed for the construction of a comprehensive model of nucleic acid/peptide co-assembly. As summarized in Figure 5-23, the structural constraints provide evidence for separate peptide and nucleic acid domains that propagate along the entire length of the multi-lamellar nanotube (Figure 5-23c-e). The anti-parallel in-register peptide conformation is energetically accessible in the absence of nucleic acids, but RNA specifically templates this strand arrangement (Figure 5-23a/b). Moreover, the RNA backbone is well-ordered along each cross-β leaflet interface of the multi-lamellar nanotube. We assume the bases are packed within the laminate groove as previously shown with aromatic bases [32], but do not attain long-range order.

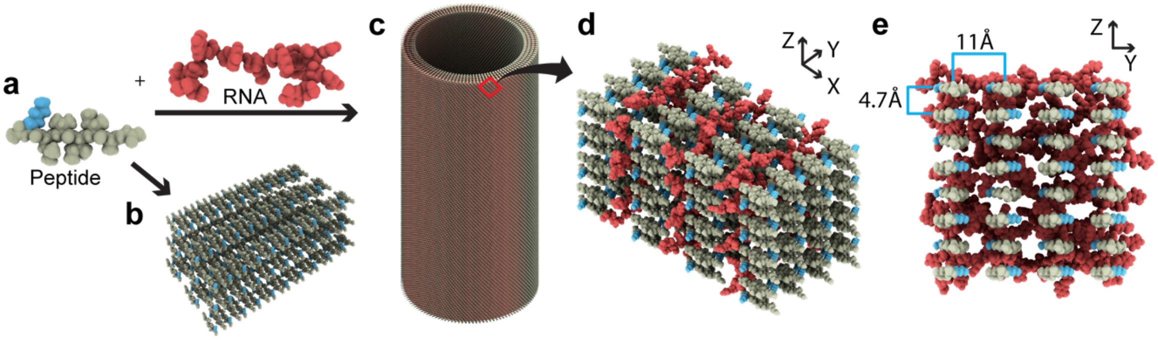

Figure 5-23 3D model describing pep-KG and nucleic acid/pep-KG assemblies. *(a) pep-KG and RNA space filled models. (b) pep-KG assemblies access anti-parallel, in-register arrays. (c/d) model depicting multi-lamellar nanotube and a closer look at the lamellae organization; anti-parallel, in-register peptide monolayers are passivated by nucleic acid at cross-β interfaces. (e) Nucleic acids densely pack at cross-β interfaces. 11Å corresponds to intersheet distance determined by PXRD. 4.7Å corresponds to interstrand distance (H-bonding) as determined by PXRD.*

Conclusions

Here we provide evidence that positively-charged, matrix-like cross-β interfaces are compatible with the nucleic acid phosphate backbone, placing each phosphorus atom on average 8.9Å from the second residue backbone carbonyl of the cross-β core. In mRNP granules we have yet to determine the actual sequence of events that must accompany the initial phase separation and transitions to the more crystalline phases characterized here, but these processes are also likely to be critical to the functioning of different processes such as transitioning through the nuclear pore and reversible stabilization of mRNP granules in the cytoplasm [33-36].

These reported structures now provide insight to the composition, the energetic assembly landscape, and the dynamics of amyloid/nucleic acid co-assemblies. This more complete understanding of the nature of these interactions between peptides and nucleic acids may lead to the development of more comprehensive and mutualistic models for the maturation and disease transitions globally associated with RNA processing [17,21]. These structures also contribute to our understanding of the context-dependent assembly of amyloid nanostructures [22-24]. Nucleic acid sequestration to inclusions of protein-misfolding disorders likely influences amyloid gross morphology and may select for neurotoxic strains in the case of neurodegenerative amyloidosis.

Technologically, nucleic acid/peptide co-assemblies have been explored for DNA delivery in several forms [37-39]. Optimization of the interactions between the nucleic acids and the peptides of these structures will constrain and extend these efforts for the development of biosensors, matrices for 3D printing of tissues, and nanocircuitry, which were explored in Chapter 3 [39-41]. Finally, such mutualistic relationships have been argued as critical for our understanding of life’s origins [42,43], and efforts to explore the functional significance beyond disease etiology now has a firm structural foundation.

Methods

Peptide Synthesis

Peptides were synthesized using Solid Phase Peptide Synthesis (SPPS) with a Rink-Amide MBHA resin, 0.4mmol/g substitution, and capped at the N-terminus with an acetyl group. Isotope-enriched amino acids [1-^{13}C]Leu and [^{15}N]Ala were used in place of Leucine and Alanine, respectively, during synthesis. Peptides were cleaved and deprotected using a cocktail of 90% TFA, 2% anisole, 3% 1,2-ethanedithiol, and 5% thioanisole. All chemicals were purchased from Sigma-Aldrich. Following cleavage and deprotection, peptides were purified by reverse-phase HPLC using acetonitrile and water with 0.1%TFA and a C18 column to a >98% purity. After purification, acetonitrile was removed by rotavaporation. The remaining aqueous solution was frozen at -80°C or flash frozen using liquid nitrogen and lyophilized to yield a white powder.

Peptide Assembly

Due to the salt sensitivity of peptides used in this study, following purification and lyophilization, peptides were desalted using Sep-Pak® C18 cartridges. Peptides were then placed in 40% Acetonitrile, vortexed briefly and sonicated for 5 minutes to promote solubility. The pH was not adjusted; each sample was examined at pH5. A stock solution of 2mM peptide was used to set up all assemblies. Experimental samples were set up within five minutes of dissolution. All nucleic acid oligomers were purchased from Integrated DNA Technologies. For NA/Peptide co-assemblies, a stock solution of 1mM NA was used. Order of addition was as follows: Peptide, solvent, nucleic acid. Assemblies were kept at 4°C unless otherwise noted. Final peptide concentration in all experimental setups was 1mM. Final nucleic acid concentration was approximately 100μM. All co-assemblies were established with a 1:1 (peptide: nucleic acid) charge ratio.

Powder X-Ray Diffraction

Experimental samples were flash frozen using liquid nitrogen and lyophilized to yield a white powder. The samples were loaded into mylar capillaries and the diffraction patterns measured using a Bruker APEX-II diffractometer with graphite monochromated Cu radiation, K-alpha radiation, λ=1.54184Å, 40kV and 35mA, with a 0.5 pinhole collimator and with exposure times of 900s per frame. The data integration software XRD2SCAN and the Bruker AXS software were used for analysis of the resulting diffraction patterns. The following equation was used to convert spectra from 2θ to d-spacing(Å): $1.54184/(2\times \sin\left(2\theta\times \frac{\frac{\pi}{180}}{2}\right))$

Solid-State NMR (REDOR and DQF-DRAWS)

Pep-KG was synthesized via SPPS with isotopically enriched Leucine [1-^{13}C] and Alanine [^{15}N] (Cambridge isotopes). A Bruker Avance 600mHz solid-state NMR spectrometer with a Bruker 4mm HCN BioSolids magic-angle spinning (MAS) probe was used to collect REDOR and DQF-DRAWS spectra. MAS frequency was actively maintained at 10kHz +/- 2 Hz with the exit cooling and spinning air temperature below -1°C, to prevent sample denaturation. ^{13}C (150.928 MHz) CP-MAS spectra before and after ^{13}C{^{15}N}REDOR, ^{13}C{^{31}P}REDOR, and DQF-DRAWS experiments, confirmed sample preservation. Samples were centered in MAS ceramic rotors with boron nitride spacers or custom teflon spacers.

The pulse sequence of ^{13}C{^{15}N}REDOR [27] consisted of two parts, an 'S' sequence that contains both ^{13}C (150.928 MHz) and ^{15}N (60.818 MHz) rotor synchronized π-pulses, and the 'S_0' sequence which is identical but does not contain any ^{15}N dephasing pulses. The ^{13}C{^{31}P}REDOR pulse sequence was identical except that 'S' contained both ^{13}C and ^{31}P pulses, while 'S_0' did not contain ^{31}P pulses. REDOR data points are the integrated sum of center- and sideband peaks. Error bars are calculated using the noise of each spectrum as the maximum peak height deviation. To normalize for the decay due to T_2 (spin-spin relaxation), individual REDOR curves are plotted as $\Delta S/S_0$. The slope steepness of the REDOR dephasing curves is directly related to the ^{13}C-^{15}N or ^{13}C-^{31}P dipolar recoupling, in $^{13}C\{^{15}N\}$REDOR and $^{13}C\{^{31}P\}$REDOR, respectively, hence the distance between the spins. When more than one ^{15}N is present, the resulting $^{13}C\{^{15}N\}$REDOR curve depends on both the ^{13}C-^{15}N distances as well as the relative orientations of the ^{13}C-^{15}N internuclear vectors. This is identical for $^{13}C\{^{31}P\}$REDOR with ^{31}P in place of ^{15}N. All ^{31}P nuclei within 10Å of [1-^{13}C]Leu of Ac-KLVIIAG-NH_2 contributed to non-linear fit calculations.

By plotting REDOR as $\Delta S/S_0$, the plateau (maximum dephasing) is directly related to the number of spins that are coupled. For example, if only half of the observe spins (in this case ^{13}C) are coupled to a dephasing spin (in this case ^{15}N or ^{31}P), the REDOR curve will achieve half the value observed when all the spins are coupled. The experimental data was fit to a linear combination of 3-spin (one ^{13}C and two ^{15}N's) and $^{13}C\{^{15}N\}$REDOR curves corresponding to the ^{13}C-^{15}N distances sufficient to fit the experimental data points using the Non-Linear Fit routine in Mathematica.

DQF-DRAWS [26] experiments were implemented with the addition of spin-temperature alternation of the initial ^1H (600.3 MHz) 1.9μs $\pi/2$ pulse to the pulse sequence and phase cycling previously described [44]. ^1H cross-polarization RF fields were ramped from 50 to 70 kHz and the ^{13}C (150.8 MHz) cross-polarization RF field was kept constant at 50kHz. SPINAL-64 [45] ^1H decoupling at 128 kHz was used during both dipolar evolution and acquisition. For DRAWS S4 recoupling, a 41.23 kHz ^{13}C RF field, measured by fitting a ^{13}C nutation curve to a sine function with a decaying exponential, was used. The rotor period (206.2μs $\rightarrow \nu_r$= 4.85 kHz) was set to 8.5 times the ^{13}C π pulse length.

DQF-DRAWS curves were calculated using SIMPSON [46], where an array of 13C spins were approximated with a three spin “infinite loop” model [47] and chemical shift tensor components δ_{11}=74.1ppm, δ_{22}=6.0ppm and δ_{33}=-80.1ppm, which were measured from the ^{13}C CP-MAS spectra. The infinite loop model consists of three spins with identical dipolar recouplings but with the orientation of the CSA to dipolar tensors identical between spins 1-2 and spins 3-1. The effects of DQ-relaxation were approximated by multiplying the calculated SQ intensity with a decaying exponential [46] of the form $e - \frac{t}{2 \times T_2 DQ}$. DRAWS curves were calculated from 3Å to 9Å and used to find a best fit to the experimental data points by minimizing the residual:

$\chi = \sqrt{\frac{\sum_{i=1}^{n} w_i (x_i - x_{calc})^2}{n}}$, where x_i and w_i are the experimental data and error respectively.

Synthesis of $Zr[(O_3PCH_2)(HO_3PCH_2)NHCH_2COOH]_2 \cdot 2H_2O$ as a $^{31}P\{^{13}C\}$REDOR Calibration Standard

A clear solution of (2-13C) Glyphosine (300mg, 1.2mmol) in 9mL of water was added to a solution of ZrOCl2·8H_2O (192mg, 0.6mmol) in 2.9M HF (2.46mL, 7.2mmol) in a closed HDPE vessel. The mixture was maintained at 80°C for 7 days in a mineral oil bath. White crystals were obtained and isolated using vacuum filtration. After washing with water, crystals were placed in a vacuum desiccator where they were dried for 48 hours [31]. A 97mg quantity of product was recovered. The product was confirmed to be the correct structure by PXRD with unit cell dimensions as follows: a = 5.44 angstroms, b = 14.95 angstroms, c = 13.31 angstroms, alpha = 90 degrees, beta = 95.26 degrees, gamma = 90 degrees.

$^{13}C\{^{31}P\}$REDOR of $Zr[(O_3PCH_2)(HO_3PCH_2)NHCH_2COOH]_2 \cdot 2H_2O$

$Zr[(O_3PCH_2)(HO_3PCH_2)NHCH_2COOH]_2\cdot 2H_2O$ was loaded into a ceramic solid state NMR sample rotor with a 1mm teflon spacer and a 2mm plastic drive tip. $^{13}C\{^{31}P\}$REDOR was carried out as described in the main text. All ^{31}P nuclei within 10Å of [2-^{13}C] Glyphosine of $Zr[(O_3PCH_2)(HO_3PCH_2)NHCH_2COOH]_2$ contributed to non-linear curve calculations.

Molecular Dynamics Simulations

Models for molecular dynamics were built in Schrodinger suite's Maestro. A peptide monolayer of 16 β-strands by 10 β-sheets was constructed using *pep-KG.* Distance from PXRD were used to create the *pep-KG* monolayer. Eight DNA$(A)_{10}$ strands were placed at each cross-β interface and manually manipulated to place phosphates toward terminal lysines. DNA$(A)_{10}$ strands were oriented along the H-bonding direction. Periodic boundaries approximating infinite H-bonded β-sheets were defined as 76Å in the direction of H-bonding, 110Å in the direction of β-sheet lamination, and 200Å parallel with extended peptides. The box defining these boundaries was solvated with simple point charge water (SPC) and defined under optimized parameters for liquid systems. Minimization was performed after solvation. Molecular dynamics simulations were carried out using Desmond. The time of each simulation was defined as 1.2ns.

Modeling of Peptides.

The individual peptide model and RNA model were generated in Chimera [48]. Based on the experimental data, the peptide model and RNA model were further organized to the models of 3D superstructures using Strata 3D (https://www.strata.com/). Peptides were oriented anti-parallel with all amino acids in-register, the interstrand distance set to 4.7Å, and the intersheet distance set to 11Å for both peptide-only assemblies and RNA/peptide co-assemblies. Peptide Ac-KLVIIAG-NH_2 was used in all models. RNA was placed at high-density between peptide monolayers in RNA/peptide co-assembly models to account for 100% dipolar recoupling of ^{13}C and ^{31}P in $^{13}C\{^{31}P\}$REDOR.

References

[1] Marcinkiewics, M. βAPP and Furin mRNA concentrates in immature senile plaques in the brain of Alzheimer patients. *J. Neuropathol. Exp. Neurol.* **61,** 815-829 (2002).

[2] Macedo, B. *et al.* Nonspecific prion protein-nucleic acid interactions lead to different aggregates and cytotoxic species. *Biochemistry* **51,** 5402-5413 (2012).

[3] Supattapone, S. What makes a prion infectious? *Science* **327,** 1091-1092 (2010).

[4] Geoghegan, J. C. *et al.* Selective incorporation of polyanionic molecules into hamster prions. *J. Biol. Chem.* **282,** 36341-36353 (2007).

[5] Ginsberg, S. D. *et al.* Predominance of neural mRNAs in individual Alzheimer's Disease senile plaques. *Ann. Neurol.* **45,** 174-181 (1999).

[6] Ginsberg, S. D. *et al.* RNA sequestration to pathological lesions of neurodegenerative diseases. *Acta Neuropathologia*, **96,** 487-494 (1998).

[7] Cherny, D., Hoyer, W., Subramaniam, V., Jovin, T. M. Double-Stranded DNA Stimulates the Fibrillation of α-Synuclein *in vitro* and is Associated with the Mature Fibrils: An Electron Microscopy Study. *J. Mol. Biol.* **344,** 929-938 (2004).

[8] Ginsberg, S. D., Crino, P. B., Lee, V. M-Y., Eberwine, J. H., Trojanowski J. Q. Sequestration of RNA in Alzheimer's Disease Neurofibrillary Tangles and Senile Plaques. *Ann. Neurol*. **41,** 200-209 (1997).

[9] Erickson, S. L., Lykke-Andersen, J. Cytoplasmic mRNP granules at a glance. *J. Cell Sci.* **124,** 293-297 (2011).

[10] Aguzzi, A., Altmeyer, M. Phase separation: linking cellular compartmentalization to disease. *Trends in Cell Biol.* **26,** 547-558 (2016).

[11] Schwartz, J. C., Wang, X., Podell, E. R., Cech, T. R. RNA seeds higher-order assembly of FUS protein. *Cell Rep.* **5,** 918-925 (2013).

[12] Wang, M., Law, M., Duhamel, J., Chen, P. Interaction of a self-assembling peptide with oligonucleotides: complexation and aggregation. *Biophys. J.* **93,** 2477-2490 (2007).

[13] Braun, S. *et al.* Amyloid-Associated Nucleic Acid Hybridisation, *PLoS one* **6,** e19125 (2011).

[14] Banani, S. F. *et al.* Compositional control of phase-separated cellular bodies. *Cell* **166,** 651-663 (2016).

[15] Hayes, M. H., Weeks, D. L. Amyloids assemble as part of recognizable structures during oogenesis in *Xenopus*. *Biol. Open* **5,** 801-806 (2016).

[16] Patel, A. *et al.* A liquid-to-solid phase transition of the ALS Protein FUS accelerated by disease mutation. *Cell* **162,** 1066-1077 (2015).

[17] Ramaswami, M., Taylor, J. P., Parker, R. Altered ribostasis: RNA-protein granules in degenerative disorders. *Cell* **154,** 727-736 (2013).

[18] Sunde, M., Blake, C. The structure of amyloid fibrils by electron microscopy and x-ray diffraction. *Adv. Protein Chem.* **50,** 123-159 (1997).

[19] Glenner, G. G. Amyloid deposits and amyloidosis. *N. Engl. J. Med.* **302,** 1283-1292 (1980).

[20] Ow, S., Dunstan, D. E. A brief overview of amyloids and Alzheimer's disease. *Protein Sci.* **23,** 1315-1331 (2014).

[21] Shin, J., Salameh, J. S., Richter, J. D. Impaired neurodevelopment by the low complexity domain of CPEB4 reveals a convergent pathway with neurodegeneration. *Sci. Rep.* **6,** (2016).

[22] Mehta, A. K. *et al.* Context dependence of protein misfolding and structural strains in neurodegenerative diseases. *Biopolymers* **100,** 722-730 (2013).

[23] Jones, E. M., Surewicz, W. K. Fibril conformation as the basis of species- and strain-dependent seeding specificity of mammalian prion amyloids. *Cell* **121,** 63-72 (2005).

[24] Guo, J. L. *et al.* Distinct α-Synuclein strains differentially promote tau inclusions in neurons. *Cell* **154,** 103-117 (2013).

[25] Mehta, A. K. *et al.* Facial symmetry in protein self-assembly. *J. Am. Chem. Soc.* **130,** 9829-9835 (2008).

[26] Bower, P. V., Oyler, N., Mehta, M. A., Long, J. R., Stayton, P. S., Drobny, G. P. Determination of torsion angles in proteins and peptides using solid state NMR. *J. Am. Chem. Soc.* **36,** 8373-8375 (1999).

[27] Gullion, T., Schaefer, J. ROTATIONAL-ECHO DOUBLE-RESONANCE NMR. J. Magn. Reson. **81,** 196-200 (1989).

[28] Bloembergen, N., Purcell, E. M., Pound, R. V. Relaxation effects in nuclear magnetic resonance absorption. *Physical Review* **73,** 679-712 (1948).

[29] Sugawara, Y., Iwasaki, H. Structure of Disodium Uridine Diphosphoglucose Dihydrate, $C_{15}H_{22}N_2O_{17}P_2^{2-}.2Na^+.2H_2O$, and Refinement of Dipotassium Glucose 1-Phosphate Dihydrate, $C_6H_{11}O_9P^{2-}.2K^+.2H_2O$ (Monoclinic Form). *Acta. Cryst.* **40,** 389-393 (1984).

[30] Lis, T. Monopotassium Phosphoenolpyruvate: New Diffractometer Data. *Acta. Cryst.* **43,** 1898-1900 (1987).

[31] Taddei, M., Donnadio, A., Constantino, F., Vivani, R., Casciola, M. Synthesis, Crystal Structure, and Proton Conductivity of One-Dimensional, Two-Dimensional, and Three-Dimensional Zirconium Phosphonates Based on Glyphosate and Glyphosine. *Inorganic Chemistry* **52,** 12131-12139 (2013).

[32] Childers, W. S., Mehta, A. K., Lu, K., Lynn, D. G. Templating molecular arrays in amyloid's cross-β grooves. *J. Am. Chem. Soc.* **131,** 10165-10172 (2009).

[33] Schmidt, H. B., Görlich, D. Transport selectivity of nuclear pores, phase separation, and membraneless organelles. *Trends Biochem. Sci.* **41,** 46-61 (2016).

[34] Bellini, T. *et al.* Liquid crystal self-assembly of random-sequence DNA oligomers. *Proc. Natl. Acad. Sci. USA* **109,** 1110-1115 (2012).

[35] Nielsen, F. C., Hansen, H. T., Christiansen, J. RNA assemblages orchestrate complex cellular processes. *Bioessays* **38,** 674-681 (2016)

[36] Courchaine, E. M., Lu, A., Neugebauer, K. M. Droplet organelles. *EMBO J.* **35,** 1603-1612 (2016).

[37] Ni, R., Chau, Y. Structural mimics of viruses through peptide/DNA co-assembly. *J. Am. Chem. Soc.* **136,** 17902-17905 (2014).

[38] Marreiros, R. *et al.* Viral capsid assembly as a model for protein aggregation diseases: active processes catalyzed by cellular assembly machines comprising novel drug targets. *Virus Res.* **207,** 155-164 (2015).

[39] Li, C. Rapid formation of a supramolecular polypeptide-DNA hydrogel for in situ three-dimensional multilayer bioprinting. *Angewandte Chemie* **54,** 3957-3961 (2015).

[40] Shuai, H-L., Huang, K-J., Xing, L-L., Chen, Y-X. Ultrasensitive electrochemical sensing platform for microRNA based on tungsten oxide-graphene composites coupling with catalyzed hairpin assembly target recycling and enzyme signal amplification. *Biosens. Bioelectron.* **86,** 337-345 (2016).

[41] Katz, E., Willner, I. Biomolecule-functionalized carbon nanotubes: applications in nanobioelectronics. *ChemPhysChem* **5,** 1084-1104 (2004).

[42] Carny, O., Gazit, E. A model for the role of short self-assembled peptides in the very early stages of the origin of life. *FASEB J.* **19,** 1051-1055 (2005).

[43] Goodwin, J., Mehta, A. K., Lynn, D. G. Analog and Digital Chemical Evolution. *Acc. Chem. Res.* **45,** 2189-2199 (2012).

[44] Mehta, M. A., Eddy, M. T., McNeill, S. A., Mills, F. D., Long, J. R. Determination of peptide backbone torsion angles using double-quantum dipolar recoupling solid-state NMR Spectroscopy. *J. Am. Chem. Soc.* **130,** 2202-2212 (2008).

[45] Fung, B. M., Khitrin, A. K., Ermolaev, K. An improved broadband decoupling sequence for liquid crystals and solids. *J. Magn. Reson.* **142,** 97-101 (2000).

[46] Bak, M., Rasmussen, J. T., Nielsen, N. C., SIMPSON: A general simulation program for solid-state NMR spectroscopy. *J Magn Reson* **147,** 296-330 (2000).

[47] Gregory, D. M. *et al.* Dipolar recoupling NMR of biomolecular self-assemblies: determining inter- and intrastrand distances in fibrilized Alzheimer's beta-amyloid peptide. *Solid State Nucl. Magn. Reson*. **13,** 149-166 (1998).

[48] Pettersen, E. F. *et al.* UCSF Chimera--a visualization system for exploratory research and analysis. *J. Comput. Chem.* **25,** 1605-1612 (2004).

Chapter 6: Nucleic Acid/Peptide Co-assemblies and Disease Etiology

Introduction

Protein and peptide/nucleic acid interactions are often associated with neurodegeneration when protein misfolding is a hallmark of disease onset [1-9]. For example, Furin and βAPP mRNAs are enriched in immature senile plaques of Alzheimer's patients brains [2], and prion proteins in association with nucleic acids display enhanced cytotoxicity [3]. Double-stranded DNA has also been identified in association with mature α-synuclein fibrils and *in vitro*, stimulates fibrillation [9]. While much work has focused on the pathogenic cross-seeding of amyloid-forming proteins [10,11], little is known of the association between pathogenic proteins and RNA.

In degenerative diseases, the accumulation of mutated RNAs in nuclear foci and the redistribution of certain RNA binding proteins to the nucleus or cytoplasm underlie molecular pathogenesis [12-16]. In myotonic dystrophy, microsatellite expansion of RNAs DMPK and ZNF9 leads to the sequestration of splicing factors to nuclear foci, disrupting normal RNA processing [17,18]. A similar pathology is observed in Alzheimer's disease where sequestration of RNA processing machinery, including U1-70K, leads to their presence in large insoluble tangle-like inclusions and presumably splicing defects [19]. The mutation of a key RNA binding protein involved in stress granule assembly and alternative splicing, TIA1 [20,21], in Welander distal myopathy leads to the persistence of cytosolic inclusions, highlighting the granule maturation events discussed extensively in Chapter 4 [22,23]. Inclusions with ALS pathologies have also identified markers of stress granules [24,25]. Interception of messenger ribonucleoprotein (mRNP) granules, sites of RNA processing, by pathogenic proteins may well lead to the disruption of RNA homeostasis, a process the granules exclusively manage [26-30]. In this chapter we begin to dissect the interactions between the β-amyloid peptides of Alzheimer’s disease, Aβ40 and 42, and nucleic acids. The dysregulation of RNA binding proteins and the aggregation of β-amyloid in Alzheimer’s disease are intimately linked in our model describing the nucleation and propagation events necessary for disease etiology [31,32].

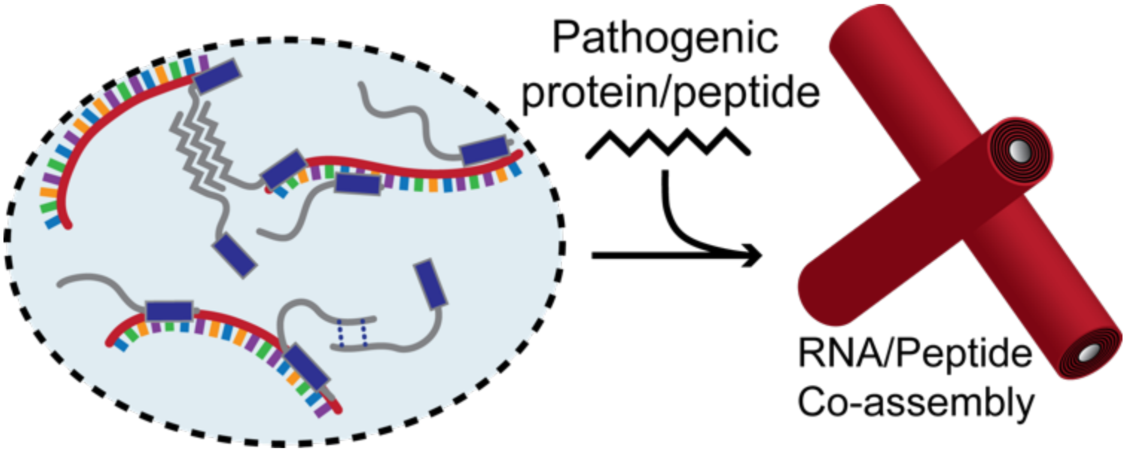

Figure 6-1 Interception of mRNP granules by β-sheet-prone infectious domains of pathogenic proteins/peptides leads to nucleation and propagation of infectious domains and sequestration of nucleic acids.

Results

The global and structural characterization of a designed RNA/peptide co-assembly in Chapters 4 and 5 uniquely positions us to examine other nucleic acid/peptide interactions that might persist in protein-misfolding and degenerative diseases. Determining how nucleic acid presence affects amyloid formation will provide insight to the mechanism by which nucleic acids are sequestered to and associated with mature amyloid fibrils [2,7-11]. The interception of mRNP granules by β-sheet-prone infectious domains of pathogenic proteins and peptides likely contributes to the propagation of mature fibrils and altered ribostasis [6].

Aβ40 and 42 fibril surfaces are ideal for templating nucleic acids

Aβ40 and Aβ42, which only vary by two amino acids at the C-terminus, vary considerably in their published 3D structures [33,34]. Despite these variations, examination of surface charges suggests some complementarity with the phosphate backbone of nucleic acids is possible, and disordered regions may promote flexibility or plasticity in nucleic acid association.

In 2013, Lu et al. [33] published an article in *Cell* describing the structure of Aβ40 fibrils seeded from Alzheimer's patient brain homogenate. From selective isotope-enrichment and two-dimensional solid state NMR data, they published a model with three-fold cross-β symmetry. On the surface of Aβ40 fibrils, The N-terminal cationic residues remain largely solvent-exposed. Our global and structural data from Chapters 4 and 5, which purports that interactions between amyloid-forming peptides and nucleic acids are primarily electrostatic, support a comprehensive model for Aβ/nucleic acid co-assembly via electrostatic interactions. As seen with *pep-KG* in Chapters 4 and 5, nucleic acid/peptide co-assembly may influence the global morphology of fibrils as well.

Prior to the publication of these data by Lu et al., Lührs et al. [34] contrived a model for Aβ42 fibril structure based on quenched hydrogen/deuterium exchange NMR and pairwise mutagenesis studies. This structure was further constrained by previous solid state NMR studies aligning peptides parallel, in-register. From their data, they published a fibril structure with two-fold symmetry and the N-terminal 17 amino acids disordered. Amino acids 18-42 form a beta-turn that propagates perpendicular to the fibril long-axis. The bundling of at least four protofibrils was revealed by cryo electron microscopy and supported by simulations. Unlike the published Aβ40 structure, the disordered arrangement of the majority of charged residues at the N-terminus of Aβ42 allows for a more dynamic association with nucleic acid.

^{1}DAEFRHDSGYEVHHQKLVFFAEDVGSNKGAIIGLMVGGVV^{40}IA

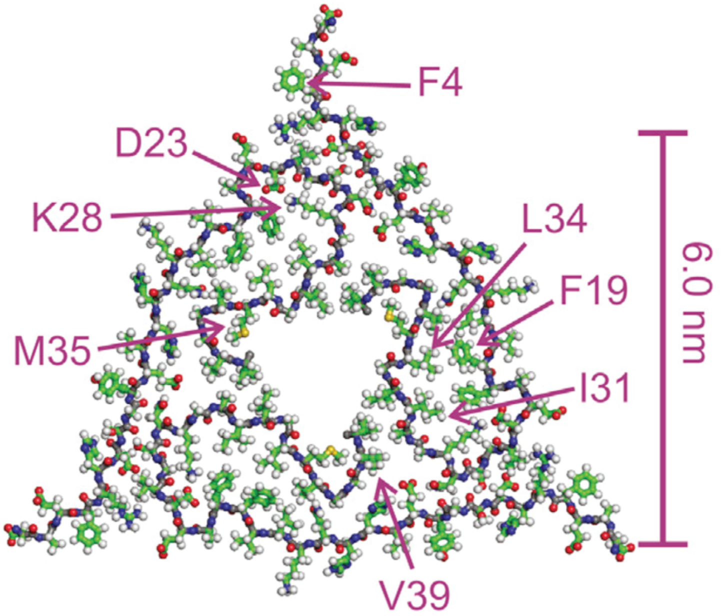

Figure 6-2 Amino acid sequence of Aβ40 and Aβ42, and published structure of Aβ40 fibril with three-fold symmetry. *Residues highlighted in green are acidic and solvent exposed. Residues highlighted in blue are basic and solvent exposed. Structure adapted with permission by author, from Lu et al. [33].*

Co-assembly of Aβ40 and 42 with RNA

Initial examination of Aβ/RNA co-assembly began with transmission electron microscopy (TEM). With TEM, large scale changes in amyloid morphology are observable. TEM can be a subjective measure of the degree of peptide assembly, but is most often used to highlight the presence or emergence of nanostructures over time.

To assess co-assembly of Aβ and RNA, the following samples were set up: Aβ40 90μM, Aβ42 90μM, Aβ40 90μM with RNA$(A)_{10}$ 90μM, and Aβ42 90μM with RNA$(A)_{10}$ 90μM. All samples were prepared in 10mM Phosphate Buffer with 0.02% azide and kept at 37°C. At 24 hours of assembly, TEM grids were prepared. Although not quantitative, electron micrographs reveal the start of fibril formation in three out of four of the samples (Figure 6-3). Aβ40 with RNA, at 24 hours, did not appear to assemble; amorphous aggregates were observed by TEM.

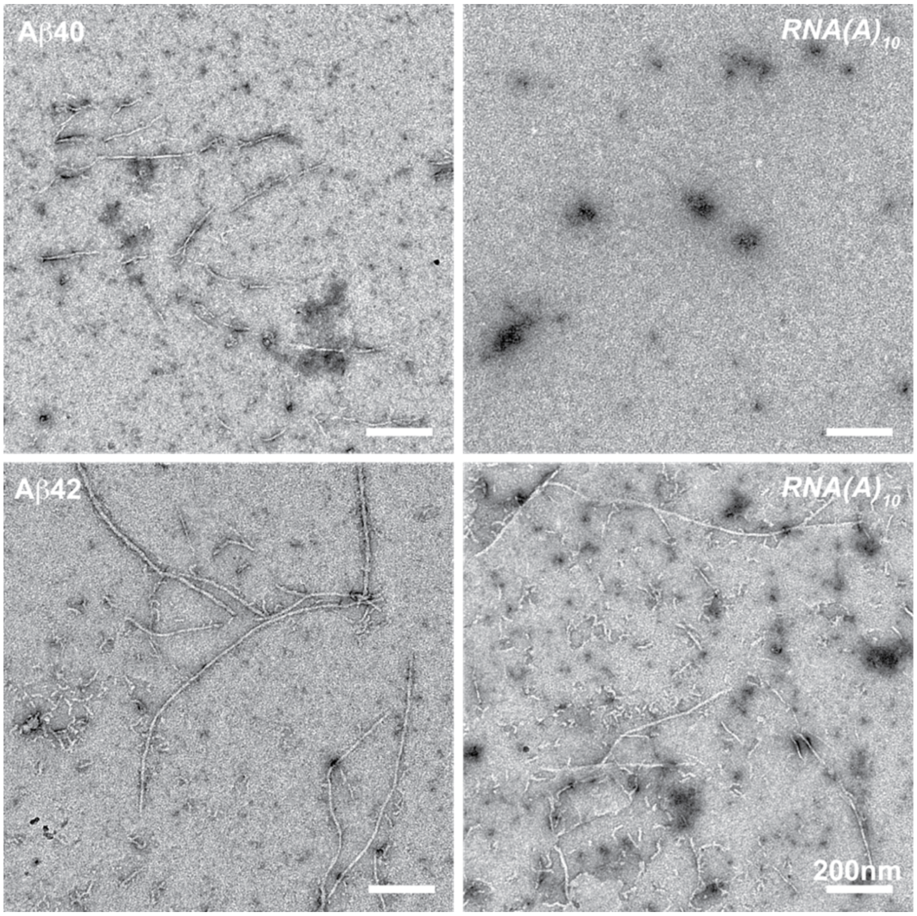

Figure 6-3 Aβ40/42 assembly and Aβ40/42 co-assembly with RNA as scored by TEM at 24 hours. *Aβ-alone assemblies are shown in first column. Aβ/RNA co-assemblies are present in second column. All scale bars are 200nm.*

Assembly and co-assembly maturation was examined again at one week post-mixing. In contrast to assemblies at 24 hours, short protofibrils were primarily present in peptide-alone samples, while RNA-containing samples showed more organized supramolecular architectures. Aβ40/RNA co-assemblies appeared as short fibrils with smooth edges and aggregated in plaque-like clusters. Fibers were observed in Aβ42/RNA co-assemblies with lengths often exceeding 1μm.

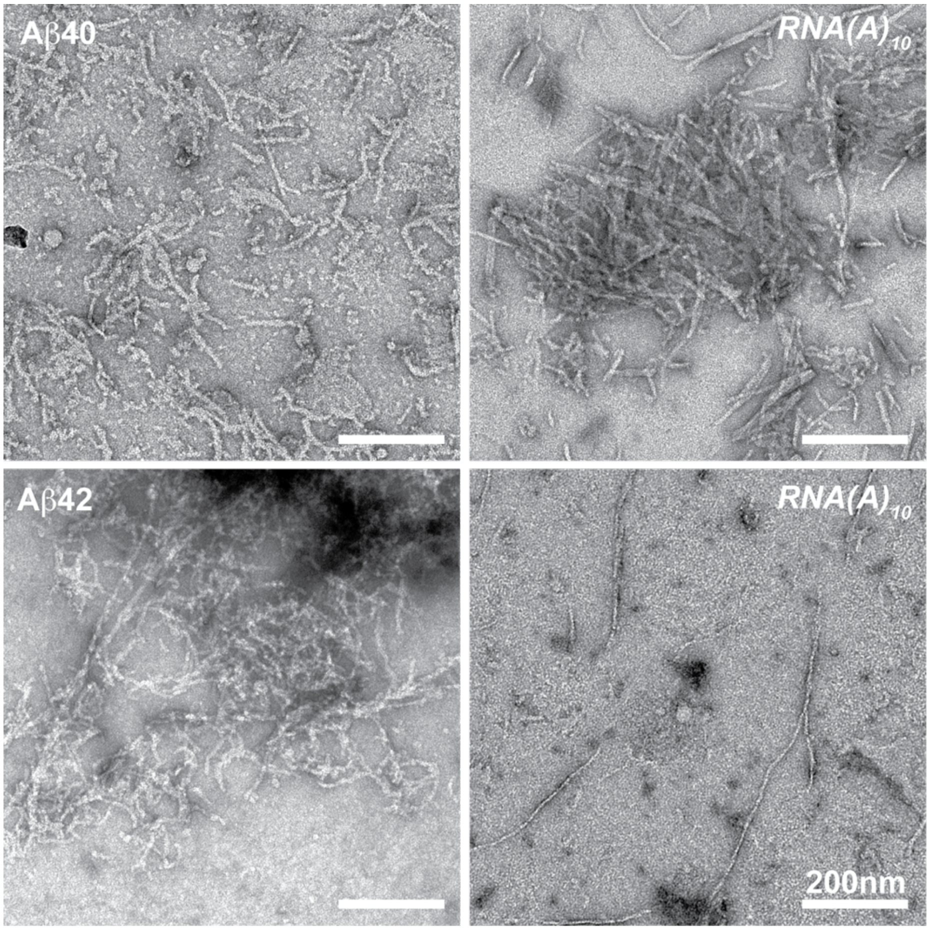

Figure 6-4 Aβ40/42 assembly and Aβ40/42 co-assembly with RNA as scored by TEM at one week post-mixing. *Aβ-alone assemblies are shown in first column. Aβ/RNA co-assemblies are present in second column. All scale bars are 200nm.*

At two weeks post-mixing, homology between assemblies and co-assemblies was observed; nanostructures aggregated to form branching and network-like architectures. In Aβ40 samples, the typical twisting and pitch of long fibers was observed. However, shorter protofibrils persisted. As compared with one week co-assemblies, Aβ40/RNA fibril aggregates were not abundant. Aβ42 assemblies and Aβ42/RNA co-assemblies did not possess any discernible differences by TEM.

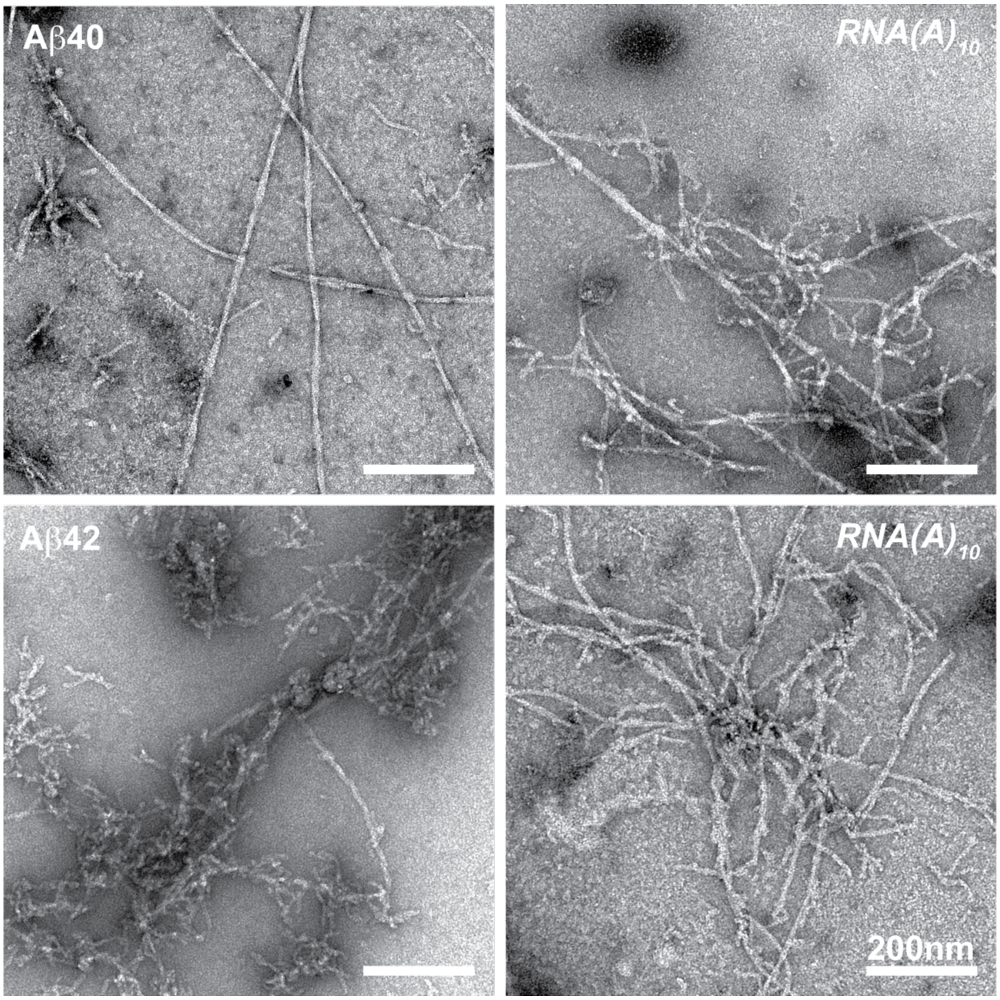

Figure 6-5 Aβ40/42 assembly and Aβ40/42 co-assembly with RNA as scored by TEM at two weeks post-mixing. *Aβ-alone assemblies are shown in first column. Aβ/RNA co-assemblies are present in second column. All scale bars are 200nm.*

By TEM, at three weeks post-mixing, Aβ40 assembly appeared as short protofibrils less than 200nm in length. This is in contrast to the long fibers observed the previous week and may be due more to sample preparation than a reflection of assembly maturity. Aβ42 assemblies appeared similar to previous weeks where aggregated short fibrils dominated the grid. For both Aβ/RNA co-assemblies, aggregation of fibrils into plaque-like clusters was observed. For all samples examined, finding nanostructures on prepared grids proved difficult. A low assembly concentration may limit our ability to examine these structures subjectively by TEM and other microscopy techniques.

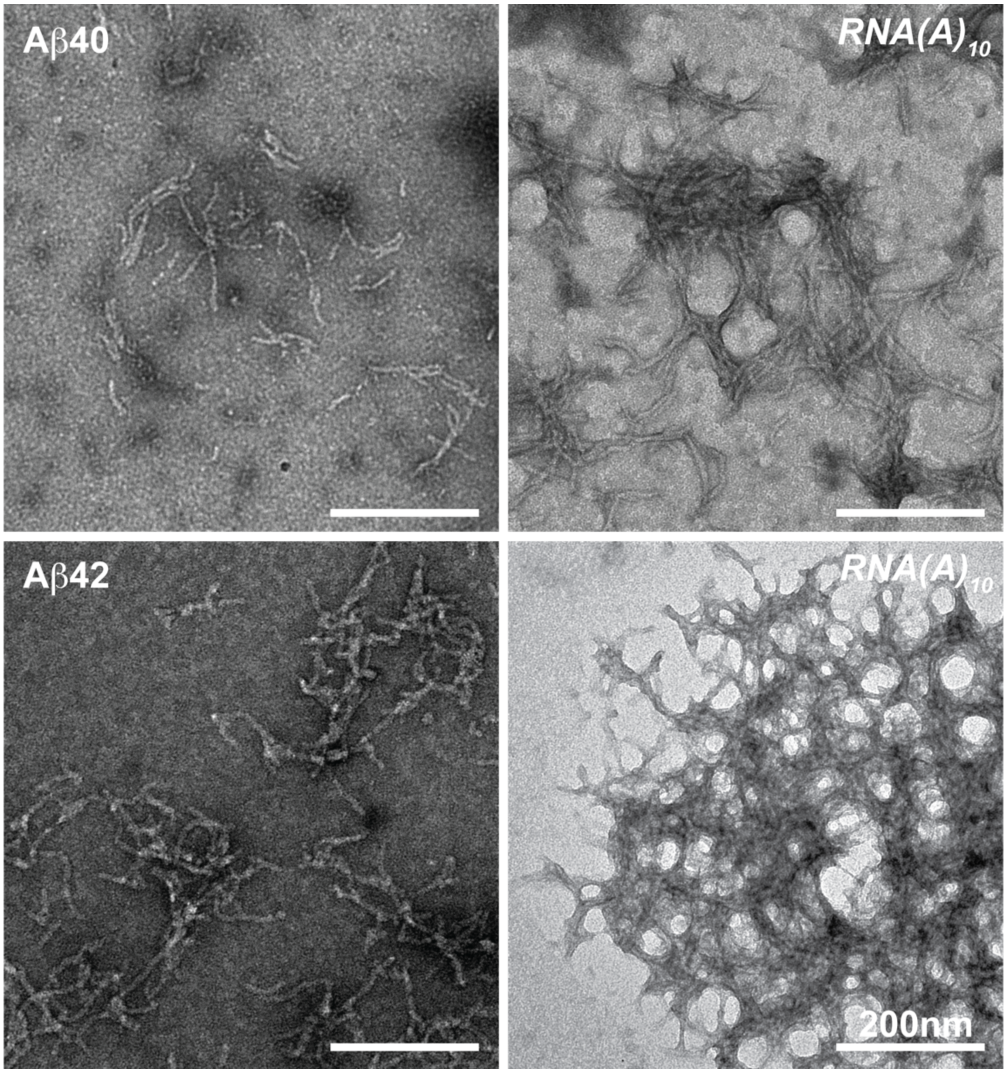

Figure 6-6 Aβ40/42 assembly and Aβ40/42 co-assembly with RNA as scored by TEM at three weeks post-mixing. *Aβ-alone assemblies are shown in first column. Aβ/RNA co-assemblies are present in second column. All scale bars are 200nm.*

Visualization of co-assembly by fluorescence microscopy

Despite variable assembly by TEM, laser-scanning confocal fluorescence microscopy was used to further assess Aβ co-assembly with RNA. For examination by fluorescence microscopy, Aβ40 and Aβ42 were co-assembled with RNA$(A)_{10}$-Cy3, where Cy3 was covalently attached to the 3'-end. Thioflavin T, a small molecule whose excitation and emission changes upon binding cross-β was used as an indicator of amyloid. The co-localization of Thioflavin T (peptide-field) and Cy3 (RNA field) would suggest the co-assembly of Aβ peptides and RNA. As expected based on TEM analysis, identifying assembly by fluorescence microscopy proved difficult. However, both Aβ40/RNA and Aβ42/RNA samples showed some co-localization of Thioflavin T and Cy3 suggesting co-assembly (Figure 6-7).

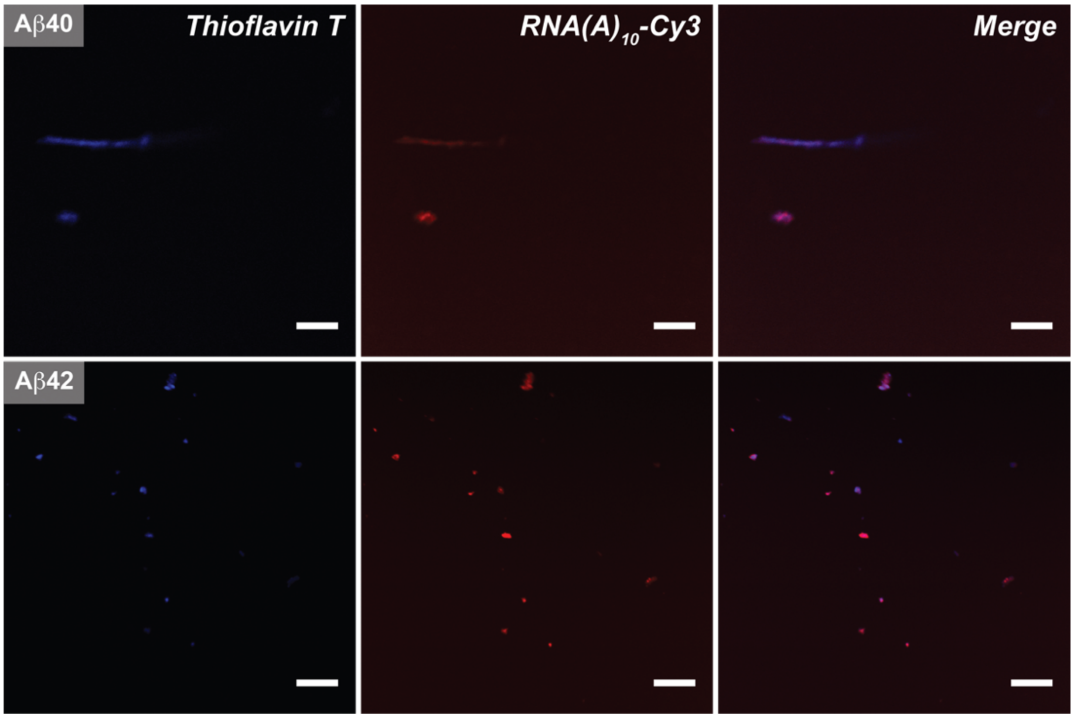

Figure 6-7 Laser-scanning confocal fluorescence microscopy of Aβ40/RNA and Aβ42/RNA co-assemblies. *RNA(A)$_{10}$ was covalently tagged with Cy3 at the 3'-end. Thioflavin T was used as a marker of amyloid. The merge of the two fields is shown in the right-most column. Scale bars are 10μm.*

Co-assembly maturation of Aβ40 and 42 with RNA(A)$_{10}$-Cy3 was confirmed by TEM, and no anomalies appeared between micrographs containing Cy3-tagged RNA and untagged RNA at three weeks post-mixing (Figure 6-6 and 6-8).

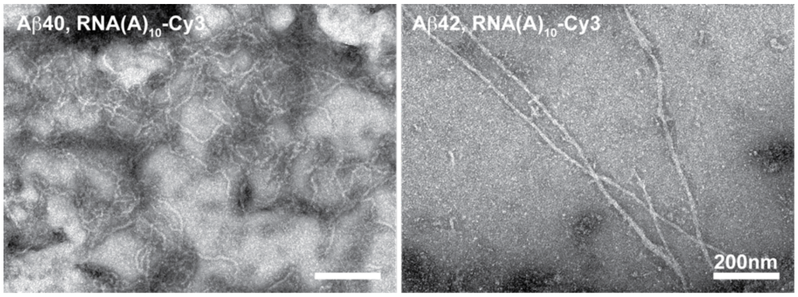

Figure 6-8 Aβ40/42 co-assembly with RNA-Cy3 as scored by TEM at three weeks post-mixing. *Scale bars are 200nm.*

Circular Dichroism identifies order in co-assemblies

Conformational information about incorporated RNA(A)$_{10}$ in Aβ/RNA co-assemblies can be extrapolated from Circular Dichroism (CD) data. In the absence and presence of Aβ at three weeks post-mixing, canonical RNA ellipticities are observed. The presence of Aβ enhances molar ellipticity signatures suggesting an increase in the ordering of RNA within co-assemblies [35,36]. Double stranded RNA, which natively folds as an A-form helix is stabilized by vertical base-base stacking and the hydrogen-bonding of base pairs [37]. Base-base stacking, which contributes almost twice as much to stability as hydrogen-bonding, is responsible for the maintenance of A-form helices in single stranded RNA samples [35,37]. RNA is unable to access the B-form conformation because the 2'-hydroxyl of its ribose prevents C2'-endo and selects for C3'-endo sugar puckering [37]. The contribution of this homogeneous sugar puckering is observed at 265nm for Poly(rA) oligomers [35]. The positive long-wavelength contribution, in accordance with UV absorption, confirms the formation of the right-handed helix [37]. With the exception of the sugar puckering contribution, the remaining elliptical signatures are attributed to base-base stacking and sugar-base torsion angles [35.38]. The observed increase in ellipticities for RNA in association with Aβ is attributed to the existence of a higher concentration of RNAs fixed in the A-form helical conformation. Co-assembly of Aβ with RNA(A)$_{10}$ stabilizes the single stranded helix, increasing the hydrophobic environment surrounding bases and increasing the ellipticity of the base-base contributions. These data support the co-assembly of Aβ and RNA and highlight the maintenance of RNA structural integrity in co-assemblies. CD of Aβ40 and Aβ42 assemblies at three weeks post-mixing lack the negative cotton effect associated with β-sheet-rich assemblies. The concentration of assembled amyloid fibrils is likely below the detection threshold.

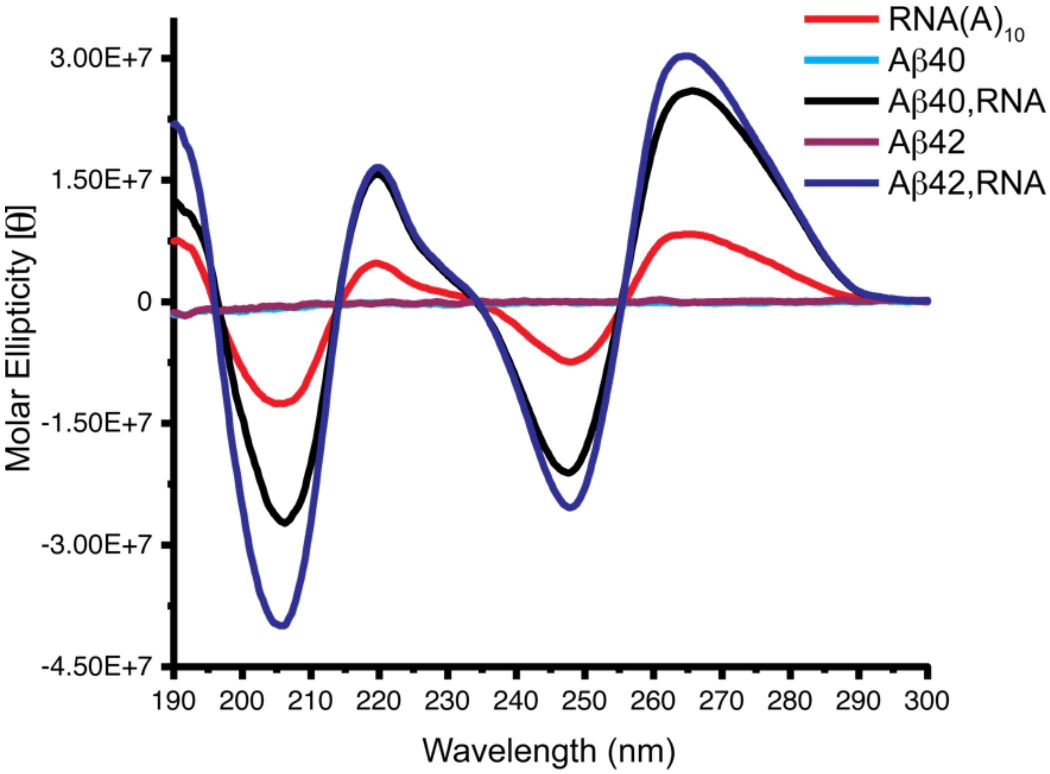

Figure 6-9 Circular Dichroism analysis of Aβ40/42 assemblies and Aβ40/ and Aβ42/RNA co-assemblies. *Molar Ellipticity [θ] is plotted on the y-axis and calculated based on the following equation:* $[\theta] = \theta/(10 \times c \times l)$ *where c=concentration (mol/L) and l=pathlength (cm).*

Powder x-ray diffraction of co-assemblies

With fibril concentration below the detection threshold of Circular Dichroism for characterization of the beta-sheet architecture, powder x-ray diffraction (PXRD) was explored for more detailed analysis. By PXRD, Aβ40/RNA co-assembly was assigned as cross-β. Diffraction data at short distances was complicated by the diffraction of the $NaHPO_4$ salt of the buffer, but cross-β reflections were unaffected. Because of the sample size, removal of buffer prior to sample prep for PXRD was not possible. Bands at 4.7/4.85Å, 9.56Å and 10.05Å are attributed to peptide secondary structure and correspond with interstrand and intersheet distances, respectively. A reflection at 2.28Å may represent the base rise along the incorporated A-form RNA helix, but the RNA phase was not conclusively solved.

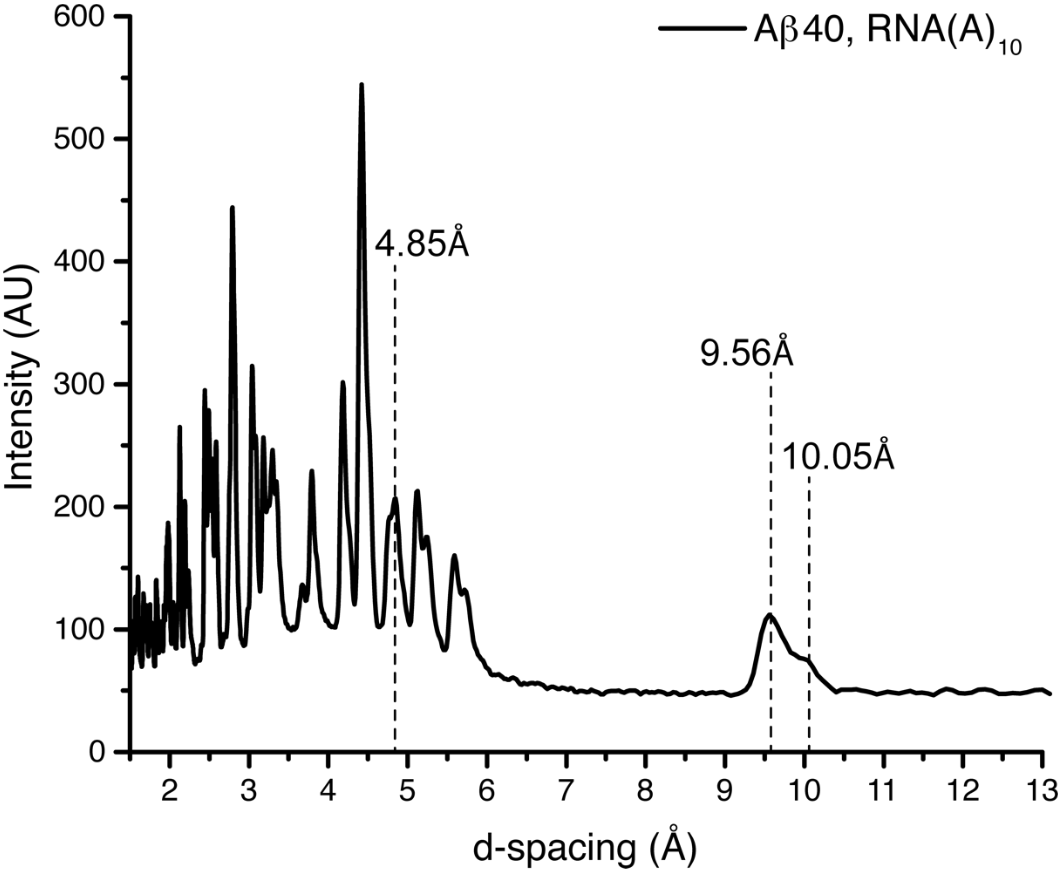

Figure 6-10 PXRD analysis of Aβ40/RNA(A)$_{10}$ co-assembly. *Reflections at 4.7/4.85Å, 9.56Å, and 10.05Å are attributed to peptide secondary structure. Abundance of short distances by diffraction are assigned to NaHPO$_4$ from the buffer.*

Examination of Ab42/RNA co-assemblies by PXRD was less conclusive in terms of secondary or tertiary assembly structure. A small peak at 3.2Å, hidden peaks 5.5Å and 6.1Å, and the peak at 4.85Å can be attributed to the peptide phase. These reflections alone do not support cross-β architecture. A reflection at 2.3Å may indicate base stacking in A-form RNA helices. However, the RNA phase has not been solved for these data.

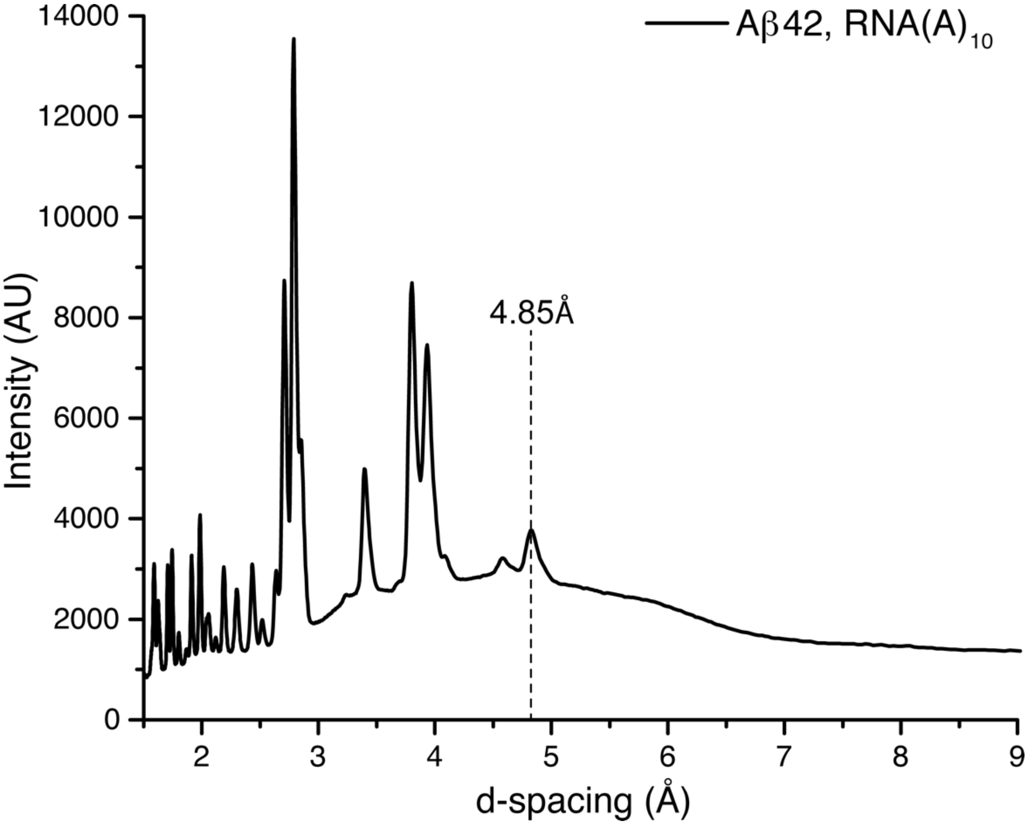

Figure 6-11 PXRD analysis of Aβ42/RNA(A)$_{10}$ co-assembly. *Reflections at 3.2Å, 4.85Å, 5.5Å, and 6.1Å are attributed to peptide secondary structure. Abundance of short distances by diffraction are assigned to NaHPO$_4$ from the buffer.*

Conclusions

The interactions between pathogenic proteins or peptides and nucleic acid are without doubt. In a multitude of protein-misfolding diseases, the association of nucleic acids with protein inclusions has been described [1-3,7-11]. Investigation into the role of nucleic acids in disease pathogenesis has begun, and the mechanism of its sequestration evaluated. RNA, which has been shown to nucleate the formation of FUS fibrils [39] and increase the cytotoxicity of prions [3], is highly-processed in the cell through the use of ribonucleoprotein (RNP) granules [27-29]. The interception of RNP granules by pathogenic proteins would account for the disruption of RNA homeostasis and the sequestration of RNA to protein inclusions in protein-misfolding diseases [7-16,26-30].

The dynamic interactions between RNA and amyloid-forming peptides was described in chapters 4 and 5 where nucleic acid was shown to be essential to the nucleation and propagation of homogeneous RNA/peptide co-assemblies, and in chapter 3 where DNA secondary structure was necessary for conical homogeneous architectures. The use of Aβ40 and Aβ42 of Alzheimer's disease begins to interrogate the mechanism of RNP granule interception during disease etiopathogenesis.

In this chapter, we begin to assess the interactions between Aβ40/42 and RNA. Through use of microscopy, spectroscopic methods, and x-ray diffraction, the assembly of peptides and conformational homogeneity of RNA was characterized. Aβ40/RNA and Aβ42/RNA co-assemblies show co-localization of amyloid and RNA domains by laser-scanning confocal microscopy. These data support the co-assembly of RNA and full-length amyloid-β peptides. The CD signature for RNA in the presence of Aβ peptides was increased compared to RNA alone, suggesting a higher concentration of ordered base-base contributions in the A-form helices [35,37]. Macromolecular crowding would easily explain this phenomenon. However, aggregation of peptides impedes the measurable effect of macromolecular crowding [40]. Therefore, the change in RNA ellipticity should be attributed to its ordered co-assembly with Aβ peptides. Finally, PXRD analysis of Aβ40/RNA co-assemblies identifies the persistence of cross-β domains, an architecture regularly identified in Alzheimer's disease patient brains [33].

With the identification of RNA at the site of immature senile plaques [7,8], understanding the role RNA might have in plaque morphology is crucial. Our characterization of RNA/peptide co-assemblies in chapters 4 and 5, that of a peptide/DNA conjugate assembly in chapter 3, and the sustained interaction between Aβ peptides and RNA here, begins to describe the influence of RNA presence and co-assembly on gross morphology, and informs on the amyloid/nucleic acid interactions that might dominate protein-misfolding disorders.

Methods

Peptide Synthesis. Peptides were synthesized using Solid Phase Peptide Synthesis (SPPS) with a PEG resin, and left uncapped at the N-terminus. Peptides were cleaved and deprotected using a cocktail of 90% TFA, 2% anisole, 3% 1,2-ethanedithiol, and 5% thioanisole. All chemicals were purchased from Sigma-Aldrich. Following cleavage and deprotection, peptides were purified by reverse-phase HPLC using acetonitrile and water with 0.1%TFA and a C18 column to a >98% purity. Purification was performed twice because of breadth of peak on the chromatogram and to increase purity. After purification, acetonitrile was removed by rotavaporation. The remaining aqueous solution was frozen at -80°C or flash frozen using liquid nitrogen and lyophilized to yield a white powder.

Peptide Assembly. Peptides were placed in 10mM Phosphate buffer 0.02% azide, vortexed briefly and sonicated for 5 minutes to promote solubility. A stock solution of 100μM peptide was used to set up all assemblies. Experimental samples were set up within five minutes of dissolution. All nucleic acid oligomers were purchased from Integrated DNA Technologies. For NA/Peptide co-assemblies, a stock solution of 1mM

NA was used. Order of addition was as follows: Peptide, solvent, nucleic acid. Assemblies were kept at 37°C. Final peptide concentration in all experimental setups was 90μM. Final nucleic acid concentration was approximately 90μM.

Transmission Electron Microscopy. Electron microscopy images were obtained using a Hitachi H-7500 and a Jeoul transmission electron microscope. All samples were placed on 200 mesh copper grids with carbon coating and negatively stained using 2%w/w uranyl acetate (Sigma-Aldrich). The microscope was operated at 75kV. Cross-section images were obtained by embedding pelleted assemblies in resin. Using a microtome, embedded assemblies were sliced 1μm thick and placed on grids for analysis by TEM.

Laser-Scanning Fluorescence Confocal Microscopy. Fluorescence micrographs were obtained using an Olympus FluoView 1000 (FV1000) laser-scanning confocal microscope. Samples were prepared on microscope slides, with coverslips sealed using clear nail polish. Samples were examined using the 60X 1.42NA oil immersion objective. Thioflavin T was added to samples at a final concentration of 2mM prior to sample prep and the 405nm laser line was used to visualize its staining. The RNA$(A)_{10}$ with Cy3 covalently attached at the 3'-end was purchased from Integrated DNA Technologies. The 559nm laser line was used to visualize Cy3 signals. Images for Thioflavin T and Cy3 fields were obtained concurrently and processed using Fiji [56].

Circular Dichroism. A Jasco-810 Spectropolarimeter was used to record CD spectra. Samples were examined at room temperature in a 50μL cell with a 0.1mm path length. The reported spectra were acquired from 260nm to 190nm with a step size of 0.2nm and a speed of 100nm/s, and are the average of three independent scans. Ellipticity, in mdeg, was converted to Molar ellipticity (θ) with $[\theta] = \theta/(10 \text{ x c x } l)$, where 'c' is peptide concentration in moles/L and '*l*' is the pathlength in cm. Melting curves of *pep-KG* and NA/*pep-KG* samples were obtained using a gradient of temperature from 4°-60°C and a focal wavelength of 220nm and 260nm, respectively.

Powder X-Ray Diffraction. Experimental samples were flash frozen using liquid nitrogen and lyophilized to yield a white powder. The samples were loaded into mylar capillaries and the diffraction patterns measured using a Bruker APEX-II diffractometer with graphite monochromated Cu radiation, K-alpha radiation, λ=1.54184Å, 40kV and 35mA, with a 0.5 pinhole collimator and with exposure times of 900s per frame. The data integration software XRD2SCAN and the Bruker AXS software were used for analysis of the resulting diffraction patterns. The following equation was used to convert spectra from 2θ to d-spacing(Å): $1.54184/(2\times \sin\left(2\theta\times\frac{\frac{\pi}{180}}{2}\right))$

References

[1] Lim, L., Wei, Y., Lu, Y., Song, J. ALS-causing mutations significantly perturb the self-assembly and interaction with nucleic acid of the intrinsically disordered prion-Like domain of TDP-43. *PLOS Biology* **14,** (2016).

[2] Marcinkiewics, M. βAPP and Furin mRNA concentrates in immature senile plaques in the brain of Alzheimer patients. *J. Neuropathol. Exp. Neurol.* **61,** 815-829 (2002).

[3] Macedo, B. *et al.* Nonspecific prion protein-nucleic acid interactions lead to different aggregates and cytotoxic species. *Biochemistry* **51,** 5402-5413 (2012).

[4] Supattapone, S. What makes a prion infectious? *Science* **327,** 1091-1092 (2010).

[5] Geoghegan, J. C. *et al.* Selective incorporation of polyanionic molecules into hamster prions. *J. Biol. Chem.* **282,** 36341-36353 (2007).

[6] Ramaswami, M., Taylor, J. P., Parker, R. Altered ribostasis: RNA-protein granules in

degenerative disorders. *Cell* **154,** 727-736 (2013).

[7] Ginsberg, S. D. *et al.* Predominance of neural mRNAs in individual Alzheimer's Disease senile plaques. *Ann. Neurol.* **45,** 174-181 (1999).

[8] Ginsberg, S. D. *et al.* RNA sequestration to pathological lesions of neurodegenerative diseases. *Acta Neuropathol.* **96,** 487–494 (1998).

[9] Cherny, D., Hoyer, W., Subramaniam, V., Jovin, T. M. Double-stranded DNA stimulates the fibrillation of α-Synuclein *in vitro* and is associated with the mature fibrils: an electron microscopy study, *J. Mol. Biol.* **344,** 929-938 (2004).

[10] Jones, E. M., Surewicz, W. K. Fibril conformation as the basis of species- and strain-dependent seeding specificity of mammalian prion amyloids. *Cell* **121,** 63-72 (2005).

[11] Guo, J. L. *et al.* Distinct α-Synuclein strains differentially promote tau inclusions in neurons. *Cell* **154,** 103-117 (2013).

[12] DeJesus-Hernandez, M. *et al.* Expanded GGGGCC hexanucleotide repeat in noncoding region of C9ORF72 causes chromosome 9p-linked FTD and ALS. *Neuron* **72,** 245–256 (2011).

[13] Renton, A. E. *et al.* ITALSGEN Consortium. A hexanucleotide repeat expansion in C9ORF72 is the cause of chromosome 9p21-linked ALS-FTD. *Neuron* **72,** 257–268 (2011).

[14] Kim, H. J. *et al.* Mutations in prion-like domains in hnRNPA2B1 and hnRNPA1 cause multisystem proteinopathy and ALS. *Nature* **495,** 467–473 (2013).

[15] Hagerman, P. J., and Hagerman, R. J. The fragile-X premutation: a maturing perspective. *Am. J. Hum. Genet.* **74,** 805–816 (2004).

[16] Chen-Plotkin, A. S., Lee, V. M., and Trojanowski, J. Q. TAR DNA-binding protein 43 in neurodegenerative disease. *Nat. Rev. Neurol.* **6,** 211–220 (2010).

[17] Fardaei, M. *et al.* Three proteins, MBNL, MBLL and MBXL, co-localize in vivo with nuclear foci of expanded-repeat transcripts in DM1 and DM2 cells. *Hum. Mol. Genet.* **11,** 805–814 (2002).

[18] Miller, J. W. *et al.* Recruitment of human muscleblind proteins to (CUG)(n) expansions associated with myotonic dystrophy. *EMBO J.* **19,** 4439–4448 (2000).

[19] Diner, I. *et al.* Aggregation properties of the small nuclear ribonucleoprotein U1-70K in Alzheimer's Disease. *J. Biol. Chem.* **289,** 35296-35313 (2014).

[20] Wang, I. *et al.* Structure, dynamics and RNA binding of the multi-domain splicing factor TIA-1. *Nucleic Acids Res.* **42,** 5949-5966 (2014).

[21] Gilks, N. *et al.* Stress granule assembly is mediated by prion-like aggregation of TIA-1. *Mol. Biol. Cell* **15,** 5383–5398 (2004).

[22] Hackman, P. *et al*. Welander distal myopathy is caused by a mutation in the RNA-binding protein TIA1. *Ann. Neurol.* 23831 (2012).

[23] Klar, J. *et al.* Welander distal myopathy caused by an ancient founder mutation in TIA1 associated with perturbed splicing. *Hum. Mutat.* **34,** 572–577 (2013).

[24] Li, Y. R., King, O. D., Shorter, J., Gitler, A. D. Stress granules as crucibles of ALS pathogenesis. *J. Cell Biol.* **201,** 361–372 (2013).

[25] Liu-Yesucevitz, L. *et al.* Tar DNA binding protein-43 (TDP-43) associates with stress granules: analysis of cultured cells and pathological brain tissue. *PLoS ONE 5*, e13250 (2010).

[26] Aguzzi, A., Altmeyer, M. Phase separation: linking cellular compartmentalization to disease. *Trends in Cell Biol.* **26,** 547-558 (2016).

[27] Moore, M. J. From birth to death: the complex lives of eukaryotic mRNAs. *Science* **309,** 1514–1518 (2005).

[28] Parker, R., Sheth, U. P bodies and the control of mRNA translation and degradation. Mol. *Cell* **25,** 635–646 (2007).

[29] Anderson, P., Kedersha, N. Stress granules. *Curr. Biol.* **19,** R397–R398 (2009).

[30] Buchan, J. R., Parker, R. Eukaryotic stress granules: the ins and outs of translation. *Mol. Cell* **36,** 932–941 (2009).

[31] Wolozin, B. Regulated protein aggregation: stress granules and neurodegeneration. *Mol. Neurodegener.* **7,** 56 (2012).

[32] Raposo, G., Stoorvogel, W. Extracellular vesicles: exosomes, microvesicles, and friends. *J. Cell Biol.* **200,** 373–383 (2013).

[33] Lu, J-X. *et al.* Molecular structure of b-amyloid fibrils in Alzheimer's Disease Brain Tissue. *Cell* **154,** 1257-1268 (2013).

[34] Lührs, T. *et al.* 3D structure of Alzheimer's amyloid-β(1-42) fibrils. *Proc. Natl. Acad. Sci. USA* **102,** 17341-17347 (2005).

[35] Bush, C. A., Brahms, J. Conformation of nucleic acid, oligo- and polynucleotides by circular dichroism investigations. *Physico-Chemical Properties of Nucleic Acids*, edited by Duchesne, J. Academic Press Inc. (London) Ltd. 147-186 (1973).

[36] Bush, C. A., Tinoco Jr., I. Calculation of the optical rotary dispersion of dinucleoside phosphates. *J. Mol. Biol.* **23,** 601-614 (1967).

[37] Olsthoorn, C. S. M., Bostelaar, L. J., De Rooij, J. F. M., Van Boom, J. H., Altona, C. Circular Dichroism study of stacking properties of oligodeoxyadenylates and polydeoxyadenylate. *Eur. J. Biochem.* **115,** 309-321 (1981).

[38] Holmén, A., Broo, A., Albinsson, B., Nordén, B. Assignment of electronic transition moment directions of adenine from linear Dichroism. *J. Am. Chem. Soc.* **119,** 12240-12250 (1997).

[39] Schwartz, J. C., Wang, X., Podell, E. R., Cech, T. R. RNA seeds higher-order assembly of FUS protein. *Cell Rep.* **5,** 918-925 (2013).

[40] Ellis, R. J. Macromolecular crowding: obvious but underappreciated. *Trends Biochem. Sci.* **26,** 597-604 (2001).

Chapter 7: Mutualisms in Nucleic Acid/Peptide Domain Arrays

Nucleic acids and proteins are intimately linked in the cell. The ribosome, a conglomerate of proteins and ribosomal RNAs is essential to the central dogma and has been heralded as the Darwinian threshold of extant cellular life [1]. Beyond the ribosome, distinct interactions of RNA- and DNA-binding proteins with their respective targets finely tune spatial and temporal gene expression patterns [2-5]. The complexity and level of mutualism found in DNA/protein and RNA/protein interactions is astounding. Perhaps most prominent, are the effects observed when minor disruption of these interactions occurs. In myotonic dystrophy, microsatellite expansion of two RNAs leads to sequestration of splicing factors to nuclear foci and a disruption of normal RNA processing [6]. Ribonucleoprotein granule diseases encompass a large class of pathologies, and highlight how minor alterations in nucleic acid/protein interactions have dire consequences [7-12]. What we know about nucleic acids, proteins, and their interactions has been exploited for years in the pursuit of biomolecular nanotechnology. Specifically, the production of DNA origami [13] is founded on the basic set of principles Watson and Crick established in describing the double helix and base-pairing [14]. Others have attempted to exploit protein secondary structure interactions for the production of protein origami, succeeding in the formation of tetrahedra from coiled-coil domains [15]. Production of aptamer-based biosensors for detection of antibodies and other proteins has proved to be a valuable method in disease diagnoses, and specifically requires the interactions of nucleic acids and proteins [16].

In this dissertation, I described the mutualisms that likely persisted in the prebiotic environment between nucleic acids and short peptides, and how their collaboration might have supported archaic cellular networks. The manipulation of nucleic acid and peptide folding was explored in chapter 3 through the development of insulated guanine wires and responsive hydrogel systems for biomolecular nanotechnology. RNA processing was the focus of chapters 4 and 5 through the global and structural characterization of nucleic acid/peptide co-assemblies, nanostructures that provide insight to the pathological transition of mature RNP granules to fibrillar aggregates. Finally, I examined the interactions between RNA and the full-length Aβ40 and Aβ42 peptides of Alzheimer's disease, to further define the effects interception of mRNP granules by pathogenic proteins or peptides might produce. The conclusions and implications of these findings are described below.

Development of chimeras for bionanotechnology

Guanine quadruplexes, which are found naturally at telomeres, centromeres, and in multiple promoters [17,18], are capable of long-range electron transport and assemble to form micrometer long assemblies [17,19]. Peptides, which often have little to no conductivity [20], form nanostructures that are sequence- and context-dependent [21], and were chosen as insulators in the production of coated guanine wires. In chapter 3, the successful conjugation of the quadruplex-forming DNA sequence 'GGTG4TGG' to Ac-aELVIIAG-NH_2 was demonstrated. Guanine quadruplex peptide conjugates (GQPC) were co-assembled with free peptides (Ac-KLVIIAG-NH_2) to promote peptide assembly. Assembly was biased towards guanine quadruplex formation by heating the assembly components to 95°C for five minutes and allowing the solution to cool slowly to room temperature. GQPC/Ac-KLVIIAG-NH_2 co-assemblies revealed a unique conical nanotube morphology, which proved to be dependent on guanine quadruplex assembly; GQPC/Ac-KLVIIAG-NH_2 co-assemblies in lithium phosphate buffer did not form conical nanotubes. Guanine quadruplex assembly was further confirmed through use of the quadruplex-specific dye ISCH-oa1 by fluorescence spectroscopy [22]. From these data, we have yet to define the exact location of guanine quadruplexes within the co-assemblies, or their degree of stacking, but it is clear these results provide a firm foundation for the exploitation of mutualisms in the production of nanodevices.

Engineering homogeneous nucleic acid/peptide co-assemblies

RNP granule disorders often result from the mislocalization of essential RNA processing components [7-12]. Altered ribostasis has been offered as an explanation for neurodegenerative and other protein-misfolding diseases [23], most notably Amyotrophic Lateral Sclerosis, where accumulation of nuclear foci containing protein aggregates often accompany cellular pathologies [11,24]. In chapters 4 and 5 we sought to characterize the interactions between aggregation-prone peptides and nucleic acids through the design and production of homogeneous nucleic acid/peptide co-assemblies. After sampling congeners derived from Aβ16-22, the nucleating core of Aβ40/42 of Alzheimer's disease, the peptides Ac-KLVIIAG-NH_2 and Ac-RLVIIAG-NH_2 were chosen for further investigation. Both, Ac-KLVIIAG-NH2 and Ac-RLVIIAG-NH2 self-assemble as fibers in 40% acetonitrile and water. However, interactions with nucleic acids influence global morphology, giving rise to ribbons 10 to 20 times the width of fibers, in the same conditions. Co-assembly of nucleic acids and peptides was first confirmed by fluorescence and electrostatic force microscopy, where co-localization of amyloid and RNA domains and surface charges were mapped, respectively. Examination of multi-lamellar ribbon and nanotube wall architecture identified each lamella with a width corresponding to the extended peptide length of 2.6 nm, and consistent with a single β-sheet peptide monolayer defining each layer. CD melting curves assessed thermal stability and nuclease digestion revealed dynamic components of co-assembly architecture.

Structural characterization of DNA/Ac-KLVIIAG-NH_2 co-assemblies was the focus of chapter 5. Through use of solid state NMR, $^{13}C\{^{15}N\}$REDOR, the peptide orientation and registry was assigned as anti-parallel, in-register for 92% of co-assemblies and only 37% of Ac-KLVIIAG-NH_2 fibrous assemblies, suggesting nucleic acids select for anti-parallel in-register conformations during nucleation. $^{13}C\{^{31}P\}$REDOR defined the position of phosphorus nuclei as 8.9Å from the ^{13}C-enriched carbonyl of the leucine residue, with a Gaussian distribution of 2.4Å in width. For $^{13}C\{^{31}P\}$REDOR, 100% of the ^{13}C nuclei were dephased by ^{31}P, placing DNA between the lamellae of the ribbon and nanotube walls and supporting a model that precisely defines the passivation of the cross-β interface by nucleic acids.

Comprehensive models for RNA processing and disease etiology

To interrogate the altered ribostasis hypothesis, chapter 6 focused on the characterization of Aβ40/42 co-assembly with RNA. Defining these interactions would support the interception of mRNP granules by β-sheet-prone infectious domains and offer an explanation for the sequestration of RNAs to immature senile plaques of Alzheimer's disease [25-28] and mature fibrils of other protein-misfolding diseases [29]. Through use of TEM, the observed fibrillation of Aβ in the presence of and absence of RNA was characterized. The ordering of RNA in Aβ/RNA co-assemblies was examined by CD where a typical A-form helix elliptical signature was observed. Compared to RNA alone, the RNA of Aβ/RNA co-assemblies was more ordered giving rise to an increase in the observed molar ellipticities of A-form RNA helices by CD.

In summary, the mutualisms examined within this dissertation provide a firm foundation for understanding the diverse interactions nucleic acids and proteins/peptides maintain. In chapters 2 and 3, the sequence- and context-dependent folding of peptide and nucleic acid/peptide conjugate assemblies was investigated. The results from these chapters begin to reveal how mutualisms may be exploited in the development of devices for biomolecular nanotechnology. Disruption of canonical nucleic acid/protein mutualisms was explored in chapters 4, 5, and 6, and provide a comprehensive model for mRNP granule interception and altered ribostasis in disease etiology. These data also provide insight into the influence of nucleic acid sequestration on amyloid gross morphology in neurodegenerative amyloidosis where nucleic acids may select for neurotoxic strains. The manipulation of the nucleic acid/peptide interactions described here provide the groundwork for future work interrogating biopolymer mutualism.

We can now use the mutualisms described herein to develop more comprehensive models of protein/nucleic acid complementarity. The manipulation of these precise, yet accommodating, interactions provide support for the production of dynamic, responsive systems for use in biotechnology, and their dispersion *in vivo* through novel therapeutics will contribute to our understanding of nucleic acid/peptide interactions at disease lesions in protein misfolding disorders. Specifically, the continuation of the project outlined in chapter 6 will culminate in a better understanding of the role of mRNA at senile plaques, and how it might influence amyloid gross morphology or neurotoxicity. These findings may lead to the development of novel therapeutics targeting these specific co-assemblies. Cross-seeding of beta-sheet prone infectious domains with low complexity domains (LCD) of RNA binding proteins at ribonucleoprotein granules is currently being explored as an avenue for RNA sequestration to disease lesions, and may provide further insight to the etiology of RNP granule disorders and the emergence of fibrillar assemblies in a multitude of diseases.

In chapter 3, the description of peptide-insulated guanine nanowires for nanocircuitry continues with the interrogation of nanostructure morphology. The data and conclusions from chapters 4 through 6 provide a firm foundation for identifying the prominent contributing interactions to conical tube morphology, and may help to define the location and degree of stacking of the guanine quadruplexes within the conical nanostructures.

References

[1] Woese, C.R. On the evolution of cells. *Proc. Natl. Acad. Sci. USA* **99,** 8742–8747 (2002).

[2] Lunde, B.M.; Moore, C.; Varani, G. RNA-binding proteins: Modular design for efficient function. *Nat. Rev. Mol. Cell Bio.* **8,** 479–490 (2007).

[3] Hoffman, M.M.; Khrapov, M.A.; Cox, J.C.; Yao, J.; Tong, L.; Ellington, A.D. AANT: The amino acid-nucleotide interaction database. *Nucleic Acids Res.* **32,** D174–D181 (2004).

[4] Jones, S.; van Heyningens, P.; Berman, H.M.; Thornton, J.M. Protein-DNA interactions: A structural analysis. *J. Mol. Biol.* **287,** 877–896 (1999).

[5] Nadassy, K.; Wodak, S.J.; Janin, J. Structural features of protein-nucleic acid recognition sites. *Biochemistry* **38,** 1999–2017 (1999).

[6] Miller, J. W. *et al.* Recruitment of human muscleblind proteins to (CUG)(n) expansions associated with myotonic dystrophy. *EMBO J.* **19,** 4439–4448 (2000).

[7] DeJesus-Hernandez, M. *et al.* Expanded GGGGCC hexanucleotide repeat in noncoding region of C9ORF72 causes chromosome 9p-linked FTD and ALS. *Neuron* **72,** 245–256 (2011).

[8] Renton, A. E. *et al.* ITALSGEN Consortium. A hexanucleotide repeat expansion in C9ORF72 is the cause of chromosome 9p21-linked ALS-FTD. *Neuron* **72,** 257–268 (2011).

[9] Kim, H. J. *et al.* Mutations in prion-like domains in hnRNPA2B1 and hnRNPA1 cause multisystem proteinopathy and ALS. *Nature* **495,** 467–473 (2013).

[10] Hagerman, P. J., and Hagerman, R. J. The fragile-X premutation: a maturing perspective. *Am. J. Hum. Genet.* **74,** 805–816 (2004).

[11] Chen-Plotkin, A. S., Lee, V. M., and Trojanowski, J. Q. TAR DNA-binding protein 43 in neurodegenerative disease. *Nat. Rev. Neurol.* **6,** 211–220 (2010).

[12] Diner, I. *et al.* Aggregation properties of the small nuclear ribonucleoprotein U1-70K in Alzheimer's Disease. *J. Biol. Chem.* **289,** 35296-35313 (2014).

[13] Ke, Y., Ong, L. L., Shih, W. M., Yin, P. Three-Dimensional Structures Self-Assembled from DNA Bricks. *Science* **338,** 1177-1183 (2012).

[14] Watson, J.D.; Crick, F.H.C. Molecular structures of nucleic acids. *Nature* **171,** 737–738 (1953).

[15] Gradišar, H., Jerala, R. Self-assembled bionanostructures: proteins following the lead of DNA nanostructures. *J. Nanobiotechnol.* **12** (2014).

[16] Zhang, L., Lei, J., Liu, L., Li, C., Ju, H. Self-assembled DNA hydrogel as switchable material for aptamer-based fluorescent detection of protein. *Anal. Chem.* **85,** 11077-11082 (2013).

[17] Marsh, T. C., Henderson, E. G-wires: self-assembly of a telomeric oligonucleotide, d(GGGGTTGGGG), into large superstructures. *Biochemistry* **33,** 10718-10724 (1994).

[18] Changenet-Barret, P., Hua, Y., Gustavsson, T., Markovitsi, D. Electronic excitations in G-quadruplexes formed by the human telomeric sequence: a time-resolved fluorescence study. *Photochem. Photobiol.* **91,** 759-765 (2015).

[19] Woiczikowski, P. B., Kubar, T., Gutiérrez, R., Cuniberti, G., Elstner, M. Structural stability versus conformational sampling in biomolecular systems: why is the charge transfer efficiency in G4-DNA better than in double-stranded DNA? *J. Chem. Phys.* **133,** 035103 (2010).

[20] Domigan, L. *et al.* Dielectrophoretic manipulation and solubility of protein nanofibrils formed from crude crystallins. *Electrophoresis* **34,** 1105-1112 (2013).

[21] Mehta, A. K. *et al.* Context dependence of protein misfolding and structural strains in neurodegenerative diseases. *Biopolymers* **100,** 722-730 (2013).

[22] Chen, S-B. *et al.* Visualization of *NRAS* RNA G-quadruplex structures in cells with an engineered fluorogenic hybridization probe. *J. Am. Chem. Soc.* **138,** 10382-10385 (2016).

[23] Ramaswami, M., Taylor, J. P., Parker, R. Altered ribostasis: RNA-protein granules in degenerative disorders. *Cell* **154,** 727-736 (2013).

[24] Schwartz, J. C., Wang, X., Podell, E. R., Cech, T. R. RNA seeds higher-order assembly of FUS protein. *Cell Rep.* **5,** 918-925 (2013).

[25] Marcinkiewics, M. βAPP and Furin mRNA concentrates in immature senile plaques in the brain of Alzheimer patients. *J. Neuropathol. Exp. Neurol.* **61,** 815-829 (2002).

[26] Ginsberg, S. D. *et al.* Predominance of neural mRNAs in individual Alzheimer's Disease senile plaques. *Ann. Neurol.* **45,** 174-181 (1999).

[27] Ginsberg, S. D. *et al.* RNA sequestration to pathological lesions of neurodegenerative diseases. *Acta Neuropathologia*, **96,** 487-494 (1998).

[28] Ginsberg, S. D., Crino, P. B., Lee, V. M-Y., Eberwine, J. H., Trojanowski J. Q. Sequestration of RNA in Alzheimer's Disease Neurofibrillary Tangles and Senile Plaques. *Ann. Neurol*. **41,** 200-209 (1997).

[29] Cherny, D., Hoyer, W., Subramaniam, V., Jovin, T. M. Double-Stranded DNA Stimulates the Fibrillation of α-Synuclein *in vitro* and is Associated with the Mature Fibrils: An Electron Microscopy Study. *J. Mol. Biol.* **344,** 929-938 (2004).